

# Complex (dusty) plasmas: Current status, open issues, perspectives

V.E. Fortov<sup>a</sup>, A.V. Ivlev<sup>b,\*</sup>, S.A. Khrapak<sup>b</sup>, A.G. Khrapak<sup>a</sup>, G.E. Morfill<sup>b</sup>

<sup>a</sup>*Institute for High Energy Densities, Russian Academy of Sciences, 125412 Moscow, Russia*

<sup>b</sup>*Max-Planck-Institut für Extraterrestrische Physik, D-85741 Garching, Germany*

Accepted 30 August 2005

Available online 7 October 2005

editor: S. Cowley

## Abstract

The field of complex (dusty) plasmas—low-temperature plasmas containing charged microparticles—is reviewed: The major types of experimental complex plasmas are briefly discussed. Various elementary processes, including grain charging in different regimes, interaction between charged particles, and momentum exchange between different species are investigated. The major forces on microparticles and features of the particle dynamics in complex plasmas are highlighted. An overview of the wave properties in different phase states, as well as recent results on the phase transitions between different crystalline and liquid states are presented. Fluid behaviour of complex plasmas and the onset of cooperative phenomena are discussed. Properties of the magnetized complex plasmas and plasmas with nonspherical particles are briefly mentioned. In conclusion, possible applications of complex plasmas, interdisciplinary aspects, and perspectives are discussed.

© 2005 Elsevier B.V. All rights reserved.

PACS: 52.27.Lw

Keywords: Dusty plasmas; Complex plasmas

## Contents

1. Introduction	3
2. Types of experimental complex plasmas	4
2.1. Complex plasmas in rf discharges	4
2.1.1. Ground-based experiments	4
2.1.2. Microgravity experiments	4
2.2. Complex plasmas in dc discharges	6
2.2.1. Ground-based experiments	6
2.2.2. Microgravity experiments	7
2.3. Other types of complex plasmas	7
2.3.1. Complex plasmas at cryogenic temperatures	7
2.3.2. Thermal complex plasmas	8
2.3.3. Nuclear-induced and track complex plasmas	9
3. Charging of particles in complex plasmas	9
3.1. Charging in isotropic (bulk) plasmas	9

\* Corresponding author.

E-mail address: [ivlev@mpe.mpg.de](mailto:ivlev@mpe.mpg.de) (A.V. Ivlev).

3.1.1. Motion of a particle in the central field	9
3.1.2. Orbit motion limited (OML) approximation	12
3.1.3. Accuracy of the OML approximation	14
3.1.4. Charging in a weakly collisional regime	15
3.1.5. Charging in a strongly collisional regime	18
3.1.6. Transitions between the charging regimes	19
3.2. Charging in anisotropic plasmas	19
3.3. Other effects important for particle charging	23
3.4. Role of microparticles in plasma charge balance	24
3.5. Fluctuations of the particle charge	25
4. Electrostatic potential around a particle	26
4.1. Isotropic plasmas	26
4.2. Anisotropic plasmas	28
5. Interaction between particles in complex plasmas	30
5.1. Isotropic plasmas	30
5.2. Anisotropic plasmas	31
5.3. Experiments	31
6. Momentum exchange in complex plasmas	32
6.1. Momentum transfer cross section	33
6.2. Momentum exchange rates	36
6.2.1. Grain–electron collisions	37
6.2.2. Grain–ion collisions	37
6.2.3. Grain–grain collisions	38
6.3. Momentum exchange diagram	38
7. Forces on particles in complex plasmas	40
7.1. Ion drag force	41
7.1.1. Binary collision approach	41
7.1.2. Kinetic approach	42
7.1.3. Complementarity of the two approaches	45
7.2. Other forces	45
8. Dynamics of single particles and particle ensembles	47
8.1. Single particle dynamics	47
8.2. Role of charge fluctuations in the particle dynamics	47
8.3. Dynamics of ensembles with spatially varying charges	49
8.4. Complex plasmas as non-Hamiltonian systems	49
9. Waves and instabilities in complex plasmas	50
9.1. Wave excitation technique	50
9.2. Waves in ideal (gaseous) complex plasmas	51
9.2.1. Major wave modes	52
9.2.2. Damping and instabilities of the DIA and DA mode	55
9.3. Waves in strongly coupled (liquid) complex plasmas	58
9.3.1. Longitudinal waves	58
9.3.2. Transverse waves	60
9.4. Waves in plasma crystals	60
9.4.1. One-dimensional string	60
9.4.2. Two-dimensional triangle lattice	61
9.4.3. Three-dimensional plasma crystals	63
9.4.4. Instabilities in plasma crystals	65
9.5. Nonlinear waves	66
9.5.1. Ion solitons and shocks	66
9.5.2. Dust solitons and shocks	66
9.5.3. Mach cones	68
10. Phase transitions in strongly coupled complex plasmas	69
10.1. Strong coupling of dust species	69
10.2. Phase diagram of Debye–Hückel (Yukawa) systems	71
10.3. Experimental investigation of phase transitions in complex plasmas	72
10.3.1. Melting	73
10.3.2. Crystallization	74
11. Fluid behaviour of complex plasmas	76
11.1. Transport properties	76
11.2. Hydrodynamic instabilities	77
12. Onset of cooperative phenomena in complex plasmas	79

12.1. Coulomb clusters .....	79
12.2. Nanofluidics .....	83
13. Magnetized complex plasmas .....	83
14. Complex plasmas with nonspherical particles .....	86
15. Possible applications .....	88
16. Interdisciplinarity and perspectives .....	89
17. Conclusion .....	91
Acknowledgements .....	91
References .....	91

## 1. Introduction

“Dusty”, or “complex” plasmas are plasma containing solid or liquid particles (dust) which are charged. The charges can be negative or positive, depending on the charging mechanisms operating in the plasmas. Dust and dusty plasmas are quite natural in space. They are present in planetary rings, comet tails, interplanetary and interstellar clouds [1–3], found in the vicinity of artificial satellites and space stations [4,5], etc. Also, dusty plasmas are actively investigated in laboratories. Currently, the term “complex plasmas” is widely used in the literature to distinguish dusty plasmas specially “designed” for such investigations.

The presence of massive charged particles in complex plasmas is essential for the collective processes. Ensembles of microparticles give rise to new very-low-frequency wave modes which represent the oscillations of particles against the quasiequilibrium background of electrons and ions. Overall dynamical time scales associated with the dust component are in the range 10–100 Hz. The particles themselves are large enough to be visualized individually and, hence, their motion can be easily tracked. This makes it possible to investigate phenomena occurring in complex plasmas at the most fundamental kinetic level.

Micron size particles embedded in a plasma do not only change the charge composition, they also introduce new physical processes into the system, e.g., effects associated with dissipation and plasma recombination on the particle surface, variation of the particle charges, etc. These processes imply new mechanisms of the energy influx into the system. Therefore, complex plasmas are a new type of non-Hamiltonian systems with the properties which can be completely different from those of usual multicomponent plasmas.

Dust plays an exceptionally important role in technological plasma applications, associated with the utilization of plasma deposition and etching technologies in microelectronics, as well as with production of thin films and nanoparticles [6–8]. To control these processes, it is necessary to understand the basic mechanisms determining, e.g., transport of dust particles, influence of dust on plasma parameters, etc.

Due to large charges carried by the grains (typically, of the order of thousand elementary charges for a micron-size particle), the electrostatic energy of the mutual interaction is remarkably high. Hence, the strong electrostatic coupling in the dust subsystem can be achieved much more easily than in the electron–ion subsystem. In complex plasmas, one can observe transitions from a disordered gaseous-like phase to a liquid-like phase and the formation of ordered structures of dust particles—plasma crystals. The first experimental observation of the ordered (quasicrystalline) structures of charged microparticles obtained in a modified Paul’s trap was reported in 1959 by Wuerker et al. [9]. The possibility of dust subsystem crystallization in a nonequilibrium gas discharge plasma was predicted by Ikezi in 1986 [10]. The first experimental observations of ordered particle structures were reported in 1994 in rf discharges [11–14]. Later on, plasma crystals were found in dc discharges [15], thermal plasmas at atmospheric pressure [16], and even in nuclear-induced dusty plasmas [17].

The enormous increase of interest in complex plasmas was triggered in the mid 1990’s, by the laboratory discovery of plasma crystals. Today, the physics of complex plasmas is a rapidly growing field of research, which covers various fundamental aspects of the plasma physics, hydrodynamics, kinetics of phase transitions, nonlinear physics, solid states, as well as the industrial applications, engineering, and astrophysics. More and more research groups throughout the world have become involved in the field, and the number of scientific publications is growing exponentially. In this review, we have made an attempt to provide a balanced and consistent picture of the current status of the field, by covering the latest development in the most important directions of the experimental and theoretical complex plasmas, and outlined the perspective issues to pursue in future. We decided to omit the discussion of the space and atmospheric

dusty plasmas, chemical plasmas with growing particles, etc. —their properties are so diverse and the whole field is so huge that one cannot span it in the framework of a single review.

## 2. Types of experimental complex plasmas

Since the discovery of plasma crystals in 1994, the experimental investigations of complex plasmas have been going on in dozens of laboratories throughout the world. In this section we briefly discuss the major types of the experimental setups employed to study various phenomena occurring in complex plasmas.

### 2.1. Complex plasmas in rf discharges

#### 2.1.1. Ground-based experiments

Plasma crystals were discovered in a capacitively coupled low-pressure rf discharge in inert gases almost simultaneously in several laboratories [11–14]. The schematic of a typical experimental setup [18] is shown in Fig. 1. The experimental apparatus includes a lower electrode 5–10 cm in diameter capacitively coupled to an rf generator (at frequency 13.56 MHz) and an upper grounded electrode. The electrodes are placed in a vacuum chamber. Micron-size dust particles fill a container and can be introduced into the discharge through a metallic grid. The electrode separation is typically 3–10 cm. The particle visualization is performed with the use of laser illumination. The laser beam is transformed into a sheet approximately 100  $\mu\text{m}$  thick using a lens and illuminates the particles in the horizontal or vertical plane. The particles introduced into the discharge become (highly) charged negatively and levitate in the pre-sheath or sheath region above the lower electrode, where the electric force balances the gravity. To confine the particles horizontally, a metallic ring with an inner diameter of 3–6 cm and a height of 1–3 mm is placed on the lower electrode. Sometimes, instead of a ring, a special curved electrode is used. The light scattered by the particles is recorded by a video camera.

Under certain conditions, the particles form ordered structures consisting of several fairly extended horizontal layers. The number of particles in such crystalline structures can be as high as  $\sim 10^4$ – $10^5$ , and the number of layers can vary from one to a few dozen [19]. Usually the particles assemble themselves into hexagonal structures in each layer. Vertically, they often settle strictly below each other, forming a cubic lattice between neighbouring layers—the so-called “vertically aligned” hexagonal lattices. Such an arrangement is believed to be a consequence of ion focusing downstream from the particles—the wake effect (see Sections 5.2 and 10.3).

For reference, we summarize typical parameters of rf discharges and complex plasmas in laboratory experiments: Particle sizes are in the range  $\sim 1$ – $30 \mu\text{m}$ . The neutral (typically inert) gas pressure  $\sim 1$ – $100 \text{ Pa}$ . The plasma concentration in the bulk of a discharge is  $n_e \sim n_i \sim 10^7$ – $10^{10} \text{ cm}^{-3}$ , the electron temperature is  $T_e \sim 1$ – $5 \text{ eV}$ , and ions are typically assumed to be in equilibrium with neutrals (usually at room temperature), so that  $T_i \sim T_n \sim 0.03 \text{ eV}$ . The sheath is a region of a positive space charge where the ion concentration exceeds that of electrons even in the absence of dust. The ion velocity at the edge of the collisionless sheath satisfies the Bohm criterion  $u_i \geq C_{\text{IA}} \equiv \sqrt{T_e/m_i}$ . For the collisional sheath, the ion directed velocity can be lower than the velocity of sound, but the ions are still typically superthermal:  $u_i \gtrsim v_{T_i}$ . The characteristic spatial scale of the charge screening in the sheath is given by the electron Debye radius  $\lambda_{De}$ , because fast ions do not contribute substantially to the screening. The interparticle interaction is essentially anisotropic in this case.

#### 2.1.2. Microgravity experiments

Complex plasmas formed under microgravity conditions have been intensively investigated in rf discharges during the last few years. A typical sketch of the experimental setup is shown in Fig. 2. The results of the first sounding rocket (TEXUS) experiments (with about 6 min of microgravity) and their qualitative analysis were reported by Morfill et al. [20]. Currently, the “Plasma Crystal” (PKE-Nefedov) laboratory is in operation onboard the International Space Station (ISS), created within the framework of the Russian–German scientific cooperation program [21]. The major tasks of the PKE-Nefedov include investigations of dusty plasma crystals, phase transitions, wave phenomena, properties of boundaries between different plasma regions, etc. in a three-dimensional isotropic dusty plasma at the kinetic level. The first “basic” experiments designed to study the behaviour of the dust component over a broad range of dusty plasma

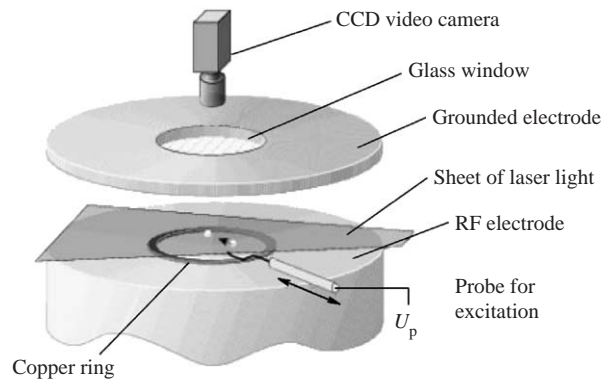


Fig. 1. Sketch of typical experimental setup used for laboratory investigations of complex plasmas in a rf discharge [18].

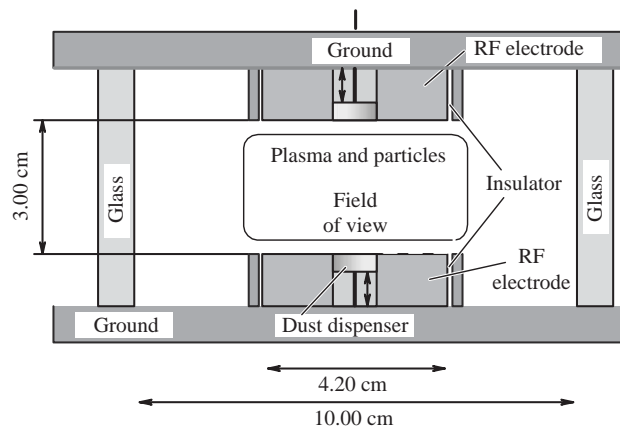


Fig. 2. Sketch of the rf parallel plate discharge used in microgravity experiments [20]. Monodisperse particles of different sizes can be injected into the plasma chamber from two dispensers mounted in the upper and lower electrodes. The microparticles are illuminated by a thin (about  $150\ \mu\text{m}$ ) sheet of laser light perpendicular to the electrode system. Slow-speed scanning of the laser into the depth of the plasma chamber is used to measure the 3D positions of the microparticles.

parameters were performed at the beginning of March 2001. Currently, most of the investigations are in the active phase or in the stage of data analysis.

The typical static and dynamic behaviour of complex plasmas under microgravity conditions is illustrated in Fig. 3. The figure shows the trajectories of microparticles. The dominant features are: (i) a microparticle free “void” in the centre of the system for most experimental parameters, (ii) a sharp boundary between the void and the complex plasma, (iii) demixing of complex plasma clouds formed by microparticles of different sizes, (iv) crystalline structures along the central axis, and (v) torus-shaped vortices in different areas away from the central axis.

The microparticle-free centre between the electrodes—the void—can be explained by the balance of forces acting on the particles in the discharge (see, e.g., [22–24]). Since the dominant force on earth—gravity—is reduced by orders of magnitude the weaker forces start playing major role. These forces are the electrostatic force arising from the electric field in the discharge and pointed toward the centre (plasma potential has a maximum in the centre), and the ion drag force which pushes particles to the periphery. It is well established that even a relatively small number of particles is repelled from the centre, suggesting that the void formation is *not* a collective particle effect. At present, the ion drag is commonly believed to be the most probable mechanism responsible for the void formation (see, e.g., Ref. [25] and references therein). The ion drag force and the electrostatic force have different dependencies on the grain size. This causes demixing of different particle sizes: an equilibrium position of smaller particles is closer to the centre than that of larger ones. The void can be closed under special experimental conditions. These conditions are neutral gas

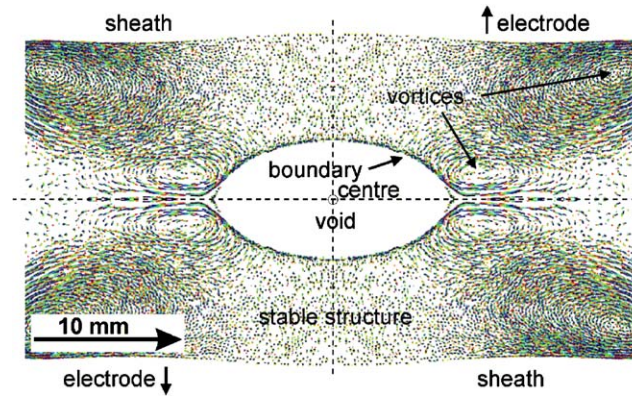


Fig. 3. Typical image of the dust cloud obtained in the PKE-Nefedov experiments under microgravity conditions [21]. Trajectories of particles are shown over 3 s.

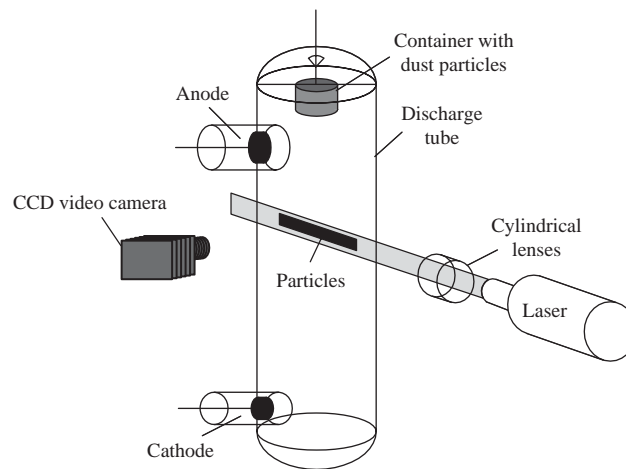


Fig. 4. Sketch of typical experimental setup used for laboratory investigations of complex plasmas in a dc glow discharge.

pressures below 50 Pa and the lowest possible rf-voltages, close to the plasma-off condition. At these parameters the plasma density is so low and the electric field is so weak that the electrostatic force dominates and the particles are pushed to the centre.

The possible mechanisms responsible for the vortex formation are discussed in Section 8.3.

## 2.2. Complex plasmas in dc discharges

### 2.2.1. Ground-based experiments

A dc gas discharge is also widely used for experimental investigations of complex plasmas [15,26–28]. Usually, a dc glow discharge is employed, as shown in Fig. 4. The particles are illuminated by a laser light and their positions are registered by a video camera. Typically, a neutral gas pressure is in the range  $\sim 10$ –500 Pa and a discharge current is  $\sim 0.1$ –10 mA. The ordered structures are usually observed in standing striations of the positive column of the glow discharge but can also be seen in an electric double layer formed in the transition region between the narrow cathode part of the positive column and the wide anode part, or in a specially organized multielectrode system having three or more electrodes at different potentials, etc. —that is, in the regions where the vertical electric field can be strong enough to levitate the particles. For these regions, some sheath properties considered above in the context of an rf discharge (e.g., plasma anisotropy, ion drift) are also relevant.



In the positive column of a low-pressure discharge, the loss of electron energy in elastic collisions is small and the electron distribution function is formed under the action of the electric field and inelastic collisions. This can lead to the appearance of striations—regions of spatial periodicity of the plasma parameters with the characteristic scale of an order of a few centimeters [29–31]. The electron concentration, their energy distribution, and the electric field are highly nonuniform along the striation length. The electric field is relatively strong (around 10–15 V/cm at a maximum) at the head of striation—this region may occupy 25–30% of the total striation length, and relatively weak (around 1 V/cm) outside this region. The maximum value of the electron concentration is shifted relative to the maximum strength of the electric field in the direction of the anode. The electron energy distribution is essentially bimodal, with the head of the striation being dominated by the second maximum whose centre lies near the excitation energy of neutral gas atoms. The centre-to-wall potential difference at the head of the striation reaches 20–30 V. Therefore, an electrostatic trap is formed, which allows us to levitate particles against gravity (provided the particles are not too heavy).

The complex plasma structures in dc glow discharges typically form as follows: after being injected into the plasma of the positive column, the charged particles fall past their equilibrium position and then, over the course of several seconds, emerge and form a regular structure which is preserved sufficiently long (until the end of observation) provided that the discharge parameters are unchanged. The simultaneous existence of ordered structures in several neighbouring striations can be observed, indicating the possibility of forming structures much more extended in the vertical direction compared to rf discharges. Three-dimensional quasicrystalline structures in a dc discharge were reported for the first time in Ref. [26].

In addition to a glow dc discharge, other types of combined dc discharges can be also employed. For example, a dusty double plasma device is used for experimental investigations of ion–acoustic waves [32]: The system is separated into a source and target sections by a mesh grid kept at a floating potential. The source and target plasma are produced by the dc discharges between filaments and magnetic cages (a magnetic field is used for the plasma confinement). The experiments are performed at low pressures,  $\sim 10^{-2}$  Pa, which is essential to ensure weak collisional damping of ion–acoustic waves.

### 2.2.2. Microgravity experiments

The microgravity experiments with complex plasmas in a dc discharge were performed onboard the “Mir” space station [33–35]. The major difference between this experimental apparatus and that used for the ground-based experiments (see Fig. 4) was the presence of a two-grid electrode placed between the cathode and the anode. During the experiments, the electrode was at the floating potential and prevented negatively charged particles from escaping to the anode. Microgravity allowed us to perform experiments with very large (bronze) particles with a mean radius  $a \simeq 65 \mu\text{m}$ .

By analysing the video images of the complex plasma structure formed near the grid electrode, the static (pair correlation function) and dynamic (diffusion coefficient) characteristics of the dust particle system were recovered. Measured pair correlation functions revealed the formation of ordered structures of dust particles of a liquid-like type (short-range order). Such experiments can provide deeper insight into the physics of charging and interaction of large particles ( $a \geq \lambda_{Di}$ ), a subject relatively poorly studied, mainly because ground-based experiments with such large particles are typically impossible.

Also, a combination of a dc and rf (inductively coupled) discharges—the “Plasma Kristall-4” (PK-4) facility shown in Fig. 5—is planned to be used in future microgravity experiments [36,37]. The PK-4 setup mainly utilizes a dc discharge plasma, which can optionally be combined with one or two rf coils installed on the discharge tube. This offers in particular the capability to perform kinetic studies of a great variety of dynamical phenomena in complex plasmas, such as laminar shear flows and their transition into the turbulent regime, formation of waves and their propagation, collision experiments and shock wave generation, cooperative phenomena, etc.

## 2.3. Other types of complex plasmas

### 2.3.1. Complex plasmas at cryogenic temperatures

The first experiments with cryogenic dusty plasmas at a liquid-nitrogen temperatures (77 K) were performed recently in dc glow discharge and capacitively coupled rf discharge [38,39]. Dust structures were formed with MgO particles

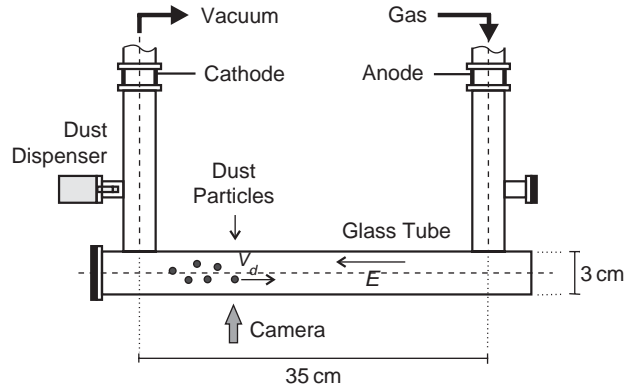


Fig. 5. Sketch of experimental setup PK-4 for investigations of complex dc and combined dc/rf plasmas under microgravity conditions [37]. A dc discharge is operated in a U-shaped glass tube with a radius of 1.5 cm filled with neon gas at pressures 20–200 Pa. The complex plasma is formed by injecting spherical particles into the discharge.

(3–5  $\mu\text{m}$  in diameter) and observed in striations of the positive column of a dc glow discharge in a quartz discharge tube (2 cm in diameter) immersed vertically into a cryostat filled with liquid nitrogen. The capacitive rf discharge was ignited between two copper-foil rings mounted 4 cm from each other outside the tube. Air at pressures below 10 Pa served as a plasma-forming gas.

In experiments with dc plasmas, the whole character of the discharge changes at cryogenic temperatures—visually, even the shape of the striations in the glow discharge at 77 K is absolutely different from that seen at room temperature. Very extended (about 20 cm) ordered structures consisting of long chains and occupying practically the whole volume below the level of liquid nitrogen are formed. The key role in the stability of such structures is played by the longitudinal thermophoretic force. Strong temperature gradients arise from two sides—from below, at the cathode (because of the heat release in the cathode zone) and from above, at the boundary of liquid nitrogen. Therefore, the dust structure is confined in an “electro-thermal” trap, where the vertical stability is provided by the balance of gravity, the longitudinal electric field, and the thermophoretic forces. The dust structure becomes separated into several parts, each 4–5 cm long, as the pressure decreases. The resulting structure is, however, unstable with respect to longitudinal low-frequency perturbations. This is probably caused by onset of the ion streaming instability (see Section 9.2.2).

In experiments with an rf discharge it was found that at cryogenic temperatures the density of dust particles in the main volume of the ordered structures can increase considerably. Probably, this is related to the decrease of the screening radius, which allows the particles to approach closer to each other [38,39]. In the lower part of dust structures, the propagation of nonlinear density waves was observed. The dust–acoustic wave velocity in cryogenic conditions was several times larger than in normal conditions. At lower pressures, the emerging instabilities led to the formation of multiple horizontal layers with clear boundaries.

### 2.3.2. Thermal complex plasmas

A thermal plasma is a low-temperature plasma characterized by equal temperatures of the electron, ion, and neutral components. The existence of liquid or solid small-sized particles in such a plasma can significantly affect its electro-physical properties. Effects associated with the presence of particles were observed in early experiments focused on studying plasmas of hydrocarbon flames (see, e.g., [40]).

Experimental investigations of the ordered dust structure formation in a thermal plasma were performed in a quasilaminar, weakly ionized plasma flow at temperatures of 1700–2200 K and atmospheric pressure in Refs. [16,41–49]. A plasma source formed an extended and uniform volume (about 30 cm<sup>3</sup>) of quasineutral thermal plasma, where the particles of CeO<sub>2</sub> were introduced. The main plasma components were the charged particles, electrons, and singly charged Na<sup>+</sup> ions. The electron density varied in the range 10<sup>9</sup>–10<sup>12</sup> cm<sup>−3</sup>. The dust particles were charged by background electron and ion fluxes and via thermionic emission. The latter mechanism played the dominant role and therefore the particle were charged positively, up to 10<sup>2</sup>–10<sup>3</sup> elementary charges.



### 2.3.3. Nuclear-induced and track complex plasmas

Nuclear-induced plasmas are produced by nuclear-reaction products which, passing through a medium, create ion–electron pairs as well as excite atoms and molecules in their tracks. The experiments were performed in an ionization chamber which is placed in a hermetical transparent cell [17]. Either  $\beta$ -particles (decay products of  $^{141}\text{Ce}$ ) or  $\alpha$ -particles and fission fragments (decay products of  $^{252}\text{Cf}$ ) were used as ionizing particles [17,50]. In terms of physical characteristics, the nuclear-induced plasma of inert gases is very different from thermal and gas discharge plasmas. Because of enormous spatial and temporal inhomogeneities of the plasma density, the charge of each individual particle changes substantially whenever it crosses the electron or the ion clouds, so that the average charge is derived from the statistical treatment of these events [17,50].

Recently, experimental investigations of the track complex plasmas produced by proton beams were performed [51,52]. The motion of  $\text{CeO}_2$  grains arranged in compact vortex structures was observed. The collective behaviour of dust particles was found to depend critically on the strength of the external electric field.

## 3. Charging of particles in complex plasmas

The particle charge is one of the most important parameters of complex plasmas. It determines the particle interactions with plasma electrons and ions, with electromagnetic fields, between the particles themselves, etc. Hence all studies of complex plasmas necessarily begin with a model for the particle charge. This section presents an overview of recent achievements in the understanding of particle charging in plasmas. We mostly focus on gas-discharge plasmas, where the charging is due to the collection of electrons and ions from the plasma, so that the charge is determined by the competition between the electron and ion fluxes on the particle surface. Other processes which can also affect charging (e.g., secondary, thermionic and photoelectric emission of electrons from the particle surface) are discussed only briefly. We address problems such as stationary particle charge, kinetics of the charging, the effect of ion–neutral collisions, the self-consistent effect of the presence of dust, and the charge fluctuations. Theoretical results are complemented by the available experimental data.

### 3.1. Charging in isotropic (bulk) plasmas

In the absence of emission processes, the charge of a dust particle immersed in a plasma of electrons and ions is negative. This is because the electrons have higher velocities, so that the electron thermal flux exceeds considerably that of the ions. The emerging negative charge on the particle leads to the repulsion of the electrons and the attraction of the ions. The absolute magnitude of the charge grows until the electron and ion fluxes on the particle surface are balanced. On longer timescales, the charge is practically constant and experiences only small fluctuations around its equilibrium value, as described in Section 3.5.

The stationary surface potential of the dust particle  $\varphi_s$  is determined by the electron temperature  $T_e$ , viz.  $\varphi_s \sim -T_e/e$ . Physically, this is because in the stationary state most of the electrons have to be reflected by the potential barrier between the particle surface and surrounding plasma in order for the electron and ion fluxes to balance each other. The coefficient depends on the particular regime which is realized for the electron and ion fluxes to the particle surface.

One of the most frequently used approaches to describe the electron and ion fluxes collected by the particle is the orbital motion limited (OML) approximation [53–55]. This approach deals with collisionless electron and ion trajectories in the vicinity of a small individual probe (dust particle) and allows the determination of the collection cross sections from the conservation of energy and angular momentum. We will derive these cross sections in Section 3.1.2. To clarify some of the assumptions underlying the OML approach we first briefly discuss the properties of particle motion in the central field.

#### 3.1.1. Motion of a particle in the central field

For a particle moving ballistically in central field  $U(r)$ , the total energy,  $\mathcal{E} = \frac{1}{2} m(v_r^2 + v_\theta^2) + U(r)$ , and the angular momentum,  $m\rho v$ , are conserved. Here  $m$  is the particle mass,  $\rho$  is the impact parameter,  $v_r$  and  $v_\theta$  are the radial and tangential velocities, respectively, and  $v$  is the velocity at  $r \rightarrow \infty$ . It follows from the conservation laws that the radial

motion of particle is fully determined by the *effective* potential energy,

$$U_{\text{eff}}(r, \rho) = \frac{\rho^2}{r^2} + \frac{2U(r)}{mv^2}, \quad (1)$$

where  $U_{\text{eff}}$  is normalized to the initial kinetic energy,  $\mathcal{E} = \frac{1}{2}mv^2$ . The particle motion is restricted to the region where  $U_{\text{eff}} \leq 1$ . This means that if for a given  $\rho$  an equation

$$U_{\text{eff}}(r, \rho) = 1 \quad (2)$$

has root(s) then the largest of them determines the distance of the closest approach to the centre,  $r_0$ . For a spherical centre of radius  $a$ , the particle is collected when  $r_0 \leq a$ , whilst for  $r_0 > a$  it experiences elastic scattering by the centre potential, but does not reach its surface.

For a *repulsive* potential,  $U(r) > 0$ , the effective potential is a positive, monotonically decreasing function of  $r$ . Therefore, Eq. (2) has one solution. The maximum impact parameter corresponding to particle collection is

$$\rho_c^-(v) = \begin{cases} a\sqrt{1 - \frac{2U(a)}{mv^2}}, & \frac{2U(a)}{mv^2} < 1, \\ 0, & \frac{2U(a)}{mv^2} \geq 1. \end{cases} \quad (3)$$

For an *attractive* potential,  $U(r) < 0$ , there are several possibilities, depending on the particular behaviour of  $U(r)$  [56]. The extremum values of  $U_{\text{eff}}(r)$  are determined from the condition

$$r^3(dU/dr) = mv^2\rho^2. \quad (4)$$

If  $|U(r)|$  decreases everywhere more slowly than  $1/r^2$ , then the left-hand side of Eq. (4) grows monotonically, and there is only one solution to this equation. This solution corresponds to a minimum in  $U_{\text{eff}}$ . Hence Eq. (2) has only one solution and similarly to (3) we obtain for the maximum impact parameter corresponding to collection

$$\rho_c^+(v) = a\sqrt{1 - \frac{2U(a)}{mv^2}}. \quad (5)$$

On the other hand if  $|U(r)|$  decreases slower than  $1/r^2$  at small  $r$ , but decreases faster than  $1/r^2$  at large  $r$ , then Eq. (4) can have two solutions, and, hence,  $U_{\text{eff}}$  has both maximum and minimum. Maximum is determined by the conditions  $U'_{\text{eff}}(r_M) = 0$  and  $U''_{\text{eff}}(r_M) < 0$ . The maximum in  $U_{\text{eff}}$  always occurs at larger distances than the minimum.

If  $U_{\text{eff}}(r_M) \geq 1$ , then Eq. (2) has multiple solutions: Physically, this means that the potential barrier emerges, which reflects the particle. This is illustrated in Figs. 6 and 7. From Eq. (1) we see that there is a *transitional impact parameter*,

$$\rho_* = r_M\sqrt{1 - \frac{2U(r_M)}{mv^2}},$$

which separates particle trajectories in two groups: no barrier for  $\rho < \rho_*$ , but for  $\rho > \rho_*$  the potential barrier emerges and the particle is reflected at  $r \geq r_M$ . This causes a discontinuity in the dependence of the distance of closest approach on  $\rho$ , see Fig. 7. In the case  $r_M > a$ , the particles with  $\rho > \rho_*$  cannot be collected by the centre. Thus Eq. (5) should be modified:

$$\rho_c^+(v) = \begin{cases} a\sqrt{1 - \frac{2U(a)}{mv^2}}, & a\sqrt{1 - \frac{2U(a)}{mv^2}} < \rho_*(v), \\ \rho_*(v), & a\sqrt{1 - \frac{2U(a)}{mv^2}} \geq \rho_*(v). \end{cases} \quad (6)$$

As a useful example let us consider the attractive Yukawa-type interaction potential,  $U(r) = -(U_0/r)\exp(-r/\lambda)$ , where  $\lambda$  is the effective plasma screening length.

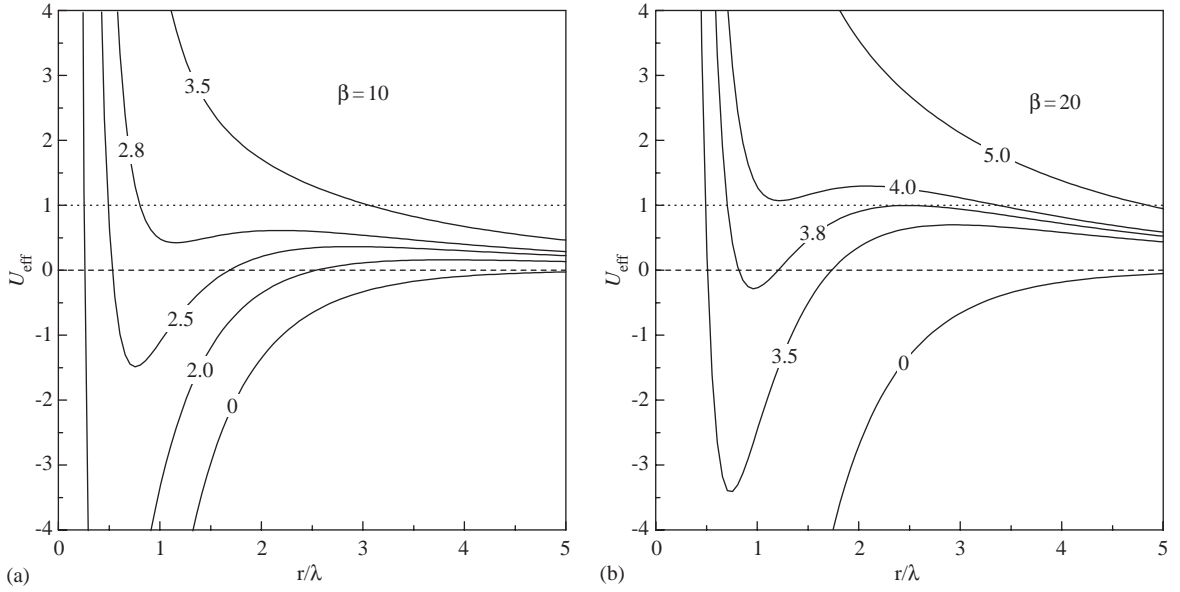


Fig. 6. Curves of the effective potential for the radial particle motion in the central field (for the Yukawa potential) for two values of the scattering parameter  $\beta$  (see text) and different dimensionless impact parameters  $\rho/\lambda$  (indicated in the figures). The potential barrier is absent at  $\beta = 10$  and present at  $\beta = 20$ .

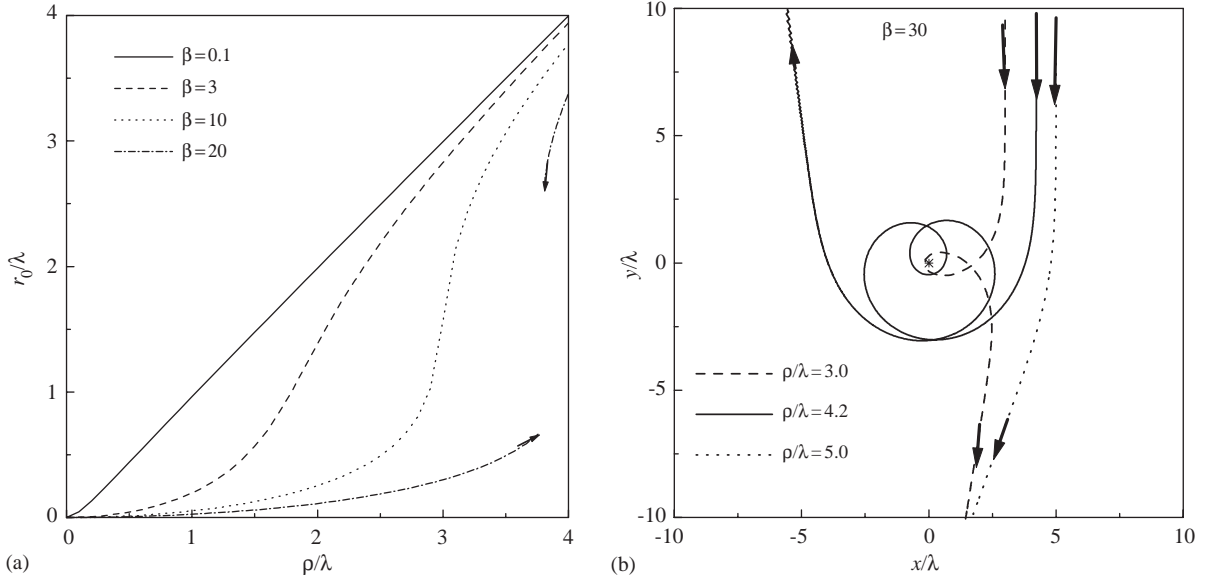


Fig. 7. (a) Normalized distance of the closest approach to the centre  $r_0$  vs. normalized impact parameter  $\rho$ . The curves are calculated for the Yukawa potential for different values of the scattering parameter  $\beta$ . When  $\beta \geq \beta_{\text{cr}} \simeq 13.2$  a discontinuity appears due to a barrier in the effective potential. (b) Particle trajectories during collisions for different impact parameters for the Yukawa interaction potential and scattering parameter  $\beta = 30$ . Impact parameters are chosen to be below, about, and above the transitional value  $\rho_* \simeq 4.24\lambda$ .

Let us normalize all the distances to  $\lambda$ . Then the behaviour of the effective potential  $U_{\text{eff}}$  is governed by two dimensionless parameters, the so-called *scattering parameter*

$$\beta = \frac{|U_0|}{mv^2\lambda}, \quad (7)$$

and the normalized impact parameter, viz.,  $U_{\text{eff}}(r) = \rho^2/r^2 + 2(\beta/r) \exp(-r)$ . Curves of the effective potential are illustrated in Fig. 6 for two values of  $\beta$  and different values of  $\rho$ . The potential barrier is absent at  $\beta = 10$ , whilst at  $\beta = 20$  the existence of the barrier leads to an abrupt jump in the distance of the closest approach, from  $r_0 \simeq 0.7$  to  $r_0 \simeq 2.6$ , at  $\rho \simeq 3.8$ . An inflection point in the Yukawa potential occurs at  $r \simeq 1.62$  [56]. The position of the potential barrier is the solution of the transcendental equation  $r_M \exp(r_M) = \beta(r_M - 1)$ . A solution exists only if  $\beta \geq \beta_{\text{cr}} \simeq 13.2$  and grows monotonically with  $\beta$ . The transitional impact parameter is

$$\rho_* = r_M \sqrt{\frac{r_M + 1}{r_M - 1}}$$

and also increases with  $\beta$  starting from  $\rho_*(\beta_{\text{cr}}) \simeq 3.33$ . For large  $\beta$  the following asymptotic solutions can be obtained [57]

$$r_M \simeq \ln \beta - \ln^{-1} \beta, \quad \rho_* \simeq \ln \beta + 1 - \frac{1}{2} \ln^{-1} \beta. \quad (8)$$

The trajectories of scattered particles and the dependence of the distance of closest approach on the impact parameter calculated for the attractive Yukawa potential are shown in Fig. 7.

### 3.1.2. Orbit motion limited (OML) approximation

In the OML approach three major assumptions are employed: (i) the dust grain is isolated in the sense that other dust grains do not affect the motion of electrons and ions in its vicinity; (ii) electrons and ions do not experience collisions during their approach to the grain; (iii) the barriers in the effective potential are absent. Then the cross sections for electron and ion collection are determined from the laws of conservation of energy and angular momentum.

The collection cross sections is  $\pi \rho_c^2$ , where  $\rho_c$  is the maximum impact parameter for the collection. In the OML approach the latter are given by Eq. (3) for the electrons and by Eq. (5) for the ions. Thus, the (velocity-dependent) collection cross sections are

$$\sigma_e(v) = \begin{cases} \pi a^2 \left( 1 + \frac{2e\varphi_s}{m_e v^2} \right), & \frac{2e\varphi_s}{m_e v^2} > -1, \\ 0, & \frac{2e\varphi_s}{m_e v^2} \leq -1, \end{cases} \quad (9)$$

and

$$\sigma_i(v) = \pi a^2 \left( 1 - \frac{2e\varphi_s}{m_i v^2} \right), \quad (10)$$

where  $m_{e(i)}$  is the electron (ion) mass,  $v$  denotes the velocity of the electrons and ions relative to the dust particle, the grain surface potential  $\varphi_s$  is negative ( $\varphi_s < 0$ ), and the ions are singly charged. An obvious advantage of the OML approximation is that the cross sections are independent of the plasma potential distribution around the grain. This is, however, only true when the potential satisfies certain conditions, see the preceding section. Limitations to the OML approach are considered in the next section.

Electron and ion fluxes to the particle surface are determined by the integral of the corresponding cross sections with the velocity distribution functions  $f_{e(i)}(v)$ :

$$I_{e(i)} = n_{e(i)} \int v \sigma_{e(i)}(v) f_{e(i)}(v) d^3 v,$$

where  $n_{e(i)}$  is the electron (ion) number density. Using the Maxwellian velocity distribution of plasma particles  $f_{e(i)}(v) = (2\pi v_{Te(i)}^2)^{-3/2} \exp(-v^2/2v_{Te(i)}^2)$ , where  $v_{Te(i)} = \sqrt{T_{e(i)}/m_{e(i)}}$  is the electron (ion) thermal velocity, we get after the integration

$$I_e = \sqrt{8\pi} a^2 n_e v_{Te} \exp\left(\frac{e\varphi_s}{T_e}\right), \quad (11)$$

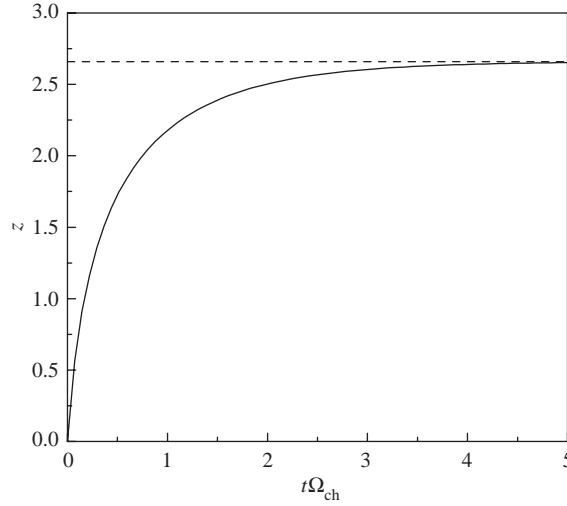


Fig. 8. Dimensionless charge  $z = |Z|e^2/aT_e$  of an isolated spherical particle as a function of dimensionless time  $t\Omega_{\text{ch}}$  for an argon plasma with  $\tau = 50$ . The particle is initially uncharged. The horizontal dashed line corresponds to the stationary value of the charge.

$$I_i = \sqrt{8\pi}a^2n_i v_{T_i} \left(1 - \frac{e\varphi_s}{T_i}\right). \quad (12)$$

The evolution of the dust grain charge is governed by the equation

$$\frac{dZ}{dt} = I_i - I_e, \quad (13)$$

so that the stationary charge is determined from the flux balance,

$$I_e = I_i. \quad (14)$$

It is convenient to introduce the following dimensionless parameters which are widely used throughout this paper:

$$z = \frac{|Z|e^2}{aT_e}, \quad \tau = \frac{T_e}{T_i}.$$

Here,  $z$  is the absolute magnitude of the particle charge,  $eZ$ , in units of  $aT_e/e^2$ , and  $\tau$  is the electron-to-ion temperature ratio, respectively. Typically, in gas discharge plasmas  $\tau \gg 1$  ( $\tau \sim 10$ – $100$ ) and  $z \sim 1$ . It is also assumed that the particle charge and surface potential are related to each other via  $Ze = a\varphi_s$ . This “vacuum” relation is usually a good approximation for small particles ( $a \ll \lambda$ ), whilst, in principle, there may be some deviations due to strongly nonlinear screening and/or nonequilibrium distribution of the electrons and ions around the dust particle.

Let us define the *charging frequency*  $\Omega_{\text{ch}}$  (inverse charging time) as the relaxation frequency for small deviations of the charge from the stationary value  $Z_0$ :  $\Omega_{\text{ch}} = -d(I_i - I_e)/dZ|_{Z_0}$ . Using Eqs. (11) and (12), we obtain

$$\Omega_{\text{ch}} = \frac{1+z}{\sqrt{2\pi}} \frac{a}{\lambda_{Di}} \omega_{pi}, \quad (15)$$

where  $\lambda_{Di} = \sqrt{T_i/4\pi e^2 n_i}$  is the ionic Debye radius, and  $\omega_{pi} = v_{T_i}/\lambda_{Di}$  is the ion plasma frequency. In deriving (15) it is also assumed  $\tau \gg 1$ . The charging frequencies for charging by the thermionic and photoelectric mechanisms are derived in Refs. [58,59] for the simplest system consisting of dust particles and electrons emitted from their surfaces.

The solution of nonlinear Eq. (13) with fluxes from Eqs. (11) and (12) and the initial condition  $z|_{t=0} = 0$  is shown in Fig. 8. One can see that the overall time scale of the nonlinear charging is also determined by  $\Omega_{\text{ch}}$ .

In the framework of the OML approximation, the dimensionless surface potential  $z$  depends on two parameters—the electron-to-ion temperature ratio, and the gas type (electron-to-ion mass ratio). In Fig. 9, values of  $z$  are presented for

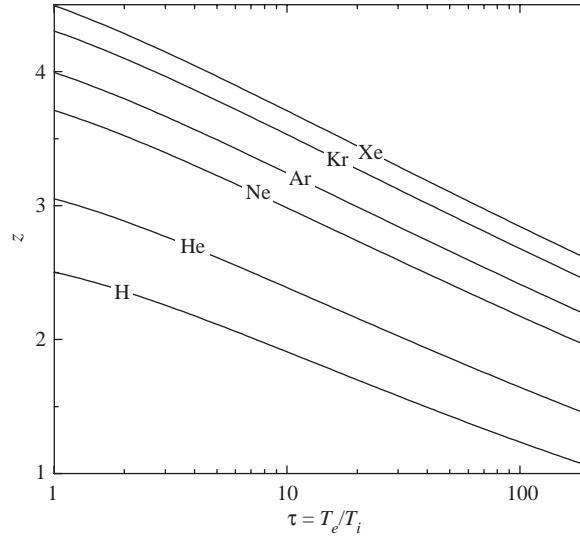


Fig. 9. Dimensionless charge  $z = |Z|e^2/aT_e$  of an isolated spherical particle as a function of electron-to-ion temperature ratio  $\tau = T_e/T_i$  for isotropic plasmas of different gases.

different gases (H, He, Ne, Ar, Kr, Xe) as functions of  $\tau$ . The particle potential decreases with  $\tau = T_e/T_i$  and increases with the gas atomic mass. For typical values of  $\tau \sim 10$ –100, the dimensionless charge is in the range  $z \sim 2$ –4. For a particle with  $a \sim 1 \mu\text{m}$  and  $T_e \sim 1 \text{ eV}$ , the characteristic charge number is  $|Z| \sim (1\text{--}3) \times 10^3$ .

### 3.1.3. Accuracy of the OML approximation

The assumptions underlying OML theory are seldom met in reality. Below we discuss three major reasons, which can make the OML approach inapplicable.

The first is associated with finite dust density in experiments and is known as the effect of “closely packed” grains. This effect is two-fold. The grain component contributes to the quasineutrality condition, making the ion density larger than the electron density [60]. This increases the ratio of the ion-to-electron flux and hence reduces the absolute magnitude of the grain charge compared to the case of an individual grain. The strength of the effect can be characterized by the value of the parameter  $P = |Z|n_d/n_e \equiv z(aT_e/e^2)(n_d/n_e)$  (often called “Havnes parameter”), which is the ratio of the charge residing on the dust component to that on the electron component ( $n_d$  is the grain number density). If we simply use expressions (11) and (12) for the electron and ion fluxes together with the quasineutrality condition  $n_e = n_i + Zn_d$  we get in dimensionless units

$$\sqrt{\tau} \exp(-z) = \sqrt{\frac{m_e}{m_i}} (1 + z\tau)(1 + P),$$

The charge tends to that of an individual particle when  $P \ll 1$ , while it is reduced considerably for  $P \gg 1$ . In addition, when the interparticle separation  $\Delta$  is smaller than the characteristic length of interaction between ions (electrons) and the dust grain, then the ion (electron) trajectories are affected by the presence of neighbouring particles, thus influencing grain charging. Barkan et al. [61] demonstrated experimentally that the effect of “closely packed” grains can lead to substantial charge reduction.

The second reason is associated with the fact that OML theory presumes the absence of a barrier in the effective potential energy. As discussed in Section 3.1.1 the barrier is absent for repulsive interaction (i.e., for the electrons) but it can emerge when the interaction is attractive (i.e., for the ions). The electrostatic potential around the small absorbing object in plasmas scales as  $\propto 1/r$  close to the object,  $\propto 1/r^2$  far from it, and at intermediate distances the potential decreases faster [56]. Hence, according to the discussion in Section 3.1.1, a barrier in the effective potential can exist for ions moving towards the grain and some (low energy) ions will be reflected from this barrier. This effect leads to a decrease in the ion current compared to OML theory and, hence, to an increase in  $|Z|$ . For a Maxwellian ion velocity



distribution there are always sufficiently slow ions, which are reflected from the barrier [62]. However, if the fraction of the ions which are not collected because of the barrier is small then the corrections to OML are also small. Using Eq. (6) this requirement can be formulated in terms of the ion thermal velocity  $a\sqrt{1+2U(a)/T_i} < \rho_*(v_{T_i})$ . For the Yukawa interaction potential with the thermal scattering parameter for the ions  $\beta(v_{T_i}) \simeq z\tau(a/\lambda) > \beta_{\text{cr}}$  we can write the condition of the OML applicability in the form [63]

$$\sqrt{2z\tau(a/\lambda)} \lesssim \ln[z\tau(a/\lambda)] .$$

For typical complex plasma parameters  $z \sim 1$  and  $\tau \sim 100$  we get that OML is applicable for  $a/\lambda \lesssim 0.2$ . This example shows that OML works well for sufficiently small grains. Essentially the same conclusion is drawn by Kennedy and Allen [64] from a consistent numerical solution for the surface potential and potential distribution around the probe in a collisionless plasma.

The third reason is due to ion–neutral collisions. In the OML approach collisions of electrons and ions are neglected on the basis that the electron and ion mean free paths  $\ell_{e(i)}$  are long compared to the plasma screening length [55]. However, theory has shown that ion–neutral charge-exchange collisions in the vicinity of a small probe or dust grain can lead to a substantial increase in the ion current to their surfaces even when  $\ell_i$  is larger than  $\lambda$  [65–67]. An increase of the ion current to a cylindrical Langmuir probe at moderate pressures is also a known effect, which is attributed to the ion–neutral collisions [68–71]. An increase in the ion current can considerably suppress the grain charge. Recent experimental results on grain charges in a bulk dc discharge plasma by Ratynskaia et al. [36] show that the particle charge can be several times smaller than predicted by the collisionless OML model. We discuss a simple analytical model of grain charging accounting for ion–neutral collisions and compare its predictions with the available experimental data on particle charge in the bulk of gas discharges in the next section.

### 3.1.4. Charging in a weakly collisional regime

Shulz and Brown [72], and then Zakrzewski and Kopiczynski [68] made the following argument for the role of ion–neutral collisions in the perturbed plasma region (‘sheath’ in their notation) around a probe. They noted that the collisions in the sheath cause the destruction of the ion orbital motion. When an orbiting ion makes a collision with an atom in the sheath it will lose energy and be trapped in the region of high negative potential. Such an ion cannot escape and will eventually reach the probe surface. Especially effective are charge-exchange collisions which lead to a substitution of the original ion by a low-energy ion created from neutrals. In this case essentially every charge-exchange collision in the sheath will result in an ion absorption on the probe surface, either directly or through subsequent collisions. Thus, when an average ion experiences not too many collisions in the perturbed plasma region, the collisions lead to an increase in the ion flux to the probe. On the other hand, when the gas pressure is so high that ions make many collisions on their way to the probe, then their motion is controlled by mobility. Mobility decreases with pressure and so does the ion flow. These arguments were used to explain a maximum in the ion current collected by a negatively biased probe occurring when increasing neutral gas pressure [68,70,71].

To obtain an approximation for the ion current to the particle in the presence of ion–neutral collisions we use the ideas discussed by Zakrzewski and Kopiczynski [68] and more recently by Zobnin et al. [65] and Lampe et al. [67]. First let us define the relevant (for this particular problem) length scale for the perturbed plasma region,  $R_0$ . Since the energy of an ion after a charge-exchange collision is  $\sim T_n \sim T_i$ , it is convenient to assume that  $R_0$  can be determined from the condition  $|U(R_0)| \simeq T_i$ , where  $U(r)$  denotes the potential energy of ion–particle interaction. For the Yukawa potential the strength of the perturbation is characterized by the scattering parameter  $\beta$  [Eq. (7)], evaluated at the ion thermal velocity, viz.  $\beta_T \simeq |Z|e^2/T_i\lambda \equiv z\tau(a/\lambda)$ . When  $\beta_T \ll 1$  we have  $R_0 \simeq |Z|e^2/T_i \ll \lambda$ . In the opposite limit ( $\beta_T \gg 1$ ) the perturbation region can extend beyond  $\lambda$  substantially.

In this section we consider the *weakly collisional regime* for the ions, characterized by the condition  $\ell_i \gtrsim R_0$ . Beyond the sphere of radius  $R_0$  the plasma density is weakly perturbed, ions have a Maxwellian velocity distribution and their random flux into the perturbed region is given by

$$I_{R_0} \simeq \sqrt{8\pi} R_0^2 n_i v_{T_i} .$$

The probability for an ion to experience a charge-exchange collision inside the perturbed region can be estimated as  $\sim R_0/\ell_i$ , provided  $R_0/\ell_i \ll 1$ . After such a collision, the ion is (very likely) trapped by the particle field and eventually

absorbed by the grain. Thus, the net ion flux on the grain is simply  $I_i \simeq (1 - R_0/\ell_i)I_{\text{OML}} + (R_0/\ell_i)I_{R_0}$  [where  $I_{\text{OML}}$  is given by Eq. (12)], i.e.,

$$I_i \simeq \sqrt{8\pi}a^2n_i v_{Ti} [1 + z\tau + (R_0^3/a^2\ell_i)] . \quad (16)$$

This expression was derived by Lampe et al. [67].

Assuming the Yukawa potential around the grain the radius of the perturbed plasma region normalized to the plasma screening length,  $R_0/\lambda$ , is given by the root of the transcendental equation  $\beta_T \exp(-x) = x$ . In this case expression (16) can be further simplified [73]. The last term in the parentheses in Eq. (16) can be rewritten in the form  $\mathcal{H}(\beta_T)z^2\tau^2(\lambda/\ell_i)$ , where  $\mathcal{H}(\beta_T) = (R_0/\lambda)^3\beta_T^{-2}$  is a relatively weak function of  $\beta_T$  in the range  $0.1 \lesssim \beta_T \lesssim 10$ , with a characteristic value  $\mathcal{H} \sim 0.1$  [73]. Thus we have

$$I_i \simeq \sqrt{8\pi}a^2n_i v_{Ti} [1 + z\tau + 0.1z^2\tau^2(\lambda/\ell_i)] , \quad (17)$$

Note, that in this approximation  $z$  depends on  $\tau$  and  $\lambda/\ell_i$ , but is independent of the ratio  $a/\lambda$ . From Eq. (17) we can see that the contribution to the charging flux due to ion–neutral collisions is dominant when  $\ell_i \lesssim 0.1z\tau\lambda$ . Thus, for typical dusty plasma parameters  $z \sim 1$  and  $\tau \sim 100$  collisions can affect particle charging even when the mean free path is an order of magnitude larger than the screening length.

Let us check the predictions of this simple analytical approximation for particle charge against available experimental results and numerical simulations.

Recently experimental results on grain charges in a bulk dc discharge plasma extending over a wide range of neutral gas pressures were reported [36,73]. The experiment was performed with the PK-4 facility (see Section 2.2) in ground-based conditions. It uses horizontally oriented tube filled with neon gas at pressures 20–150 Pa and particles of radii  $a \simeq 0.6, 1.0 \mu\text{m}$ , and  $a \simeq 1.3 \mu\text{m}$ . For these particle sizes the weak ambipolar radial electric field in the bulk plasma is sufficient to compensate against gravity so that the grains can levitate in an isotropic plasma near the tube axis.

The dynamics of particles of different size is studied varying the neutral gas pressure  $p$  and the number of injected particles (controlled by settings of the particle dispenser), which allows us to change the particle number density  $n_d$  inside the tube. For a sufficiently low number of injected particles the flow is stable for all pressures studied. The flow is recorded for a number of different pressures. The charge can then be estimated from the *force balance condition* using the measured particle velocities. The most important forces are the electric force, the neutral drag force, and the ion drag force. For the ion drag force the model [74] is used. For a larger number of injected particles (and larger  $n_d$ ) an easily identifiable transition to unstable flow (with a clear wave behaviour) occurs at a certain threshold pressure  $p_*$ , which can be found experimentally with an accuracy of about 1 Pa [36,75]. This transition is a manifestation of the ion streaming instability, caused by the relative drift between the dust and the ion components. The value of  $p_*$  depends on  $n_d$  (shifting towards higher pressures when  $n_d$  is increased). In this case the charge can be estimated from a *linear dispersion relation* describing the transition of the particle flow to the unstable regime at  $p_*$ . The applicability of the linear dispersion relation method is, however, limited due to nonnegligible effect of particles on plasma parameters at large particle column densities  $a^2n_d$  [73]. In practice this method is used only for smallest grains and low particle densities. The charges determined from this experiment are shown in Fig. 10 by open symbols.

Two experiments reporting estimates for the particle charge have been performed under microgravity conditions with the use of the PKE-Nefedov facility [21] (see Section 2.1). It is possible to excite the waves in the particle cloud by applying a low-frequency modulation voltage to the electrodes. The charge can then be estimated by comparing the measured dispersion relations with the theoretical ones. In this way the dimensionless charge was found to be  $z \sim 0.4$  (at  $p \simeq 25$  Pa argon gas pressure) [76] and  $z \sim 0.8$  (at  $p \simeq 12$  Pa argon gas pressure) [77]. The results of these experiments are shown in Fig. 10 by solid circle and square, respectively.

Another experimental method to determine the particle charge reported recently is based on gravity-driven heavy “test” particle collisions with smaller particles levitating in the quasiisotropic region of an inductively coupled rf discharge plasma [78]. A heavy particle falls down in a vertical glass tube and interacts with the cloud of small particles suspended in the diffuse edge of the discharge. The interaction process is recorded with a high-speed video camera and individual elastic “collisions” are analysed. Assuming the Debye–Hückel potential around each particle both the particle charge and effective screening length can be estimated. In Ref. [78] the particle charge is estimated for three different pressures of neon gas (20, 30, and 50 Pa). The results are shown in Fig. 10 by solid triangles.

A self-consistent molecular dynamics (MD) simulation of micron-size particle charging in a low-pressure plasma was reported by Zobnin et al. [65]. It was shown that charge-exchange ion–neutral collisions significantly affected

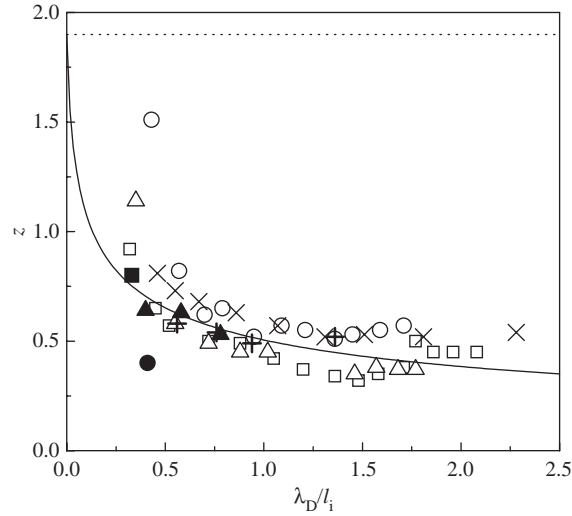


Fig. 10. The dimensionless particle charge  $z = |Z|e^2/aT_e$  as a function of the ion collisionality parameter,  $\lambda/\ell_i$  (assuming  $\lambda \simeq \lambda_D$ ). Open symbols correspond to the charges measured in Ref. [73] for particle radii  $a \simeq 0.6 \mu\text{m}$  (squares),  $a \simeq 1.0 \mu\text{m}$  (triangles), and  $a \simeq 1.3 \mu\text{m}$  (circles). The symbols  $\times(+)$  are for the charges found from MD simulation for  $a = 0.6 \mu\text{m}$  ( $a = 1.25 \mu\text{m}$ ) and plasma conditions similar to those in [73]. Solid circle and square are the charges estimated from wave excitation technique in PKE-Nefedov facility in Ref. [76,77], respectively. Solid triangles correspond to the charges obtained in Ref. [78]. The dotted line is calculated using the collisionless OML approach for an individual particle for plasma parameters of Ref. [73]. The solid line shows a calculation using an analytical approximation of Eq. (17) for the ion flux to the particle. These analytical calculations are done for plasma conditions relevant to experiment [73]: neon plasma with  $T_e = 7 \text{ eV}$  and  $T_i = 0.03 \text{ eV}$ .

(reduced) the charge already at pressures corresponding to a ion mean free path considerably larger than the Debye length. Later on this code was applied to calculate the charges in conditions similar to those of experiments [36,73]. Some modifications were made to the code to include the effects of finite particle number density. The charges obtained using this modified code were smaller than those obtained with the original code for an isolated particle. This was apparently caused by an increase in the ion density compared to the electron density (effect of “closely packed” grains). However, the difference was not very significant (usually less than 10%) for the conditions investigated, i.e., the effect of ion–neutral collisions was dominant under this parameter regime.

Fig. 10 summarizes the results of different experiments and MD simulations for the grain charge. (It is assumed here that the effective plasma screening length is  $\lambda \simeq \lambda_D \simeq \lambda_{Di}$  for the conditions investigated.) It demonstrates reasonable agreement between the results of different experiments, although they were performed under completely different plasma conditions (e.g., different types of discharges, different gases, different particle sizes, and different plasma parameters). This indicates that the ion collisionality index  $\lambda/\ell_i$  is one of the most important parameters, which controls the particle charge in isotropic dusty plasmas. The experimental uncertainties in charges (not shown in the figure) are due to uncertainties in plasma parameters and simplification in theoretical models employed to estimate the charge. They are different in different experiments. For example, in Ref. [73] the uncertainties in  $z$  are  $\sim 60\%$  at lowest pressures and  $\sim 30\%$  at higher pressures. In addition, it was noted that the experimental results at low pressures can contain systematic errors due to the violation of some simplifying assumptions used in the theoretical models. Strictly speaking, for the described experiments one cannot expect the accuracy better than  $\sim 30\%$  in both  $z$  and  $\lambda/\ell_i$ . Taken this into account, the results of numerical simulations are in good agreement with the experimental results.

Fig. 10 shows that the obtained charges are much smaller than the collisionless OML theory predicts (dotted line). At the same time a simple analytical approximation of Eq. (17) provides a reasonable fit for the available experimental and numerical data (solid line), especially taking into account experimental errors. In the parameter regime investigated the dimensionless charge decreases with the ion collisionality parameter, in agreement with Eq. (17). Note, however, that for sufficiently large ion collisionality ( $R_0/\ell_i \gtrsim 1$ ) the assumptions used in deriving Eq. (17) are no longer satisfied. At  $R_0/\ell_i \gg 1$  a transition to the mobility-limited (hydrodynamic) regime of ion collection should occur. In this regime the charge should increase with collisionality [65,79], see next section. This regime is not reached in the experiments discussed in this section.

Thus, ion–neutral collisions can be the main process affecting and regulating particle charging in the bulk of gas discharges. All the considered evidence clearly indicates that for a typical quasiisotropic complex plasma  $z \lesssim 1$ , contrary to the results of collisionless OML theory.

To conclude this section we note, that ion–neutral collisions can lead to the appearance of “trapped ions”. Trapped ions are those ions that move in closed orbits around the dust particle. They can affect both the particle charging and the particle charge screening by the surrounding plasma. Apparently, this effect can be substantial for the almost collisionless regime for ions ( $\ell_i \gg \lambda$ ), because the creation and loss rates of trapped ions are both proportional to the ion–neutral collision frequency. However, this question is not fully understood yet. Hence, we only give reference to original works [66,67,80,81] where the effect of trapped ions was discussed.

### 3.1.5. Charging in a strongly collisional regime

When the condition  $\ell_i \ll R_0$  is satisfied the ion motion to the particle is highly collisional and is controlled by mobility. In noble gases the characteristic cross section for ion–neutral collisions  $\sigma_{in}$  is typically between one and two orders of magnitude larger than that for electron–neutral collisions  $\sigma_{en}$ . Note that in argon, krypton, and xenon  $\sigma_{en}$  has a pronounced minimum for the electron energies of about 1 eV, due to the Ramsauer–Townsend effect [82]. Consequently, there is a wide pressure range where the electrons still are collisionless while the ions are not. In the stationary state we have

$$\nabla \mathbf{j}_i = Q_{Li} - Q_{Li}, \quad \mathbf{j}_i = n_i \mu_i \mathbf{E} - D_i \nabla n_i,$$

where  $Q_{Li}$  and  $Q_{Li}$  are the source and loss rates, respectively (e.g., ionization by external sources, chemical reactions, volume recombination etc.),  $\mathbf{E}$  is the electric field around the grain, and  $\mu_i$  and  $D_i$  are the mobility and the diffusion coefficient of the ions, respectively. Except for a region of strong electric field around the particle (where the mobility depends on the electric field, see e.g., [83]) the mobility can be assumed constant. The electron distribution around a negatively charged particle is to a good accuracy given by the Boltzmann relation  $n_e \simeq n_0 \exp(e\varphi/T_e)$ , where  $n_0$  is the unperturbed plasma density. The electrostatic potential  $\varphi(r)$  around the particle satisfies the Poisson equation

$$\frac{d^2\varphi}{dr^2} + \frac{2}{r} \frac{d\varphi}{dr} = -4\pi e(n_i - n_e) \quad (18)$$

with the following boundary conditions:

$$\varphi(a) = \varphi_s, \quad n_i(a) = 0,$$

$$\varphi(\infty) = 0, \quad n_i(\infty) = n_0.$$

A number of investigations were dedicated to solving such problems (e.g., with different ionization and recombination mechanisms in the vicinity of a collecting body, modifications of boundary conditions, etc.) starting from electric probe theory to investigation of dust particle charging in different types of plasmas. Solutions have been obtained and their applicability conditions discussed, for example, in Refs. [84–90]. Below we give some estimates for the simplest case, when ionization and recombination processes in the vicinity of particles can be neglected.

The ion flux in the absence of external sources of ionization and recombination is conserved and can be written as

$$I_i = 4\pi r^2 \left( n_i \mu_i \frac{d\varphi}{dr} + D_i \frac{dn_i}{dr} \right) \equiv I_0, \quad (19)$$

Far from the particle the plasma is quasineutral,  $n_i \simeq n_e \simeq n_0[1 + e\varphi(r)/T_e]$ . Integration of Eq. (19) yields ion and electron distribution in the quasineutral region

$$n_i(r) \simeq n_e(r) \simeq n_0(1 - R/r),$$

$$I_0 = 4\pi R n_0 \mu_i (T_i/e)(1 + T_e/T_i). \quad (20)$$

The electrostatic potential in this region is of the “partially screened” Coulomb form,  $e\varphi(r) \simeq -T_e R/r = Z_{\text{eff}} e/r$ , with some effective charge  $Z_{\text{eff}}$ . Obviously  $|Z_{\text{eff}}| < |Z|$ . In a more realistic situations when ionization in the vicinity

of the particle is taken into account the charge is screened at finite distances, which can be, however, much larger than the Debye radius [90].

Physically, the radius  $R$  corresponds to the boundary of the space charge that separates the particle from the quasineutral region. In order to evaluate  $R$  one can solve the Poisson equation in the space charge layer. However, no compact expression can be obtained in general case, even though the integration does not involve any fundamental problems [83]. For this reason we consider two limiting cases. If the particle is very large  $a \gg \lambda$  the sheath is usually thin, and we can assume  $R \sim a$ . In this case we get

$$I_0 \simeq 4\pi a n_0 \ell_i v_{Ti} (1 + T_e/T_i) .$$

In the opposite limit of very small particle,  $a \ll \lambda$ , we use the following argument: the electric field in the vicinity of the particle is determined by the “vacuum” Coulomb potential,  $\varphi(r) \simeq Ze/r$ . This potential holds as long as either of the two “geometrical” terms on the left-hand side of the Poisson (18) are considerably larger than the right-hand side. In this region  $n_i \gg n_e$  and, hence, we conclude that the screening does not play a role *at least* for  $r \lesssim \lambda_{Di} \beta_T^{1/3}$  (assuming  $n_i = n_0$ ; also, we suppose that the effective screening length is determined by ions,  $\lambda \simeq \lambda_{Di}$ ). Beyond this region, the potential tends asymptotically to the “partially screened” Coulomb form,  $\varphi(r) \simeq Z_{\text{eff}} e/r$ . In the “transition zone”,  $r \sim \lambda_{Di} \beta_T^{1/3}$ , the potential is of the order of  $\sim \beta_T^{2/3} T_i$  and, hence, the density perturbation in this region is small, provided  $\beta_T \ll 1$ . In this case, the ion flux on the particle can be written as

$$I_0 \simeq -4\pi r^2 \mu_i n_0 (Ze/r^2) = 4\pi a n_0 \ell_i v_{Ti} (T_e/T_i) z . \quad (21)$$

Using Eq. (20) and taking into account that  $Z_{\text{eff}} \equiv (T_e/e)R$ , we can evaluate the effective charge:  $Z_{\text{eff}}/Z = z^{-1}$  for large particles and  $Z_{\text{eff}}/Z = (1 + T_i/T_e)^{-1}$  for small particles. We note that an increase of  $Z_{\text{eff}}/Z$  and saturation at a value of  $\sim 0.5$  when increasing  $\lambda/a$  was found in Ref. [90], where particle charging in high pressure thermal plasma ( $T_i = T_e$ ) was numerically investigated.

It is noteworthy that radius  $R$  should not be in general equal to the radius of the perturbed plasma region  $R_0$ , introduced in the preceding section: within  $R_0$  the ions are strongly coupled to the particle, but this does not necessarily imply violation of quasineutrality at  $r \lesssim R_0$ .

### 3.1.6. Transitions between the charging regimes

Let us identify the conditions when the transitions between different regimes of particle charging occur. For the electron flux we use the OML expression (11). The expression for the ion flux depends on the ion collisionality: for collisionless ions we use Eq. (12), for the weakly collisional regime—Eq. (16), and for the strongly collisional regime—Eq. (21), which are appropriate estimations for small particles ( $a \ll \lambda$ ). The result of calculations for typical complex plasma parameters and three different values of the ratio  $\lambda/a$  are shown in Fig. 11. The figure shows that the collisionless regime is realized at extremely small  $\lambda/\ell_i \lesssim 0.01$ . In this regime the deviation from the OML result is small. In a typical situation for complex plasmas,  $\lambda/\ell_i \lesssim 1$ , the charge decreases with collisionality and can be up to several times smaller than the collisionless OML theory predicts. The transition to the mobility-limited regime of charging occurs somewhere in the range  $1 \lesssim \lambda/\ell_i \lesssim 10$ , depending on  $\lambda/a$ . The theoretical model for this transitional regime still needs to be constructed. For very large ion collisionality the charge increases, because collisions reduce the ion mobility and hence the ion flux. This qualitative dependence of the particle charge on ion collisionality is in full agreement with the results of numerical simulations reported by Zobnin et al. [65].

## 3.2. Charging in anisotropic plasmas

Dusty plasmas are usually subject to electric fields. For example, in ground-based experiments with rf discharges the particles can levitate in the (pre) sheath above the lower electrode, while in dc discharges the particles are often trapped in striations. Both these regions are characterized by high degree of plasma anisotropy and strong electric fields. The larger the particle size is, the stronger the electric field is required in order to compensate for gravity. The presence of the electric fields causes plasma drifts relative to the dust component. This in turn can affect particle charging by changing the collection cross sections and velocity distribution functions of ions and electrons. The problem of charging becomes much more complicated than in the case of an isotropic plasma, and we are not aware of any self-consistent analytical solution.

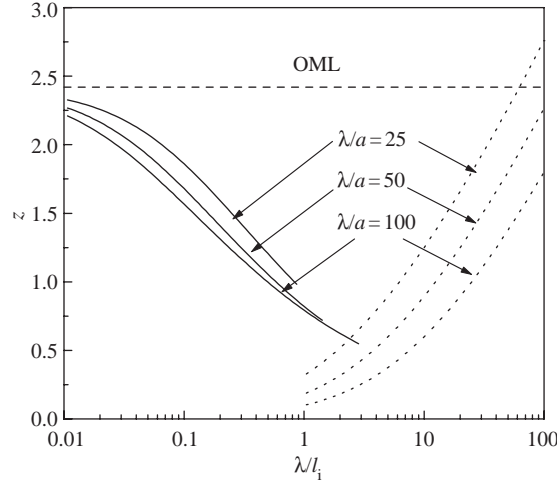


Fig. 11. Dimensionless charge  $z = |Z|e^2/aT_e$  as a function of the ion collisionality parameter  $\lambda/\ell_i$ . The calculations are for an argon plasma with  $T_e = 3$  eV and  $T_i = 0.03$  eV and three different ratios of the effective plasma screening length to the particle radius,  $\lambda/a$ . The solid lines represent the weakly collisional regime [Eq. (16)] and are terminated at the point  $\ell_i = R_0$ . Dotted lines correspond to the strongly collisional regime [Eq. (21)]. The horizontal dashed line shows the result of the collisionless OML theory.

To get an idea how the plasma drifts can affect particle charging the following simplification is usually used. The OML collection cross sections are assumed, but instead of isotropic Maxwellian distribution function one uses the shifted Maxwellian distribution, viz.

$$f_{i(e)}(\mathbf{v}) = (2\pi v_{Ti(e)}^2)^{-3/2} \exp \left[ \frac{(\mathbf{v} - \mathbf{u}_{i(e)})^2}{2v_{Ti(e)}^2} \right], \quad (22)$$

where  $\mathbf{u}_{i(e)}$  is the average drift velocity of ions (electrons). Integration of the cross (10) with the shifted Maxwellian function (22) yields the following expression for the ion flux [4,91,92]

$$I_i = \sqrt{\pi} \frac{a^2 n_i v_{Ti}^2}{u_i} [\sqrt{\pi}(1 + 2\xi^2 + 2z\tau) \operatorname{erf}(\xi) + 2\xi \exp(-\xi^2)], \quad (23)$$

where  $\xi = u_i/\sqrt{2}v_{Ti}$ . Similarly, integrating (9) with (22), the electron flux can be written as [91]

$$I_e = \sqrt{\pi} \frac{a^2 n_e v_{Te}^2}{u_e} \{ \sqrt{\pi}(1/2 - \xi_+ \xi_-) [\operatorname{erf}(\xi_+) - \operatorname{erf}(\xi_-)] + \xi_+ e^{-\xi_-^2} - \xi_- e^{-\xi_+^2} \}, \quad (24)$$

where  $\xi_{\pm} = \sqrt{z} \pm u_e/\sqrt{2}v_{Te}$ . In the limit  $u_i \ll v_{Ti}$  and  $u_e \ll v_{Te}$  expressions (23) and (24) reduce to (12) and (11), respectively. In the opposite limit we have

$$I_i = \pi a^2 n_i u_i [1 + (1 + 2z\tau)(v_{Ti}/u_i)^2] \quad (25)$$

and

$$I_e = \pi a^2 n_e u_e [1 + (1 - 2z)(v_{Te}/u_e)^2]. \quad (26)$$

Often, the drift of electrons is negligible while the ion drift is large. For example, this occurs in the regime of ambipolar plasma, in the (pre)sheath regions, i.e., where the electron distribution is close to Boltzmann, implying that the electric force acting on the electrons is compensated by the electron pressure. In this case the electron flux to the particle surface is given by Eq. (11) while for the ions one should use Eq. (23). The resulting dimensionless charge of the dust particle as a function of the ion drift velocity is shown in Fig. 12 for three values of  $n_e/n_i$ . The charge is practically constant for  $u_i \leq v_{Ti}$ , then it increases with  $u_i$ , attains a maximum at  $u_i \sim (2 - 3)C_{IA}$  (where  $C_{IA} = \sqrt{T_e/m_i}$  is the



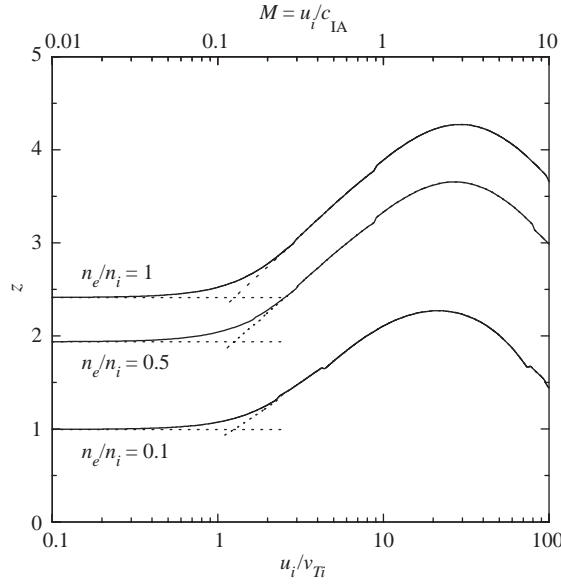


Fig. 12. Dimensionless charge  $z = |Z|e^2/aT_e$  of an isolated spherical particle as a function of the ion drift to ion thermal velocity ratio,  $u_i/v_{Ti}$  (or Mach number  $M = u_i/C_{IA}$ ), for a plasma with the ion drift. The calculations are for three different electron-to-ion density ratios and correspond to an argon plasma with  $\tau = 100$ .

ion–acoustic phase velocity), and starts decreasing. Comparison of results calculated with exact flux (23) and with asymptotic expressions (12) and (25) (the latter are indicated by dotted lines) shows almost no discrepancy, except for a narrow region near  $u_i \sim v_{Ti}$ .

Fig. 12 illustrates the behaviour of the particle charge in a sheath above the electrode in rf/dc discharges. The averaged electric field here increases almost linearly towards the electrode (see, for example, Ref. [93] and references therein). The ions are accelerated by the electric field, which leads to an increase of  $z$  until  $u_i$  becomes several times larger than  $C_{IA}$ . A positive space charge is developed in the sheath so that  $n_i/n_e > 1$  as the electrode is approached. This causes  $z$  to decrease compared to the quasineutral region. Thus, when approaching the electrode from the unperturbed bulk plasma the dimensionless charge  $z$  first somewhat increases, reaches a maximum, and then decreases. The charge can even reach positive values sufficiently close to the electrode. Examples of numerical calculations of the dependence of the particle surface potential on the distance from the electrode in collisionless and collisional sheaths of rf and dc discharges can be found in Ref. [94] for a set of plasma parameters.

The accuracy of neglecting the potential anisotropies caused by the ion flow (i.e., the assumption of the OML collection cross section) was checked by Lapenta [95] and Hutchinson [96,97] using particle-in-cell codes. It was shown that the potential asymmetry is virtually negligible with respect to the total ion flux for a conducting particle. However, the agreement between simulation and theory is worse for a dielectric particle. The latter acquires a significant dipole moment and the absolute magnitude of the charge of dielectric particle is larger than that of conductive particle. Such trend was predicted analytically by Ivlev et al. [98]: Fig. 13 shows that the deviation between the charges can be quite substantial. Another circumstance which can affect the accuracy of expression (23) is the deviation of the ion velocity distribution function from shifted Maxwellian, see e.g., Eq. (53) and Ref. [99].

Experimental examination of dust particle charges is of extreme importance, especially in cases where the plasma parameters are unknown or cannot be determined with sufficient accuracy. This is especially the case of anisotropic plasmas (e.g., sheaths) where in addition to the charging model (already complicated by plasma anisotropy, nonneutrality, presence of “superthermal” ions and electrons, etc.), one needs to choose an appropriate model for the sheath, which is not trivial itself.

Several experimental methods were proposed to measure particle charge in sheath or striation regions of discharges. Some of them are described below.

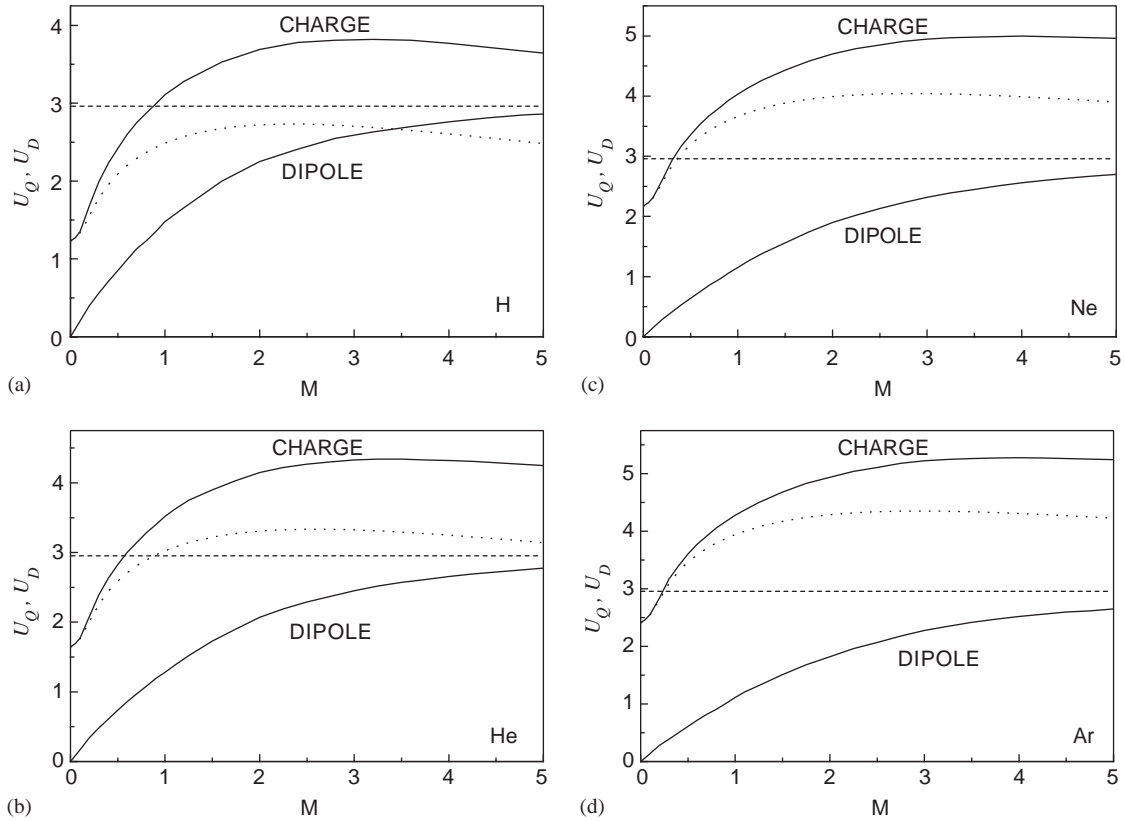


Fig. 13. The dimensionless charge,  $U_Q = e^2|Z|/aT_e$  (in the text  $z$  is adopted), and the dimensionless dipole moment,  $U_D = ed/a^2T_e$ , of the dielectric particle (solid lines) versus Mach number of the plasma flow,  $M$  [98]. The dotted line corresponds to a metal particle. The dashed line is the asymptote for the dipole curve. The figures correspond to (a) H, (b) He, (c) Ne, and (d) Ar.

*Vertical resonance method.* Characteristics of the vertical oscillations of a single particle in the sheath are determined by the particle charge (see Section 8). Typical values of the vertical resonance frequency  $\Omega_v$  are in the range 1–100 Hz and, hence, one can use low-frequency excitations to estimate the charge. As a simplest example, we refer to linear (harmonic) oscillations. By measuring the amplitude of the particle oscillations at different frequencies and then fitting the obtained frequency response curve with the well-known theoretical expression [100], it is possible to determine the resonance frequency,  $\Omega_v$  and the neutral damping rate  $\nu_{dn}$  simultaneously. This technique was employed for the first time in Ref. [14], and later it was used to determine the particle charge in Refs. [101–105]. The excitation is usually performed by applying a low-frequency signal to the rf electrode (in a modified variant—to a Langmuir probe or a wire inserted into a plasma in a vicinity of the levitated particle), or by using a focused laser beam.

The main difficulty in estimating the particle charge from experimental results is to establish the relation between  $\Omega_v$  and  $Z$ . It is often supposed that the dependence of  $Z$  on the height is much weaker than that of the electric field, i.e., in the first approximation one can assume  $Z \simeq \text{const}$ , and therefore  $\Omega_v^2 \simeq -ZE'_0/m_d$ , where  $E'_0$  denotes the derivative of the electric field evaluated at the particle equilibrium position. At sufficiently high pressures, the value of the derivative  $E'$  is practically constant over the sheath and can be estimated using a certain theoretical model. (Probe measurements in the sheath are not reliable, because of uncertainty in their interpretation.) This introduces some inaccuracy in the measurement results. Nevertheless, this method is often used in experiments because of its particular simplicity.

*Vertical equilibrium.* The method is based on the fact that when the potential distribution in the sheath is suitably determined, the charge on isolated dust particles levitated in the sheath can be estimated from their equilibrium heights by using balance between gravity and electric force. The method was used by Tomme et al. [93] and later by Samarian and Vladimirov [106]. In this method care must be taken in choosing an appropriate model for the sheath. Another possible source of uncertainties is the effect of forces that are not taken into account (e.g., ion drag, thermophoresis, etc.)

*Dust lattice waves.* Excitation of dust waves in strongly ordered particle structures (e.g., particle chains or two-dimensional lattices) is often employed as a diagnostic tool in studying dusty plasmas. The dispersion relations of the dust–lattice waves can be derived assuming certain form of the interparticle interaction potential (see Section 9.4). Usually the Yukawa potential is used. In this case the main parameters entering into the dispersion relation are the particle charge  $Z$ , and the ratio of the interparticle distance to the effective screening length—the lattice parameter  $\kappa = \Delta/\lambda$ . Other parameters are either known in advance (e.g., particle mass) or can be easily determined in the experiment (e.g., interparticle distance). Hence,  $Z$  and  $\kappa$  can be estimated by comparing an experimental dispersion relation with a relevant theoretical model. The dispersion relations measured in Refs. [107–111] were used to estimate the particle charge.

Other methods of charge determination were also used. In the *collision method* proposed by Konopka et al. [18] two-particle collisions are produced in a sheath region of an rf discharge using a horizontal electric probe, which allows to manipulate the particles. The form of the interaction potential is reconstructed from the analysis of particle trajectories. It was found that for low discharge powers and pressures the interaction potential can be fitted with the Yukawa potential within experimental uncertainties. From the fit the effective particle charge and plasma screening length can be estimated.

Measurements of the particle charge in a stratified dc discharge plasma were performed by Fortov et al. [112]. In this work, aperiodic oscillations of an isolated particle were excited by a focused laser beam. Analysis of particle trajectory yielded the charge.

A nonlinear dependence of the particle charge on the particle size was evidenced in experiments in anisotropic plasmas (see e.g., Refs. [93,106,112]). This nonlinear dependence can be attributed to the dependence of surrounding plasma parameters on particle size [113]: the particles with different radii levitate in different regions of the sheath or striation characterized by different plasma parameters, i.e., different ion and electron densities, ion drift velocity, electron temperature, etc. This makes the particle surface potential dependent on particle size and thus causes a nonlinear dependence of the particle charge on size, in contrast to the charging in the bulk of gas discharges.

The effect of ion–neutral collisions on particle charging, discussed in detail in connection with charging in isotropic plasmas, can apparently be also important in anisotropic plasmas. In this case the effect is two-fold: in addition to destroying collisionless ion trajectories in the vicinity of the particle, collisions change the structure of the sheath or striation. Thus the charge can depend on the ion collisionality in a quite complicated way and we are not aware of any consistent theoretical study of this effect. We note in this context an experiment of Fortov et al. [112] where some increase of the particle surface potential with pressure was reported.

### 3.3. Other effects important for particle charging

The collection of ions and electrons from the plasma is not the only possible charging mechanism. Electrons can also be emitted from the particle surface due to thermionic, photoelectric, and secondary electron emission processes. These processes are of importance for dust charging in the working body of solid-fuel MHD generators and rocket engines [40,114–116], in the upper atmosphere, in space [4,117,118], and in some laboratory experiments, for instance, in thermal plasmas [16,41–49] or in plasmas induced by UV irradiation [119], with photoelectric charging of dust particles [120], charging by electron beams [121], etc. Emission of electrons increases the dust particle charge and, under certain conditions, the particles can reach a positive charge, in contrast to the situation discussed previously. Due to the emission processes two-component systems consisting of dust particles and the electrons emitted by them can in principle exist. In this case, the equilibrium potential (charge) of the dust particle is determined by the balance of the fluxes that are collected by the particle surface and emitted from it, so that the quasineutrality condition is  $Zn_d \simeq n_e$ . Such a system serves as the simplest model for investigating different processes associated with emission charging of dust particles [40,58,114]. Let us briefly consider each of the emission processes listed above.

*Thermionic emission.* For an equilibrium plasma characterized by a temperature  $T$ , it is common to use the following expressions for the flux of thermoelectrons [115]:

$$I_{\text{th}} = \frac{(4\pi a T)^2 m_e}{h^3} \exp\left(-\frac{W}{T}\right) \times \begin{cases} 1, & \varphi_s < 0, \\ \left(1 + \frac{e\varphi_s}{T}\right) \exp\left(-\frac{e\varphi_s}{T}\right), & \varphi_s > 0. \end{cases}$$

Values of the work function  $W$  of thermoelectrons for different metals and semiconductors lie typically within the ranges from 2 to 5 eV. In the case of dielectric particles, where free electrons appear due to ionization, thermionic emission cannot play a significant role because the particles usually melt before thermionic emission makes a substantial contribution to the electron flux. For negatively charged particles its electric field accelerates the electrons from the particle surface and some increase in emission current can be expected due to reduction of the work function by the Schottky effect. Thermionic emission was identified as the dominant charging mechanism in thermal plasmas (see Section 2.3).

*Photoelectric emission.* The electron emission can be caused by an incident flux of photons with energies exceeding the work function of photoelectrons from the particle surface [122,123]. The characteristic value of the work functions for most of the materials does not exceed 6 eV, and hence photons with energies  $\leq 12$  eV can charge dust particles without ionizing a buffer gas. The flux of emitted electrons can be written as [55,124]:

$$I_{pe} = 4\pi a^2 Y J \begin{cases} 1, & \varphi_s < 0, \\ \exp\left(-\frac{e\varphi_s}{T_{pe}}\right), & \varphi_s > 0, \end{cases}$$

where  $J$  is the photon flux density, and  $Y$  is the quantum yield for the particle material. It is also assumed that the radiation is isotropic, the efficiency of radiation absorption is close to unity, which occurs when the particle size is larger than the radiation wavelength, and the photoelectrons possess a Maxwellian velocity distribution with the temperature  $T_{pe}$ . The last of these lies in most cases within the ranges from 1 to 2 eV. The quantum yield is very low just above the threshold, but for the most interesting regime of a vacuum ultraviolet it can reach a value of one photoelectron per several photons. Therefore, the photoelectric emission mechanism of particle charging can be quite important in space.

Sickafoose et al. [120] studied experimentally photoelectric emission charging of dust particles with diameters of  $\sim 100$   $\mu\text{m}$ . Conducting particles acquired a positive floating potential and charge both increasing linearly with the decreasing work function of photoelectrons. Behaviour of dust particles charged by solar radiation in microgravity conditions was investigated in Refs. [28,119]. An analysis of particle dynamics after UV irradiation, reported in [119], revealed that the particles with mean radius 37.5  $\mu\text{m}$  were charged to approximately  $10^4 e$ .

*Secondary electron emission.* The flux  $I_{se}$  of secondary electrons is connected to that of primary electrons,  $I_e$ , through the secondary emission coefficient  $\delta$ , viz.  $I_{se} = \delta I_e$ . The coefficient  $\delta$  depends both on the energy  $\mathcal{E}$  of primary electrons and on the dust particle material. The dependence  $\delta(\mathcal{E})$  turns out to be practically universal for different materials, if  $\delta$  is normalized to the maximum yield  $\delta_m$  of electrons, and  $\mathcal{E}$  is normalized to the value  $\mathcal{E}_m$  of energy at which this maximum is reached. The corresponding expressions for the case of monoenergetic electrons can be found in Refs. [4,55]. The values of the parameters  $\delta_m$  and  $\mathcal{E}_m$  for some materials given in [4] lie within the ranges:  $\delta_m \sim (1-4)$ , and  $\mathcal{E}_m \sim (0.2-0.4)$  keV. For the case of Maxwellian-distributed electrons, the expression for  $\delta$  was given, for instance, in [55].

Walch et al. [121] experimentally investigated the charging of particles of various materials and diameters from 30 to 120  $\mu\text{m}$  by thermal and monoenergetic superthermal electrons. When the charging was dominated by superthermal electrons, the particles were charged to the potential proportional to the electron energy and the charge proportional to the particle radius. However, when the electron energy reached a threshold value (different for various materials), from which the secondary electron emission became important, a sharp decrease in the absolute magnitude of the charge was found.

### 3.4. Role of microparticles in plasma charge balance

The dust particles immersed in a plasma act as ionization and recombination centres. Particles that emit electrons may increase the electron concentration in the plasmas. Conversely, when the particles absorb electrons from the plasma they become negatively charged and reduce the electron density compared to the ion density. From the quasineutrality condition it is clear that the presence of dust influences the plasma charge composition when  $|Z|n_d/n_e \equiv P \geq 1$ .

In the absence of emission processes, electrons and ions recombine on the dust particles. Plasma loss rates are determined by the expression  $Q_{Le(i)} = I_{e(i)}n_d$ , where  $I_{e(i)}$  is the flux of electrons (ions) absorbed by the dust particle surface. For large dust concentrations, the losses of electrons and ions on the particles can exceed the recombination losses in the dust-free plasma (volume recombination and/or plasma losses to the walls of a discharge camera). In self-sustained plasmas an increase in the recombination frequency has to be compensated for by a corresponding

increase in the ionization frequency [26,125]. This can for instance lead to an increase in the electron temperature and the discharge electric field.

When particles emit electrons, they serve as ionization sources as well. The particle contribution to the ionization is characterized by the flux of emitted electrons (see the previous section). In the limiting case, emission from particles embedded into a neutral gas completely determines the charge composition of the plasma, playing the role of sources and sinks for the electrons.

### 3.5. Fluctuations of the particle charge

In the previous sections the particle charge was treated as a continuous *regular* variable. However, the charging currents represent in reality sequences of events bound to electron and ion absorption or emission by the dust particle surface. These sequences and time intervals between the successive acts of absorption and emission are random. As a result, the particle charge can fluctuate around its average value. The importance of charge fluctuations was recognized as early as in the 1980s: Morfill et al. [126] suggested that charge fluctuations can have a major influence on dust transport in astrophysical plasmas. Several studies in recent years addressed the problem of charge fluctuations that arise from the random nature of the charging process [127–130]. In particular, gas discharge plasmas, where dust is charged by collecting electrons and ions, were considered within the framework of the OML approach. Several different charging mechanisms, including thermionic and photoelectronic emission processes, were also considered in Ref. [58].

Charge fluctuations due to discrete nature of charging can be described as a stationary, Gaussian and Markovian process (or the Ornstein–Uhlenbeck process [131]). This process was originally adopted to describe the stochastic behaviour of the velocity of a Brownian particle. In the above case, it describes the behaviour of the deviation of a particle charge from its average value:  $Z_1(t) = Z(t) - Z_0$ , where  $Z_0 = \langle Z(t) \rangle$  is the average charge. Let us derive the main properties of charge fluctuations. For simplicity, we limit consideration to the particle charging by electron and ion collection in the OML approximation. Generalization to other charging mechanisms is trivial. The Langevin equation for  $Z_1(t)$  is

$$\frac{dZ_1}{dt} + \Omega_{ch} Z_1 = f(t) , \quad (27)$$

where  $f(t)$  is the stochastic term, associated with random acts of electron/ion collection. Function  $f(t)$  satisfies the following properties:  $\langle f(t) \rangle = 0$  and  $\langle f(t) f(t') \rangle = 2I_0 \delta(t - t')$ , where  $I_0$  is the flux of electrons and ions to the particle in the stationary state [which determines the average charge, see Eq. (14)]. Applying these properties to the solution to Eq. (27),

$$Z_1(t) = Z_1(0) \exp(-\Omega_{ch} t) + \exp(-\Omega_{ch} t) \int_0^t f(t') \exp(\Omega_{ch} t') dt' ,$$

we obtain the following properties of charge fluctuations:

- (1) The charge fluctuation amplitude has zero average:

$$\langle Z_1 \rangle = 0 .$$

- (2) The charge autocorrelation function decays exponentially,

$$\langle Z_1(t) Z_1(t') \rangle = \langle Z_1^2 \rangle \exp(-\Omega_{ch} |t - t'|) , \quad (28)$$

where the relative charge dispersion (squared fluctuation amplitude) is

$$\sigma_Z^2 \equiv \frac{\langle Z_1^2 \rangle}{Z_0^2} = \frac{\gamma_Z}{|Z_0|} . \quad (29)$$

Using OML theory we get

$$\gamma_Z = \frac{1 + z\tau}{z(1 + \tau + z\tau)} \simeq \frac{1}{1 + z} ,$$

assuming that  $\tau \gg 1$ .

- (3) The process  $Y(t) = \int_0^t Z_1(t') dt'$  is Gaussian but neither stationary nor Markovian. With the help of Eq. (28) we obtain

$$\langle Y(t)^2 \rangle = \frac{2\langle Z_1^2 \rangle}{\Omega_{\text{ch}}^2} [\Omega_{\text{ch}} t + \exp(-\Omega_{\text{ch}} t) - 1] .$$

Usually, it is enough to use these properties for investigating the influence of charge fluctuations on dynamic processes in dusty plasmas. In particular, the following investigations can be mentioned: dust particle “heating” (in terms of the kinetic energy) in an external electric field due to charge fluctuations was studied in Refs. [132–135]; instabilities of dust particle oscillations due to charge fluctuations were considered by Morfill et al. [136] and Ivlev et al. [137], dust diffusion across a magnetic field due to random charge fluctuations was investigated by Khrapak and Morfill [138] with application to astrophysical plasma.

We note that the discreteness of the charging process is not the only reason for particle charge fluctuation. Spatial and temporal variations in plasma parameters, collective effects in dusty plasmas constitute other sources of charge fluctuations. These issues, however, have been much less investigated.

#### 4. Electrostatic potential around a particle

##### 4.1. Isotropic plasmas

The distribution of the electrostatic potential  $\varphi(r)$  around an isolated spherical particle of charge  $Z$  in an isotropic plasma satisfies the Poisson equation (18) with the boundary conditions  $\varphi(\infty) = 0$  and  $\varphi(a) = \varphi_s$ . The potential is connected to the particle charge through the relationship

$$\left. \frac{d\varphi}{dr} \right|_{r=a} = -\frac{Ze}{a^2} .$$

In a plasma with a Boltzmann distribution of electrons and ions the right-hand side of Eq. (18) can be linearized, provided the condition  $|e\varphi_s/T_{e(i)}| < 1$  is satisfied. This yields

$$\varphi(r) = \varphi_s(a/r) \exp\left(-\frac{r-a}{\lambda_D}\right) , \quad (30)$$

where  $\lambda_D^{-2} = \lambda_{De}^{-2} + \lambda_{Di}^{-2}$  is the linearized Debye length. The surface potential is  $\varphi_s = (Ze/a)(1 + a/\lambda_D)^{-1}$ . For small particles,  $a \ll \lambda_D$ , Eq. (30) is simplified to

$$\varphi(r) = (Ze/r) \exp(-r/\lambda_D) . \quad (31)$$

Expression (31) is the Debye–Hückel potential which is often used in complex plasmas. If the surface potential is not small compared to the temperatures of electrons and/or ions, then one can still use Eq. (31) at sufficiently large distances from the particle. In this case, the surface potential  $\varphi_s$  should be replaced by some effective surface potential  $\varphi_{\text{eff}}$ , with  $|\varphi_{\text{eff}}| < |\varphi_s|$ . For given plasma parameters, the value of  $\varphi_{\text{eff}}$  can be calculated numerically [139–141].

In fact, however, this simple approach to derive Eq. (31) is not really justified for most of complex plasmas. First, the Boltzmann distribution cannot be employed (at least for ions), because usually  $|e\varphi_s/T_i| \gg 1$ . Second, the Boltzmann distributions do not represent accurately the actual plasma distribution around the particle, especially for the species which is attracted to the particle (e.g., ions for a negatively charged particle). Moreover, due to plasma absorption on the particle the electron and ion fluxes directed from the particle are absent (in the absence of emission, of course). This makes distribution functions of ions and electrons anisotropic in the velocity space. Thus, strictly speaking, there is no sufficient physical grounds in applying formula (31) directly to complex plasmas.

To get an idea what is the realistic form of the particle potential, let us consider a negatively charged perfectly absorbing particle immersed in a collisionless electron–ion plasma. Assuming that we have Maxwellian plasma in the



unperturbed region far from the particle, the electron (ion) distribution is given by the integral over the corresponding velocity distribution function,

$$n_{e(i)}(r) = n_0 \int_{\Xi_{e(i)}} f_{e(i)}(v_r, v_\theta, r) 2\pi v_\theta dv_\theta dv_r, \quad (32)$$

where

$$f_{e(i)}(v_r, v_\theta, r) = (2\pi v_{Te(i)})^{-3/2} \exp \left[ -\frac{\mathcal{E}(v_r, v_\theta, r)}{T_{e(i)}} \right],$$

in the phase space domain,  $\Xi_{e(i)}$ , accessible for electrons (ions), and  $f_{e(i)} = 0$  outside the domain. Three conditions determine the boundaries of the integration domains  $\Xi$ : (i) The total energy  $\mathcal{E}$  should be always positive, (ii) the electron and ion trajectories satisfying the conditions for absorption end on the particle (i.e.,  $v_r < 0$  for these trajectories), and (iii) if the barrier in the effective potential energy exists then the ions/electrons are reflected from this barrier.

For the description of motion in the central force field we refer to Section 3.1.1. For electrons the total energy is positive and there is no barrier in the effective potential. Consequently, the difference of the actual electron distribution from the Boltzmann one is associated only with condition (ii)—the electron absorption on the particle. This difference is noticeable only in the region close to the particle, where the density is a half of the Boltzmann value,  $n_e \rightarrow (n_0/2) \exp(e\varphi_s/T_e)$  [56]. Since the contribution from the ions to the Poisson equation is dominant in this region, the effect of electron absorption is of minor importance for the potential distribution, and the use of the Boltzmann distribution is sufficiently accurate.

For ions, all three conditions have to be taken into account when determining  $\Xi_i$ . If we for a moment neglect the ion absorption and the barrier in the effective potential, then integration in Eq. (32) with the only constraint  $\mathcal{E}(v_r, v_\theta, r) \geq 0$  yields [56,142]

$$\frac{n_i(r)}{n_0} = \frac{2}{\sqrt{\pi}} \sqrt{-\frac{e\varphi(r)}{T_i}} + \exp \left[ -\frac{e\varphi(r)}{T_i} \right] \left[ 1 - \operatorname{erf} \left( \sqrt{-\frac{e\varphi(r)}{T_i}} \right) \right]. \quad (33)$$

The ion density increases towards the particle, but not as rapidly as the Boltzmann distribution does. This important conclusion is rather general in view of the assumptions made in deriving Eq. (33): ion absorption and the barrier in the effective potential further deplete the ion density in the vicinity of the particle.

An approximate solution to the Poisson equation with Boltzmann electrons and ion distribution given by Eq. (33) was recently delivered by Tsytoich et al. [143]. It deviates considerably from the Yukawa form (31). The obtained solution is, however, not a self-consistent one, because it contradicts with the initial assumption that there is no barrier in the effective potential.

In general case the ion density  $n_i$  is expressed in terms of the electrostatic potential  $\varphi$  via an integral, in a very complicated fashion [56,144]. The ion density at a point  $r$  depends not only on the value of the potential at this point, but on the whole  $\varphi(r)$  behaviour. The Poisson equation then represents a nonlinear integro-differential equation which requires numerical solution [144]. In the context of dusty plasmas only a few numerical calculations for a limited set of plasma parameters were performed. For example, Daugherty et al. [81] followed Bernstein and Rabinowitz [144] assuming monoenergetic ions in order to simplify the solution procedure. The electrostatic potential was then calculated numerically. The main results can be formulated as follows: in a vicinity of the particle, at  $r$  less than a few  $\lambda$ , the potential can be well approximated by the Yukawa form, Eq. (31). For small particles ( $a \ll \lambda_D$ ), the effective screening length  $\lambda$  is close to the ion Debye radius,  $\lambda \sim \lambda_{Di}$ , and for larger particles ( $a \gtrsim \lambda_D$ ),  $\lambda$  increases with  $a$  and can reach values comparable to  $\lambda_{De}$ . At larger distances, the potential tends asymptotically to  $\propto r^{-2}$  dependence, which is well known from the probe theory [56]. Similar results were later obtained in Ref. [26].

Recently a consistent numerical calculations for the particle surface potential and potential distribution around the particle in a plasma with Maxwellian ions was reported [64]. Although, the emphasis of this work was on the effect of the barrier in effective potential on the ion current that the particle could collect, some results for the potential distribution were also presented. It was found that there is a vacuum-like region near the particle surface where the potential scales as  $\varphi(r) \propto r^{-1}$ , while far from the particle  $\varphi(r) \propto r^{-2}$ . In between, there is a transition region where the potential decreases faster. Apparently, for not too large distances from the particle, the potential can be approximated

by the Yukawa form with some effective screening length. However, detailed consideration of this issue is absent in Ref. [64].

Thus, available numerical results suggest that at intermediate distances from the particle the actual potential in collisionless plasmas can be approximated by the Yukawa form (31) with an appropriately chosen screening length. At the same time, no strong physical arguments have been given to justify this approximation, and, hence there is no reason to believe that this is the best approximation among other possibilities. This issue obviously needs further investigation. Far from the particle the potential scales as  $\varphi(r) \propto r^{-2}$  due to plasma absorption. This scaling can be easily derived analytically. Neglecting the barrier in the effective potential, the condition for the ion absorption can be formulated in accordance with Eq. (6):  $\rho \leq a\sqrt{1 - 2e\varphi_s/m_i v^2}$ . Rewriting it in terms of  $v_r$  and  $v_\theta$  and using the fact that  $|\varphi_s| \gg |\varphi(r)|$  at  $r \gg a$ , we get that for  $v_\theta \lesssim (a/r)\sqrt{v_r^2 - 2e\varphi_s/m_i}$  only the ions with  $v_r < 0$  are present. Integration in (32) yields

$$n_i(r) \simeq n_0 \exp \left[ -\frac{e\varphi(r)}{T_i} \right] \left[ 1 - \frac{a^2}{4r^2} \left( 1 - \frac{2e\varphi_s}{T_i} \right) \right].$$

The potential distribution in this region is determined from the quasineutrality condition  $n_e \simeq n_i$ . Assuming  $\varphi_s \simeq Ze/a$  and using dimensionless parameters we arrive at the following asymptote [3,56,62,145,146]:

$$\frac{e\varphi(r)}{T_e} \simeq -\frac{1 + 2z\tau}{4(1 + \tau)} \frac{a^2}{r^2} \quad (34)$$

at large  $r$ . Usually  $\tau \gg 1$  and  $z \sim 1$ , so that we have  $\varphi(r) \simeq Zea/2r^2$ .

An additional complication in the theory of electrostatic potential around the dust particle is associated with ion–neutral collisions. The possible importance of this effect should not be underestimated. In the weakly collisional situation  $\ell_i \gg \lambda$  the collisions, no matter how infrequent, will create ions with negative total energy in the vicinity of the minima in the effective potential energy. These ions are trapped in the potential well and orbit the particle until another collision untraps an ion or it is absorbed on the particle surface. Because the creation and loss rates of trapped ions are both proportional to the collision frequency, the number of orbiting ions in the stationary state is independent of collision frequency. Trapped ions increase the ion density in the vicinity of the particle and can considerably affect the electrostatic potential. For example Lampe et al. [66] showed that under certain conditions the presence of trapped ions can lead to better agreement between the potential calculated in a self-consistent way and the Debye–Hückel potential for distances up to several Debye radii. The effect of ion–neutral collisions on the potential was also documented by Zobnin et al. [65], who observed that with increasing ion collisionality a transition from the Yukawa to the unscreened (Coulomb) potential occurs. This is in agreement with the fact that in the highly collisional regime for the ions the potential scales as  $\varphi(r) \propto r^{-1}$  in the absence of ionization/recombination processes (see Section 3.1.5).

To conclude the section, one should note that a self-consistent calculation of the electrostatic potential around the particle and its dependence on parameters of the ambient plasma still is a very important unsolved problem in complex plasmas.

#### 4.2. Anisotropic plasmas

Strong electric fields are often present in laboratory conditions (e.g., in rf sheaths or dc striations). This causes the ion drift relative to the particles and, hence, creates a perturbed region of plasma density downstream from the particle—a wake. One can apply the linear dielectric response formalism (see e.g., [147]) to calculate the potential distribution in this case. This approach is applicable provided ions are weakly coupled to the particle (nonlinear region around the particle is small compared to the plasma screening length). Note that larger ion drift velocities imply better applicability of the linear theory. The electrostatic potential created by a point-like charge at rest is defined in this approximation as

$$\varphi(\mathbf{r}) = \frac{Ze}{2\pi^2} \int \frac{e^{i\mathbf{k}\mathbf{r}} d\mathbf{k}}{k^2 \varepsilon(0, \mathbf{k})}, \quad (35)$$

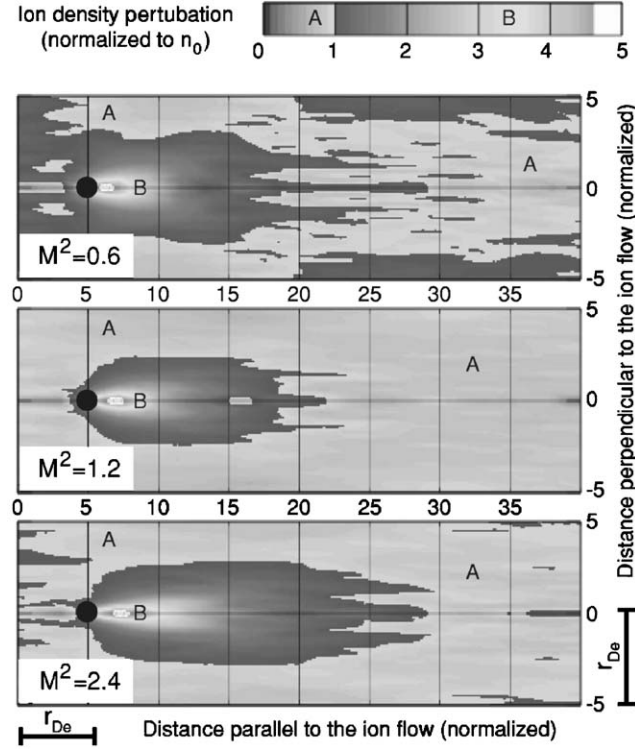


Fig. 14. Contour plot of the ion density, showing ion focusing, for three different velocities of ion flow measured in units of  $\sqrt{5/3} C_{IA}$  [156]. The plot is presented in the grey-scale topograph style: regions A correspond to depressed ion densities,  $n < n_0$ , whereas regions B are for  $n > n_0$ . The ions are focusing behind the grain thus forming the region with highly enhanced ion density. The distances are measured in units of the electron Debye length.

where  $\varepsilon(\omega, \mathbf{k})$  is the plasma permittivity. Using a certain model for the permittivity [see, e.g., Eqs. (54), (76) and (78) for the ion response], one can calculate the anisotropic potential distribution [148–154]. The potential profile can also be obtained from numerical modelling [145,155–159]. Fig. 14 shows the contour plot of the ion density in the wake, as obtained from the MD simulations [156].

Physically, generation of electrostatic wakes in anisotropic dusty plasmas is analogous to the generation of electromagnetic waves by a particle at rest, which is placed in a moving medium [160,161] and the analogy with the Vavilov–Cherenkov effect can be useful.

The qualitative description of this effect is the following: in the directions upstream from and perpendicular to the ion flow, anisotropy is of minor importance. Within a certain solid angle downstream from the flow, the potential is no longer monotonic, but has a well pronounced extremum (maximum for a negatively charged particle). As shown by numerical modelling, the shape of the wake potential is sensitive to ion collisions (ion–neutral collisions) [162] and the electron-to-ion temperature ratio which governs Landau damping [163]. In typical situations, these mechanisms can effectively “smear out” the oscillatory wake structure, leaving a single maximum. The shape of the wake potential depends on the value of the Mach number  $M = u_i / C_{IA}$ , however, the wake itself appears both in supersonic and subsonic regimes of the ion drift. In this context, we mention the work of Lampe et al. [145] where some examples of the wake structures calculated numerically for different plasma conditions are presented. The effects of finite particle size and asymmetry of the charge distribution over its surface are considered in Refs. [164,165].

In this section we considered the potential distribution around an isolated particle. Such a consideration is justified when the number density of the dust component is low enough and the interparticle separation significantly exceeds the Debye radius. Otherwise, the dust collective effects can be of significant importance, so that dust can also contribute to the plasma screening of a test charge. The details can be found in the recent review by Morfill et al. [166].

## 5. Interaction between particles in complex plasmas

### 5.1. Isotropic plasmas

The potential of interaction between dust particles is, generally speaking, not only of electrostatic nature. This is due to variability of the particle charges, particle coupling to the surrounding plasma, etc. In addition, “collective interactions” can operate when the dust can be treated as the “true” plasma component [166]. In this review we consider the case of sufficiently low dust concentrations, when the interparticle interaction (as well as screening and charging) can be calculated in the approximation of “isolated” particles. In this case, the absolute value of the electrostatic force acting on a particle with *fixed* charge  $Z$  and located at a distance  $r$  from the test particle is  $F_{\text{el}} = -dU_{\text{el}}(r)/dr$ , where

$$U_{\text{el}}(r) = Ze\varphi(r) .$$

Thus, it is necessary to know the distribution of the electrostatic potential  $\varphi(r)$  in the plasma around the dust particle. It was shown in the preceding section that this problem is fairly complicated and requires further investigation. At the current level of understanding it seems reasonable to adopt the Yukawa-type potential [Eq. (31)] at intermediate distances from the particle, in order to model the interaction in isotropic plasmas. Then the interaction potential energy is

$$U_{\text{el}}(r) \simeq \frac{Z^2 e^2}{r} \exp\left(-\frac{r}{\lambda}\right) .$$

At longer interparticle distances (typically more than several screening lengths) the long-range asymptote operates [Eq. (34)] and the interaction energy can be written as  $U_{\text{el}} \simeq Z^2 e^2 a / 2r^2$ . This estimate holds for distances not exceeding the mean free path of ions, because collisions effectively destroy the anisotropy in the ion velocity distribution.

In addition to that, different attraction and repulsion mechanisms can exist as a consequence of the openness of dusty plasma systems—the openness caused by continuous exchange of energy and matter between the particles and surrounding plasma.

The continuous flow of the plasma electrons and ions on the surface of a dust particle leads to a drag experienced by neighbouring particles. This can result in an effective attractive force between the particles, which is called the ion shadowing force. The magnitude of this force is mainly determined by the ion component due to larger ion masses. Such an attractive mechanism was first considered by Ignatov [167] and Tsytovich et al. [168], and later on in Refs. [145,146,169]. Note that the ion shadowing force basically represents the ion drag force in the ion flow directed to the surface of a test particle. Strictly speaking, the ion shadowing force is not pairwise, since the interaction between several particles (more than two) depends on their mutual arrangement.

Another attraction (repulsion) between the particles can be associated with neutral atoms, provided they are scattered from the particle surface with the energy distribution different from that of the ambient neutral gas. This can happen, e.g., if the surface temperature  $T_s$  is different from the neutral gas temperature  $T_n$  and full or partial accommodation takes place. The temperature of the particle surface is governed by the balance of various processes, such as radiative cooling, exchange of energy with neutrals, and recombination of electrons and ions on the surface [170]. In the case  $T_s \neq T_n$ , there exist net fluxes of energy and momentum between gas and particles. Hence, if two particles are located sufficiently close to each other, an anisotropy in momentum fluxes on the particles will also exert a shadowing force between them, which in this case is associated with the neutral component. The force is repulsive when  $T_s > T_n$  and is attractive in the opposite case. This effect was first considered by Tsytovich et al. [171].

Both for neutral and ion shadowing effects, the corresponding potentials scale as  $\propto 1/r$ . Hence, at large distances the shadowing interaction will overcome the long-range electrostatic repulsion. The existence of attraction makes the formation of dust molecules possible (an association of two or more particles coupled by long-range attraction). The theoretical examination of the conditions of molecular formation can be found in Refs. [3,146]. For isotropic plasmas, however, the formation of dust molecules has not yet been experimentally established. First of all, this can be explained by the fact that rather large particles are needed for the substantial shadowing effect. In ground-based experiments, such particles can levitate only in the sheath regions of discharges, where the electric field is strong enough to balance the

gravity and the effects of plasma anisotropy are of primary importance. The ions drifting with superthermal velocities provide almost no contribution neither to screening nor to shadowing.

## 5.2. Anisotropic plasmas

In anisotropic plasmas the wake effect is important (see Section 4.2). This effect is usually invoked for explaining the vertical ordering of the dust particles (chain formation) often observed in ground-based experiments. Recently, another effect was pointed out, which might play some role in the vertical ordering of dust particles along the ion flow. This effect is connected with a distortion of the ion velocity field by the upstream particle and the appearance of a horizontal component of the force, caused by the ion momentum transfer to the downstream particle [158]. This force—the ion drag force—pushes the downstream particle back to the axis with the origin at the upstream particle position and parallel to the ion flow. Numerical modelling of the ion velocity field in the wake showed that for certain conditions the ion drag mechanism prevails over the electrostatic one [158].

Note that both effects are sensitive to ion–neutral collisions. First, the collisions reduce the ion directed velocity in an external electric field (and, hence, plasma anisotropy). Second, they limit the perturbed plasma region (both the potential and the ion velocity field) around a probe particle to a length scale on the order of the ion mean free path. Therefore, both mechanisms can only operate at sufficiently low pressures.

## 5.3. Experiments

Determination of the interaction potential constitutes a delicate experimental problem. Only a few such experiments have been performed so far [18,172–176].

An elegant method based on an analysis of elastic collisions between the two particles was proposed by Konopka et al. [18,172]. In this experiment the particles are introduced into an rf discharge through a small hole in the glass window built into the upper electrode and are levitated above the lower electrode, where the electric field compensates for gravitational force. To confine the particles horizontally, a ring is placed on the lower electrode, which introduces a horizontal parabolic confining potential. The manipulation of the particles and activation of elastic collisions between them is performed with the use of a horizontal electric probe introduced into the discharge chamber. During the collision, the particle trajectories are determined by the confining potential and the interparticle interaction potential which is a function of interparticle spacing. An analysis of recorded particle trajectories during collisions yields the coordinates and velocities of both the particles during collision. Then, the form of the interaction potential can be reconstructed from the equation of motion. Application of this method [18] showed that for low discharge powers and pressures the interaction potential is of the Yukawa form (31) within experimental uncertainties. This is illustrated in Fig. 15. The role of other interaction mechanisms is insignificant for the plasma conditions used in these experiments, which, however, does not exclude the possibility of their existence (see Ref. [146]).

A method based on the laser manipulation of the dust particles was proposed to study interaction between the particles in anisotropic plasmas [173]. Melzer et al. [174] employed this method for two particles suspended simultaneously in the rf sheath: a single particle of radius  $a \simeq 1.7 \mu\text{m}$ , and a cluster of two particles (of the same size) stuck together. The particles were introduced into a plasma of an rf discharge in helium at a pressure of  $p \sim 50\text{--}200 \text{ Pa}$ . Because of the different charge-to-mass ratios, the double particle levitated closer to the lower electrode. Both particles, meanwhile, were almost free to move in the horizontal plane. The first observation was the following: for sufficiently low pressures, the particles tend to form a bound state, in which the lower particle is vertically aligned to the upper one. With increasing pressure, the bound state can be destroyed, and then the particle separation in the horizontal plane is limited only by a very weak horizontal confinement produced by a specially concave electrode. The backward decrease of pressure brings the system back into the bound state. It was found that the effect exhibits hysteresis.

In order to prove that the observed bound state is not due to external confinement, the particles were manipulated by laser radiation. The laser beam was focused either on the upper or the lower particle, causing the motion. It was found that when the upper particle is pushed, the lower particle follows its motion. This behaviour proves that the lower particle is subject to an attractive horizontal force mediated by the upper particle. In contrast, when the lower particle is pushed, the response of the upper particle is much weaker and the bound state can be easily destroyed. Hence, the interaction between the particles is clearly nonreciprocal.

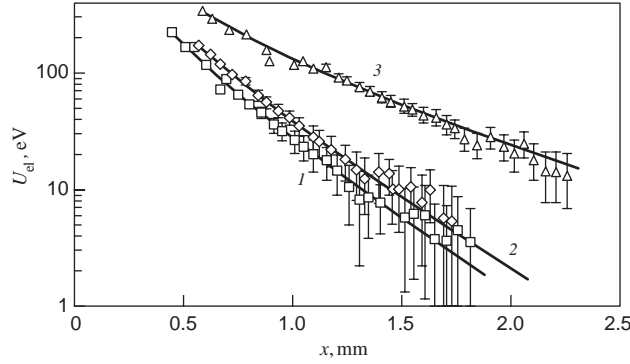


Fig. 15. Potential energy  $U_{el}$  of interaction between two particles in a rf sheath versus the horizontal distance  $x$  between them [18]. Measurements were taken with the particles of radius  $a \simeq 4.5 \mu\text{m}$  at  $p = 2.7 \text{ Pa}$  in argon and different rf peak-to-peak voltages  $U_p$ . Symbols correspond to experimental results, solid lines show their fit to the Yukawa potential  $U_{el}(x) = (e^2 Z^2 / x) \exp(-x/\lambda)$  leading to the following effective particle charge  $Z$  and screening length  $\lambda$  ( $T_e$  is the measured electron temperature): 1 –  $|Z| = 13, 900$ ,  $\lambda = 0.34 \text{ mm}$ ,  $T_e = 2.0 \text{ eV}$ ,  $U_p = 233 \text{ V}$ ; 2 –  $|Z| = 16, 500$ ,  $\lambda = 0.40 \text{ mm}$ ,  $T_e = 2.2 \text{ eV}$ ,  $U_p = 145 \text{ V}$ ; 3 –  $|Z| = 16, 800$ ,  $\lambda = 0.90 \text{ mm}$ ,  $T_e = 2.8 \text{ eV}$ ,  $U_p = 64 \text{ V}$ . Note that the screening length determined from the experiment is closer to the Debye radius for electrons than for ions. This is in qualitative agreement with the assumption that the ion velocity is close to the ion sound velocity  $C_{IA} = \sqrt{T_e/m_i}$  in the (collisionless) sheath and ions do not contribute to the screening.

Another set of experiments to measure forces produced by the ion wake field from the upper (lighter) “target” particle by colliding the latter with the (heavier) “probe” particle levitated at a lower height in a sheath of an rf discharge was reported by Hebner et al. [175,176]. In this experiments attractive and repulsive interactions between charged particles were calculated using Newton’s equations of motion for various experimental conditions (using different particles sizes and neutral gas pressures). It was shown that the magnitude of attractive potential increases with lowering the gas pressure, as expected (see discussion at the end of the preceding section). It was also found that the attractive forces decay fairly rapidly as the vertical distance between the particles increases. Fits to repulsive and attractive forces were proposed.

It is obvious that the experimental results reported in [174–176] can be explained by the wake effect. However, the question of whether the attractive force has an electrostatic nature or is associated with the ion drag mechanism [158] still needs to be investigated.

## 6. Momentum exchange in complex plasmas

The momentum exchange between different species plays an exceptionally important role in complex plasmas. For example, the momentum transfer in collisions with the neutral gas “cool down” the system, in particular grains and ions, introducing some damping. The forces associated with the momentum transfer from electrons and ions to the charged grains—i.e., the electron and ion drag forces—often determine static and dynamical properties of the grain component, affect wave phenomena, etc. The momentum exchange in grain–grain collisions and its competition with the momentum transfer in grain–neutral gas collisions governs grain transport properties, scalings in fluid flows, etc. While various aspects of electron–ion interaction (collisions) as well as electron, ion, and grain collisions with neutrals have been well studied, comparatively little work has been done on grain–electron, grain–ion and grain–grain collisions.

In this section, we assume the Debye–Hückel (Yukawa) potential around the dust particle and perform a detailed analysis of the binary collisions involving the particles. First, the momentum transfer cross section for different types of collisions is calculated and analytical approximations for some limiting cases are derived. These approximations are used to estimate the characteristic momentum exchange rates in complex plasmas. This provides us with a unified theory of momentum exchange in complex plasmas in the *binary collision approximation*. Some direct applications of the obtained results are also considered, e.g., classification of possible complex plasma states in terms of momentum exchange, the hierarchy of the momentum exchange in grain–grain and grain–neutral collisions and corresponding dynamical states of complex plasmas. In the next section these results are used to calculate the electron and ion drag forces.



### 6.1. Momentum transfer cross section

We consider binary collision between two particles of masses  $m_1$  and  $m_2$  interacting via an isotropic potential of the form

$$U(r) = -(U_0/r) \exp(-r/\lambda),$$

where  $\lambda$  is the *effective* screening length,  $U_0 > 0$  for attraction and  $U_0 < 0$  for repulsion. The particle trajectories during collision are ballistic, i.e., any types of multiple collisions are neglected. The problem is equivalent to the scattering of a single particle of reduced mass,  $\mu = m_1 m_2 / (m_1 + m_2)$ , in the central field  $U(r)$  (whose centre is at the centre of masses of the colliding particles). The analysis of motion in the central field was given in Section 3.1.1 and below we employ the results of this analysis. First, we study the case of point-like particles. The role of the finite grain size will be addressed later.

The momentum transfer (scattering) cross section in this approximation is given by the integral over impact parameters

$$\sigma_s = 2\pi \int_0^\infty [1 - \cos \chi(\rho)] \rho d\rho, \quad (36)$$

where  $\chi$  is the deflection (scattering) angle. The latter depends on the impact parameter in the following way,  $\chi(\rho) = |\pi - 2\varphi(\rho)|$ , where  $\varphi(\rho) = \rho \int_{r_0}^\infty dr r^{-2} [1 - U_{\text{eff}}(r, \rho)]^{-1/2}$  and  $U_{\text{eff}}(r, \rho) = \rho^2/r^2 + 2U(r)/\mu v^2$  is the normalized effective potential energy. The distance of closest approach,  $r_0(\rho)$ , in the integral above is the largest root of the equation  $U_{\text{eff}}(r, \rho) = 1$ .

The scattering parameter,  $\beta(v) = |U_0|/\mu v^2 \lambda$ , introduced in Section 3.1.1 is the ratio of the Coulomb radius,  $R_C = |U_0|/\mu v^2$ , to the effective screening length  $\lambda$ . It characterizes the “coupling” between colliding particles: the coupling is weak when the characteristic distance of interaction  $R_0 \sim R_C$ , introduced through  $|U(R_0)| = \frac{1}{2}\mu v^2$ , is shorter than the screening length, i.e., when  $\beta(v) \ll 1$ . In the opposite limit,  $\beta(v) \gg 1$ , when  $R_0 \gg \lambda$ , the coupling is strong. In addition, the normalized momentum transfer cross section,  $\sigma_s/\lambda^2$ , depends only on  $\beta$  [57,177,178], which makes  $\beta(v)$  a *unique parameter* which describes momentum exchange for Yukawa interactions.

Note that the theory of Coulomb scattering, which assumes an unscreened (Coulomb) potential and a cutoff at  $\rho_{\text{max}} = \lambda$  in integral (36), is widely used to describe momentum exchange in collisions between charged particles (e.g., electron–ion collisions in plasmas). It holds for  $R_C \sim R_0 \ll \lambda$  or  $\beta \ll 1$ , i.e., in the limit of weak coupling. However, for  $\beta \geq 1$  the theory of Coulomb scattering is not applicable: in this case the interaction range  $R_0$  is larger than the screening length and a considerable fraction of the interaction occurs outside the Debye sphere providing substantial contribution to the momentum transfer. The use of a cutoff at  $\rho_{\text{max}} = \lambda$  considerably underestimates the momentum transfer in this case [74].

Now let us estimate the characteristic values of the scattering parameter for different types of collisions involving dust grains. Taking into account that  $|U_0| \sim |Z|e^2$  for grain–electron and grain–ion collisions, and  $|U_0| \sim Z^2 e^2$  for grain–grain collisions we get the following hierarchy of characteristic scattering parameters: (i) *Grain–electron* collisions,  $\beta_T^{de} \sim z(a/\lambda) \sim 0.01\text{--}0.3$ ; (ii) *Grain–ion* collisions,  $\beta_T^{di} \sim z\tau(a/\lambda) \sim 1\text{--}30$ ; *Grain–grain* collisions,  $\beta_T^{dd} \sim z_d(a/\lambda) \sim 10^3\text{--}3 \times 10^4$ , where  $z_d = Z^2 e^2 / a T_d \equiv z|Z|(T_e/T_d)$  is the normalized potential energy of two dust grains which are just touching. We also assumed  $z \sim 1$ ,  $\tau \sim 10^2$ ,  $a/\lambda \sim 0.01\text{--}0.3$ ,  $|Z| \sim 10^3$ , and  $z_d = z|Z|\tau = 10^5$  (for  $T_d = T_i$ ), which is typical for complex plasmas. These estimates show that the coupling is weak only for grain–electron collisions. At the same time, coupling for grain–ion and grain–grain collisions is usually strong, and the theory of Coulomb scattering fails to describe such collisions. In connection with grain–ion collisions, this issue was recently discussed in detail in Refs. [57,74,177,179–181].

The numerical calculation of the momentum transfer cross sections for a wide range of  $\beta$  ( $0.1 < \beta < 10^3$ ) for both attractive and repulsive Yukawa potential was recently reported [63]. First, the dependence of the scattering angle on the impact parameter,  $\chi(\rho)$ , was obtained. Then, Eq. (36) was numerically integrated yielding the momentum transfer cross sections. The obtained results are presented in Figs. 16 and 17.

The scattering angle  $\chi(\rho)$  decreases monotonically for repulsive interactions for all  $\beta$ . In contrast, for attractive interactions a monotone decrease of the scattering angle is observed only for  $\beta \lesssim 1$ , whilst for  $1 \lesssim \beta \lesssim \beta_{\text{cr}}$  it becomes a nonmonotone function of  $\rho$ , and at  $\beta > \beta_{\text{cr}} \simeq 13.2$  the scattering angle diverges at the “transitional” impact parameter  $\rho_* \simeq \lambda(\ln \beta + 1 - \frac{1}{2} \ln^{-1} \beta)$ , see Eq. (8). The divergence of the scattering angle for attractive interactions arises from the

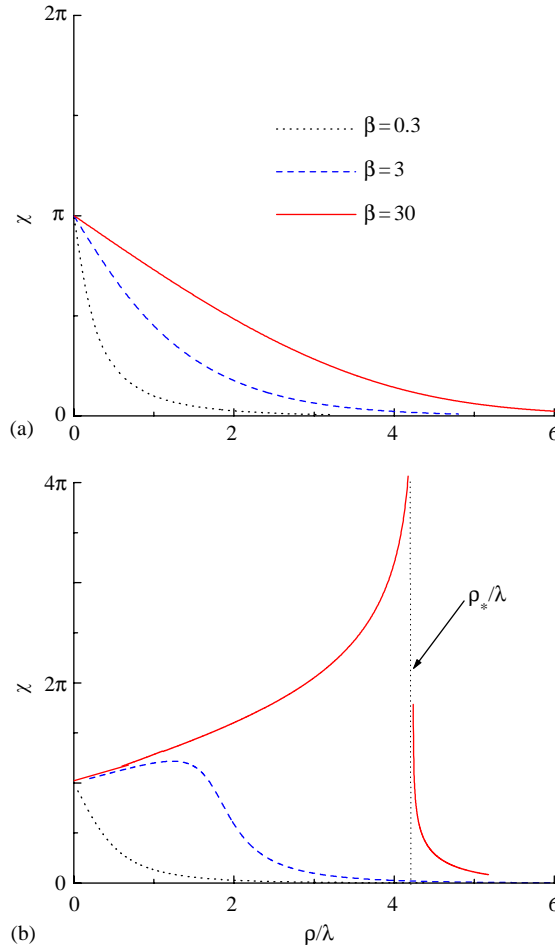


Fig. 16. Scattering angle  $\chi$  versus the normalized impact parameter  $\rho/\lambda$ , where  $\lambda$  is the effective screening length. The numerical calculations for a repulsive (a) and attractive (b) Yukawa interaction potential are plotted for three different scattering parameters  $\beta = 0.3, 3$  and  $30$ . The vertical dotted line at  $\rho \simeq 4.2\lambda$  in (b) indicates the transitional impact parameter  $\rho_*$  at which  $\chi$  diverges.

barrier in the effective potential  $U_{\text{eff}}$ . Note also that when  $\beta \ll 1$  the trajectories are mainly deflected within the plasma screening length (at  $\rho/\lambda \lesssim 1$ ). In the opposite case  $\beta \gg 1$  the scattering angle can be substantial even for  $\rho \gg \lambda$ , both for repulsive and attractive interaction. (This is another demonstration of the fact that the Coulomb scattering theory is inapplicable for  $\beta \gtrsim 1$ , as discussed above.)

The results obtained for the momentum transfer cross section (Fig. 17) show the following features: the cross section for the attractive potential is always larger than that for the repulsive potential (they converge in the limit of weak coupling  $\beta \ll 1$ ). The cross section for the repulsive potential grows monotonically, while for the attractive potential a local maximum and minimum appear near  $\beta = \beta_{\text{cr}}$ . This nonmonotonic behaviour is a consequence of the bifurcation which the scattering angle  $\chi(\rho)$  experiences in the range  $1 \lesssim \beta \lesssim \beta_{\text{cr}}$ . It is also evident from Fig. 17 that the Coulomb scattering theory (shown by the dotted line) considerably underestimates the cross section for both repulsion and attraction when  $\beta \gtrsim 1$ .

Now let us consider different limiting cases when an analytical description for the momentum transfer cross section is possible.

**Repulsive potential.** In the limit of weak coupling the Coulomb scattering theory is applicable as discussed above. The well known expression for the *Coulomb* scattering cross section

$$\sigma_s^C / \pi \lambda^2 = 2\beta^2 \ln(1 + 1/\beta^2) \quad (37)$$

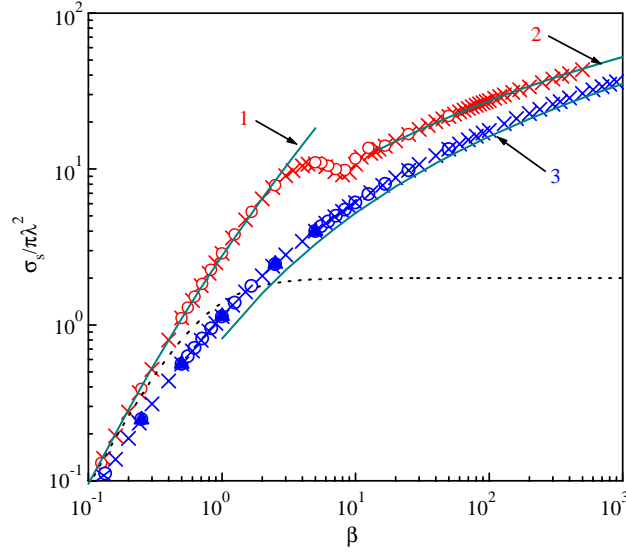


Fig. 17. Momentum transfer cross section,  $\sigma_s$ , normalized to  $\pi\lambda^2$  (where  $\lambda$  is the effective screening length), versus the scattering parameter  $\beta$ . The upper data are for attractive and the bottom data are for repulsive Yukawa potentials. Crosses correspond to the numerical results by Khrapak et al. [63], (blue) triangles are numerical results by Lane and Everhart [178], and circles are numerical results by Hahn et al. [181]. Solid curves correspond to the following analytical expressions: 1—Eq. (39); 2—Eq. (40); 3—Eq. (38). The dotted line corresponds to the Coulomb scattering theory [Eq. (37)]. All the results are for point-like particles.

is shown by the dotted line in Fig. 17. For  $\beta \gtrsim 1$  Eq. (37) is no longer applicable, however, an asymptotic analytical approximation for the case  $\beta \gg 1$  can be obtained as follows. The relevant characteristic of the steepness of the potential is the parameter  $\gamma_0 = |d \ln U(r)/d \ln r|_{r=R_0}$ . The case  $\gamma_0 \gg 1$  corresponds to a rapidly decreasing steep potential so that the momentum is mostly transferred in a spherical “shell” of radius  $R_0$ , and thickness  $\sim R_0/\gamma_0$ . Hence, the scattering resembles that of a hard sphere potential [182,183] and with increasing  $\gamma_0$  the momentum transfer cross section tends to

$$\sigma_s^{\text{HS}} / \pi \lambda^2 \simeq (R_0/\lambda)^2. \quad (38)$$

For the Yukawa potential  $\gamma_0 = 1 + R_0/\lambda \gg 1$ , provided  $\beta \gg 1$ . A rapidly converging analytical solution for  $R_0(\beta)$  is  $R_0/\lambda \simeq \ln 2\beta - \ln \ln 2\beta$  [63].

*Attractive potential.* For weak coupling ( $\beta \ll 1$ ) the theory of Coulomb scattering is applicable. The momentum transfer cross section is the same as for the repulsive potential and is given by Eq. (37). It was shown [74,179] that even for moderate  $\beta$  the extension of the standard Coulomb scattering theory is possible by taking into account all the trajectories with a distance of closest approach shorter than  $\lambda$ . The definition of the maximum impact parameter (cutoff) then becomes  $r_0(\rho_{\text{max}}) = \lambda$  instead of  $\rho_{\text{max}} = \lambda$  and leads to a modification of the Coulomb logarithm. The *modified Coulomb* momentum transfer cross section is

$$\sigma_s^{\text{MC}} / \pi \lambda^2 \simeq 4\beta^2 \ln(1 + 1/\beta). \quad (39)$$

Although the approach of [74,179] is not rigorous, Eq. (39) shows very good agreement with numerical results [63,181,184] up to  $\beta \sim 5$  (see Fig. 17) and agrees exactly, of course, with Coulomb scattering theory for  $\beta \ll 1$ .

The case of strong coupling ( $\beta \gg 1$ ) requires a new physical approach. Such an approach was formulated in Ref. [57]. The existence of the potential barrier in  $U_{\text{eff}}$  at  $\beta > \beta_{\text{cr}}$  and the discontinuity in  $\chi(\rho)$  it causes, play a crucial role for the analysis of collisions. As shown in Fig. 16 the dependence of the scattering angle on the impact parameter in the limit of strong coupling ( $\beta = 30$ ) has the following features: for “close” ( $\rho < \rho_*$ ) collisions we have  $\chi \rightarrow \pi$  at  $\rho \rightarrow 0$ , and  $\chi(\rho)$  grows monotonically until  $\rho = \rho_*$ , where it diverges; for “distant” collisions ( $\rho > \rho_*$ ) the scattering angle decreases rapidly, due to the exponential screening of the interaction potential.

It is convenient to consider the contributions from close and distant collisions into the momentum transfer separately. As shown in Ref. [57] the behaviour of  $\chi$  as a function of the normalized impact parameter  $\rho/\rho_*$  is *practically independent* of  $\beta$  for  $\rho < \rho_*$ . This self-similarity allows us to present this contribution to the cross section (normalized to  $\pi\lambda^2$ ) as  $\simeq \mathcal{A}(\rho_*/\lambda)^2$ , where  $\mathcal{A} = 2 \int_0^1 [1 - \cos \chi(\xi)] \xi d\xi$  and  $\xi = \rho/\rho_*$ . The numerical factor  $\mathcal{A}$  can be determined by direct numerical integration. It was found that  $\mathcal{A} = 0.81 \pm 0.01$  for all  $\beta$  in the range  $\beta_{cr} \leq \beta \leq 500$  [57]. For distant collisions the scattering angle decreases rapidly in the vicinity of  $\rho_*$ . This makes it possible to apply the small angle approximation to estimate their contribution to the cross section (normalized to  $\pi\lambda^2$ ) as  $\simeq 2.0 + 4.0 \ln^{-1} \beta$  [57]. Combining these contributions and keeping terms up to  $O(1)$ , we can write the momentum transfer cross section in the limit of *strong coupling* as

$$\sigma_s^{SC}/\pi\lambda^2 \simeq 0.81(\rho_*/\lambda)^2 + 2.0, \quad (40)$$

where  $(\rho_*/\lambda)^2 \simeq \ln^2 \beta + 2 \ln \beta$ . Expression (40) is valid for  $\beta \geq \beta_{cr}$  and point-like particles. Fig. 17 shows the very good agreement between Eq. (40) and numerical calculations. A sufficiently accurate and even simpler approximation is  $\sigma_s^{SC} \simeq \pi\rho_*^2$ , which can be further justified when the finite size of the dust grain is taken into account.

Concluding this section we briefly discuss the role of finite particle size. In this case a new lengthscale enters the problem. In contrast to the case of point-like particles, where the scattering is described by the single parameter  $\beta$ , we now have a second parameter,  $a/\lambda$ . If the distance of the closest approach,  $r_0$ , is smaller than  $a$  (or  $2a$  for particle–particle collisions), then the direct (touching) collision takes place. In this case we will assume absorption for grain–electron and grain–ion collision, and specular reflection for grain–grains collisions.

A detailed discussion of the effect of finite grain size on the momentum transfer is given in Ref. [63]. It is shown that for the repulsive interaction (grain–electron and grain–grain collisions) the effect of finite size considerably affect the momentum transfer only when coupling is very weak,

$$\beta \lesssim (a/\lambda) A^{-1/2}, \quad (41)$$

where  $A \simeq \ln(1/\beta) \gg 1$  is the Coulomb logarithm. Recalling that  $\beta_T^{de} \sim z(a/\lambda)$  and  $\beta_T^{dd} \sim z_d(a/\lambda)$  and since  $z \sim 1$ ,  $z_d \gg 1$  we conclude that the effect of finite size can usually be neglected for grain–electron and grain–grain collisions.

The effect of finite size is more important for attractive (grain–ion) interactions. For example, for sufficiently large  $\beta$  the maximum impact parameter corresponding to ion collection is  $\rho_c^+ = \rho_*$ , as follows from Eq. (6). At the same time the contribution to the momentum transfer from ions with  $\rho > \rho_*$  vanishes at large  $\beta$ . Hence in this case the momentum transfer is associated mostly with ions collected by the particle and the total momentum transfer cross section  $\sigma_\Sigma$  (sum of the contributions due to scattering and due to absorption) tends to  $\pi\rho_*^2$ . However, this does not imply much difference compared to the case of point-like particles, because scattering with large angles at  $\rho < \rho_*$  and absorption (which formally corresponds to the scattering at  $\pi/2$ ) produce comparable effects. The dependence  $\sigma_\Sigma(\beta)$  for an attractive Yukawa potential is shown in Fig. 18 for different values of  $a/\lambda$ . One can see that the momentum transfer can decrease or increase (in comparison with point-like particles), depending on the values of  $a/\lambda$  and  $\beta$ . At the same time, the momentum transfer cross section is not very sensitive to the particle size—the deviation from  $\sigma_s$  for a point-like particle does not exceed  $\sim 50\%$ .

## 6.2. Momentum exchange rates

Let us consider a *test* particle (dust grain) moving through a gas of *field* particles (electrons, ions, or dust grains) having an isotropic Maxwellian velocity distribution function. The test particle velocity  $u_d$  is assumed to be smaller than the field particle thermal velocity  $v_{T_\alpha}$ . Introducing the momentum exchange rate  $v_{d\alpha}$  through  $du_d/dt = -v_{d\alpha}u_d$  we get [63]

$$v_{d\alpha} = \frac{1}{3} \sqrt{\frac{2}{\pi}} \frac{n_\alpha \mu_{d\alpha}}{m_d v_{T_\alpha}^5} \int_0^\infty v^5 \sigma_\Sigma(v) \exp(-v^2/2v_{T_\alpha}^2) dv,$$

where  $\sigma_\Sigma(v)$  is the corresponding total momentum transfer cross section (function of the relative velocity),  $\mu_{d\alpha}$  is the reduced mass, and  $\alpha = e, i, d$ . Some results following from this expression are given below.

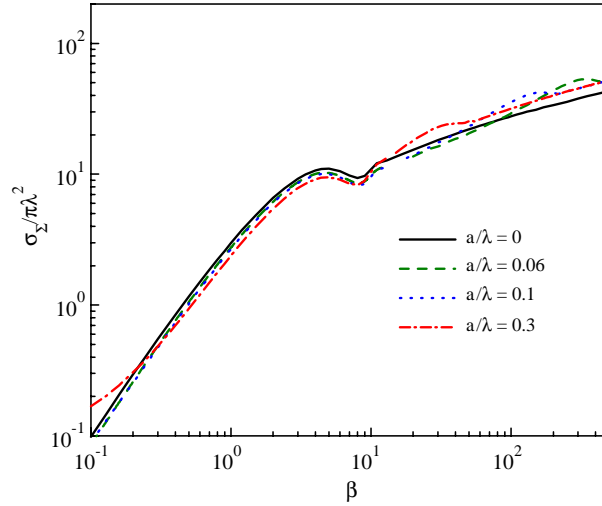


Fig. 18. The total momentum transfer cross section,  $\sigma_{\Sigma}$ , normalized to  $\pi\lambda^2$  (where  $\lambda$  is the effective screening length), versus the scattering parameter  $\beta$  for the attractive Yukawa potential. The numerical results for different values of  $a/\lambda$  are shown to illustrate the role of finite particle radius  $a$ .

### 6.2.1. Grain–electron collisions

For grain–electron interactions usually  $\beta_T^{de} \ll 1$  and the standard Coulomb scattering approach is applicable. This yields

$$v_{de} \simeq (2\sqrt{2\pi}/3)(m_e/m_d)n_e v_{Te} a^2 z^2 \Lambda_{de}, \quad (42)$$

where  $n_e$ ,  $m_e$ , and  $v_{Te}$  are the density, mass, and thermal velocity of electrons, and

$$\Lambda_{de} = z \int_0^\infty e^{-zx} \ln[1 + 4(\lambda/a)^2 x^2] dx - 2z \int_1^\infty e^{-zx} \ln(2x - 1) dx,$$

is the Coulomb logarithm for grain–electron collisions integrated over the Maxwellian distribution [185]. In the typical case  $(2/z)(\lambda/a) \gg 1$  we obtain  $\Lambda_{de} \simeq 2 \ln[(2/z)(\lambda/a)]$  with logarithmic accuracy.

### 6.2.2. Grain–ion collisions

For grain–ion interaction  $\beta_T^{di}$  often exceeds unity and then the Coulomb scattering approach is not applicable. In the case  $\beta_T^{di} \lesssim 5$ , Eq. (39) can be used. This yields

$$v_{di} \simeq (2\sqrt{2\pi}/3)(m_i/m_d)n_i v_{Ti} a^2 z^2 \tau^2 \Lambda_{di}, \quad (43)$$

where  $n_i$ ,  $m_i$ , and  $v_{Ti}$  are the density, mass, and thermal velocity of ions, and

$$\Lambda_{di} \simeq 2z \int_0^\infty e^{-zx} \ln[1 + 2\tau^{-1}(\lambda/a)x] dx \quad (44)$$

is the *modified* Coulomb logarithm for grain–ion scattering [74,179] integrated over the Maxwellian distribution [in Eq. (44) we took into account that  $\tau \gg 1$ ]. In the limit of small  $\beta_T^{di}$  or  $(1/z\tau)(\lambda/a) \gg 1$  the result reduces to that of the Coulomb scattering theory and we have  $\Lambda_{di} \simeq 2 \ln[(2/z\tau)(\lambda/a)]$ . In the opposite limit of very large scattering parameters,  $\beta_T^{di} > \beta_{cr} \simeq 13.2$ , the total momentum transfer cross section is to good accuracy  $\sigma_{\Sigma} \simeq \pi\rho_*^2$ , where  $\rho_* \sim \lambda \ln \beta_T^{di}$ . This yields

$$v_{di} \simeq (8\sqrt{2\pi}/3)(m_i/m_d)n_i v_{Ti} \rho_*^2. \quad (45)$$

### 6.2.3. Grain–grain collisions

For grain–grain interactions the standard Coulomb scattering approach can be employed only for extremely small grain charges and/or extremely high grain energies, so that  $\beta_T^{dd} = z_d(a/\lambda) \ll 1$ . In this situation we have

$$v_{dd} \simeq (4\sqrt{2\pi}/3)n_d v_{Td} a^2 z_d^2 \Lambda_{dd}, \quad (46)$$

where  $n_d$ , and  $v_{Td}$  are the density, and thermal velocity of the dust grains, and

$$\Lambda_{dd} = z_d \int_0^\infty e^{-z_d x} \ln[1 + (\lambda/a)^2 x^2] dx - 2z_d \int_1^\infty e^{-z_d x} \ln(2x - 1) dx,$$

is the Coulomb logarithm for the grain–grain collisions integrated over the Maxwellian distribution. If  $(1/z_d)(\lambda/a) \gg 1$ , the Coulomb scattering approach is applicable and we have  $\Lambda_{dd} \simeq 2 \ln[(1/z_d)(\lambda/a)]$  with logarithmic accuracy. In the regime  $\beta_T^{dd} \gg 1$ , which is more typical for complex plasmas, the analogy with hard sphere collisions can be used. The result is [63]

$$v_{dd} \simeq (4\sqrt{2\pi}/3)n_d v_{Td} R_0^2. \quad (47)$$

The obtained results for the momentum exchange in grain–grain collisions will be used below to investigate the possible states of complex plasmas.

### 6.3. Momentum exchange diagram

The grain charges in complex plasmas, as well as the plasma screening length are not constant. This is why the strength of the electrostatic coupling between the grains can be easily changed experimentally over a fairly wide range (by varying, e.g., the discharge conditions [186]). This is a major distinguishing feature of complex plasmas compared to usual plasmas, where the ion charges are normally constant (single). In complex plasmas, one can observe the transitions from the disordered, weakly coupled to strongly coupled states and the formation of ordered structures of grains—plasma crystals [3,11–14,26,104,180,186–192].

Another major distinguishing feature of complex plasmas is that the overall dynamical time scales associated with the dust component are relatively long (dust plasma frequency  $\sim 10$ – $100$  Hz) [3,76,104]. Furthermore, the grains themselves are large enough to be easily visualized individually. All together this makes it possible to investigate phenomena occurring in different phases at the most fundamental kinetic level [180,186,191]. Although there is always some damping introduced into the complex plasma systems due to neutral gas friction [104], the resulting damping rate is many orders of magnitude smaller than that in colloidal suspensions, and it can easily be made much smaller than the major eigenfrequencies of the dust dynamics. Hence the most interesting dynamical phenomena have usually enough time to evolve [191].

Let us dwell upon these features of complex plasmas in detail.

Fig. 19 represents different “phase states” of complex plasmas as functions of the electrostatic coupling parameter  $\Gamma_S$  and the mean grain separation  $\Delta$ , normalized either to the grain size  $a$  or to the screening length  $\lambda$  (“finiteness parameter”  $\alpha = \Delta/a$  and “lattice parameter”  $\kappa = \Delta/\lambda$ , respectively). The parameter  $\Gamma_S = \Gamma \exp(-\kappa)$ , which characterizes the “actual” coupling ratio (potential energy/kinetic energy) at the average intergrain distance, is expressed in terms of the (Coulomb) coupling scale  $\Gamma = e^2 Z^2 / \Delta T_d$  (note that in terms of  $\Gamma$  and  $\kappa$  the thermal scattering parameter is  $\beta_T^{dd} = 2\Gamma\kappa$ ). The use of  $\Gamma_S$  implies that the calculations should be representative to some extent for other types of “similar” interaction potentials, too (viz., with “similar” long- and short-range asymptotes). The vertical line  $\kappa = 1$  conditionally divides the diagram into weakly screened (Coulomb) and strongly screened (Yukawa) parts. In Fig. 19 we have set  $\lambda/a \equiv \alpha/\kappa = 100$ , which is typical of complex plasmas studied so far, but there is in principle a wide range of variation, depending on grain size and plasma conditions chosen. The “melting line” which indicates the liquid–solid phase transition and is shown by the upper solid line in Fig. 19 is discussed in Section 10.

Further insight into the possible phase states shown in Fig. 19 are obtained from our above results on the momentum transfer cross section for grain–grain collisions. This approach allows us to obtain a clear physical classification of complex plasmas. The lower solid line indicates the “transition” between “ideal” and “nonideal” plasmas. We determine this transition from the condition  $\sqrt{\sigma_\Sigma/\pi} = (4\pi/3)^{-1/3} \Delta$ , which implies that the characteristic range of grain interaction (in terms of the momentum exchange) is comparable to the intergrain distance (in terms of the Wigner–Seitz radius).

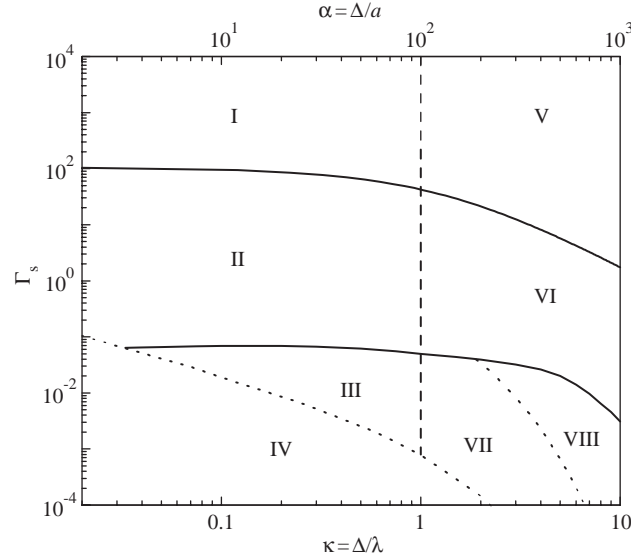


Fig. 19. “Momentum exchange” diagram of complex plasmas in  $(\Gamma_S, \kappa)$  parameter space. The vertical dashed line at  $\kappa = 1$  conditionally divides the system into “Coulomb” and “Yukawa” parts. Different states are marked in the figure. Regions I (V) represent Coulomb (Yukawa) crystals; Regions II (VI) are for Coulomb (Yukawa) nonideal plasmas; Regions III (VII and VIII) correspond to Coulomb (Yukawa) ideal plasmas; note that in region VIII the pair Yukawa interaction asymptotically reduces to the hard sphere limit, forming a “Yukawa granular medium”; In region IV the electrostatic interaction is not important and the system is like a usual granular medium. For further explanations see text.

Above this line the interaction is essentially multiparticle, whereas below the line only pair collisions are important. This refines the standard condition used to define a “boundary” between ideal and nonideal plasmas,  $\Gamma_S \sim 1$ . From the thermodynamical point of view, this line determines the limit of employing expansions of the thermodynamical functions (e.g., virial expansion) over the (small) coupling parameter.

It is important to note that for a Yukawa potential (as well as for any monotonic interaction potential) no liquid–gas phase transition is possible (formally, the critical point occurs at  $T_d = 0$ ). This is different, if the pair potential is not monotonic, e.g., a long range attractive component added to a repulsive electrostatic potential exists, as has been suggested by several authors (see e.g., Refs. [3,146,180]). So far, however, there are no reliable experiments reporting on the observation of, e.g., the coexistence of liquid and gaseous phases, or other indications of a first order phase transition in gaseous complex plasmas.

The regions where the system is similar to a granular medium are also shown in Fig. 19: below the lower dotted curve the electrostatic interaction is too weak and the momentum exchange occurs due to direct grain collisions, i.e., we have a usual granular medium where charges do not play any noticeable role. This line corresponds to  $\beta_T^{dd} = (a/\lambda)A_{dd}^{-1/2}$  [see Eq. (41)]. The upper dotted curve marks the transition boundary for a very interesting state, which we have called “Yukawa granular medium”. Here the “mean” scattering parameter for grain–grain collisions exceeds unity ( $\beta_T^{dd} > 1$ ) and, hence, the strongly screened electrostatic interaction reduces asymptotically to the hard sphere limit with radius  $R_0 \simeq \lambda \ln(2\beta_T^{dd})$ .

Next, we investigate complex plasma properties in terms of the competition between the momentum exchange in mutual grain–grain collisions and the interaction with the surrounding medium.

Complex plasmas can be “engineered” as essentially a “one-phase fluid” (when the interactions between the grains dominate), or as a “particle laden two-phase flow” (when the interactions with the background medium are of similar or greater importance). We have illustrated this by plotting contours of constant ratios of the grain–grain/grain–background momentum exchange rates,  $v_{dd}/v_{dn}$ , in the  $(\Gamma_S, \kappa)$  diagram in Fig. 20.

In complex plasmas the exchange of momentum with the background medium is mostly through grain–neutral gas collisions,

$$v_{dn} = \delta(8\sqrt{2\pi/3})(m_n/m_d)a^2n_n v_{T_n}, \quad (48)$$



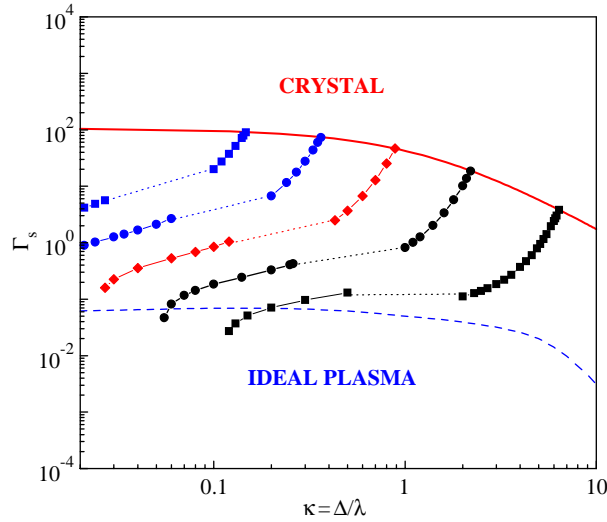


Fig. 20. Typical contours are shown of constant ratios of the momentum exchange rates in grain–grain collisions relative to grain–background (neutral gas) collisions. The values  $v_{dd}/v_{dn} = 10^2, 10, 1, 10^{-1}$ , and  $10^{-2}$  are depicted in a phase diagram for complex plasmas in  $(\Gamma_s, \kappa)$  parameter space (from left to right). Also shown in the figure are the lines corresponding to crystal melting (solid line) and the boundary between ideal and nonideal plasmas (dashed line). For the calculations we use the following parameters: Grains of radius  $a = 1 \mu\text{m}$  and material mass density of  $1 \text{ g/cm}^3$  in argon plasma at neutral gas pressure 100 Pa; room temperature ions and neutrals  $T_i \sim T_n \sim 0.03 \text{ eV}$ , and  $a/\lambda = 10^{-2}$ .

where  $m_n$ ,  $n_n$ , and  $v_{T_n}$  are the mass, density, and thermal velocity of neutrals, respectively [193]. The value of the numerical factor  $\delta$  depends on the exact process of neutral scattering from the particle surface. For example,  $\delta = 1$  for the cases of complete absorption and specular reflection, whilst  $\delta = 1 + \pi/8 \simeq 1.4$  for diffuse scattering with full accommodation. We choose the later value which is more consistent with recent experimental results [194].

For the momentum exchange rate in grain–grain collisions we use Eq. (47) at  $\beta_T^{dd} \gg 1$  (upper symbols in the figure) and Eq. (46) at  $\beta_T^{dd} \ll 1$  (lower symbols). In the transition regime  $\beta_T^{dd} \sim 1$  none of these approximations is applicable and we have therefore simply linked the two regimes by dotted lines.

Fig. 20 shows that there is a broad range of parameters where complex plasmas have the properties of one-phase fluids ( $v_{dd}/v_{dn} \gg 1$ ), and those of two-phase fluids  $v_{dd}/v_{dn} \sim 1$ . In the extreme limit of very small  $v_{dd}/v_{dn}$  we can also, of course, have “tracer particles” in the background medium, which provide practically no disturbance to the background flow. Taking into account that a number of plasma parameters (e.g., the neutral gas pressure, plasma screening length, the ratio  $a/\lambda$ ) can be varied relatively easily within approximately one order of magnitude, most of the possible states can be investigated.

In concluding this section we note that not all of the assumptions employed to simplify the calculations are necessarily satisfied in real complex plasmas. A few examples are: deviation of grain potential from the Yukawa form [3,146,180], dependence of the grain charge on intergrain distance [166], destruction of ballistic trajectories by collisions with neutrals [195], etc. Nevertheless, in many cases this simple model does provide reasonable predictions and hence it can be considered as the basis for more sophisticated models. The obtained results can be important for “engineering” experiments which aim to make use of special properties of complex plasmas.

## 7. Forces on particles in complex plasmas

Knowledge of the major forces acting on microparticles in complex plasmas is essential for understanding dynamic phenomena and equilibrium configurations of complex plasmas observed in experiments. The forces can be naturally divided into two groups: the first one includes the forces which have electric nature—electron drag, ion drag, and electrostatic forces, whereas the second one includes the charge-independent forces—gravity, neutral drag, and thermophoretic forces. The calculation of the ion drag force is rather complicated in some cases. At the same time, this force is of particular importance in complex plasmas and therefore it is a subject of a separate section.

### 7.1. Ion drag force

The ion drag force—the momentum transfer from the flowing ions to charged microparticles (grains) embedded into a plasma—is inevitable and exceptionally important factor in dusty (complex) plasmas. Ion flows are usually induced due to “global” large-scale electric fields that always exist in plasmas (e.g., ambipolar or sheath fields in plasma discharges). Knowledge of the ion drag force as a function of the plasma parameters (which may vary over a quite broad range) is necessary for understanding phenomena occurring in laboratory and space environment. The very fact that the ion drag force can be important in dusty plasmas was ascertained even before the active laboratory investigation of dusty plasmas started [196,197]. Presently, it is considered to be established that ion drag affects (or even determines) location and configuration of the dust structures in laboratory plasma facilities [22,198,199], is responsible for the rotation of dust structures (e.g., clusters) in the presence of a magnetic field [200–202], affects the properties of low-frequency waves in dusty plasmas [203–205], causes the formation of a void in the central part of rf discharges in experiments under microgravity conditions [20,23,180], determines diffusion and mobility of dust particles in strongly ionized plasmas [206,207], etc.

The traditional way to derive the ion drag force on the test charged particle is based on the “binary collision approach”. The force is determined by the momentum exchange rate in the dust–ion collisions, averaged over given velocity distribution of ions (see Section 6.2). Initially, the binary collision approach was applied by Uglov and Gnedovets [91] to calculate the ion drag in the “Coulomb scattering” limit—basically, this is the linear approximation assuming the ion scattering with small angles within the Debye sphere. A simplified treatment of this problem was given by Barnes et al. [198]. Recently, the approach was extended by Khrapak et al. [57,74,177,179] to calculate the force in the case of large angle scattering.

An alternative way to calculate the ion drag force is the kinetic approach based on the so-called “linear dielectric response formalism” (e.g., [208,209]). Instead of calculating single ion trajectories and then integrating the resulting momentum transfer, one can solve the Poisson equation coupled to the kinetic equation for ions and obtain the self-consistent electrostatic potential around the particle. The polarization electric field at the origin of the test charge gives us the force on the particle. Recently, Ivlev et al. [195,210,211] applied this formalism for calculating the ion drag force for arbitrary velocity of the ion flow and arbitrary frequency of the ion–neutral collisions.

In this section we present the results of both approaches and discuss unresolved issues.

#### 7.1.1. Binary collision approach

In the framework of this approach, the ion drag force  $F_{id}$  is completely determined by the (velocity-dependent) total momentum transfer cross section for the dust–ion collisions,  $\sigma_\Sigma$ , which was introduced in Section 6.1. The force is  $F_{id} = m_d v_{di} u$ , where  $u$  is the ion flow velocity and  $v_{di}$  is the momentum exchange rate (the latter is given by averaging over the ion velocity distribution). The force depends on the magnitude of the thermal scattering parameter,  $\beta_T = e^2 |Z| / \lambda T_i$ , where  $\lambda$  is the effective screening length (which does not necessarily coincide with the Debye screening length, see Sections 4.1 and 7.1.3).

For subthermal flows (when the *thermal* Mach number is small,  $M_T \equiv u_i / v_{Ti} \ll 1$ ), we directly employ results of Section 6.2.2: at moderate  $\beta_T \lesssim 5$ , Eq. (43) yields

$$F_{id} = \frac{1}{3} \sqrt{\frac{2}{\pi}} \left( \frac{T_i}{e} \right)^2 \Lambda \beta_T^2 M_T, \quad (49)$$

where  $\Lambda(\beta_T) \simeq \int_0^\infty e^{-x} \ln(1 + 2x/\beta_T) dx \equiv -e^{\beta_T/2} \text{Ei}(-\beta_T/2)$  is the modified Coulomb logarithm integrated over the Maxwellian distribution function. Here we also assume  $\lambda \simeq \lambda_{Di}$  (see Section 7.1.3). Eq. (49) yields the scaling  $F_{id} \propto (Z/\lambda)^2$ . In the linear regime  $\beta_T \ll 1$  the logarithm is reduced to  $\Lambda \simeq \ln \beta_T^{-1}$ , which is identical to the results of the Coulomb scattering theory. In the opposite regime of strongly nonlinear scattering,  $\beta_T \gg \beta_{cr} \simeq 13$ , we obtain from Eq. (45)

$$F_{id} \simeq \frac{2}{3} \sqrt{\frac{2}{\pi}} \left( \frac{T_i}{e} \right)^2 \ln^2 \beta_T M_T. \quad (50)$$

In this case the force depends logarithmically on the scattering parameter and, hence, on  $Z$  and  $\lambda$ . Note that for  $M_T \ll 1$  the effective screening length is determined by ions, since the electron temperature is typically two orders of magnitude higher than the ion (neutral) temperature.

For superthermal ion flows with  $M_T \gg 1$ , the drift velocity rather than the thermal velocity should be used to evaluate the scattering parameter  $\beta$ . Also, the screening is determined by the electrons rather than by ions in this case,  $\lambda \simeq \lambda_{De}$  (see Section 7.1.3). Therefore, we conclude from Eq. (7) that the scattering parameter decreases rapidly with the Mach number, and we can expect the linear scattering (weak coupling,  $\beta \sim \beta_T/M_T^2 \ll 1$ ) to be typical for  $M_T \gg 1$ . Then the momentum transfer cross section is given by Eq. (37) and after the integration over the shifted Maxwellian distribution the force is

$$F_{id} \simeq \left(\frac{T_i}{e}\right)^2 \ln \left(\frac{\lambda_{De}}{\lambda_{Di}} \frac{M_T^2}{\beta_T}\right) \frac{\beta_T^2}{M_T^2}. \quad (51)$$

(Application of the binary collision approach implies that the ion mean free path should nevertheless exceed the electron screening length  $\lambda_{De}$ ). The ion drag decreases as  $\propto M_T^{-2}$  at large Mach numbers (neglecting a weak logarithmic dependence). For sufficiently high flow velocities the momentum flux onto the grain (collection) dominates over the scattering part and then the force tends to the “geometrical asymptote”,  $F_{id} \simeq (T_i/e)^2 (a/2\lambda_{Di})^2 M_T^2$ , which does not depend on the grain charge [212].

### 7.1.2. Kinetic approach

The binary collision approach is intrinsically inconsistent. There are the following reasons for that: (i) While the ion interacts with the charged particle, the interactions with other species (in particular— the ion–neutral collisions) are *neglected*. (ii) The approach *presumes* certain potential distribution around the test charge, although the potential is a self-consistent function of the plasma environment (e.g., ion flow velocity). (iii) The approach *presumes* certain distribution function for ions (usually, the shifted Maxwellian distribution). All these issues can be successfully resolved by employing the *self-consistent* kinetic approach.

Calculation of the ion drag force is based on the linear dielectric response formalism: the self-consistent distribution of the electrostatic potential around a grain of charge  $eZ$  is given by Eq. (35). Being embedded into a flowing plasma, the grain induces the plasma polarization. The magnitude of the polarization field at the charge origin  $\mathbf{r} = 0$  determines the force acting on the grain due to flowing ions:  $\mathbf{F}_{id} = -eZ \nabla \phi|_{\mathbf{r}=0}$  [195,213]. Of course, the ion drag acts on the grain together with the usual electrostatic force due to the global field,  $\mathbf{F}_{el} = eZ\mathbf{E}$ . The ion drag force is obviously parallel to the flow and can be written as [210,211]

$$F_{id} = -\frac{ie^2 Z^2}{\pi} \int_0^{k_{\max}} \frac{dk}{k} \int_{-k}^k \frac{k_{\parallel} dk_{\parallel}}{\varepsilon(0, \mathbf{k})}. \quad (52)$$

The linear kinetic approach is not valid in the immediate vicinity of the charged particle, where the electrostatic perturbations are too strong. The size of this vicinity is equal by the order of magnitude to the ion Coulomb radius  $R_C \sim R_T(1 + M_T^2)^{-1}$ , which defines the upper limit of integration,  $k_{\max} \sim R^{-1}$ . The criterium of applicability of Eq. (52) is the relative smallness of the *actual* contribution to the force from the “nonlinear” region  $r \leq R$  (this is discussed below). Since  $k_{\max}$  enters the final formula logarithmically (and the argument of the logarithm is assumed to be large), one can use the obtained order-of-magnitude estimate for the calculations (e.g., [195,213]).

The plasma permittivity  $\varepsilon(\omega, \mathbf{k}) = 1 + \chi_e + \chi_i$  is determined by the electron and ion responses. For electrons the Boltzmann form is assumed,  $\chi_e \simeq (k\lambda_{De})^{-2}$ , and the ion contribution is obtained from the solution of the linearized kinetic equation coupled to the Poisson equation. In order to include the ion–neutral collisions, it was proposed [99,210,211] to write the ion collision integral,  $\text{St}f_i$ , in the model Bhatnagar–Gross–Krook (BGK) form [147,214]:  $\text{St}f_i = v_{in}(n_i\Phi - f_i)$ , where  $\Phi(v) = (2\pi v_{Tn}^2)^{-3/2} \exp(-v^2/2v_{Tn}^2)$  is the (isotropic) Maxwellian velocity distribution of neutrals normalized to unity,  $n_i = \int f_i d\mathbf{v}$  is the ion density, and  $v_{in}$  is the ion–neutral collision frequency. The *functional form* of the BGK collision integral is particularly suitable for the description of the charge-exchange collisions [210,211]. Generally, the ion–neutral collision cross section is a complicated (monotonically decreasing) function of the ion velocity which cannot be generally approximated by any simple scaling [83,215]. It is reasonable, therefore, to choose the approximation  $v_{in} = \text{const}$  which allows us to represent the model collision operator in the convenient algebraic form.

The kinetic equation with the BGK collision integral yields the following solution for the steady-state ion distribution function in the electric field  $E$  [99,210,211]:

$$f_i(v_{\parallel}, v_{\perp}) = n_{i0} \Phi_{\perp}(v_{\perp}) \int_0^{\infty} \Phi_{\parallel}(v_{\parallel} - u_i x) e^{-x} dx. \quad (53)$$

Here  $\Phi_{\parallel} = (2\pi v_{T_n}^2)^{-1/2} \exp(-v_{\parallel}^2/2v_{T_n}^2)$  and  $\Phi_{\perp} = (2\pi v_{T_n}^2)^{-1} \exp(-v_{\perp}^2/2v_{T_n}^2)$ , are the longitudinal and transverse factors of the neutral velocity distribution, respectively, so that  $\Phi \equiv \Phi_{\parallel} \Phi_{\perp}$ , and  $u_i = eE/m_i v_{in}$  is the velocity of the ion drift in the mobility limit. When  $u_i \rightarrow 0$  we have  $f_i \rightarrow n_{i0} \Phi$ , where  $n_{i0}$  is the ambient (constant) ion density. For subthermal ion drift, distribution (53) is close to the shifted Maxwellian function,  $f_i \simeq n_{i0} \Phi(v)(1 + u_i v_{\parallel}/v_{T_n}^2)$ . However, for  $u_i \geq v_{T_n}$  the deviation from the Maxwellian form is significant. Using Eq. (53) one can derive the self-consistent ion response in a collisional plasma with electric field [99,210,211],

$$\chi_i(\omega, \mathbf{k}) = \frac{(k\lambda_{Di})^{-2}}{1 + i(k_{\parallel} v_{in}/k^2 v_{T_n}) M_T} \left[ \frac{1 + \langle \mathcal{F}(\xi_2) \rangle}{1 + \frac{iv_{in}}{\omega + iv_{in}} \mathcal{F}(\xi_1)} \right], \quad (54)$$

where the variables  $\xi_{1,2}$  are

$$\xi_1 = \frac{(\omega + iv_{in})/\sqrt{2}kv_{T_n}}{\sqrt{1 + i(k_{\parallel} v_{in}/k^2 v_{T_n}) M_T}}, \quad \xi_2 = \frac{(\omega - k_{\parallel} v_{T_n} M_T x + iv_{in})/\sqrt{2}kv_{T_n}}{\sqrt{1 + i(k_{\parallel} v_{in}/k^2 v_{T_n}) M_T}},$$

$\mathcal{F}(\xi)$  is the dispersion function of the Maxwellian plasma [216], and the average is  $\langle \dots \rangle = \int_0^{\infty} \dots e^{-x} dx$ . Without the field (i.e.,  $M_T = 0$ ), Eq. (54) reduces to the well-known expression for the Maxwellian plasma (see, e.g., [147]): the variables  $\xi_{1,2}$  tend to  $\xi = (\omega + iv_{in})/\sqrt{2}kv_{T_n}$  and, correspondingly,  $\langle \mathcal{F}(\xi_2) \rangle \rightarrow \mathcal{F}(\xi)$ .

Substituting plasma permittivity with the ion response (54) in Eq. (52), one can numerically calculate the ion drag force for arbitrary collision frequency (mean free path) and Mach number (electric field), using the tabulated values of  $\mathcal{F}(\xi)$ . In the limiting cases of small and large Mach numbers the analytic expressions can be obtained. For  $M_T \ll 1$  the force is [195,210,211]

$$F_{id} \simeq \frac{1}{3} \sqrt{\frac{2}{\pi}} \left( \frac{T_i}{e} \right)^2 \left[ \ln \beta_T^{-1} + \frac{1}{\sqrt{2\pi}} \mathcal{K}(\lambda_D/\ell_i) \right] \beta_T^2 M_T + O(M_T^3), \quad (55)$$

where

$$\mathcal{K}(x) = x \arctan x + \left( \sqrt{\frac{\pi}{2}} - 1 \right) \frac{x^2}{1 + x^2} - \sqrt{\frac{\pi}{2}} \ln(1 + x^2)$$

is the “collision function”,  $\ell_i = v_{T_n}/v_{in}$  is the ion mean free path, and  $\lambda_D \simeq (\lambda_{Di}^{-2} + \lambda_{De}^{-2})^{-1/2}$  is the linearized Debye length. For  $\ell_i \geq \lambda_D$  the function  $\mathcal{K}$  is negligibly small compared to the Coulomb logarithm and Eq. (55) yields the standard collisionless expression for the ion drag force [Eq. (49) for  $\beta_T \ll 1$ ] derived from the binary collision approach [74,198]. In terms of the ion kinetics, the origin of this force is the Landau damping. In the opposite limit  $\ell_i \ll \lambda_D$  the hydrodynamic effects become more important, and the expression in the brackets in Eq. (55) changes from  $\ln \beta_T^{-1}$  to  $\ln[(\ell_i/\lambda_D)\beta_T^{-1}] + \sqrt{\pi/8}(\lambda_D/\ell_i)$ . If collisions become “very frequent”,  $\ell_i \leq \beta_T \lambda_D$ , the kinetic effects disappear completely and the force can be derived from the fluid dynamics approach, resulting to  $F_{id} \simeq \frac{1}{6}(T_i/e)^2(\lambda_D/\ell_i)\beta_T^2 M_T$ .

The conventional susceptibility is no longer applicable for ions at large Mach numbers, so that Eq. (54) should be used instead. Eq. (52) yields the force for  $M_T \gg 1$  [210,211],

$$F_{id} \simeq \sqrt{\frac{2}{\pi}} \left( \frac{T_i}{e} \right)^2 \ln \left( 4 \frac{\ell_i}{\lambda_D} \frac{M_T}{\beta_T} \right) \frac{\beta_T^2}{M_T} + O(M_T^{-2}). \quad (56)$$

Fig. 21 shows the ion drag force normalized to  $\beta_T^2(T_i/e)^2$  versus the Mach number for different values of  $\beta_T$  and  $\lambda_D/\ell_i$ . One can see that analytic asymptotes agree fairly well with the numerical results—depending on the value of  $\lambda_D/\ell_i$ , the discrepancy is  $\leq 10\%$  at  $M_T \leq 0.2 - 0.3$  [Eq. (55)] and  $M_T \geq 10 - 20$  [Eq. (56)].

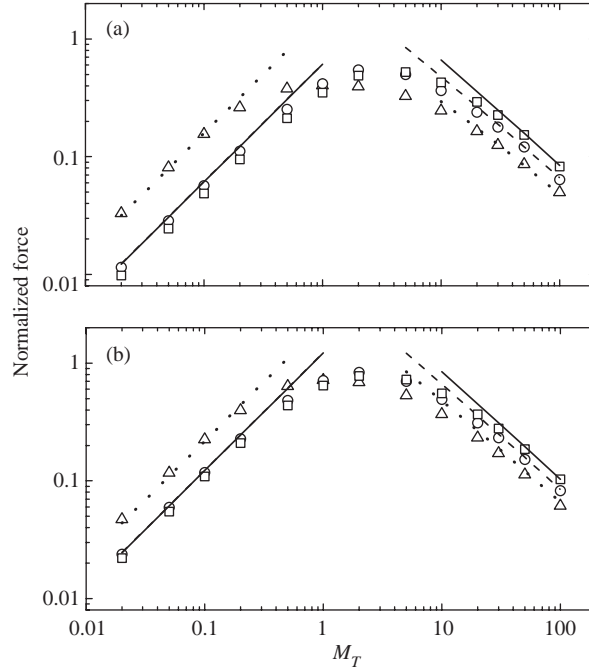


Fig. 21. Normalized ion drag force versus the thermal Mach number of the ion flow  $M_T$  [211]. The force depends on two parameters: scattering parameter  $\beta_T = R_T/\lambda_D$ , and ratio of the screening length to the thermal mean free path,  $\lambda_D/\ell_i$ . The data points are obtained by numerical integration of Eq. (52) with the ion susceptibility from Eq. (54), for  $\beta_T^{-1} = 10$  (a) and  $\beta_T^{-1} = 100$  (b). Symbols represent  $\lambda_D/\ell_i = 0.1$  (square),  $\lambda_D/\ell_i = 1$  (circle), and  $\lambda_D/\ell_i = 10$  (triangle). Analytic asymptotes at small and large Mach numbers [Eqs. (55) and (56), respectively] correspond to the same values of  $\lambda_D/\ell_i$  (solid, dashed, and dotted lines, respectively).

At large  $M_T$  the kinetic approach yields the force which scales as  $F_{id} \propto M_T^{-1}$ , in contrast to the scaling  $\propto M_T^{-2}$  in the binary collision approach [see Eq. (51)]. This is because the ion distribution (53) deviates significantly from the Maxwellian form in the superthermal regime. The scaling  $F_{id} \propto M_T^{-1}$  is not affected by a particular dependence of  $v_{in}$  on the ion velocity and, hence, it is a generic feature of the self-consistent approach at large Mach numbers. Another feature which follows from the kinetic consideration is the dependence of the force on the ion mean free path. Fig. 21 shows that frequent ion–neutral collisions ( $\ell_i \ll \lambda_D$ ) enhance the force at small  $M_T$ . This is due to the ion focusing [195]: each collision “eliminates” the angular momentum the ion had (with respect to the particle) before the collision. Therefore, the motion of the flowing ions becomes more “radial” due to the attraction towards the charged particle—the “focusing centre” downstream moves closer to the particle. This additional focusing implies the local increase of the ion density and, hence, increase of the polarization (force). This mechanism, however, can operate only if the field of the charged particle is stronger than the global field  $E$ . Otherwise, if  $E$  is relatively strong (Mach number is large), it should de-focus the ion trajectories: after each collision, the ions should accelerate mostly along  $E$ . Increase of collisionality (decrease of  $\ell_i$ ) at constant  $M_T \propto E\ell_i$  implies increase of the global electric field and, hence, stronger de-focusing. In turn, the latter implies the decrease of the polarization (force) which we see in Fig. 21.

The linear kinetic approach is valid when the arguments of the logarithms in Eqs. (55) and (56) are large—this provides the so-called “logarithmic accuracy” of the results [210,211]. For  $M_T \ll 1$ , the applicability of Eq. (55) is  $\beta_T \ll 1$ . In this limit, the collisionless part of Eq. (55) coincides with the results of the binary collision approach [see Eq. (49)]. Larger Mach numbers imply better applicability—similar to the results of the binary collision approach [Eq. (51)], the argument of the logarithm in Eq. (56) grows with  $M_T$ . Note that at large Mach numbers the ion absorption by the grain can contribute to the force. The absorption can be neglected at  $M_T \leq [(\lambda_D/a)\beta_T]^{2/3}$ , which is  $M_T \leq 30 - 50$  for typical parameters of complex plasmas [210,211].

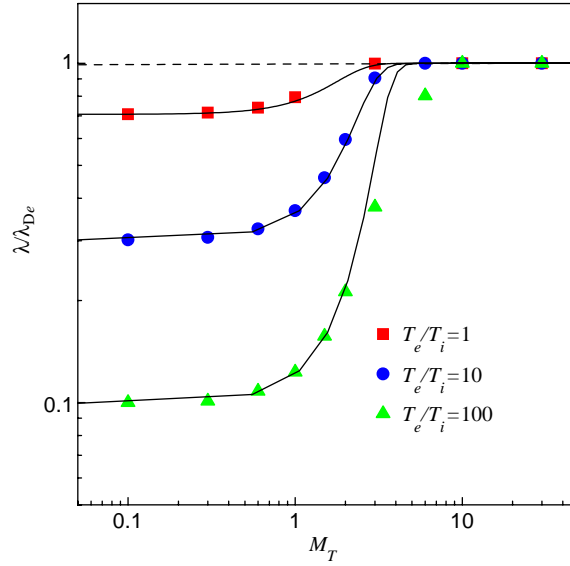


Fig. 22. The effective screening length  $\lambda$  of the charged grain in the flowing plasma versus the thermal Mach number  $M_T$  (ion flow velocity normalized to the ion thermal velocity) for different electron-to-ion temperature ratios [212]. Symbols are numerical calculations, lines are simple analytical fits.

### 7.1.3. Complementarity of the two approaches

Comparing the results of the linear kinetic approach and the binary collision approach, the most important conclusion to be drawn is that these approaches are not really competitive but rather *complementary*: binary collision approach is more suitable to describe highly nonlinear collisionless cases when both the ion Coulomb radius  $R_C$  and the mean free path exceed the screening length [57,74]. This situation is typical for subthermal ion flows, when  $R_C$  is relatively large. Small Mach numbers also imply weak distortion of the potential around the charged particle and weak deviation of the ion distribution from the shifted Maxwellian function. Therefore, there is no need to employ the self-consistent kinetic approach in this case. On the other hand, for superthermal ions (when  $R_C$  decreases rapidly with the Mach number and, hence, the linear theory can be better applied!) both the particle potential and ion distribution function are highly anisotropic, and then the self-consistent kinetic approach is necessary. Also, in contrast to the binary collision approach, the kinetic approach allows us to take into account the ion–neutral collisions.

The kinetic approach also allows us to deduce how the *effective* screening length of the particle potential,  $\lambda$ , depends on the ion flow velocity [212]. This is an important issue which was discussed recently [217,218]. At  $M_T \lesssim 1$  the potential distribution around the grain is weakly affected by the flow, so that the screening is determined by the linearized screening length,  $\lambda \simeq (\lambda_{Di}^{-2} + \lambda_{De}^{-2})^{-1/2}$ . At superthermal flows the ion contribution to the screening rapidly vanishes and the effective screening length tends to asymptote  $\lambda \simeq \lambda_{De}$ . Fig. 22 shows that this transition occurs in a fairly narrow range of velocities around  $M_T \simeq 1 - 3$ . The exact analytical form of  $\lambda(M_T)$  is rather complicated, but it can be approximated reasonably well with formula  $\lambda^{-2} \simeq f(M_T)\lambda_{Di}^{-2} + \lambda_{De}^{-2}$ , where the fitting function is  $f = \exp(-M_T^2/2)$  (shown in Fig. 22) or  $f = (1 + M_T^2)^{-1}$  [212].

One should emphasize, however, that often the experimental conditions are such that the linear treatment is not possible (e.g., bulk plasmas, when the linear approach can be applied only for submicron particles), but at the same time the collisions are important (pressures  $\sim 30$  Pa or higher) [195,210,211]. So far, there have been no approach proposed to treat this case analytically, and this issue remains the major challenge for the theory of the ion drag.

### 7.2. Other forces

Similar to the ion drag force, the *electron drag force* arises due to the momentum transfer from the electrons drifting relative to the charged particles. In the binary collision approximation the electron drag force is  $F_{ed} = m_d v_{de} u_e$ , where  $v_{de}$  is given by Eq. (42). Compared to the ion drag force, the effect of the electron drag is usually ignored because



the electron-to-ion mass ratio is small. This is true when  $u_e \sim u_i$ , e.g., in rf discharges, where electrons and ions drift together due to the ambipolar diffusion. However, in the case of *independent* (mobility limited) drift (e.g., in the positive column of a dc discharge) the ratio of the ion-to-electron drag forces is *independent* of masses and can be approximately estimated as  $F_{id}/F_{ed} \sim (T_e/T_i)^2 (\sigma_{en}/\sigma_{in})$ , where  $\sigma_{e(i)n}$  is the transport cross section for electron (ion) collisions with neutrals [185]. A detailed investigation shows that the electron drag force can indeed dominate over the electric and ion drag force in most of noble gases with relatively small electron temperatures ( $T_e \lesssim 1$  eV) [185].

In ground-based conditions the *gravitational force*  $F_g = m_d g$  usually plays an important role. In order to levitate the particle, it should be counterbalanced by other forces. The *electric force* due to electric field in the (pre)sheath or striation regions of discharges can provide the balance. The magnitude of the electric force is  $F_{el} = ZeE$ , where  $E$  is the electric field strength. A correction to  $F_{el}$  due to plasma polarization in the vicinity of the dust particle (of the order of  $a/\lambda_D$ , induced by the external electric field) was derived by Daugherty et al. [219]. This effect increases the absolute magnitude of the electric force. The external field induces also a dipole moment on a particle,  $\sim a^3 E$ , which is pointed along the field. For a dielectric particle, an additional dipole moment can be induced due to anisotropy in charging [98]. In the nonuniform electric field such a dipole will experience an additional force  $\sim \frac{1}{2} a^3 (E^2)'$ . It is worth mentioning that the particle charge in the electric field is implicitly dependent on the field magnitude through e.g., induced plasma and/or charging anisotropy, ion (electron) drift velocities, etc. The problem of trapped ions is also important issue related to the electric force acting on a particle in plasmas: ions on trapped orbits can shield the particle from external electric field, leading to a decrease of the electric force.

If a temperature gradient is present in a neutral gas, then the particle experiences a *thermophoretic force*. The force is due to asymmetry in the momentum transfer from neutrals and is directed towards lower gas temperatures. In the case of full accommodation of neutrals colliding with the particle surface [213] the thermophoretic force can be expressed as [220]

$$\mathbf{F}_{th} = -\frac{4\sqrt{2\pi}}{15} \frac{a^2}{v_{T_n}} \kappa_n \nabla T_n, \quad (57)$$

where  $\kappa_n$  is the thermal conductivity coefficient of gas. For atomic gases  $\kappa_n \simeq 1.33(v_{T_n}/\sigma_{nn})$ , where  $\sigma_{nn}$  is the cross section of neutral–neutral collisions [83]. In this case  $\mathbf{F}_{th} \simeq -1.8(a^2/\sigma_{nn})\nabla T_n$ , i.e., the thermophoretic force depends on the particle radius, gas type (through  $\sigma_{nn}$ ), and temperature gradient, but does not depend on the gas pressure and temperature. For particles of about  $1 \mu\text{m}$  radius and mass density  $\sim 1 \text{ g cm}^{-3}$  in an argon plasma, the force is comparable to the force of gravity at temperature gradients  $|\nabla T_n| \sim 10 \text{ K cm}^{-1}$ . The corrections to Eq. (57) for the case when the dust particle is situated near the electrode or the walls of a discharge chamber, which basically change the numerical factor in Eq. (57), were derived by Havnes et al. [221]. Experimental investigation of the effect of thermophoretic force on the behaviour of dust particles in gas discharge plasmas was performed in Refs. [222–224]. In these works, it was shown that the thermophoretic force can be used for particle levitation in ground-based conditions as well as for controlled action on the ordered structures of particles.

And finally, the *neutral drag force* is the main mechanism responsible for friction when a particle is moving through a stationary plasma. This is because the ionization fraction is usually quite low, on the order of  $10^{-7}$ – $10^{-6}$ . Neutral drag can be also important when gas is flowing relative to the particles. When the Knudsen number  $Kn = \ell_n/a$  is large and the relative velocity between the particle and the gas  $u_d$  is small compared to the thermal velocity of neutrals  $v_{T_n}$  then

$$F_{nd} = -m_d v_{dn} u_d, \quad (58)$$

where  $v_{dn}$  is the momentum exchange rate given by Eq. (48). The minus sign means that the force acts in the direction opposite to the relative velocity. For high relative velocities ( $u_d \gg v_{T_n}$ ), the neutral drag force is proportional to the velocity squared (see, for example, [225]),  $F_{nd} \simeq -\pi a^2 n_n m_n u_d^2$ . In the opposite limit of small Knudsen numbers  $Kn \ll 1$  the Stokes expression (see e.g., [226]) applies,  $F_{nd} = -6\pi\eta a u_d$ , where  $\eta$  is the viscosity of neutral gas. In most cases Eq. (58) is applicable to calculate the neutral drag force in complex plasmas. It should be noted that this expression was originally derived for uncharged particles in a neutral gas, i.e., neglecting the polarization interaction, which is associated with a nonuniform electric field in the vicinity of the dust particle. Nevertheless, this is still a good approximation because the radius of the polarization interaction is usually much smaller than the particle size.



## 8. Dynamics of single particles and particle ensembles

### 8.1. Single particle dynamics

In most of the ground-based experiments, negatively charged dust particles can only levitate in the regions of sufficiently strong electric fields, where the electric force and other forces exerted in a plasma (e.g., ion drag) compensate for gravity (unless the particles are too heavy). This occurs, for example, in the pre-sheath and sheath regions of an rf discharge, where the electric field averaged over the oscillation period is directed along gravity force (due to the large mass, neither the dust particles nor the ions respond to the rf field at frequency 13.56 MHz). This is also true for striations in a dc discharge. The electric field  $E$  in these regions rapidly increases downwards. The particle charge  $Z$  varies with height, both due to the ion acceleration in the electric field (see Fig. 12) and an increase of the ratio  $n_i/n_e > 1$  with  $E$ . Usually, the (negative) charge first somewhat decreases and attains a minimum, then it starts increasing and eventually can even reach positive values. Examples of numerical calculations of the dependence of the particle surface potential on the distance from the electrode in collisionless and collisional sheaths of rf and dc discharges can be found in Ref. [94] for a set of plasma parameters. If the vertical coordinate (height)  $h = 0$  is assigned to the equilibrium particle position, then for small displacements around the equilibrium the net force can be expanded into series,

$$F(h)/m_d = -\Omega_v^2 h + \alpha_1 h^2 + \alpha_2 h^3 + \dots \quad (59)$$

where  $\Omega_v$  is the resonance frequency of vertical oscillations and coefficients  $\alpha_i$  characterize nonlinearity. The major contribution to Eq. (59) is often due to the electrostatic force  $F_{el} = eZE$ , and then the resonance frequency is determined by  $m_d \Omega_v^2 = -d(eZE)/dh|_{h=0}$ . It is well known [93,227] that at sufficiently high pressures (e.g., above  $\simeq 20$  Pa for argon) the electric field in the sheath varies almost linearly. At lower pressures, however, the deviations from the linear profile can be significant. Therefore, depending on the discharge parameters and the particle mass, the nonlinearity in Eq. (59) is determined either by the sheath field profile or by the charge variations with the height [227,228].

Due to the relatively large mass of the dust particles, the magnitude of the resonance frequency  $\Omega_v$  is low enough—it is typically in the range 1–100 Hz. Hence, it is convenient to use low-frequency excitations for determining the parameters of the force (59) which can be then expressed through the plasma and particle parameters. As the simplest example we refer to a harmonic excitation of particle oscillations. The oscillation amplitude  $A(\omega)$  grows when  $\omega$  approaches  $\Omega_v$ .

The amplitude reaches the maximum at  $\omega = \sqrt{\Omega_v^2 - \frac{1}{2}v_{dn}^2}$ , the width of the resonance peak is  $\sim v_{dn}$ . Hence, changing  $\omega$  and measuring  $A(\omega)$ , one can determine  $\Omega_v$  and  $v_{dn}$ . As the excitation amplitude increases, the oscillations reveal all features peculiar to an unharmonic oscillator: hysteresis of the frequency response curve, shift of the resonance frequency, and secondary resonances [227,228]. Fig. 23 shows evolution of the frequency response curve,  $A(\omega)$ , with the amplitude of the sinusoidal excitation voltage applied to the wire below the particle. Knowledge of the resonance frequency as well as the nonlinear coefficients, recovered from the fitting of the measured curves with the analytical formulas, allows us to obtain the electric field and/or dust particle charge distributions in a relatively broad region across the sheath. The measurements can also be compared with the results of the numerical models, which take into account the dependencies of particle charge, electric field, and external force amplitude on the vertical coordinate, as well as the location of an excitation source with respect to the dust particle and force balance in the sheath [229].

### 8.2. Role of charge fluctuations in the particle dynamics

Vertical oscillations of particles in the sheath regions of gas discharges can be caused not only by the application of an external force, but also can be self-excited due to effects specific to dusty plasmas. For example, a drastic increase in the amplitude of vertical oscillations was examined experimentally under certain conditions (e.g., with lowering pressure) in the sheath of rf and dc discharges [230–232]. In some cases, energy of these oscillations exceeds the room temperature (which particles would have if only the collisions with neutrals are present) by orders of magnitude. Different theoretical aspects of the enhanced vertical oscillations were considered in Refs. [132,133,137].

The possible energy source for the enhanced vertical oscillations is associated with random variations of the particle charge [132,133,137]. To describe this effect, one should include the random deviation of the particle charge,  $Z_1(t)$ ,

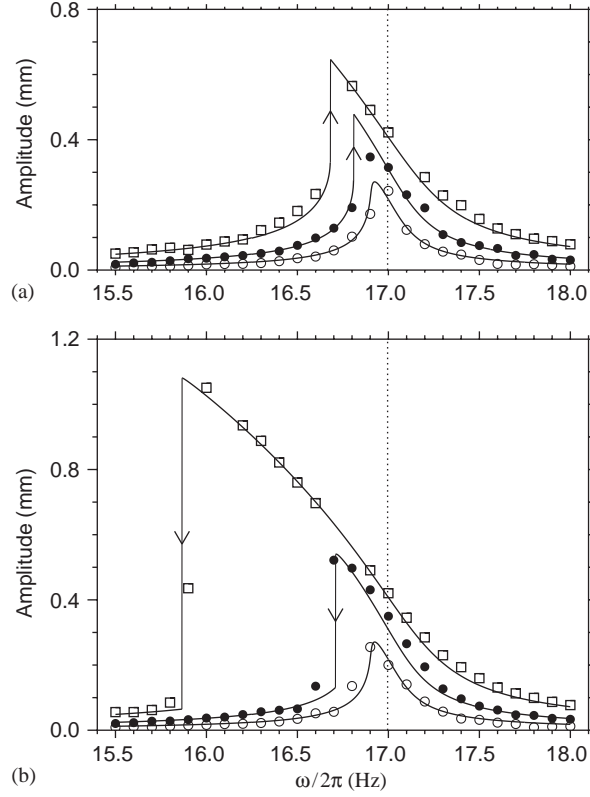


Fig. 23. Variation of the amplitude of particle oscillations close to the primary resonance for increasing (a) and decreasing (b) frequency of excitation,  $\omega$ , and for different amplitude of the sinusoidal excitation voltage: 50 mV (open circles), 100 mV (closed circles), and 200 mV (squares). Solid lines show the least-squares fit of the points to theory. The vertical dotted line indicates the position of the resonance frequency,  $\Omega_v$ , obtained from the fit.

from its average value,  $Z$ , to the equation of particle oscillations in the sheath,

$$\ddot{h} + v_{dn}\dot{h} + \Omega_v^2[1 + Z_1(t)/Z]h = gZ_1(t)/Z. \quad (60)$$

Now the oscillation amplitude is a random function of time. Using the stochastic properties of the charge fluctuations (see Section 3.5), it can be easily shown that for typical conditions  $v_{dn} \ll \Omega_v \ll \Omega_{ch}$  the mean energy of vertical oscillations associated with the random force at the right-hand side of Eq. (60) saturates at [132–134]

$$\langle \mathcal{E}_v \rangle \simeq \frac{\sigma_Z^4 |Z| m_d g^2}{2v_{dn} \Omega_{ch}},$$

as it follows from the fluctuation–dissipation theorem. In accordance with Eq. (29), the relative charge dispersion (due to charge discreteness) is  $\sigma_Z^2 \sim |Z|^{-1}$ . The neutral damping rate scales with gas pressure as  $v_{dn} \propto p$ , so that the mean energy decreases as  $\langle \mathcal{E}_v \rangle \propto p^{-1}$ . Note also that, since  $\Omega_{ch} \propto a$ ,  $v_{dn} \propto a^{-1}$ , and  $|Z| \propto a$ , we have  $\langle \mathcal{E}_v \rangle \propto a^2 \propto m_d^{2/3}$ , i.e., the mean energy of oscillations increases with the particle mass. For typical experimental conditions the energy can be of the order of a few eV or even higher. In addition to this “heating”, the charge variations can trigger the parametric instability of the oscillations [137], due to the random variations of the oscillation frequency in Eq. (60). Then the mean energy grows with time exponentially, provided the friction is low enough,

$$v_{dn} \lesssim \sigma_Z^2 \Omega_v^2 / \Omega_{ch}. \quad (61)$$

Note, however, that if the charge variations are due to the discreteness of plasma charges then the magnitude of the dispersion is fairly small and the instability is only possible at pressures far below  $\sim 1$  Pa.

Another effect associated with the variability of the particle charge results from the finite charging time. The qualitative theory of this effect was proposed in Ref. [230] to describe the following experimental evidence, and the quantitative theory was derived in Ref. [137]: due to the finite charging time, the charge of the oscillating particle experiences some delay with respect to its equilibrium local value which is a function of height  $h$ . The particle motion is not potential in this case. For a particle moving downwards (along the electric field) the absolute value of the momentary charge is smaller than the equilibrium value, and the opposite is for the particle moving upwards. Thus, the work done over the oscillation period by the electric force is always positive—the particle acquires energy from the electric field. The oscillations become unstable when the energy gain is higher than the energy dissipation due to friction—the instability condition practically coincides with Eq. (61).

### 8.3. Dynamics of ensembles with spatially varying charges

As has been pointed out by Zhakhovskii et al. [233], the very fact that the particle charge depends on the spatial coordinates immediately implies that the energy of particles in external electric fields is not conserved. This is because the electrostatic force is no longer potential,  $\nabla \times \mathbf{F}_{el} = e \nabla Z \times \mathbf{E}$  and, hence, the work done over a closed path is generally not equal to zero [473]. (Obviously, the work is zero only when the path is degenerated into a line, i.e., when the motion is one-dimensional.) The sign of the work depends on the direction of motion along the path, so that when the positive energy gain over the vortex cycle is balanced by the frictional dissipation one can expect the formation of stationary flow patterns in the particle cloud. Vaulina et al. [234,235] suggested that this mechanism can be responsible for the formation of vortices in complex plasmas. The vortex structures are almost ubiquitous in complex plasma experiments (see Fig. 3) and usually are observed at the periphery of the particle clouds. Presumably, the discharge parameters and hence the grain charge are nonuniform in these regions, which makes charge gradient mechanism favorable for the explanation of the vortices.

One should note that, in addition to the electrostatic force, also the ion drag force can be a reason for the vortex formation in complex plasmas. Indeed, by rewriting the ion drag in the following functional form:  $\mathbf{F}_{id} = \alpha(E^2)\mathbf{E}$  (assuming that the ion drift velocity is parallel to the electric field  $\mathbf{E}$ , see Section 7.1) we immediately conclude that  $\nabla \times \mathbf{F}_{id} = \nabla \alpha \times \mathbf{E} \neq 0$ .

### 8.4. Complex plasmas as non-Hamiltonian systems

Thus, one of the remarkable features distinguishing complex (dusty) plasmas from usual plasmas is that charges on the grains are not constant, but fluctuate in time around some equilibrium value which, in turn, is some function of spatial coordinates. Complex plasmas are a novel type of non-Hamiltonian systems where the energy of the particle ensemble is not conserved due to the charge variations. This is the generic feature of such systems—the energy varies not only in the presence of external electric fields, but also *due to mutual particle collisions*.

Non-Hamiltonian systems cannot be described in terms of thermodynamic potentials. An appropriate way to investigate their evolution is to employ the kinetic approach. The most general and simple way to understand generic features of the ensembles with variable charges is to study the case when no external forces are present and the energy of particles changes solely due to mutual collisions. Recently, the two cases were studied [236,237,474]: *inhomogeneous charge*— $Z$  depends on the particle coordinate but does not change in time, and *fluctuating charge*— $Z$  randomly varies in time around the equilibrium value which is constant in space. For both cases the Fokker–Planck approach was employed to derive the collision integral which describes the momentum and energy transfer in mutual particle collisions as well as in the collisions with neutrals. It was shown that the mean particle energy exhibits the explosion-like growth when the neutral friction is below a certain threshold. The analysis of the threshold conditions suggests that while the instability caused by the *fluctuating charges* cannot cause the heating of complex plasmas under typical experimental conditions [237], the instability due to *inhomogeneous charges* can certainly be a reason for such heating [236]. The obtained solutions can also be of significant importance for space plasma environments. For instance, such mechanisms might operate in protoplanetary disks and affect dust dynamics and the kinetics of the planet formation.

One more example of non-Hamiltonian dynamics is associated with the presence of ion wakes: as we discussed in Section 4.2, a charged particle embedded into a flowing plasma induces the charge polarization along the flow, because the ions focus downstream the particle—they form the wake. The overall charge of the wake is opposite to the particle charge and therefore it always exerts the electrostatic force on the particle pointed along the flow—the ion drag force.

The electric field produced by the wake of a test particle acts also on the neighbouring particles. The remarkable feature of the wakes is that the interaction of the *neighbouring* particle with the wake of the *test* particle *does not* affect the test particle, as was clearly shown in experiment [174]. Therefore, the interaction between two particles is *nonreciprocal* and, hence, is non-Hamiltonian. The energy of such ensembles is not conserved, which can be a reason for various instabilities [238,239] (see also Section 9.4.4). Also, the particle–wake interaction can change the equilibrium particle configurations—it is the reason for the formation of vertical particle strings [238] (see also Section 10.3) or the particle pairing [240–242].

## 9. Waves and instabilities in complex plasmas

The charged dust grains embedded into plasmas not only change the electron–ion composition and thus affect conventional wave modes (e.g., ion–acoustic waves), but also introduce new low-frequency modes associated with the microparticle motion, alter dissipation rates, give rise to instabilities, etc. Moreover, the particle charges vary in time and space (see Section 8), which results in important qualitative differences between complex plasmas and usual multicomponent plasmas. Depending on the magnitude of the interparticle coupling, complex plasmas can be in a weakly coupled (gaseous-like) or strongly coupled (liquid-like) states, and form crystalline structures (see Section 10). This gives us a unique opportunity to investigate wave phenomena occurring in different phase states—in particular, nonlinear waves—at the kinetic level.

Complex plasmas observed in laboratory or space experiments usually form strongly coupled liquid or crystalline states. Uncorrelated gaseous-like phase can be seen when there is a strong energy influx into the sub-system of grains, which causes substantial increase of the grain temperature and, hence, decrease of the coupling. This heating can be due to the spatial and/or temporal charge variations (as discussed in Section 8), or induced by dust wave instabilities triggered in complex plasmas (as discussed below in Sections 9.2.2 and 9.4.4). At the same time, for ideal plasmas the theoretical analysis of the wave modes and major instabilities can be performed in the most simple form. Therefore we first consider major wave properties of gaseous complex plasmas, and then discuss features peculiar to the waves in strongly coupled plasmas.

The comprehensive kinetic approach to study waves in complex plasmas is accompanied by serious difficulties: one has to deal with the dust–dust and dust–ion collision integrals which, in contrast to usual plasmas, cannot be considered in the linear approximations for realistic experimental conditions. Also, the grain charge should be treated as a new independent variable in the kinetic equation, which makes the calculations much more complicated. There have been a series of publications where the substantial progress in the self-consistent kinetic theory of complex plasmas has been achieved [243–247]. One should admit, however, that this problem is still far from being solved. On the other hand, in many cases the (relatively) simple hydrodynamic approach based on the analysis of the fluid equations allows us to catch essential physics of the processes and, hence, to understand major dynamical properties of complex plasmas. Therefore, the analysis of major wave modes and instabilities can be done with the fluid model. Of course, in some cases the applicability of the results of the hydrodynamic approach have certain limitations, especially where the damping and/or the growth rates of the modes are concerned, and then the kinetic approach has to be employed.

In this section we first briefly describe different experimental techniques used to excite the waves, and then discuss in detail the wave properties of complex plasmas in gaseous, liquid, and crystalline states.

### 9.1. Wave excitation technique

The methods used for the wave excitation in complex plasmas conditionally divide the experiments into two categories: passive and active. The former employ “natural” perturbations which are triggered spontaneously (e.g., wave instabilities [231,248–253], see Sections 9.2.2, 9.4.4, and 9.5.2, or Mach cones [254,255], see Section 9.5.3), whereas the latter use methods of controlled action produced with the specially designed devices. Generally, the active experiments provide much better flexibility, but in some particular cases the passive experiments yield remarkably good results (e.g., natural spectrum of waves in plasma crystals [256–258], see Section 9.4.2).

The methods of the active (controlled) wave excitation in complex plasmas are very diverse. First of all, this can be the electrical action produced in plasmas with biased Langmuir probes [107,259–261], wires [102,199,262–266], or electrodes [76,77,267–270], which allows the excitation of both ion and dust waves. The electrical methods are

very effective in creating waves of large amplitude and arbitrary geometry (see Section 9.5). On the other hand, the major drawback of these methods is that the electrical perturbations cannot be localized in small regions, and that this action can strongly affect global plasma parameters [199]. To produce the local action on dust particles which does not affect the discharge plasma, the laser radiation is the most widely used method [108–111,271–276]. This method is employed for manipulation by single particles and small particle sets, and allows us to excite the Coulomb cluster rotation (see Section 12.1), vertical oscillations of individual particles (see Section 8.1) and low-frequency waves in plasma crystals (see Section 9.4), and to generate Mach cones (see Section 9.5.3). This technique, however, requires very high laser power when waves of large amplitude are needed (e.g., Mach cones, solitons, etc. [271,274,276]), or when the perturbation should be simultaneously produced over an extended area (e.g., to excite planar waves in three-dimensional plasmas). The alternative method which provides local action on microparticles and, at the same time, the sufficient strength of the perturbations is the use of the electron beams [277,278]. Recently, this method was successfully employed to cause local excitation, melting, and disruption of plasma crystals, by changing the magnitude of the beam current. This technique, however, requires further development to be widely used in complex plasma experiments.

Other methods of action on the microparticles in complex plasmas employ external magnetic fields [200–202] (see Section 13) and perturbations of a neutral gas pressure (density) [279,280] (see Section 9.5.2).

## 9.2. Waves in ideal (gaseous) complex plasmas

Considering the dust species as an ideal gas, one can write the continuity and momentum equations for the dust density  $n_d$  and velocity  $\mathbf{v}_d$  in the following form:

$$\frac{\partial n_d}{\partial t} + \nabla(n_d \mathbf{v}_d) = 0, \quad (62)$$

$$\frac{\partial \mathbf{v}_d}{\partial t} + (\mathbf{v}_d \cdot \nabla) \mathbf{v}_d = -\frac{eZ}{m_d} \nabla \phi - \frac{\nabla(n_d T_d)}{m_d n_d} - \sum_{\beta} v_{d\beta} (\mathbf{v}_d - \mathbf{v}_{\beta}). \quad (63)$$

The last term in Eq. (63) describes the momentum transfer force (“drag”) on the dust particles caused by the collisions with the “light” species—electrons, ions, and neutrals ( $\beta = e, i, n$ ). The corresponding momentum exchange rates derived in the binary collision approximation,  $v_{d\beta}$ , are given in Section 6.2. As long as the flow velocities of the light species are much smaller than the thermal velocities,  $v_{d\beta}$  does not depend on  $v_{\beta}$ . An important difference between the drag force due to collisions with neutrals (“neutral drag”) and the force caused by the collisions with the charged species (“ion drag” and “electron drag”) is that the latter includes both the direct collisions with the grain surface (“collection” part) and elastic scattering by the grain electrostatic potential (“orbital” part), i.e.,  $v_{d\beta} = v_{d\beta}^{\text{coll}} + v_{d\beta}^{\text{orb}}$ . The dust viscosity usually does not play noticeable role in the gaseous phase and therefore is not included in Eq. (63).

The fluid equations for electrons and ions are ( $\alpha = e, i$ )

$$\frac{\partial n_{\alpha}}{\partial t} + \nabla(n_{\alpha} \mathbf{v}_{\alpha}) = Q_{I\alpha} - Q_{L\alpha} - I_{\alpha} n_d, \quad (64)$$

$$\frac{\partial \mathbf{v}_{\alpha}}{\partial t} + (\mathbf{v}_{\alpha} \cdot \nabla) \mathbf{v}_{\alpha} = -\frac{e_{\alpha}}{m_{\alpha}} \nabla \phi - \frac{\nabla(n_{\alpha} T_{\alpha})}{m_{\alpha} n_{\alpha}} - \sum_{\beta} v_{\alpha\beta}^{\text{orb}} (\mathbf{v}_{\alpha} - \mathbf{v}_{\beta}) - \left( \frac{Q_{L\alpha}}{n_{\alpha}} + v_{\alpha d}^{\text{coll}} \right) \mathbf{v}_{\alpha}. \quad (65)$$

The continuity equations include source terms,  $Q_{I\alpha}$ , and two types of sink—“discharge” loss  $Q_{L\alpha}$  and the “dust” loss  $I_{\alpha} n_d$ . The source of electrons and ions which sustains the discharge is usually the volume ionization in electron-neutral collisions [83,215], and then  $Q_{Ie} = Q_{Ii} = \nu_I n_e$ , where  $\nu_I$  is the ionization frequency. (In some cases the secondary, thermal, and/or photoemission from the surface of the grains can also provide contributions to  $Q_{Ie}$ , see Section 3.3). The “discharge” loss term is usually due to the diffusion towards the discharge chamber walls and can be estimated as  $Q_{Le} = Q_{Li} \sim (D_{ai}/L^2) n_i$ , where  $D_{ai}$  is the ambipolar (ion) diffusion coefficient and  $L$  is the spatial scale of the “global” plasma inhomogeneity (i.e., distance between the rf electrodes or the radius of the dc discharge tube). The “dust” loss terms are due to electron and ion absorption on the grain surface (see Section 3.4) and are determined by the corresponding fluxes on a grain,  $I_{\alpha}$ , described in Section 3.

The representation of the momentum transfer force in the form  $v_{\alpha\beta}(\mathbf{v}_\alpha - \mathbf{v}_\beta)$  is valid as long as the mean free path of the species is shorter than the spatial scale of the perturbations (e.g., the inverse wave vector  $k^{-1}$ ). Note that the change of the electron or ion momentum due to absorption by the dust grains does not depend on the grain velocity, and this is also taken into account in Eq. (65). The reciprocal momentum transfer rates are related to each other as follows:

$$m_\alpha n_\alpha v_{\alpha\beta} = m_\beta n_\beta v_{\beta\alpha} . \quad (66)$$

Variability of the grain charges implies that the fluid equations for the density and momentum should be coupled to the charge transport equation which has the following form:

$$\frac{\partial Z}{\partial t} + \mathbf{v}_d \cdot \nabla Z = I_i - I_e . \quad (67)$$

The system of equations is closed by the Poisson equation,

$$\nabla^2 \phi = -4\pi e(n_i - n_e + Zn_d) . \quad (68)$$

One can also take into account the temperature variation of the species caused by the wave perturbations. There are two limiting cases: isothermal variations—when the time scale of the perturbations exceeds the time scale of temperature relaxation due to the thermal conductivity—and adiabatic variations in the opposite case. Then the partial pressure of each species,  $n_\alpha T_\alpha$ , scales as  $\propto n_\alpha^{\gamma_\alpha}$ , where  $\gamma_\alpha$  is the effective polytropic index.

### 9.2.1. Major wave modes

In *ideal* unmagnetized plasmas only longitudinal wave modes can be sustained. The dispersion relations of these modes can be written as a sum of the partial susceptibilities (plasma responses),

$$\varepsilon(\omega, \mathbf{k}) = 1 + \chi_e + \chi_i + \chi_d = 0 , \quad (69)$$

where the electron and ion responses are expressed via density and potential perturbations as  $\chi_{e,i} = \pm 4\pi e k^{-2} \delta n_{e,i} / \delta \phi$ . The dust response depends also on the charge variations, so that  $\chi_d = -4\pi k^{-2} (Z \delta n_d + n_d \delta Z) / \delta \phi$ . By linearizing Eqs. (62)–(68) one can obtain the partial responses in general case (for the results of the kinetic theory, see, e.g., [281,282]).

In order to retrieve the wave modes existing in complex plasmas, let us first consider the case of the *multicomponent plasmas*—when the variations of the grain charges are neglected. At this point we also neglect collisions and assume the equilibrium plasma ionization and loss: this approach allows us to obtain satisfactory results for the *real part* of the dispersion relations  $\omega(k)$ , unless the actual damping (growth) rate of the waves is comparable with  $\omega$ . The partial plasma responses in this case are

$$\chi_\alpha = - \frac{\omega_{p\alpha}^2}{\omega^2 - \gamma_\alpha k^2 v_{T\alpha}^2} . \quad (70)$$

(When the flow is present with the drift velocities  $\mathbf{u}_\alpha$ , one should simply substitute  $\omega \rightarrow \omega - \mathbf{k} \cdot \mathbf{u}_\alpha$ .) For the plasma waves (plasmons with  $\omega \gg k v_{Te}$ ) the microparticles remain at rest and, therefore, the functional form of the dispersion relation,  $\omega^2 = \omega_{pe}^2 + 3k^2 v_{Te}^2$ , is not affected by the presence of the dust grains (in the hydrodynamic approach one can treat plasma waves as one-dimensional oscillations with  $\gamma_e = 3$ ). However, the electron plasma frequency,  $\omega_{pe}$ , is changed because the charged grains affect the quasineutrality condition for unperturbed densities,  $n_i = n_e + Zn_d$ , and hence the electron density. A similar effect is also observed for the ion–acoustic (IA) waves, where the electrons provide equilibrium neutralizing background and dust remains at rest,  $k v_{Ti} \ll \omega \ll k v_{Te}$ . For electrons we have  $\chi_e = (k \lambda_{De})^{-2}$  and then Eqs. (69) and (70) yield

$$\frac{\omega^2}{k^2} = \gamma_i v_{Ti}^2 + \frac{\omega_{pi}^2 \lambda_{De}^2}{1 + \lambda_{De}^2 k^2} . \quad (71)$$

The first term represents ordinary ion thermal sound mode which can exist when the ion mean free path is much smaller than the wavelength  $k^{-1}$ . Usually this term is relatively small and can be neglected compared to the second term, which



actually represents the IA mode. This IA term depends on the ion-to-electron density ratio, which can be conveniently characterized by the “Havnes parameter” [283],

$$P = \frac{Zn_d}{n_e} \equiv \frac{n_i}{n_e} - 1, \quad (72)$$

Generally, when  $P \ll 1$  the effect of dust on the conventional (plasma and ion–acoustic) modes can be neglected. Otherwise, for  $P \gtrsim 1$  the role of dust can be significant and then, in order to highlight this effect, the IA waves are referred to as the *dust ion–acoustic* (DIA) mode. In the long-wavelength limit  $k\lambda_{De} \ll 1$  the phase velocity of the DIA mode can be conveniently written as

$$C_{DIA} = \omega_{pi} \lambda_{De} \equiv \sqrt{(1 + P)\tau} v_{Ti}, \quad (73)$$

where  $\tau = T_e/T_i$  is the electron-to-ion temperature ratio, which is much larger than unity for typical rf and dc discharges, so that  $C_{DIA}$  exceeds significantly the ion thermal velocity (note that  $C_{DIA}$  does not depend on  $T_i$ ). The role of the dust species on the IA waves was first considered by Shukla and Silin [284]. The DIA waves were studied in a series of experiments (see, e.g., Refs. [268,285,286]) where the increase of the phase velocity with the grain density was clearly demonstrated.

Charged dust particles give rise to another acoustic mode associated with the motion of charged grains, whereas both the electrons and ions provide equilibrium neutralizing background. For  $kv_{Td} \ll \omega \ll kv_{Ti}$  we have  $\chi_{e,i} = (k\lambda_{De,i})^{-2}$ , and then Eqs. (69) and (70) yield

$$\frac{\omega^2}{k^2} = \gamma_d v_{Td}^2 + \frac{\omega_{pd}^2 \lambda_D^2}{1 + \lambda_D^2 k^2}, \quad (74)$$

where  $\lambda_D^{-2} = \lambda_{De}^{-2} + \lambda_{Di}^{-2}$  is the linearized Debye length. In analogy with the DIA waves [Eq. (71)], the first term represents the dust thermal mode and the second one corresponds to the *dust–acoustic* (DA) mode. The phase velocity of the DA mode does not depend on the dust temperature and in the long-wavelength limit  $k\lambda_D \ll 1$  can be written as

$$C_{DA} = \omega_{pd} \lambda_D \equiv \sqrt{|Z| \frac{T_i}{T_d}} \sqrt{\frac{P\tau}{1 + (1 + P)\tau}} v_{Td}. \quad (75)$$

There is a clear similarity between the ion and dust acoustic modes: Eqs. (73) and (75) show that the phase velocity of both modes is determined by the temperature ratio of the light-to-heavy species— $T_e/T_i$  for DIA waves and  $T_i/T_d$  for DA waves. Peculiarity of the DA waves is that the charge-to-mass ratio of the dust grains is typically  $10^8$ – $10^{10}$  times smaller than that of the ions and, therefore, the dust waves have relatively low frequencies,  $\sim 10$ – $100$  Hz. The dispersion relation for the DA wave was first derived by Rao et al. [287]. Since the typical values of  $|Z|$  are of the order of thousands, the phase velocity of DA waves can be much larger than  $v_{Td}$ , even if  $T_d$  exceeds  $T_i$  (of course, the Havnes parameter should not be too small).

The first reported observation of spontaneously excited dust waves was in a rf magnetron discharge at a frequency  $\simeq 12$  Hz [248]. Later on the dust waves, either self-sustained or excited externally, were seen in numerous experiments under quite different experimental conditions: for example, in Q-machine at  $\simeq 15$  Hz with the phase velocity  $\simeq 9$  cm/s [249], in dc discharges in the range  $\simeq 6$ – $30$  Hz with the phase velocity  $\simeq 12$  cm/s [267,268], and at  $\simeq 60$  Hz with the phase velocity  $\simeq 1$  cm/s [250,251], in rf discharges at  $\simeq 25$ – $60$  Hz [252,253], and at  $\simeq 8$ – $40$  Hz [76,77], etc. Fig. 24 shows the waves excited by a periodic modulation of the rf electrode potential obtained under microgravity conditions [77]. Most of such experiments, however, were done with strongly coupled plasmas. The weak coupling was probably achieved only when the excitation amplitude was fairly large (e.g., as seen in Fig. 24) or the waves were unstable (e.g., [249]), which eventually provided sufficiently high “temperature” of grains. A quantitative comparison with the linear dispersion relations is not really justified in these cases. Therefore, an accurate experiment to verify the DA dispersion relation in gaseous complex plasmas is still necessary, though the first experimental observations of the dust thermal mode was recently reported [258].

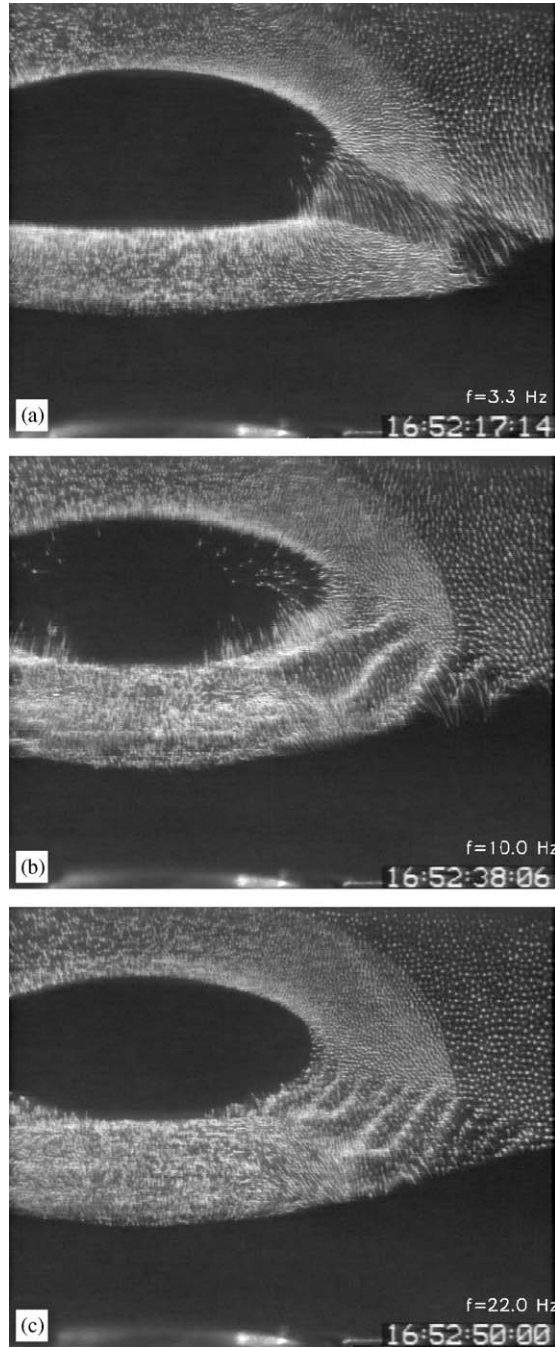


Fig. 24. Wave structures observed in PKE-Nefedov experiments [77]. The experiments were performed under microgravity conditions in argon rf-discharge plasma at pressure 12 Pa with a mixture of the melamine formaldehyde particles of 3.4 and 6.8  $\mu\text{m}$  diameter. The particles were visualized by the vertical laser sheet of about 150  $\mu\text{m}$  thickness. The waves were excited by applying a low-frequency modulation voltage to the horizontal rf electrodes. The snapshots (side view) show the response of the particles at frequencies (a) 3.3 Hz, (b) 10 Hz, and (c) 22 Hz.

Note that when the variations of the grain charges induced by waves are taken into account the DIA phase velocity remains the same, but the DA velocity is changed [251,288,289]. However, this change does not exceed the factor  $\simeq \sqrt{(2+z)/(1+z)}$  compared to Eq. (75), which is typically less than  $\simeq 15\%$ . Therefore, for practical use Eq. (75) is quite sufficient.

### 9.2.2. Damping and instabilities of the DIA and DA mode

The wave modes can only exist when the damping is weak, so that the actual imaginary part of the dispersion relation,  $|\omega_i|$ , is much smaller than the real part  $\omega_r$ —only then one can speak about the wave propagation. The waves can also be unstable, because of various mechanisms operating in complex plasmas—we discuss these mechanisms below. As long as  $|\omega_i|$  is much smaller than  $\omega_r$ , the latter is approximately determined by the real part of the permittivity (69), i.e.,  $\text{Re } \varepsilon(\omega_r, \mathbf{k}) \simeq 0$ , and the former is given by [147]

$$\omega_i \simeq - \frac{\text{Im } \varepsilon(\omega, \mathbf{k})}{\partial \text{Re } \varepsilon(\omega, \mathbf{k}) / \partial \omega} \Big|_{\omega=\omega_r}.$$

This is very convenient formula for the practical use.

First we discuss the kinetic effects—namely, the role of the Landau damping.

For each wave mode, the Landau damping can be due to wave resonance with “heavy” species (i.e., ions for DIA waves and dust for DA waves) and with “light” species (electrons for DIA waves and ions for DA waves). The damping caused by heavy species scales as  $|\omega_i/\omega_r| \propto \exp(-\frac{1}{2}C^2/v_T^2)$ , where  $C$  and  $v_T$  are the corresponding phase velocity and the thermal velocity of heavy species, respectively [213,290]. From Eqs. (73) and (75) we see that even in isothermal complex plasmas the  $C/v_T$  ratios can be quite large:  $C_{\text{DIA}}/v_{T_i}$  is large when  $P \gg 1$ , and  $C_{\text{DA}}/v_{T_d}$  is large because  $|Z| \gg 1$ . This makes substantial difference compared to usual plasmas, where  $C_{\text{IA}}/v_{T_i}$  can be large and, thus, the IA waves can propagate only when  $\tau \gg 1$  (DIA waves were studied in the double plasma device, e.g., [260], and the Q-machine, e.g. [285], where  $\tau \simeq 1$ ). Thus, the damping on heavy species is usually small in (dense) complex plasmas.

In the absence of the plasma flows the Landau damping on light species is relatively weak as well, because of the small charge-to-mass ratios: for DIA waves the (relative) damping rate is  $|\omega_i/\omega_r| \lesssim \sqrt{(1+P)m_e/m_i}$ , whereas for DA waves  $|\omega_i/\omega_r| \lesssim \sqrt{P(1+P)^{-1}|Z|m_i/m_d}$  [213,290]. Nevertheless, in experiments with the DIA waves performed at very low pressures,  $p \sim 10^{-2}$ – $10^{-3}$  Pa, the electron Landau damping can be an important mechanisms of dissipation [291]. For DA waves, however, it does not play noticeable role. The Landau damping is, of course, modified when a stream of light species exists in a plasma (see below).

Now let us dwell upon the other mechanisms responsible for the damping and instabilities of the DIA and DA waves. Below we assume that the electron-to-ion temperature ratio  $\tau$  is large, as it is usually in experiments. Such assumption allows us to simplify formulas substantially (note that even for  $\tau \simeq 1$  the resulting expressions yield fairly good quantitative agreement with the exact formulas).

**DIA mode.** Along with the Landau damping the major dissipation mechanisms are the collisions with neutrals and variations of the grain charges [289,292–295]. In addition, there is a counterplay between ionization and loss—this can cause either damping or instability, depending on the value of  $P$  [204,296,297]. All three contributions to the imaginary part  $\omega_i$  (assuming that it is much smaller than  $\omega_r$ ) can be derived from the fluid approach which yields

$$2\omega_i \simeq -v_{in} - \frac{1-P}{1+P}v_I - \frac{P^2\Omega_{ch}}{(1+P)(1+z)},$$

where  $v_{in}$  is the frequency of the ion–neutral collisions and  $\Omega_{ch}$  is the charging frequency [see Eq. (15)]. In sufficiently dense complex plasmas (when  $P \gg 1$ ) the major damping mechanism can be due to the “coherent” charge variations induced by waves (the mechanism is effective because the DIA frequency can be comparable to  $\Omega_{ch}$ ). The ion–neutral collisions as well as ionization do not usually play any significant role in the DIA wave experiments, since the gas pressure is low enough (see e.g., Refs. [260,269,285]).

As regards the DIA instabilities, the major mechanism operating in experiments is associated with the electron drift relative to ions [286,298]—the so-called “current-driven instability” which is well-known for the IA waves in usual plasmas. Essentially, this instability is the reversed electron Landau damping—the energy exchange due to the resonance electron-wave interaction changes the sign when the drift velocity  $u_e$  exceeds the phase velocity of the DIA waves  $C_{\text{DIA}}$ . The growth rate associated with this instability can be estimated as [290]

$$\frac{\omega_i}{\omega_r} \simeq \sqrt{\frac{\pi}{8} \frac{m_e}{m_i} (1+P)} \frac{(u_e/C_{\text{DIA}} - 1)}{(1+k^2\lambda_{De}^2)^{3/2}}.$$

When the damping rates discussed above (including the ion Landau damping) are low enough the current-driven instability sets on [268,298]. The charge variations can somewhat modify the growth rate [299].

**DA wave mode.** The major damping mechanism operating in experiments with complex plasmas is certainly neutral gas friction. The resulting damping,  $2\omega_i \simeq -v_{dn}$ , is determined by the corresponding momentum exchange rate [see Eq. (48)]. However, along with the damping there are a number of instability mechanisms which turn out to be quite important in experiments. Below we mention the most important types of the DA instability:

(i) Ion streaming instability: It can be triggered when ion currents are present in a plasma (e.g., due to electric fields in rf sheaths and dc striations). The mechanism of the (DA) ion streaming instability is completely identical to that of the (DIA) current-driven instability. The ion streaming instability is often observed in complex plasma experiments performed in different discharges (see, e.g., [36,249,250]), and it has been studied theoretically in numerous publications, e.g., [290,300–304].

The presence of the ion flux modifies properties of the DA mode. This can be appropriately taken into account by using the kinetic expression for the ion susceptibility. Also, the kinetic approach allows us to include properly the effect of the ion–neutral collisions: the collisions in discharges are mostly of the charge-exchange type, which makes possible to employ the model BGK form of the ion collision integral. Assuming *shifted Maxwellian* distribution, the ion response is [147]

$$\chi_i(\omega, \mathbf{k}) = \frac{1}{(k\lambda_{Di})^2} \left[ \frac{1 + \mathcal{F}(\xi)}{1 + \frac{iv_{in}}{\omega - \mathbf{k} \cdot \mathbf{u}_i + iv_{in}} \mathcal{F}(\xi)} \right], \quad \xi = \frac{\omega - \mathbf{k} \cdot \mathbf{u}_i + iv_{in}}{\sqrt{2}kv_{Ti}}, \quad (76)$$

where  $\mathcal{F}(\xi)$  is the Maxwellian dispersion function [216]. In limiting cases Eq. (76) can be substantially simplified: for  $|\xi| \ll 1$ , the power series for the dispersion function is  $\mathcal{F}(\xi) \simeq -2\xi^2 + i\sqrt{\pi}\xi$ , and for  $|\xi| \gg 1$  the asymptotic expansion is  $\mathcal{F}(\xi) \simeq -1 - \frac{1}{2}\xi^{-2} + i\sqrt{\pi}\xi e^{-\xi^2}$ . Therefore, when  $|\omega - \mathbf{k} \cdot \mathbf{u}_i + iv_{in}| \ll kv_{Ti}$  we obtain

$$\chi_i(\omega, \mathbf{k}) \simeq \frac{1}{(k\lambda_{Di})^2} \left[ 1 + i\sqrt{\frac{\pi}{2}} \frac{\omega - \mathbf{k} \cdot \mathbf{u}_i}{kv_{Ti}} \right], \quad (77)$$

where  $\mathbf{u}_i$  is the drift velocity of ions. The real part in Eq. (77) coincides with the results of the fluid approach in this limit [see Eq. (70)], the imaginary part is due to the Landau damping. In the opposite limit  $|\omega - \mathbf{k} \cdot \mathbf{u}_i + iv_{in}| \gg kv_{Ti}$  the resulting susceptibility can be written in the following form:

$$\chi_i(\omega, \mathbf{k}) \simeq -\frac{\omega_{pi}^2}{(\omega - \mathbf{k} \cdot \mathbf{u}_i)(\omega - \mathbf{k} \cdot \mathbf{u}_i + iv_{in}) - k^2v_{Ti}^2}. \quad (78)$$

This limit denotes either strongly collisional case (when the ion mean free path is shorter than  $k^{-1}$ ) or the case of “cold hydrodynamics” (when  $u_i \gg v_{Ti}$ , so that the thermal motion can be neglected). In both cases the fluid approach is applicable and, hence, Eq. (78) can be directly obtained from Eqs. (64) and (65), assuming equilibrium ionization/recombination and neglecting other collisions.

Note that Eq. (76) is derived assuming the shifted Maxwellian function for the ion velocity distribution. This assumption, however, is only justified when the ion flow is subthermal—otherwise deviations from the Maxwellian form become too strong [see Eq. (53)] which, in turn, strongly affects the expression for the ion susceptibility  $\chi_i$ . Therefore, for the superthermal flow one should use Eq. (54) [99,210,211].

The threshold for the ion streaming instability is determined from the (numerical) solution of Eq. (69), by using Eqs. (77) or (78) for the ion response and substituting  $\chi_e \simeq (k\lambda_{De})^{-2}$  and  $\chi_d \simeq -\omega_{pd}^2/\omega(\omega + iv_{dn})$ . Experiments show that by increasing the neutral gas pressure up to sufficiently high values (typically, dozens of Pa) the instability can be suppressed, apparently because the neutral gas friction increases as well. The theoretical analysis (which can be somewhat simplified for the subthermal [251] and superthermal [305] limits of the ion drift) yields the pressure threshold which is in a good agreement with the experiments.

(ii) Ionization instability: Unlike the DIA waves, ionization cannot directly cause the instability of the DA waves—because the ionization creates new ions, but not dust grains. Nevertheless, ionization can in fact trigger the DA instability, because the ions can effectively transfer their momentum to the grains via the ion drag force [203,204,306]. The whole instability mechanism operates as follows: when the dust density fluctuates in some region—say, decreases—ionization increases (because the electron density grows keeping quasineutrality), which creates additional ion outflow from the

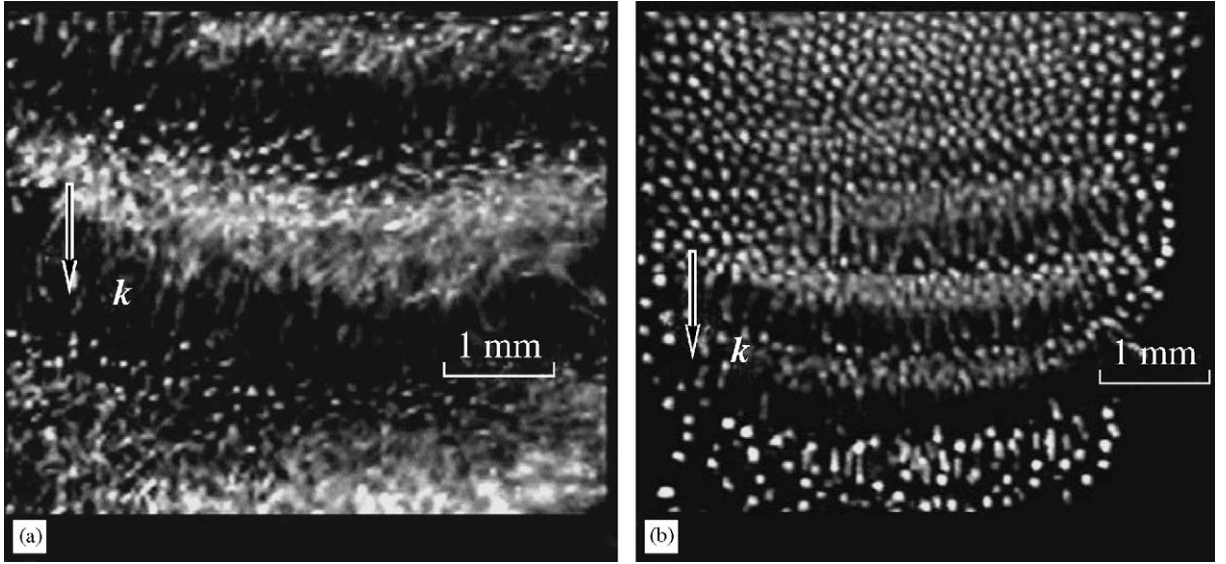


Fig. 25. Spontaneous excitation of dust waves observed in laboratory experiments [252]. The experiments were carried out in a neon rf inductive discharge with the melamine formaldehyde particles of  $1.87 \mu\text{m}$  diameter (side view on the lower part of the dust cloud is shown). The instability sets on when the particle density in the cloud exceeds a threshold, provided the gas pressure is low enough. The snapshots show dust waves triggered at pressures (a) 15 Pa and (b) 50 Pa.

region. This flux exerts an additional ion drag force pushing the grains away and, thus, the dust density decreases further. Obviously, this instability is of the aperiodic type (i.e.,  $\omega_r = 0$ ) and, thus, is independent of  $v_{dn}$ . The instability condition  $\omega_i > 0$  is satisfied when [203,204,297]

$$[P^{-1}v_{id} - (1 + P)^{-1}v_{in}]v_I \gtrsim k^2 v_{Ti}^2.$$

Here,  $v_{id}$  is the effective frequency of the ion–dust collisions, which is related to the “ion drag” rate  $v_{di}$  introduced in Section 6.2.2 via  $m_i n_i v_{id} = m_d n_d v_{di}$ . The larger the dust grains are, the higher the value of  $v_{id}$  is and, hence, the condition for the instability is more relaxed. There are grounds to believe that this instability is responsible for the onset of the void formation in complex plasmas [22,203,204,297,306].

(iii) Charge variation instability: It is due to the grain charge variations induced by the DA wave. In contrast to the DIA waves, now the charges are very close to the momentary equilibrium (because  $|\omega| \ll \Omega_{ch}$ ) and, therefore, their variations alone are unlikely to be a reason for an instability or damping. However, in the presence of an external electric field  $\mathbf{E}$  (e.g., ambipolar fields or the fields in rf sheaths and dc striations) the wave-correlated charge variations result in non-zero (average) work done by the electric force [251–253]. The sign of this work is determined by the orientation of the wave vector  $\mathbf{k}$  with the respect to the electric field. The dust susceptibility that takes into account these effects is [251]

$$\chi_d(\omega, k) \simeq -\frac{\omega_{pd}^2}{\omega(\omega + i v_{dn})} \left[ 1 + \frac{i e \mathbf{E} \cdot \mathbf{k}}{(1 + z) T_i k^2} \right].$$

This expression should be used together with Eq. (77) or (78) for the flowing ions, because the electric field causes an ion drift with a velocity which is usually determined by the ion mobility  $\mu_i$ , via  $u_i = \mu_i E$ . Numerical solution of Eq. (69) yields the instability threshold which takes into account both the ion stream and the charge variations [251]. It was shown that the charge variations can relax the conditions for the instability onset significantly, resulting into lower values of the threshold pressure. Then the instability can be triggered when the density of dust particles exceeds a critical value [251,252]. Fig. 25 shows an example of such instability observed in a rf inductively coupled discharge [252].



### 9.3. Waves in strongly coupled (liquid) complex plasmas

In the beginning of this section we already mentioned that complex plasmas are normally observed in experiments forming strongly coupled states, i.e., the coupling parameter of the grain–grain interaction  $\Gamma$  is quite large. The pair correlation function of microparticles usually exhibits short-range order indicating that plasmas are in liquid-like states, or that the particles form ordered crystalline structures. Dispersion properties of strongly coupled plasmas significantly deviate from those of ideal gaseous plasmas discussed above. There are number of different theoretical approaches to study waves in strongly coupled systems: these are, e.g., the “quasilocalized charge approximation” [307] employed for complex plasmas by Rosenberg and Kalman [308,309], the “multicomponent kinetic approach” by Murillo [310,311], and the “generalized hydrodynamic approach” applied by Kaw and Sen [312–314]. The latter is probably the most physically “transparent” approach which allows us to track evolution of the dispersion properties of complex plasmas in a broad range of  $\Gamma$ , from the ideal gaseous state up to the strongly coupled state—when the system crystallizes. There have been also numerical MD simulations of the wave modes in strongly coupled complex plasmas [315,316], which are in reasonably good agreement with the results of the above mentioned theoretical approaches.

Following the model of “very viscous liquids” originally proposed by Maxwell and generalized by Frenkel [317], in the framework of generalized hydrodynamics (GH) the ensemble of strongly coupled dust grains is treated as a continuous medium which reveals properties of viscous liquids in response to slow perturbations, but behaves as elastic body when the perturbation time scales are short enough [312,313]. The transition between these two regimes occurs at the so-called “Maxwellian relaxation time”  $\tau_M$ . The fluid equation of motion for the velocity perturbation  $\delta \mathbf{v}_d$  has the following form:

$$\frac{\partial \delta \mathbf{v}_d}{\partial t} = -\frac{eZ}{m_d} \nabla \phi - \frac{\nabla p_d}{m_d n_d} - v_{dn} \delta \mathbf{v}_d - \int_{-\infty}^t dt' \int d\mathbf{r}' \eta_d(\mathbf{r} - \mathbf{r}', t - t') \delta \mathbf{v}_d(\mathbf{r}', t'). \quad (79)$$

The integral term is the linear viscoelastic operator in a homogeneous stationary medium written in a general form. It takes into account both spatial and temporal correlations of stresses exerted in strongly-coupled systems, in addition to the local homogeneous stress—the pressure term  $\propto \nabla p_d$ . By using the simplest form of the viscoelastic operator with the exponentially decaying memory effects, we have for the Fourier transform of the dust kinematic viscosity,

$$\eta_d(\omega, \mathbf{k}) \simeq \frac{\eta k^2 + (\frac{1}{3}\eta + \zeta)\mathbf{k}(\mathbf{k})}{1 - i\omega\tau_M}.$$

Parameters of the stress operator—viscosities  $\eta$  and  $\zeta$  and relaxation time  $\tau_M$ , as well as pressure  $p_d$  are determined by the correlation part of the energy of the electrostatic interaction,  $u(\Gamma, \kappa) = U_{\text{corr}}/T_d$  (normalized by the dust temperature). In a weakly coupled regime,  $\Gamma \lesssim 1$ , the Debye–Hückel approximation yields  $u \simeq -\frac{\sqrt{3}}{2}\Gamma^{3/2}$  (here and below in this section  $\Gamma$  corresponds to the Wigner–Seitz radius). For the liquid phase in the range  $1 \lesssim \Gamma \lesssim 200$  the normalized correlation energy can be well approximated by the scaling [318]  $u = a\Gamma + b\Gamma^{1/4} + c + d\Gamma^{-1/4}$ , where coefficients  $a$ ,  $b$ ,  $c$ , and  $d$  are some functions of the lattice parameter  $\kappa$ . In the one-component plasma (OCP) limit,  $\kappa = 0$ , the Monte Carlo (MC) simulations [319] yield:  $a \simeq -0.89$ ,  $b \simeq 0.94$ ,  $c \simeq -0.80$ , and  $d \simeq 0.18$ . For  $\kappa \lesssim 1$  the dependence of the coefficients on the lattice parameter is rather weak [318], e.g.,  $a(\kappa) \simeq -0.89 - 0.10\kappa^2 + 0.0025\kappa^4 + \dots$ , which means that the OCP results are quite applicable for this range of  $\kappa$ . The relaxation time is expressed as follows [320]:  $\tau_M v_{Td}^2 = \eta_*(1 - \gamma_d \mu_d + \frac{4}{15}u)^{-1}$ , where  $\eta_* = \frac{4}{3}\eta + \zeta$  and  $\mu_d = T_d^{-1}(\partial p_d / \partial n_d)_{T_d} = 1 + \frac{1}{3}u + \frac{1}{9}\Gamma \partial u / \partial \Gamma$  is the isothermal compressibility. The first and second viscosity coefficients,  $\eta$  and  $\zeta$ , can also be deduced from the results of numerical simulations and experiments [321–324].

Using the Fourier transformation of Eq. (79) together with the continuity equation (62) one can derive the dispersion relations of different wave modes.

#### 9.3.1. Longitudinal waves

The dust susceptibility is ( $\delta \mathbf{v}_d$  parallel to  $\mathbf{k}$ )

$$\chi_d(\omega, k) = -\frac{\omega_{pd}^2}{\omega(\omega + i v_{dn}) - \gamma_d \mu_d k^2 v_{Td}^2 + \frac{i \eta_* \omega k^2}{1 - i \omega \tau_M}}. \quad (80)$$



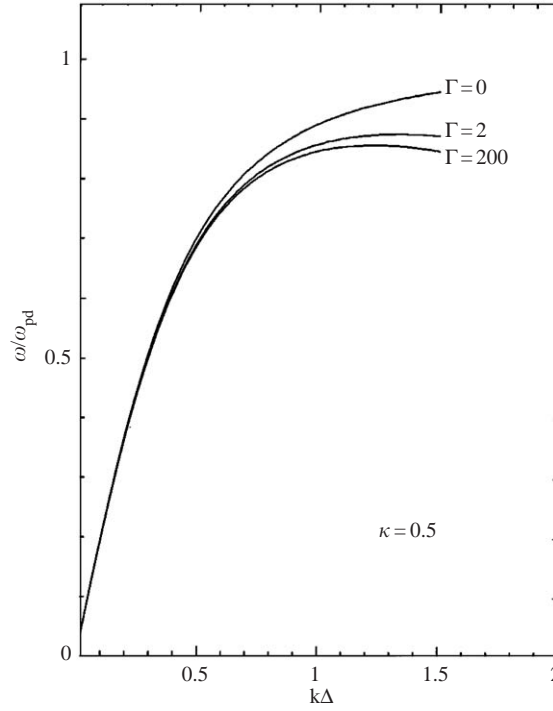


Fig. 26. Dispersion relation of dust waves in strongly coupled complex plasmas, as derived from the quasilocalized charge approximation [308]. The frequency is normalized to the dust plasma frequency  $\omega_{pd}$  and the wave vector is normalized to the particle separation  $\Delta$  (in the text  $\Delta$  is adopted). The results are shown for  $\kappa \equiv \Delta/\lambda_D = 0.5$  and different values of the coupling parameter  $\Gamma$ . The curve  $\Gamma = 0$  represents the dispersion relation for the DA waves in gaseous complex plasmas [Eq. (74) with  $T_d = 0$ ].

The dispersion relation is determined by Eq. (69) by substituting  $\chi_{e,i} \simeq (k\lambda_{De,i})^{-2}$  together with Eq. (80). Naturally, two limits can be distinguished: the “hydrodynamic regime”  $\omega\tau_M \ll 1$  and the “strongly coupled regime”  $\omega\tau_M \gg 1$  (following the terminology adopted from the OCP literature). For  $\Gamma \gg 1$  the correlation energy is mostly determined by the Madelung part,  $u \simeq -0.89\Gamma$ , and then the results are reduced to the following simple form:

$$\begin{aligned} \omega\tau_M \ll 1: \omega[\omega + i(v_{dn} + \eta_* k^2)] &\simeq \left[ \frac{1}{1 + k^2 \lambda_D^2} - 0.4 \left( \frac{v_{Td}}{C_{DA}} \right)^2 \Gamma \right] C_{DA}^2 k^2, \\ \omega\tau_M \gg 1: \omega(\omega + i v_{dn}) &\simeq \left[ \frac{1}{1 + k^2 \lambda_D^2} - 0.24 \left( \frac{v_{Td}}{C_{DA}} \right)^2 \Gamma \right] C_{DA}^2 k^2. \end{aligned} \quad (81)$$

The right-hand side of Eq. (81) is independent of  $T_d$ , and the second terms represent the “coupling correction” to the gaseous DA dispersion relation (74). At sufficiently large  $\Gamma$  these terms play a very important role—the dispersion can even change the sign, so that the group velocity becomes negative ( $\partial\omega/\partial k < 0$ ) at large  $k$ . This feature is peculiar to the longitudinal modes in plasma crystals (see Section 9.4), which indicates that there is no *qualitative* difference between the dispersion properties of (strongly coupled) liquid and crystalline complex plasmas. It is noteworthy that the other approaches yield essentially the same results for the real part of the dispersion relation (see Fig. 26). The important difference revealed in the GH approach is only for the imaginary part—in addition to the neutral friction, the viscosity contributes to the dissipation in the hydrodynamic regime. However, for typical experimental conditions the neutral gas friction prevails and the viscosity can provide the major contribution to the dissipation only if the gas pressure is low enough. Also, the neutral gas friction can hamper the role of the “coupling correction”, and when  $v_{dn}$  becomes comparable to  $\omega_{pd}$  the difference between the dispersion relations of ideal and strongly coupled complex plasmas can be washed away completely [308,312,313]. Presumably, that was the reason why in experiments where the coupling parameter was quite high the dispersion properties were nevertheless found to be very similar to those derived for ideal

plasmas (see, e.g., [262]). Note that the longitudinal waves in strongly coupled plasmas are subject to the ion streaming instability, similar to that discussed in Section 9.2.2, now with the thresholds and the growth rate functions of  $\Gamma$  (e.g., [312]).

### 9.3.2. Transverse waves

For the transverse waves ( $\delta \mathbf{v}_d$  perpendicular to  $\mathbf{k}$ ) the dispersion relation can be directly obtained from the Fourier transformed equation (79),

$$\omega[\omega + i(\tau_M^{-1} + \nu_{dn})] = \frac{\eta_* k^2 + \nu_{dn}}{\tau_M} . \quad (82)$$

This mode is also strongly affected by the neutral gas friction—the effects of strong coupling disappear when  $\nu_{dn} \gtrsim \eta_* k^2$ . If the neutral friction can be neglected then in the hydrodynamic regime  $\omega \tau_M \ll 1$  Eq. (82) reduces to the ordinary damped mode for a shear flow in viscous liquids,  $\omega \simeq -i\eta_* k^2$ . In the opposite regime we obtain a nondispersive acoustic mode,  $\omega \simeq \sqrt{\eta_*/\tau_M} k$ , which is analogous to elastic shear waves in solids. The phase velocity of the mode is determined by the coupling parameter  $\Gamma$ ,

$$\omega \tau_M \gg 1: \quad \frac{\omega}{k} \simeq 0.4 \sqrt{\Gamma} v_{Td} .$$

The shear waves triggered in liquid complex plasmas due to instability have been observed experimentally [325] (however, the mechanism responsible for the instability is not fully understood [313,325,326]).

Thus, the GH approach allows us to track evolution of the wave dispersion properties as the coupling parameter  $\Gamma$  increases, and thus to cover the transition from the ideal gaseous to the strongly coupled state. However, the phenomenological *hydrodynamic* approach can provide us only with the qualitative convergence to the wave modes in crystals and, of course, cannot retrieve features peculiar to a particular lattice type (especially when the wavelength becomes comparable to the interparticle distance). Therefore, for a quantitative study of waves in plasma crystals one should employ different approach which is discussed in the next section.

## 9.4. Waves in plasma crystals

The theoretical model of waves in crystals—the so-called “dust–lattice” (DL) waves—is based on the analysis of the equation of motion for individual particles. For a particle having the coordinate  $\mathbf{r}$  the equation of motion is

$$m_d \ddot{\mathbf{r}} + m_d \nu_{dn} \dot{\mathbf{r}} = -\nabla U_{dd} + \mathbf{F}_{\text{ext}} . \quad (83)$$

Here  $U_{dd} = e^2 Z^2 \sum_i |\mathbf{r} - \mathbf{r}_i|^{-1} \exp(-|\mathbf{r} - \mathbf{r}_i|/\lambda_D)$  is the total energy of the electrostatic dust–dust coupling (interaction potential is assumed to be of the Debye–Hückel form), the summation is over all particles with  $\mathbf{r}_i \neq \mathbf{r}$ . The force  $\mathbf{F}_{\text{ext}}$  includes all “external” forces (except for the neutral drag force which is explicitly included to the left-hand side), e.g., confinement, excitation (lasers, electric pulses, beams, etc.), thermal noise (Langevin force), etc. Such diversification of the forces is convenient because the eigenmodes of the system do not depend on  $\mathbf{F}_{\text{ext}}$ . When the particles in a crystalline state are sufficiently far from the melting line (see Fig. 33, Section 10), as a “first iteration” one can neglect the influence of the thermal motion in the dispersion properties. Then the waves can be considered as perturbations of cold particles which form in the equilibrium an ideal lattice.

### 9.4.1. One-dimensional string

The simplest model for studying waves in crystals is the one-dimensional “particle string” [327]. The motion is only allowed along the string, which formally corresponds to the infinite transverse confinement. In Ref. [328] this model was adopted to study waves in plasma crystals. The string model shows very good agreement with the first experiments performed with one-dimensional plasma crystals [107,108]. Moreover, when particle separation  $\Delta$  exceeds the screening length  $\lambda_D$ , so that only the interaction with the *nearest neighbours* is important, the string model turns out to be appropriate to describe DL waves also in two-dimensional plasma crystals [102,109]. The string model yields the following dispersion relation in the nearest neighbour approximation:

$$\omega(\omega + i\nu_{dn}) = 4\Omega_{DL}^2 e^{-\kappa} (\kappa^{-1} + 2\kappa^{-2} + 2\kappa^{-3}) \sin^2 \frac{1}{2} k \Delta , \quad (84)$$

where  $\Omega_{\text{DL}}^2 = e^2 Z^2 / m_d \lambda_D^3$  is the DL frequency scale and  $\kappa = \Delta / \lambda_D$  is the lattice parameter. The experimentally observed wave frequencies usually vary from a few Hz for strings up to a few dozens of Hz for monolayers (e.g., [102,107,256]), which is in agreement with the estimated magnitude of  $\Omega_{\text{DL}}$ . Simple formula (84) is very convenient to evaluate spectra of the longitudinal DL waves.

#### 9.4.2. Two-dimensional triangle lattice

Most of the experiments on the DL waves have been performed so far in two-dimensional complex plasmas—crystalline monolayers suspended in rf electrode sheaths [102,109–111,256–258]. Particles in the monolayers form a hexagonal (triangular) lattice (as shown in Fig. 34, see Section 10). The dispersion relation for the *in-plane* DL modes in such lattices was derived in Refs. [257,329–331]. The perturbations are determined by the following equation [257]:  $\omega(\omega + i\nu_{dn})\delta\mathbf{r}_{\omega,\mathbf{k}} = \mathbf{D}_{\omega,\mathbf{k}}\delta\mathbf{r}_{\omega,\mathbf{k}}$ , where the components of the dynamics matrix are  $D_{\omega,\mathbf{k}}^{xx} = \alpha - \beta$ ,  $D_{\omega,\mathbf{k}}^{yy} = \alpha + \beta$ , and  $D_{\omega,\mathbf{k}}^{xy} = D_{\omega,\mathbf{k}}^{yx} = \gamma$ , and the coefficients  $\alpha$ ,  $\beta$ , and  $\gamma$  are represented by the following sums over all neighbours ( $m$  and  $n$  are integers):

$$\begin{aligned}\alpha &= \Omega_{\text{DL}}^2 \sum_{m,n} e^{-K} (K^{-1} + K^{-2} + K^{-3}) \sin^2 \frac{1}{2} \mathbf{k} \cdot \mathbf{R} , \\ \beta &= \Omega_{\text{DL}}^2 \sum_{m,n} e^{-K} (K^{-1} + 3K^{-2} + 3K^{-3}) [(R_y^2 - R_x^2)/R^2] \sin^2 \frac{1}{2} \mathbf{k} \cdot \mathbf{R} , \\ \gamma &= \Omega_{\text{DL}}^2 \sum_{m,n} e^{-K} (K^{-1} + 3K^{-2} + 3K^{-3}) [2R_x R_y / R^2] \sin^2 \frac{1}{2} \mathbf{k} \cdot \mathbf{R} .\end{aligned}\quad (85)$$

Here  $K = R/\lambda_D$  is the lattice parameter for the neighbour separated by vector  $\mathbf{R} = (R_x, R_y)$ , with the components

$$R_x = m \frac{\sqrt{3}}{2} \Delta, \quad R_y = (\frac{1}{2}m + n) \Delta . \quad (86)$$

The dispersion relation for the in-plane DL modes is determined by the eigenvalues of the dynamics matrix,

$$\omega_{\pm}(\omega_{\pm} + i\nu_{dn}) = \alpha \pm \sqrt{\beta^2 + \gamma^2} . \quad (87)$$

The two branches,  $\omega_{\pm}(\mathbf{k})$ , represent the “high-frequency” and “low-frequency” modes, respectively. These modes are shown in Fig. 27 for different orientations of the wave vector with respect to the lattice (i.e., different propagation angle  $\theta$ ) [257]. In the long-wavelength limit branches  $\omega_{\pm}(\mathbf{k})$  are isotropic. The dependence on the propagation angle is only revealed at larger  $k$ , where the dispersion can be negative ( $\partial\omega/\partial k < 0$ ). Along with the theoretical curves and the results of MD simulations (Fig. 27e–h), the experimental data are shown in Fig. 27a–d. The experimental results were obtained by employing very effective technique proposed by Nunomura et al. [256]: instead of using external excitation and measuring the particle response, the naturally excited (thermal) particle motion is recorded and a Fourier transform of the velocities,  $V_{\omega,\mathbf{k}}$ , is computed. The highest values of the energy density,  $\propto |V_{\omega,\mathbf{k}}|^2$ , are concentrated in close proximity to distinct curves in  $(\omega, \mathbf{k})$ -space, which are identified as dispersion curves.

One should be reminded here that  $\omega(\mathbf{k})$  is *completely* defined by the wave vectors from the first Brillouin zone [327]. For a hexagonal lattice the first zone is a hexagon determined by the basis reciprocal vectors  $\mathbf{A} = 2\pi\Delta^{-1}(1, \frac{1}{\sqrt{3}})$  and  $\mathbf{B} = 2\pi\Delta^{-1}(0, \frac{2}{\sqrt{3}})$ , which corresponds to  $k \leq 2\pi\Delta^{-1}$  for  $\theta = 0^\circ$ , and to  $k \leq \frac{2}{\sqrt{3}}\pi\Delta^{-1}$  for  $\theta = 30^\circ$ . If  $\mathbf{k}$  is beyond the first zone then vector  $\mathbf{G} = i\mathbf{A} + j\mathbf{B}$  (with some integer  $i$  and  $j$ ) should be subtracted, so that  $\mathbf{k}' = \mathbf{k} - \mathbf{G}$  lies in the first zone and, thus,  $\omega(\mathbf{k})$  is equal to  $\omega(\mathbf{k}')$ .

Branches  $\omega_{\pm}(\mathbf{k})$  are often referred to as the “longitudinal” and “transverse” modes. Such a distinction, however, is not always appropriate [257]: the branches are purely longitudinal and transverse only when the propagation angle is  $\theta = 0^\circ$  and  $30^\circ$ . Otherwise, for an arbitrary  $\theta$ , the longitudinal polarization can be prescribed to  $\omega_+$ , and the transverse one—to  $\omega_-$  (i.e., perturbation  $\delta\mathbf{r}_{\omega,\mathbf{k}}$  is parallel or perpendicular to  $\mathbf{k}$ , respectively) only when the wave vectors are sufficiently small—in the long-wavelength limit. As  $\mathbf{k}$  approaches the first Brillouin zone the polarization of branches  $\omega_{\pm}(\mathbf{k})$  starts alternating between longitudinal and transverse, as shown in Fig. 27i–l. This is because for arbitrary  $\theta$  the short-wavelength longitudinal perturbations cause the transverse ones, and vice versa—the modes become coupled, so

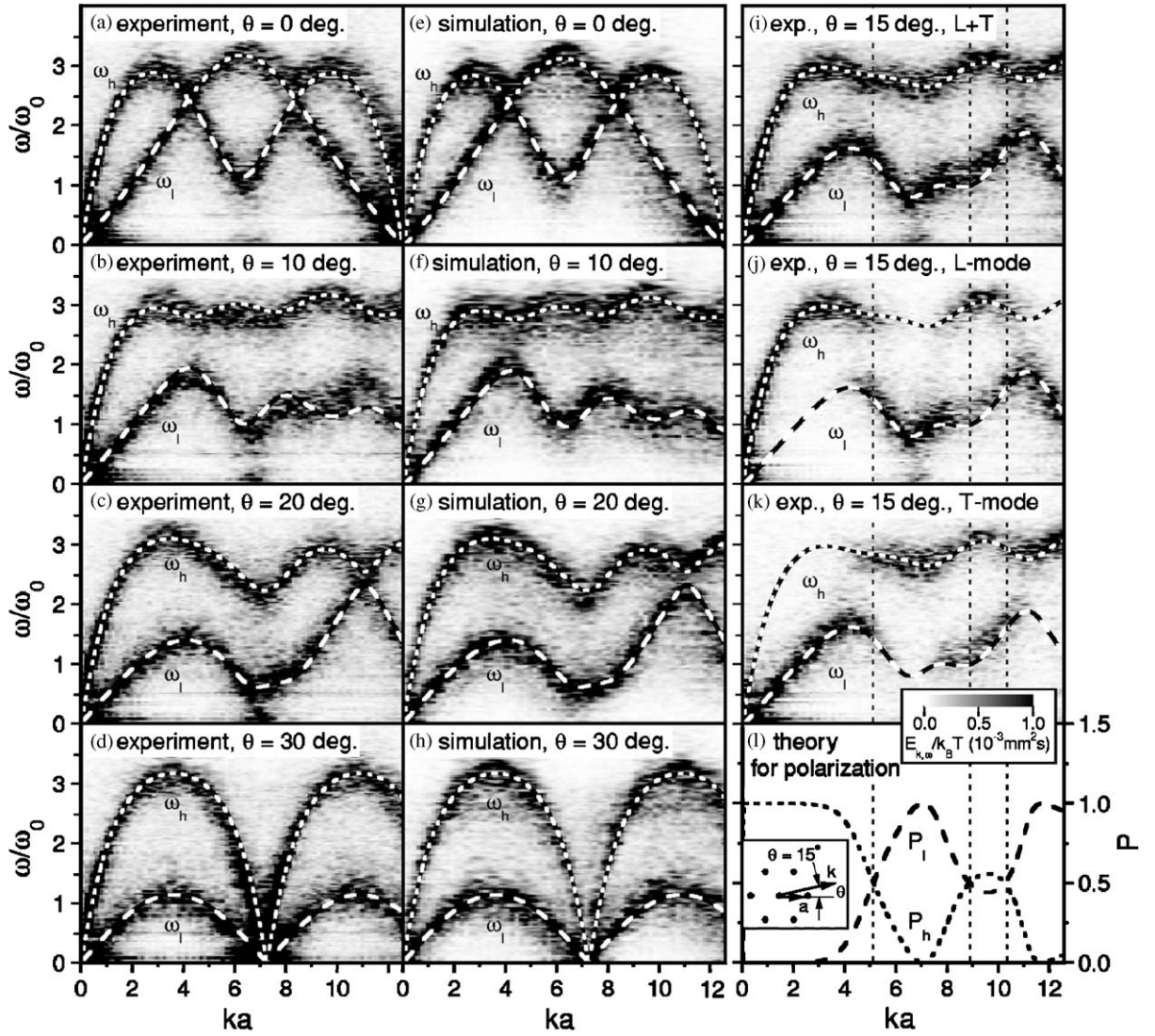


Fig. 27. Dispersion relations of the DL waves in a monolayer hexagonal lattice at different propagation angles  $\theta$  [257]. The phonon spectra of thermally excited waves is shown, as measured (a)–(d) in experiments (argon gas pressure about 1 Pa, plastic particles of  $8.9\,\mu\text{m}$  diameter) and (e)–(h) in MD simulations. The theoretical dispersion relations are superposed: dotted line for the high-frequency mode  $\omega_h$  and dashed line for the low-frequency mode  $\omega_l$  (in the text  $\omega_{\pm}$  are adopted, respectively). The frequency is normalized to  $\omega_0 \equiv \kappa^{-3/2}\Omega_{\text{DL}}$  and the wave vector is normalized to the interparticle distance  $a$  (in the text  $\Delta$  is adopted). (i) Phonon spectra of the waves propagating at  $\theta = 15^\circ$  measured experimentally. The high- and low-frequency branches have mixed longitudinal (L) and transverse (T) polarization. (l) Polarization of the high-frequency ( $P_h$ ) and low-frequency ( $P_l$ ) modes predicted by the theory. In the long-wavelength limit the high-frequency mode is purely longitudinal ( $P_h = 1$ ), and the low-frequency mode is purely transverse ( $P_l = 0$ ).

that one cannot distinguish between them. The coupling disappears only in “symmetrical” cases—when  $\theta = 0^\circ$  and  $30^\circ$ . Thus, the more general division into the “high-frequency” and “low-frequency” branches seems to be more suitable.

Note that the one-dimensional dispersion relation for the particle string can be recovered from Eqs. (85)–(87) by setting  $m = 0$ . This corresponds to the summation along the primitive translation vector  $\Delta(0, 1)$  (mode  $\omega_+$  represents perturbations parallel to the string, and mode  $\omega_-$  is prohibited). It is remarkable that in the nearest neighbour approximation ( $\kappa \gtrsim 2$ ) and in the long-wavelength limit, branch  $\omega_+(\mathbf{k})$  almost coincides with Eq. (84) [255,257,330]. Moreover, for the propagation angle about  $\theta = 30^\circ$  the high-frequency branch is well approximated by the string model at any  $k$ .



In the long-wavelength limit the DL branches (which are purely longitudinal or transverse in this case) have an acoustic dispersion, with the phase velocities  $C_{\text{DL}}^{l,t} = \lim_{k \rightarrow 0} \omega_{\pm}/k$  (superscripts “l” and “t” denote the longitudinal and transverse polarization, respectively). The velocities can be written as [329,331,332]

$$C_{\text{DL}}^{l,t} = C_{\text{DL}} F_{l,t}(\kappa), \quad (88)$$

where  $C_{\text{DL}}^2 = \Omega_{\text{DL}}^2 \lambda_{\text{D}}^2 = e^2 Z^2 / m_d \lambda_{\text{D}}$  is the DL velocity scale. The magnitude of  $C_{\text{DL}}$  is of the order of a few cm/s for typical experimental conditions [110,111]. In order to compare  $C_{\text{DL}}$  with the phase velocity of DA waves in gaseous complex plasmas, one can use the following convenient expression:  $C_{\text{DL}} \equiv \sqrt{k^3/3} \tilde{C}_{\text{DA}}$ , where  $\tilde{C}_{\text{DA}}$  is given by Eq. (75) calculated for dust density  $\tilde{n}_d = (\frac{4}{3}\pi\Delta^3)^{-1}$ . Exact formulas for functions  $F_{l,t}(\kappa)$ , which can be derived from Eqs. (85)–(87), are rather complicated. However, for a practical range of  $\kappa$  the functions can be very well approximated by simple polynomial expansions. For  $\kappa \leq 5$ , we have with accuracy  $< 1\%$  [329,332]:

$$F_l \simeq 2.70\kappa^{-1}(1 - 0.096\kappa - 0.004\kappa^2), \quad F_t \simeq 0.51\kappa^{-1/2}(1 - 0.039\kappa^2). \quad (89)$$

Note that in the OCP regime ( $\kappa \ll 1$ ) the scaling of the longitudinal velocity with  $\kappa$  as well as the magnitude of the velocity ( $C_{\text{DL}}^l \simeq 2.7\kappa^{-1}C_{\text{DL}}$ ) is different from the results for the one-dimensional string ( $C_{\text{DL}}^l \simeq 1.4\sqrt{-\kappa^{-1} \ln \kappa} C_{\text{DL}}$ ) [331]. Recently, the long-wavelength DL modes in crystalline monolayers were investigated in active experiments [110,111], where the waves were excited with chopped laser radiation. The measured dispersion relations were found to be in remarkably good agreement with the theoretical results.

In addition to the in-plane waves, the particles in crystalline monolayers can also sustain the *vertical* (out-of-plane) DL wave mode, which is shown in Fig. 28. The vertical mode is due to the balance between gravity and strongly inhomogeneous vertical electric force on a particle (e.g., in rf sheaths). This implies the (lowest-order) vertical parabolic confinement characterized by the frequency of a single particle oscillations,  $\Omega_v$ . Employing the one-dimensional string model with parabolic transverse confinement, one can derive dispersion relation for the vertical DL mode (nearest neighbour approximation) [333]

$$\omega(\omega + i\nu_{\text{dn}}) = \Omega_v^2 - 4\Omega_0^2 e^{-\kappa} (\kappa^{-2} + \kappa^{-3}) \sin^2 \frac{1}{2} k \Delta. \quad (90)$$

This is the optical branch,  $\lim_{k \rightarrow 0} \omega = \Omega_v$ , which has a negative dispersion, so that the group and phase velocities have opposite signs. An analytical dispersion relation for the vertical mode in a two-dimensional hexagonal lattice has been derived in Refs. [266,334]. In the nearest neighbour approximation *and* in the long-wavelength limit, it agrees well with Eq. (90). However, for  $\mathbf{k}$  close to the first Brillouin zone the dispersion of the two-dimensional vertical mode becomes positive for any propagation angle, and then the vertical mode cannot be approximated by Eq. (90). The theoretical dispersion relations are in reasonable agreement with the experimental results obtained for long waves [266,275]. Nevertheless, deeper experimental investigations of the vertical DL mode (similar to what has been done for the in-plane modes) are still required in order to perform comprehensive quantitative comparison with the theory.

#### 9.4.3. Three-dimensional plasma crystals

So far, no reliable experimental results on the DL waves in three-dimensional plasma crystals have been reported. Basically, there are two reasons for that:

(i) The major problem of the wave investigation in three-dimensional complex plasmas is the lack of effective 3D diagnostics. The laser sheets which are employed to render the particle motion cannot precisely reveal the information (viz., particle velocity) in the direction perpendicular to the sheet. The technique that is currently available for 3D diagnostics (based on the particle color coding of the third dimension, see brief description in Ref. [335]) restricts the analysis to a relatively small volume, and also is very complicated technically. Therefore, the major experimental efforts (to study waves and other dynamical phenomena) have been focused so far of the crystalline monolayers.

(ii) In the ground-based experiments it is almost impossible to obtain 3D plasma crystals of “good quality”: The particle clouds are very stressed in the vertical direction (unless the particles are small enough, but then their recognition becomes difficult)—the inhomogeneity scale can be comparable to the particle separation (e.g., [19,21]). One can expect that the plasma crystals produced under microgravity conditions will be in the most normal, isotropic, stress-free state which can be obtained in complex plasmas. Microgravity experiments will allow us to have a relatively small number of dislocations in crystals, which is very important for the comparison with theory.

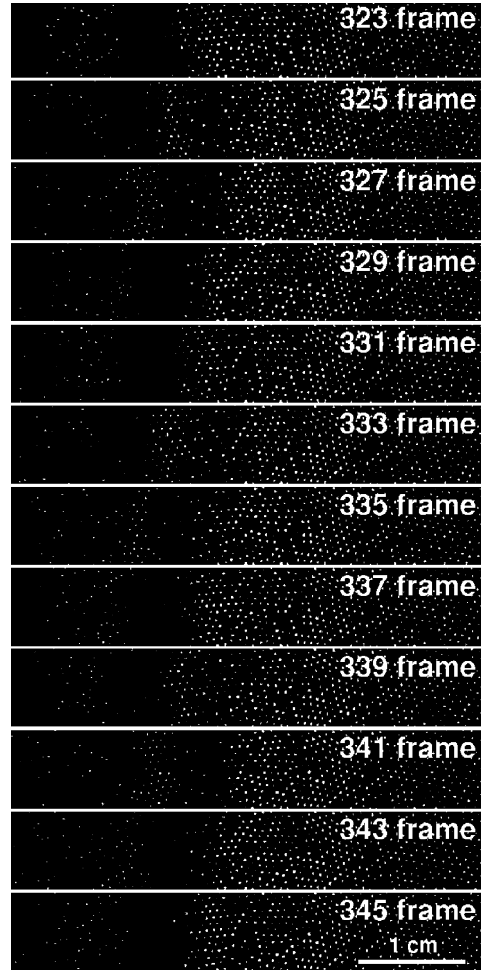


Fig. 28. Vertical DL waves observed in a monolayer hexagonal lattice [266]. Experiments were performed in a GEC rf chamber in argon gas at pressure about 1–2 Pa, with plastic particles of 8.9  $\mu\text{m}$  diameter. Particles were illuminated by a horizontal laser sheet of about 200–300  $\mu\text{m}$  thickness. The waves were excited by applying a (negative) voltage pulse to the horizontal wire positioned at the left edge. Top view of the lattice is shown at time 1.4–1.5 s after the excitation, when the wave packet was well formed. The particles are visible only if they are in the plane of the illuminating laser sheet. The stripes of particles apparently move from right to left due to the vertical wave motion, revealing the lines of constant phase. Individual particles do not move horizontally. The numbers on the images indicate the frame number (at 230.75 fps).

Below we briefly mention the main theoretical results for the DL waves in three-dimensional plasma crystals: The number of acoustic modes which can be sustained in crystals is 3. Since the number of particles per elementary lattice cell,  $r$ , can be more than one (e.g.,  $r = 2$  for bcc and  $r = 3$  for fcc lattices), the remaining  $3(r - 1)$  modes have an optical dispersion (although these modes can be degenerate) [327]. In the long-wavelength limit, the phase velocities of the (acoustic) modes are isotropic. When  $\kappa \ll 1$  (OCP regime), the  $\kappa$ -scaling of the longitudinal phase velocity,  $C_{\text{DL}}^{\text{l}} \simeq 5.0(7.0)\kappa^{-3/2}C_{\text{DL}}$  for a bcc (fcc) lattice, is different from that for one- and two-dimensional model, whereas the transverse acoustic velocity,  $C_{\text{DL}}^{\text{t}} \simeq 0.19\kappa^{-1/2}C_{\text{DL}}$ , has the same scaling [331]. Note that in comparison to monolayers, Eqs. (88) and (89), the magnitude of the phase velocity in three-dimensional crystal is larger for the longitudinal mode, and is smaller for the transverse mode. For arbitrary  $\kappa$  one can obtain the phase velocities of all modes in the long-wavelength limit by using the results for the elastic constants of Yukawa crystals (e.g., [337]).

It is noteworthy that the wave modes in three-dimensional plasma crystals are similar to those in solids. Therefore, the comprehensive investigation of particle dynamics in plasma crystals can give us an excellent opportunity to study generic wave phenomena—mode interaction, umklapp processes, phonon scattering on defects, etc.—at the kinetic level.



#### 9.4.4. Instabilities in plasma crystals

There is a number of different mechanisms which can trigger wave instabilities and cause eventual melting of plasma crystals. Some of these instabilities can operate irrespective of the phase state (although, the parameters of the instabilities depend on the coupling parameter  $\Gamma$ ), some are peculiar to plasma crystals, and some can set in only when the crystal has a particular dimensionality (e.g., the instability can be triggered in monolayers only). The common type is the ion streaming instability, which is similar to that discussed in Section 9.2.2. For strongly coupled and crystalline states the instability threshold was calculated in Ref. [338]. It was found that the strong coupling generally leads to an enhancement of the growth rates. The major wave instabilities peculiar to plasma crystals are

(i) Wake-induced instability in three-dimensional crystals: The charged grains suspended in rf sheaths or dc striations often assemble themselves into the so-called “vertically aligned” hexagonal lattices (see Section 10.3). Such structures can only be stable at sufficiently high pressures. When the pressure (and, thus, the damping rate  $\nu_{dn}$ ) decreases below a certain threshold the particles start oscillating horizontally, which indicates the instability onset [238]. The further (relatively slight) pressure decrease leads to an increase of the oscillation amplitude and melting of the crystal [339,340]. This instability occurs because the presence of wakes makes the interparticle interaction nonreciprocal and, hence, the total energy of the particle system is not conserved. The source of the energy is the ion flux. The instability was first analysed theoretically by Schweigert [238] using the model of a point-like dipole characterized by the wake charge  $Z_{\text{wake}}$  located at distance  $\Delta_{\text{wake}}$  downstream from the grain. This model yields very good qualitative agreement with experiments.

(ii) Coupling instability in monolayers: The wake potentials can play a crucial role also for the stability of the monolayer plasma crystals. It was shown that the interaction of the charged grains with the wake potential of the neighbouring grains causes a coupling between the in-plane and (vertical) out-of-plane DL wave modes. This coupling can trigger the resonance instability of the DL waves when the two branches intersect [see, e.g., Eqs. (84) and (90)], which occurs when the particle density in the monolayer exceeds a certain threshold [341]. Also, the neutral damping rate should be low enough, otherwise the instability is inhibited. These two conditions have the following form:

$$\eta \equiv 4e^{-\kappa}(\kappa^{-1} + 3\kappa^{-2} + 3\kappa^{-3})(\Omega_{\text{DL}}/\Omega_v)^2 > 1 ,$$

$$\nu_{dn} \lesssim \sqrt{\eta - 1} |Z_{\text{wake}}/Z| (\Delta_{\text{wake}}/\Delta) \Omega_v .$$

Comparison of the theoretical results with experiments and MD simulations reveals remarkably good agreement [239]. This mechanism might be the one of the main reasons for the monolayer melting at pressures below  $\sim 10$  Pa.

(iii) Instability due to defects: Another instability mechanism which can be especially important in bilayer crystals is associated with the so-called “strong defects”—the particles which are located above and below the “complete” layers [342]. These particles were shown to be very effective sources of the local heating. The instability due to strong defects starts somewhat before the wake-induced instability sets on, and makes the melting transition more smoothed as the pressure decreases.

(iv) Instability due to charge fluctuations: Stochastic variations of the grain charges can trigger another instability in plasma crystals [136]. The mechanism of energy gain in this case is similar to stochastic heating considered in Section 8.2: the charge variations provide not only an additional Langevin-like term in the equations of the particle motion, but also result in a multiplicative effect, inducing a parametric instability. The instability can be triggered when the neutral damping is below a threshold.

$$\nu_{dn} \lesssim \sigma_Z^2 \Omega_{\text{DL}}^2 / \Omega_{\text{ch}} ,$$

where  $\sigma_Z^2$  is the dimensionless charge dispersion [see also the condition for the instability of a single particle, Eq. (61)]. If the variations of the grain charges are due to the discreteness of plasma (electron and ion) charges then the magnitude of the dispersion is fairly small,  $\sigma_Z^2 \sim |Z|^{-1}$ , and the instability is only possible at pressures far below  $\sim 1$  Pa [136]. However, in sufficiently dense complex plasmas the charge fluctuations might be due to the dust grain discreteness [246], which yields substantially larger values of  $\sigma_Z^2$  and, hence, the instability can be possible at much larger pressures. Nevertheless, one should note that so far there were no reliable experiments where this type of instability was clearly identified.

### 9.5. Nonlinear waves

Complex plasmas, as any other plasmas are nonlinear media where the waves of finite amplitude cannot be generally considered independently. Nonlinear phenomena in complex plasma are very diverse, due to a large number of different wave modes which can be sustained. The wave amplitude can reach a nonlinear level because of different processes: this is not necessarily an external forcing, or the wave instabilities—it can also be a regular collective process of nonlinear wave steepening. In the absence of dissipation (or, when the dissipation is small enough), nonlinear steepening can be balanced by wave dispersion which, in turn, can result in the formation of *solitons*. When the dissipation is large, it can overcome the role of dispersion and then the balance of nonlinearity and dissipation can generate *shock waves*. In many cases the lowest-order nonlinear terms are quadratic, and then the weakly nonlinear soliton dynamics is governed by the Korteweg-de Vries (KdV) equation [343]. For solitons of arbitrary amplitude, the method of the Sagdeev pseudopotential is very convenient [344]: in particular, this method allows us to determine the upper value of the Mach number beyond which the dispersion is no longer sufficient to balance the nonlinearity and, thus, the collisionless shock is formed due to “collective” dissipation. The “conventional” dissipation is often determined by viscosity, and then the shock waves can be described by the KdV–Burgers equation [343,345]. However, in complex plasmas there is a rich variety of mechanisms which determine nonlinear and dispersive properties of the medium. This generally makes the description of nonlinear waves in complex plasmas more complicated.

#### 9.5.1. Ion solitons and shocks

The theory predicts that in complex plasmas (as well as in electronegative plasmas) both compressive and rarefactive dust ion–acoustic solitons are possible (e.g., [346,347]). It was shown that the properties of the DIA solitons (profile and the range of Mach numbers where the solitons can exist) are strongly affected by the form of the electron and ion distribution function, in particular—by the presence of “cold” and “hot” populations (e.g., in space environment) and trapped electrons (e.g., in laboratory plasmas). The compressive DIA solitons were observed in experiments by Nakamura [260] performed in a dusty plasma device at very low pressures ( $p \sim 10^{-2}$  Pa), whereas in plasmas with negative ion component also the rarefactive solitons were reported [348,349]. At such pressures the collisions with neutrals play almost no role, and a weak dissipation does not destroy the profile of DIA solitons as long as the dissipation time scales are longer than the duration of the soliton existence [291,350]. As regards the DIA shocks, they were observed in different experiments [259,261,269] performed at pressures  $p \sim 10^{-2}$ – $10^{-3}$  Pa. Depending on the parameter regime (in particular—number density of grains), different dissipation mechanisms can play the major role [291,351]: along with the ion viscosity (due to collisions with grains), these are grain charge variations (ion absorption) and Landau damping. The general trend is that in the absence of dust the shock front exhibits pronounced oscillatory structure [261] typical for collisionless ion–acoustic shocks [352]. As the dust density increases the peaks become smoothed and eventually disappear, leaving the monotonic front profile, as shown in Fig. 29.

#### 9.5.2. Dust solitons and shocks

Longitudinal dust solitons of moderate amplitude were observed in experiments by Samsonov et al. [263] and Nosenko et al. [273]. Both experiments were performed in rf discharges at low pressures ( $p \simeq 1.8$ – $2$  Pa). The solitons were excited in crystalline monolayers by electrical pulses or by the laser beams. Fig. 30 shows the evolution of the soliton propagating along the crystal [263]. Theoretical study of the soliton dynamics is based on the analysis of Eq. (83). Defining  $\mathbf{x}$  as the propagation vector and retaining the lowest-order nonlinearity and dispersion terms, the resulting equation for the nonlinear wave dynamics is [263,353]

$$\frac{\partial^2 u}{\partial t^2} + v_{dn} \frac{\partial u}{\partial t} = C^2 \frac{\partial^2}{\partial x^2} \left( u + \ell^2 \frac{\partial^2 u}{\partial x^2} + \frac{1}{2} A u^2 \right). \quad (91)$$

Here  $u = \partial \delta \mathbf{r} / \partial \mathbf{x} \simeq -\delta n_d / n_d$  is the particle density modulation expressed via the longitudinal derivative of the (in-plane) displacement,  $C$  is the long-wavelength DL phase velocity (which is independent of the direction of propagation),  $\ell^2$  is the dispersion coefficient which generally can have *either* sign (it has the dimension of squared length), and  $A$  is the nonlinear coefficient. Without the frictional dissipation, Eq. (91) is readily reduced to the KdV equation by employing the stretched coordinates  $(x - Ct, t)$ . The soliton can only exist when  $\ell^2$  and  $A$  have opposite signs, so that the following relations can be fulfilled:  $-\frac{1}{3} A A = 4 \ell^2 / L^2 = M^2 - 1$ , where  $A$  and  $L$  are the soliton amplitude and width,

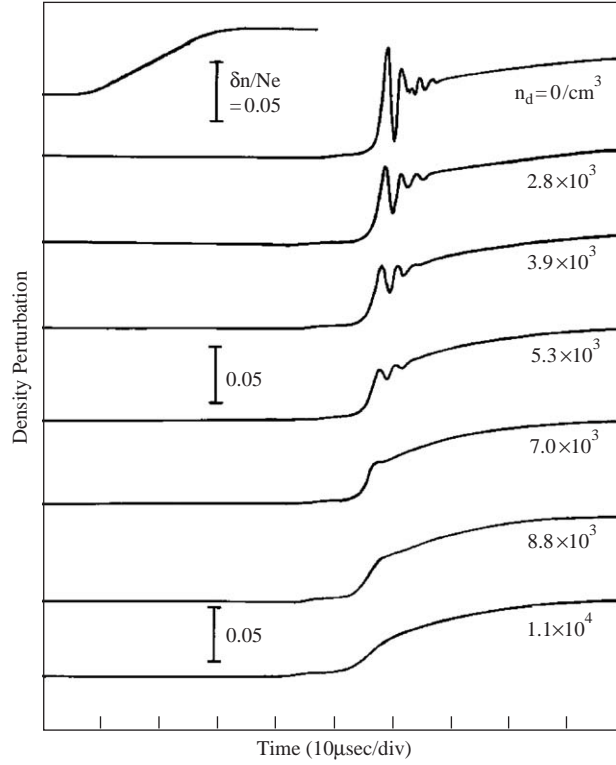


Fig. 29. DIA shock observed in a double plasma device [261]. Experiments were performed with argon gas at pressure about  $(2 - 4) \times 10^{-2}$  Pa, for different densities  $n_d$  of the dust particles of about  $8.9 \mu\text{m}$  diameter. The DIA waves were excited with a positive ramp voltage applied to the source anode, and the signals were detected by the movable Langmuir probe. The electron density perturbations were recovered from the perturbations of the electron saturation current on the probe.

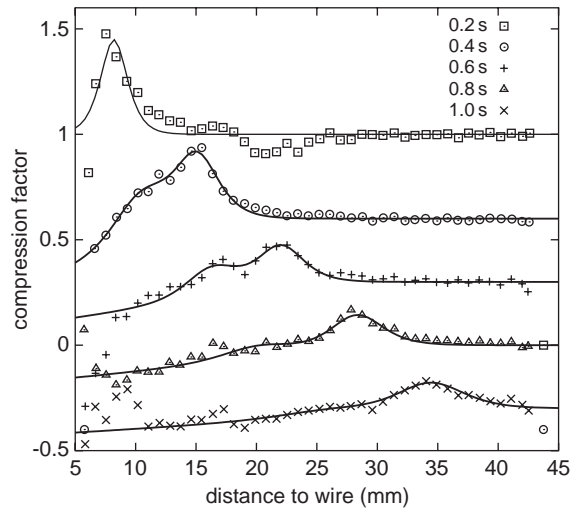


Fig. 30. Dust soliton observed in experiments with a monolayer hexagonal lattice [263]. Experimental conditions and the wave excitation technique are described in Fig. 28. Compression factor  $1 + \delta n_d/n_d$  versus distance to the wire is plotted at different times. The solid lines show the theoretical fits to the experimental data. The fits and experimental points at later times are offset down.

respectively, and  $M = V/C$  is the Mach number for the soliton velocity. The Mach number is a convenient control parameter which defines the soliton profile,  $-u = A \cosh^{-2}(\xi/L)$ , with  $\xi = x - Vt$ .

In two-dimensional hexagonal lattices [353],  $\ell^2$  is always positive and has a very weak dependence on the direction of propagation,  $A$  is always negative and can depend on the direction substantially, especially at  $\kappa \gtrsim 1$ . Such a combination of signs implies that only compressive ( $A > 0$ ) supersonic ( $M > 1$ ) solitons can propagate in crystalline monolayers, as it is observed in experiments. In the nearest neighbour approximation,  $\kappa \gtrsim 1$ , one can calculate parameters of Eq. (91) by using the results for a one-dimensional string [263],

$$\begin{aligned} C^2 &= C_{\text{DL}}^2 \kappa^2 [G(\kappa)/\kappa]'' , \\ \ell^2 &= \frac{1}{12} \lambda_{\text{D}}^2 \kappa^2 [G''(\kappa)/\kappa]'' / [G(\kappa)/\kappa]'' , \\ A &= \kappa [G(\kappa)/\kappa]''' / [G(\kappa)/\kappa]'' , \end{aligned} \quad (92)$$

where  $G(\kappa) = -\ln(e^\kappa - 1)$ . This relatively simple theoretical model provides remarkably good agreement with the experiments. If the neutral gas pressure is low enough the friction does not destroy the soliton [263]. The perturbation simply slows down, approaching the asymptote  $V = C$ , and the form of the soliton changes in accordance with the analytical solution (i.e., the amplitude decreases and the width increases, keeping the “soliton relation”  $AL^2 = \text{const}$ , see Fig. 30). Thus, one can speak about a “weakly dissipative soliton” when the dissipation time scale,  $\sim \nu_{\text{dn}}^{-1}$ , exceeds the time scale of the wave itself,  $\sim \Omega_{\text{DL}}^{-1}$ .

The theory predicts in-plane transverse (shear) solitons in two-dimensional lattices [353], as well as the solitons due to the coupling between longitudinal in-plane and vertical out-of-plane modes [354]. Such solitons, however, have not yet been observed in experiments. There have been also a number of theoretical papers on properties of the DA solitons in gaseous complex plasma [287,355–359], but no experiments have been done so far.

As regards the dust shock waves, this topic still needs to be explored, both theoretically and experimentally. The theory of shocks in weakly coupled complex plasmas has been studied, e.g., in Refs. [360,361]. It was suggested that the major dissipation mechanism providing the shock formation can be the dust charge variations, and the weak shocks can be described by the KdV–Burgers equation. These results, however, have better applicability to the space environment, where the complex plasmas can be found in the gaseous state and where the charge variation effects are not inhibited by the gas friction (see Section 9.2.2). For the strongly coupled plasmas, the generalized hydrodynamic approach (see Section 9.3) was proposed [312,345]. This approach suggests that weak shocks cannot be described by the KdV–Burgers equation in general case [312]. In experiments, “pure” shocks were only observed so far in two-dimensional crystals [264,265]. (Term “pure” implies here that the momentum exchange in dust–dust collisions prevails over the momentum loss due to neutral gas friction,  $\nu_{\text{dd}} \gg \nu_{\text{dn}}$ , so that charged grains have properties of one-phase fluids, see Section 6.3.) These shocks (generated by electrical pulses, like the solitons in experiments [263]) caused melting of the crystal behind the front, as shown in Fig. 31. As the shock propagated and weakened it was seen that the melting ceased. Further propagation of the pulse was in the form of a soliton, as described above. Other examples of strong dust discontinuities were observed in microgravity experiments with a rf discharge [279] and in ground-based dc experiments [280]. In both cases the shock-like structures were triggered in three-dimensional complex plasmas using gas pulses. The experiments were performed at high gas pressures about 50–120 Pa, when the friction dissipation is very strong,  $\nu_{\text{dn}} \sim 100\text{--}300 \text{ s}^{-1}$ . Nevertheless, the “shocks” were observed during a few seconds almost undamped, which suggests that there must be a mechanism of strong energy “influx” into the structures (e.g., modulational instability). Therefore, the dust discontinuities observed in Refs. [279,280] should rather be referred to as “dissipative structures” where pure hydrodynamic effects presumably play minor role.

### 9.5.3. Mach cones

Dispersion relations of dust modes in complex plasmas suggest that, irrespective of the plasma state [see Eqs. (74), (81), (82), (87)] the phase velocity attains the maximal value in the long-wavelength limit. For acoustic modes this velocity—the “sound speed”  $C$ —is finite and therefore, similar to conventional media, the supersonic perturbations (i.e., with Mach number  $M = V/C > 1$ ) are always localized behind the object which produces these perturbations (this can be a rapidly moving charged particle or a bunch of particles, biased probe, etc.). The perturbation front has a conical form in a three-dimensional case and therefore it is called a “Mach cone”. In a two-dimensional case the same name is adopted, although the front is a planar V-shaped perturbation. The opening angle  $\mu$  of the front at large

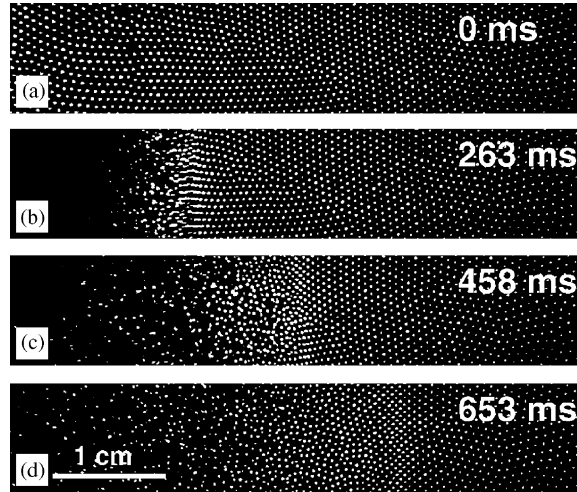


Fig. 31. Dust shock wave propagating in a monolayer hexagonal lattice [264]. Experimental conditions and the wave excitation technique are described in Fig. 28. Initially undisturbed particles (a) were swept from left to right (b) and (c) forming a shock with a sharp front. The lattice melted behind the front. At later times (d) the shock weakened due to the neutral drag and a soliton was formed.

distances from the object (where the nonlinearity should not play important role) is determined by the well-known relation  $\sin \mu = C/V \equiv M^{-1}$ .

Originally, it was suggested that the Mach cones (wakes) can be excited in space dusty plasmas—e.g., in planetary rings by big boulders [362,363] moving through the dust at a velocity that is somewhat higher than  $C$ . It was expected that the discovery of Mach cones and the measurements of the opening angles during the Cassini mission to Saturn will yield new information on the dusty plasma conditions in planetary rings. Unfortunately, no Mach cones detected during this mission were reported. The Mach cones in laboratory complex plasmas were discovered by Samsonov et al. [254,255] in two-dimensional plasma crystals. They were generated by single particles spontaneously moving beneath the monolayer along straight trajectories. (The physical mechanism which drives such motion is still an open issue; for one of the possible explanations, see [364].) In experiments [271] the Mach cones were excited by the radiation pressure of a focused laser beam. The wake reveals a multiple cone structure behind the front, as shown in Fig. 32. Generally, the wake structure is determined by the dispersion and nonlinear properties of particular wave modes excited behind the front [353,365]. The formation of the second cone behind the first one, with the opening angle smaller for the second cone can be prescribed to the shear (transverse) wave front [365,366], because the (longitudinal) sound speed is larger than the shear phase velocity [see Eqs. (88) and (89)]. Also, the shape of the cone wings can be affected by the inhomogeneity of the particle density, as suggested in Ref. [367]. It was proposed to use the Mach cones as a tool to determine the local parameters of complex plasmas [271,363], e.g., particle charge and the screening length, making use of the measured sound speed.

## 10. Phase transitions in strongly coupled complex plasmas

### 10.1. Strong coupling of dust species

As we discussed in Section 6, the interactions between different species in complex plasmas are quite diverse and depend on relations between the plasma characteristic parameters. One of the fundamental characteristics of a many-particle interacting system is the coupling parameter  $\Gamma$  defined as the ratio of the potential energy of interaction between neighbouring particles to their kinetic energy. For the Coulomb interaction between charged particles,

$$\Gamma = \frac{Z^2 e^2}{\Delta T_d},$$

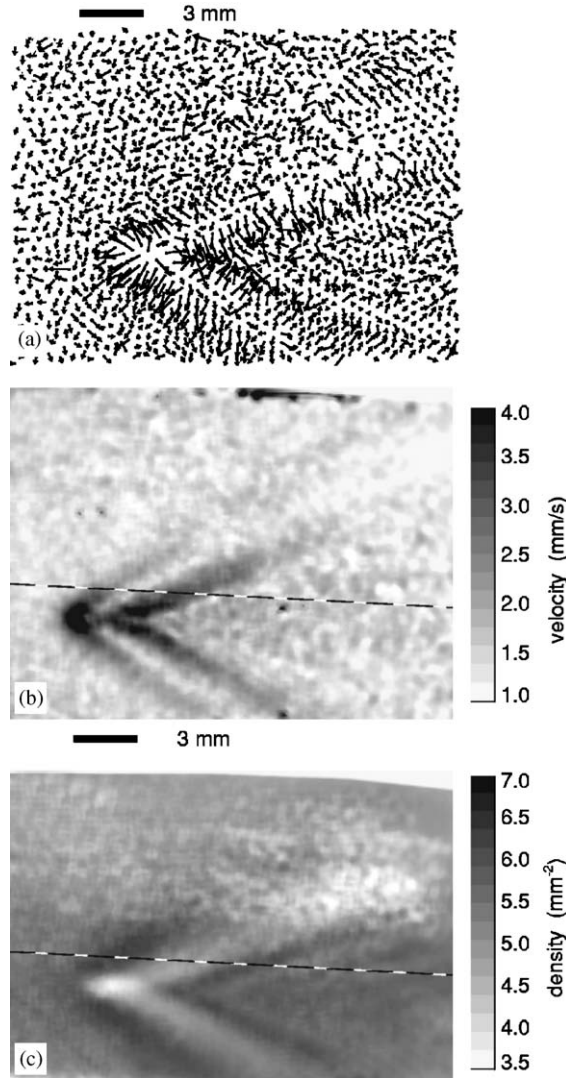


Fig. 32. Mach cone observed in a monolayer hexagonal lattice [255]. Experiments were performed in a GEC rf chamber in krypton gas at pressure about 1.2 Pa, with plastic particles of 8.9  $\mu\text{m}$  diameter. The cone was excited by a supersonic particle which moved spontaneously beneath the monolayer. (a) Particle velocity vector map derived from particle positions in two consecutive video fields, (b) grey-scale speed map, and (c) grey-scale number density map. The first cone consists of particles moving forward, and it coincides with the high density region. The second cone has particles moving backward, and it coincides with the low density region.

where  $\Delta = n_d^{-1/3}$  characterizes the average interparticle spacing, and  $T_d$  characterizes their kinetic energy. The system is usually called “strongly coupled” when  $\Gamma \gtrsim 1$ . For a Yukawa-type interaction, the “actual” coupling ratio is characterized by “screened” coupling parameter  $\Gamma_S = \Gamma \exp(-\kappa)$ , where

$$\kappa = \frac{\Delta}{\lambda},$$

is the structure (or lattice) parameter—the interparticle spacing normalized by the effective screening length.

Most theories developed so far to describe the properties of dusty plasmas employ the following model: negatively charged particles are trapped within the plasma volume due to some confining force (usually of electrostatic character) and interact with each other via the isotropic Debye–Hückel (Yukawa) repulsive potential, with the screening determined by the plasma electrons and ions. This model gives rather simplified picture of dusty plasma behaviour and is not



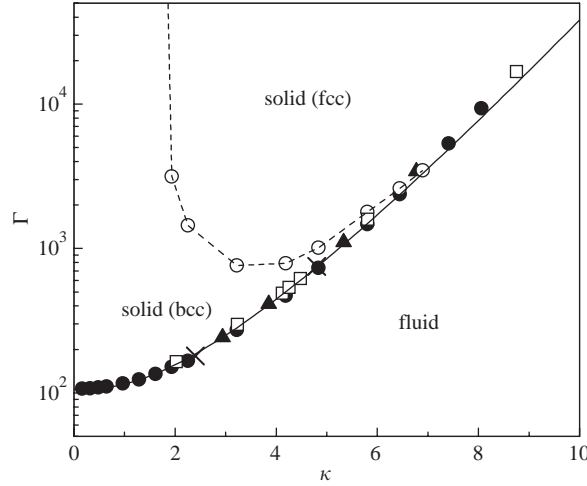


Fig. 33. Phase diagram of Debye–Hückel systems, obtained from numerical modelling. Open circles correspond to the bcc–fcc phase boundary [370]. The fluid–solid phase boundary (melting line) is marked by squares [369], solid circles [370], and triangles [371]. The crosses correspond to jumps in the diffusion constant, observed in the simulations of dissipative Debye–Hückel systems [372,373]. The solid line represents the approximation of the melting line by Eq. (93), the dashed line is the fit to the numerical data judged by eye.

applicable to some experiments, especially when the plasma anisotropy plays an important role. Moreover, this model does not take into account variations of particle charges, long-range interactions, the exact form of the confining potential, etc. However, the model was shown to be useful in providing qualitative results which are confirmed by experiments, and hence it may be considered as a reasonable basis to construct more sophisticated models in future.

### 10.2. Phase diagram of Debye–Hückel (Yukawa) systems

Besides complex plasmas, particles interacting with a Debye–Hückel potential have been extensively studied in different physical systems ranging from elementary particles to colloidal suspensions. Not surprisingly, their phase diagrams have received considerable attention. Various numerical methods (usually, MC or MD simulations) have been employed [337,368–373].

In our case, the static properties of the system are completely determined by two independent dimensionless parameters  $\Gamma$  and  $\kappa = \Delta/\lambda$ . Fig. 33 shows the phase diagram of the Debye–Hückel system in the  $(\Gamma, \kappa)$ -plane, summarizing available numerical results. Three phases were found, depending on the values of coupling and structure parameters. For very strong coupling,  $\Gamma > \Gamma_M$ , where  $\Gamma_M$  denotes the value of  $\Gamma$  in the melting curve, there are solid fcc and bcc phases and a liquid phase for  $\Gamma < \Gamma_M$ . The bcc phase is stable at small  $\kappa$ , while fcc is stable at larger  $\kappa$ . The triple point is at  $\Gamma \simeq 3.47 \times 10^3$  and  $\kappa \simeq 6.90$  [370].

Of particular interest for plasma crystallization experiments is the form of the melting (crystallization) curve  $\Gamma_M = \Gamma_M(\kappa)$  [10,337,369–371,374,375]. Results obtained for OCP systems ( $\kappa = 0$ ) indicate that the crystallization occurs at  $\Gamma \simeq 106$  [if the distance is measured in units of the Wigner–Seitz radius,  $(4\pi n_d/3)^{-1/3}$ , then  $\Gamma \simeq 172$ ] [376–378]. Different analytical approximations for  $\Gamma_M(\kappa)$  were proposed (see, e.g., [180]). Vulina and Khrapak [375] suggested to employ the Lindemann criterion where the frequency of the dust–lattice waves is used as the characteristic frequency. The melting line obtained is

$$\Gamma_M e^{-\kappa} (1 + \kappa + \frac{1}{2}\kappa^2) \simeq 106, \quad (93)$$

and yields remarkably good agreement with the results of numerical simulations at  $\kappa \lesssim 10$  (see Fig. 33). One should note, however, that the arguments used in deriving Eq. (93) are not really rigorous (for instance, there are no clear physical arguments to justify the choice of the dust–lattice frequency instead of, e.g., the Einstein frequency).

From a practical point of view, a simple criterion is often required, which allows us to judge whether the system under consideration is in a crystalline or liquid state. Different phenomenological criteria for the crystallization (melting) of

systems of interacting particles exist, which are often independent of the exact form of interaction potential between the particles. Some of them are convenient for dusty plasmas. Best known is the Lindemann criterion [379], according to which melting of the crystalline structure occurs when the ratio of the root-mean-square particle displacement to the mean interparticle distance reaches a value of  $\simeq 0.15$ . Another criterion is the value of the first maximum of the static structure factor in the liquid state [380], which reaches a value of  $\simeq 2.85$  on the crystallization curve. There also exists a simple crystallization criterion expressed in terms of the pair correlation function, the ratio of the minimum to the maximum of which should be approximately equal to  $\simeq 0.2$  on the crystallization curve. A simple dynamic crystallization criterion, similar in some sense to the Lindemann criterion, was proposed by Löwen et al. [381]. According to this criterion, crystallization occurs when the diffusion constant reduces to a value of  $\sim 0.1$  compared to the diffusion constant for noninteracting particles. Later on, it was noted that this criterion holds for both 2D and 3D systems [382].

### 10.3. Experimental investigation of phase transitions in complex plasmas

As noted in the Introduction, dusty plasmas possess a number of unique properties which make these systems extremely attractive for investigation of different collective processes, including phase transitions. In particular, relatively short temporal scales for relaxation and response to external perturbations, as well as simplicity in observation, allow us not only to study static structure characteristics, but also to investigate the dynamics of phase transitions in detail [187,189,383,384]. Usually, phase transitions from crystalline to liquid-like or gas-like states are investigated in experiments. Melting of a crystalline lattice can be initiated either by a decrease in the neutral gas pressure or by an increase in the discharge power. This can be attributed to the fact that the plasma parameters change under these conditions in such a way that the coupling parameter  $\Gamma_S$  decreases. This decrease is associated (at least in experiments with the lowering of the neutral pressure) with a significant increase in the kinetic energy of the dust particles. For example, the initial temperature which was close to the neutral gas temperature ( $T_d \sim T_n \sim 0.03$  eV) in highly ordered crystal-like structures increased with the lowering of pressure and structure melting up to  $\sim 5$  eV [189] or even  $\sim 50$  eV [384] at minimal pressures examined in these works. This “anomalous heating” of the dust component in plasmas indicates some source of energy which is effectively transferred into the kinetic energy of the dust particles. Several possible mechanisms of anomalous heating were considered in the literature: Stochastic fluctuation of the particle charge and energy gain in an external electric field [132,133,135,137,387] (see also Section 8.2), heating due to ion focusing (wakes) [238,239,340] (see also Sections 8.4 and 9.4.4), spatial variations of the particle charge [233,473,236] (see also Section 8.3), and the ion streaming instabilities [305,338] (see also Section 9.4.4).

Structural properties of strongly coupled dusty plasmas were investigated in [11–14,19,188,385,386]. Crystalline structures such as bcc, fcc, and hcp, as well as their coexistence, were found for certain plasma and particle parameters. Also, the vertically aligned hexagonal lattices—when particles form consecutive hexagonal layers in the horizontal direction, but vertically they are aligned in strings—were observed. Such lattices can exist because the lower particles are attracted by the wake potentials of the upper ones, so that this attraction overcomes the mutual particle repulsion (see Section 5.2). The vertically aligned lattices are quite common for ground based experiments and are usually formed by particles of a few microns in diameter. For smaller particles the wake effect presumably becomes too weak, so that the particles form conventional close-packed crystals.

For the quantitative analysis of the ordered structures of particles observed in the experiment, it is common to use the following three characteristics [385]: the pair correlation function, the bond-orientational correlation functions (rotational invariants) and the structure factor. The pair correlation function  $g(r)$  measures the translational order in the structure of interacting particles and represents the probability of finding two particles separated by a distance  $r$  [for a gas of uncorrelated particles,  $g(r) = 1$ ]. For the case of an ideal crystal,  $g(r)$  is a series of delta functions (peaks) whose positions and heights depend on crystal structure type. The bond-orientational correlation functions measure orientational order in the structure. For two-dimensional systems, the bond-orientational order (correlation function)  $\psi_6(r)$  is defined in terms of the nearest-neighbour bond angles with respect to an arbitrary axis. For a perfect hexagonal structure  $\psi_6(r) \equiv 1$ , while for other phases  $\psi_6(r)$  decays with distance. Finally, the static structure factor  $S(k)$  measures order in the structure, similar to  $g(r)$ . It is connected to the pair correlation function via the Fourier transform (see, e.g., [376]:  $S(k) = 1 + n_d \int d\mathbf{r} [g(r) - 1] e^{-i\mathbf{k}\cdot\mathbf{r}}$ ). These characteristics are applied for the analysis of static properties of the highly ordered dust particle structure by [385]. In the same work, a comparison between the obtained quantitative results and predictions of the KTHNY 2D melting theory is drawn.

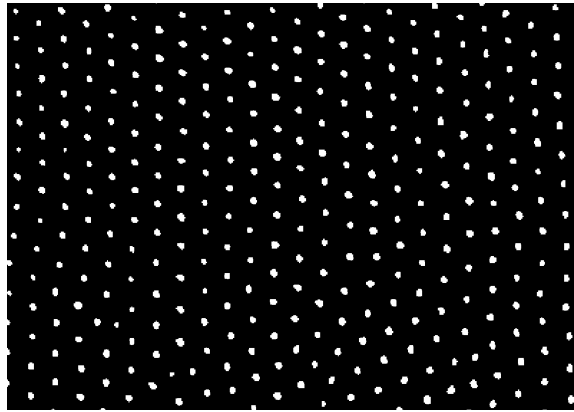


Fig. 34. Top view on a hexagonal structure formed in the sheath region of a rf discharge (fragment of one layer is shown, containing 392 particles of  $6.9\text{ }\mu\text{m}$  diameter over the area  $6.1 \times 4.2\text{ mm}^2$ ) [387]. Horizontally, the particles are highly ordered and form a hexagonal lattice. Vertically, they are settled strictly below each other, due to the ion wake effect (see text).

### 10.3.1. Melting

Let us discuss in more details the process of dusty plasma crystal melting induced by reducing pressure. Typical image of a quasi 2D plasma crystal obtained in the sheath of a rf discharge is shown in Fig. 34 [387]. We illustrate major features of the melting of such crystals with the results of a classical experiment by Thomas and Morfill [189]. The melting was initiated by the continuous lowering of pressure in krypton plasma, from  $p = 42\text{ Pa}$ , where the stable ordered state of dust particles existed, to  $p = 22\text{ Pa}$ , for which the system lost any order and formed a gaseous state. The pair correlation function, bond-orientational correlation function, and kinetic energy of the dust system were measured while lowering the pressure.

From this analysis, the four “states” during the melting transition were identified. The first, the “crystalline” state, is characterized by the conservation of the crystalline lattice in the horizontal plane and chain formation in the vertical direction as the pressure weakly reduced from the initial value. The particles in the lattice experience thermal oscillations and highly occasional large-amplitude nonthermal oscillations—mostly in the vicinity of lattice defects. The second, the “flow and floe” state, is characterized by the coexistence of islands of ordered crystalline structure (floes) and systematic directed particle motion (flows). In this state, the translational and orientational orders decrease significantly and occasional vertical particle migrations to other lattice planes are possible. Particle thermal motion still corresponds to room temperature,  $v_{T_d} \simeq 0.2\text{ mm/s}$ , while directed flow velocities are typically half of this. The third, the “vibrational” state, is characterized by some increase in orientational order and diminishing flow regions. However, isotropic particle vibrations with increasing amplitudes appear. Kinetic energy and vertical migrations of particles increase and the translational order continues to decrease. Finally, in the fourth, the “disordered” state, there is not any translational or orientational order. The particles migrate freely both in the horizontal and vertical planes. The particle kinetic energies are hundreds of times greater than the neutral temperature ( $T_d \simeq 4.4\text{ eV}$ ). Fig. 35 shows the quantitative results for correlation functions  $g(r)$  and  $g_6(r)$  during melting.

Note that the transition of quasicrystalline structures to fluid states is also observed in dc discharges. This occurs either by lowering the pressure or increasing the discharge current, as was obtained in Ref. [26].

We should note once again that, strictly speaking, theoretical concepts of 2D and 3D melting are not applicable to describe these experiments, because the observed structures are essentially anisotropic—sometimes they are referred to as “ $2\frac{1}{2}$ -dimensional” crystals. This is not solely because of the wakes, but also due to the fact that the electric forces exerted in the sheath turn out to be comparable with the interparticle forces. Therefore, the structures become very compressed and inhomogeneous in the vertical direction. Hence, the experimental investigation of a monolayer crystal melting, as well as experiments on phase transitions in 3D systems under microgravity conditions, might be much more valuable.

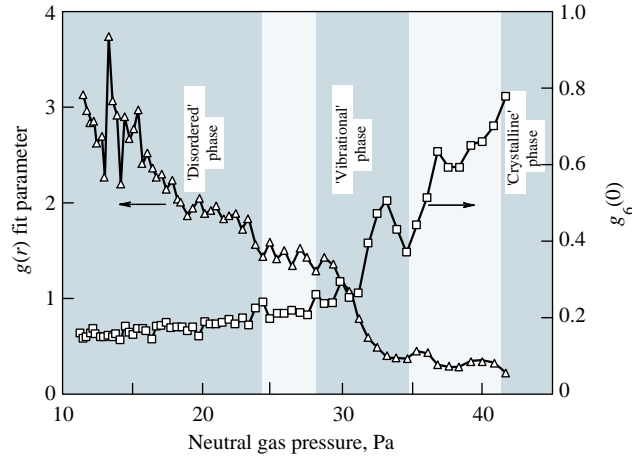


Fig. 35. The evolution of translational (triangles) and orientational (squares) order parameters during the phase transition as a function of neutral gas pressure [189]. Three regions are shaded: the “crystalline” phase at pressure  $\simeq 42$  Pa; the “vibrational” phase at  $\simeq 32$  Pa; and the “disordered” phase at  $\simeq 24$  Pa. The intermediate “flow and floe” state occurs at  $\simeq 36$  Pa.

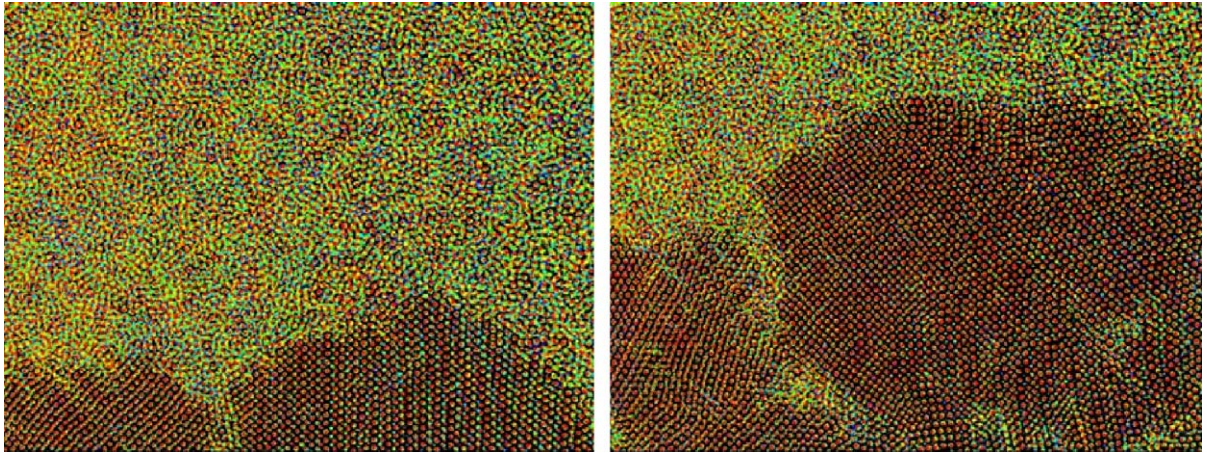


Fig. 36. The crystallization front (side view) at two different moments about 16 s apart from each other, observed on Earth in experiments with small particles of  $1.28 \mu\text{m}$  diameter in argon rf discharge at 23 Pa [388]. Each image is a superposition of 10 consecutive video frames (about 0.7 s), particle positions are colour-coded from green to red, i.e., cooler particles appear redder, hotter are multicoloured.

### 10.3.2. Crystallization

We illustrate the crystallization process in complex plasmas with the recently reported results obtained on the ground with small ( $1.28 \mu\text{m}$  diameter) particles [388]. First, the particles were brought into a disordered liquid-like phase (by a short pulse of increased discharge power). Afterwards, the system starts recrystallizing. Usually, this results in a homogeneous nucleation, but sometimes this occurs in the form of a *crystallization front*. Fig. 36 shows evolution of the crystallization front with the color-coded particle traces, which gives an impression of the particle temperature. The front is fairly narrow (about 3–4 interparticle distances) and has a well developed fractal structure. The temperature drop across the front is a factor of 2 or 3. This indicates that the observed crystallization is strongly nonequilibrium. One can also see the interface between different crystalline domains, which has a narrow width (2–3 lattice planes) and a substantially higher temperature than the crystal domains themselves—direct evidence for interfacial melting. MD simulations reveal all the qualitative features observed in the experiments.

A very important feature of the crystallization process is that the relaxation of the particle energy proceeds much more slowly than in weakly coupled states (when the energy of each particle decays independently due to neutral gas



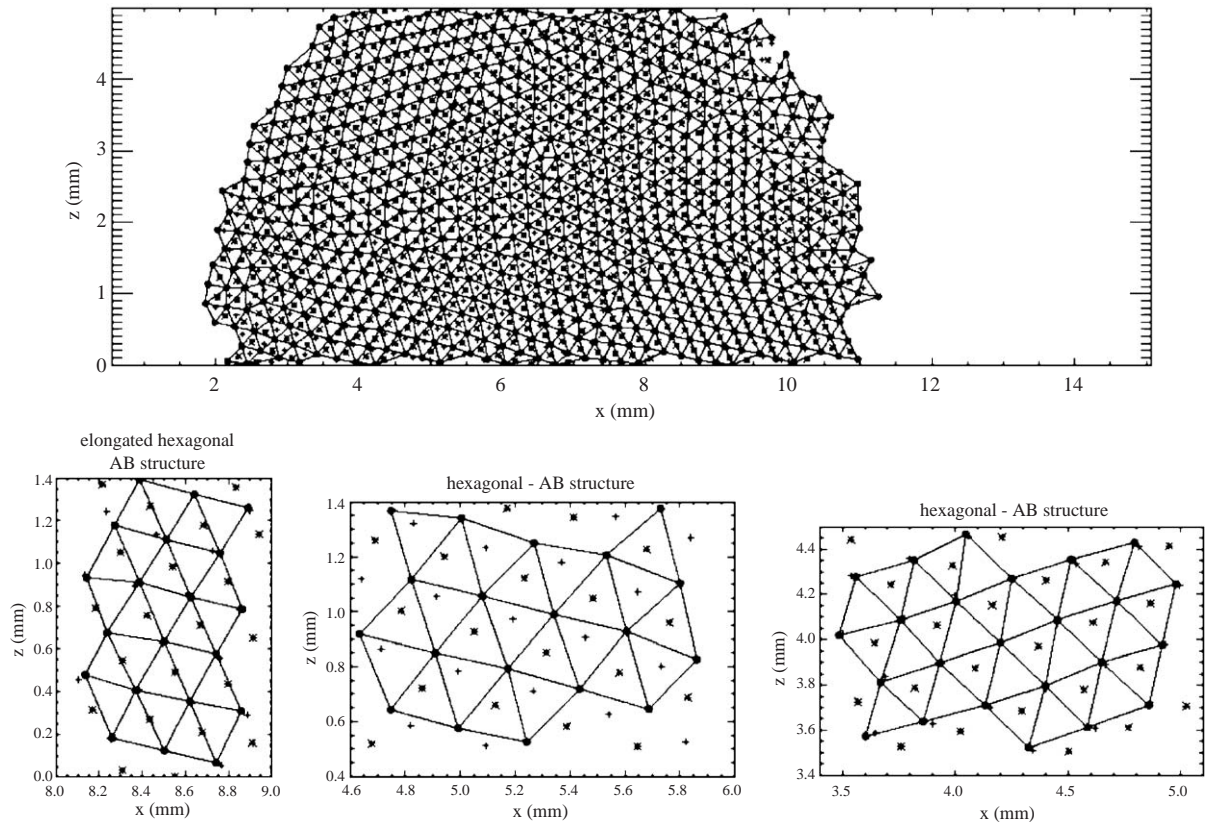


Fig. 37. Plasma crystal observed under microgravity conditions with the PKE-Nefedov experiment [21]. The symbols denote particle positions in three consecutive lattice planes. Different kinds of crystal domain can be distinguished, as presented in the lower part of the figure: In the left-hand plot the bcc 110 lattice plane is shown, the middle panel presents the fcc 111 lattice plane, and the right-hand one represents the hcp 111 lattice plane. In some regions intermediate stages are also observed.

friction) [21,388]. Transition from one metastable crystalline state to another, lower energy level can take minutes. MD simulations show that the decay of kinetic energy occurs over much longer time than that estimated from neutral gas drag. Presumably, this is because most of the energy is stored in the mutual electrostatic coupling, and each local transition between neighbouring energy levels releases only a small fraction. In some cases, even when the system reaches overall lattice equilibrium, it can remain noisy—caged particles oscillate with rather low frequencies. This can be due to the possible existence of a few shallow metastable states of the same levels (separated by potential hills of the order of the particle thermal energy). Then the whole system can continuously jump from one state to another, yet keeping the same type of lattice.

The nucleation and the subsequent growth processes in complex plasmas looks very similar to conventional crystallization in overcooled media (e.g., in semiconductors, see Refs. [389,390]). Therefore, space- and time-resolved investigation of elementary processes accompanying the nucleation and growth of plasma crystals can be very useful for understanding some basic microscopic processes in liquid–solid phase transitions.

As regards the crystallization experiments performed under microgravity, we mention the results obtained onboard the ISS with the PKE-Nefedov setup [21]. The vertically aligned lattices, usually observed in ground-based experiments with plasma crystals suspended in the sheath, have not been observed in microgravity conditions. The particle chains are believed to form due to the ion wakes downstream of the particle. In microgravity, however, particles occupy the bulk region of the discharge where (relatively weak) ambipolar fields cannot induce the wake formation. Therefore, in microgravity experiments the interaction between particles is almost isotropic.

Instead of the vertically aligned structures, the coexistence of “conventional” crystalline domains—bcc, fcc, and hcp—was observed in microgravity, as shown in Fig. 37. The presence of the first two lattice types might indicate

that the system is close to the corresponding phase equilibrium curve in the phase diagram. A hcp phase, however, is a metastable state in Yukawa systems—it cannot exist when the final (ground) state is achieved. In the experiments, small local fluctuations of the particle density and temperature might result in the transition from the equilibrium fcc to a hcp phase. These fluctuations can be induced, for instance, by external excitation caused by the vortex motion.

Another possible reason for the hcp domains to appear is the particle size dispersion. The size dispersion implies a charge dispersion which, in turn, leads to an enormous number of possible particle configurations (and thus lattice energy levels) within a given lattice type. And, of course, the existence of the hcp domains may simply indicate that the actual interaction potential is not of the Yukawa form.

The results obtained so far in experiments on the liquid–solid phase transitions in complex plasmas look quite promising. In the future, major efforts should be put into the detailed investigations of kinetics of the first order phase transitions, observing melting and crystallization (annealing) of complex plasmas as well as transitions between different lattices domains. Similar to the investigation of hydrodynamic instabilities discussed in the next section, the major objective here is to identify the mechanisms responsible for the onset of the transitions on a “quasimolecular” level. Careful experiments along with molecular dynamics simulations can help us to understand the microscopic picture and the hierarchy of the processes that govern the transitions. This will also allow us to specify the phase diagram in the vicinity of the liquid–solid phase transition. The microscopic processes of particular interest should be the relaxation of the particle energy and onset of nucleation in the beginning of the crystallization, criteria for the homogeneous nucleation or the crystallization in the form of a front, particle accommodation at the interfaces between different phases, threshold for nonequilibrium amorphous solidification (quenching), and metastable transitions in solids.

## 11. Fluid behaviour of complex plasmas

### 11.1. Transport properties

The most fundamental quantities characterizing the dynamic behaviour of the dust subsystem are the diffusion coefficient  $D_d$  and the viscosity coefficients, in particular—the shear viscosity  $\eta_d$ . They can be determined using the Green–Kubo formulas [391]. For instance, the diffusion coefficient is  $D_d = \frac{1}{3} \int_0^\infty H_v(t) dt$ , where  $H_v(t) = \langle \mathbf{v}(t) \mathbf{v}(0) \rangle$  is the velocity autocorrelation function, and the shear viscosity is  $\eta_d = T_d^{-1} \int_0^\infty H_\sigma(t) dt$ , where  $H_\sigma(t) = \langle \sigma(t) \sigma(0) \rangle$  is the autocorrelation function for the microscopic shear stress. The transport coefficients can be directly deduced from MD simulations (e.g., by using the Green–Kubo formulas). Diffusion in Debye–Hückel systems has been studied numerically in Refs. [337,372–374,381,392–394]. The viscosity coefficients have been determined numerically in Refs. [321–323]. It is important to realize that complex plasmas can be in a broad range of “dynamical states”—from one-phase fluids to particle tracers, as discussed in Section 6.3 (see Fig. 20). Therefore, the transport properties of the dust subsystem are determined not only by the mutual grain interaction, but also by neutral gas friction.

The standard diffusion theory is based on the assumption that  $\int_0^\infty H_v(t) dt < \infty$ . This excludes an important class of processes called “fractional Gaussian noises”, which leads to particle trajectories that are classified as “fractional Brownian motion” [395]. For these processes the mean square displacement scales as  $\propto t^{2H}$ , where  $H$  is called the “Hausdorff exponent” [396]. For  $H = 1/2$  we have standard diffusion, for  $H < 1/2$  the resulting motion is subdiffusive, and for  $H > 1/2$  the motion is superdiffusive [395]. Standard diffusion theory also fails if the velocity probability distribution function is non-Gaussian but has algebraic tails, so that the variance  $\langle \mathbf{v}(t)^2 \rangle$  diverges [397–399]. Even for a Markovian velocity process the resulting motion can be superdiffusive due to the presence of very large velocities (Lévy flights).

A classical discussion of all the aspects of anomalous diffusion mentioned above, with numerous physical examples, can be found in Ref. [400]. Anomalous diffusion can be described in the framework of fractional kinetics [401,402]. The solutions of fractional diffusion equations, like solutions of standard diffusion equations, yield the probability density of finding a particle at a given position, at a given time. This can be linked to the experiments as particle tracking data allow not only to determine the shape of the (non-Gaussian) distribution but also to follow its evolution in time (“coarse graining” technique [403]).

Statistical properties of particle transport in strongly coupled quasi-2D dusty plasma systems were addressed in Refs. [403–407]. These systems are 2D in the sense that they consist of several layers, but the motion is restricted to the horizontal dimensions. Superdiffusion was observed on short time scales up to 10–20 s due to collective (vortex) motion



[404] or due to cooperative fast particle cluster excitations [406], but normal diffusion was observed on longer time-scales. It was shown that the excitations of fast particles results in non-Gaussian velocity distribution and cooperatively excited cites appear in form of clusters with power-law size distributions [406]. In Refs. [404,406] the transition from superdiffusion to normal diffusion was observed to occur at time scales when the standard deviation of the particle displacement approaches the mean interparticle distance. Ratynskaya et al. [403] reported superdiffusive particle transport on time scales for which particles diffuse several interparticle distances and the self-similar nature of the particle dynamics was confirmed by a combination of different statistical analyses. In this work the position distribution was shown to be non-Gaussian with exponential tails. The development and propagation of lattice defects constitute essential elements in the particle transport. In Ref. [407] structural defects in the hexagonal lattice were identified and tracked in space and time.

So far, there have been only two experiments reported recently on the first attempts to measure the shear viscosity in liquid complex plasmas [324,408]. The particles were pushed by a laser beam and the magnitude of the viscosity coefficient was then deduced from the resulting profile of the velocities (e.g., by applying the Navier–Stokes equation with the gas friction term [324]). The experiments were performed under quite different conditions and yielded very different values of the kinematic viscosity,  $\eta_d/m_d n_d \sim 10^{-2} \text{ cm}^2/\text{s}$  in Ref. [324] (which is compatible with the kinematic viscosity of water) and  $\sim 1 \text{ cm}^2/\text{s}$  in Ref. [408]. Also, the authors of Ref. [324] argued that both the magnitude and a qualitative behaviour of the measured viscosity are in agreement with the results of numerical simulations [321–323]. One should bear in mind, however, that strongly coupled complex plasmas are apparently non-Newtonian liquids and, hence more sophisticated analysis will be required in future experiments.

It is worth noting that one should be very careful in using the numerically calculated transport coefficients, in particular—in attempts to apply these results directly for the analysis of experiments: there are a number of unresolved issues, e.g., plasma anisotropy, long-range interactions including shadowing effects, the effect of external forces and/or boundary conditions, particle charge variations, etc. which still have to be addressed.

## 11.2. Hydrodynamic instabilities

An interesting question is, of course: How relevant are liquid plasmas for the study of conventional liquids? The implication is clear—if they are relevant, this opens up a completely new approach to nanofluidics, the kinetic approach, which will then have the major impact on the field. In fact, one of the interesting aspects of complex plasmas (which was discussed in details in Section 6.3) is that although they are intrinsically multiphase systems, the rate of momentum exchange through binary (electrostatic) collisions between the microparticles can exceed that due to interactions with the neutral gas significantly—thus providing an essentially one-phase system (e.g., fluids) for kinetic studies. Moreover, comparison in terms of similarity parameters (Reynolds and Mach numbers) suggests that liquid complex plasmas are remarkably like conventional liquids, e.g., water—observed at the molecular level [191,324,409]. This suggests that liquid plasmas can indeed serve as a powerful new tool for investigating fluid flows on (effectively) nanoscales, including the all-important transition from collective fluid behaviour to individual kinetic behaviour (see Section 12.2), as well as nonlinear processes on scales that have not been accessible for studies so far. Of particular interest could be kinetic investigations of instabilities in fluids and the transition to turbulence (e.g., Ref. [410]). Individual particle observations can provide crucial new insights—e.g., whether the basic hydrodynamical instabilities (Kelvin–Helmholtz, Rayleigh–Taylor, Tollmien–Schlichting, etc.) will survive on interparticle distance scales, and whether the transition to turbulence can be seen at the particle (kinetic) level.

To illustrate fluid properties of complex plasmas let us consider examples of highly resolved shear flows generated in a rf discharge chamber [191] and shown in Fig. 38. In different regions of the microparticle cloud different flow topologies are observed, with the (average) flow lines being either straight (a) or curved (b). The lower part of the system is in the crystalline state at rest. The observations suggest that the width and the structure of the transition (mixing) layer strongly depends on the geometry. For the planar flow the crystalline interface is remarkably smooth, with the flow along a particular (crystalline) monolayer. The trajectories of individual flowing particles experience only weak deflections and the overall flow appears to be stable and laminar. In contrast, the curved flow interface has a curious “rough” structure, the flow is unstable and not laminar, a “mixing layer” is formed between the flowing regime and the crystalline region—this is where momentum transfer takes place. It is also apparent that the mixing layer becomes unstable at the individual particle level. The microscopic driving mechanism for the instability seen in Fig. 38(b) is identified as the centrifugally driven Rayleigh–Taylor instability. Analysing a whole sequence of such

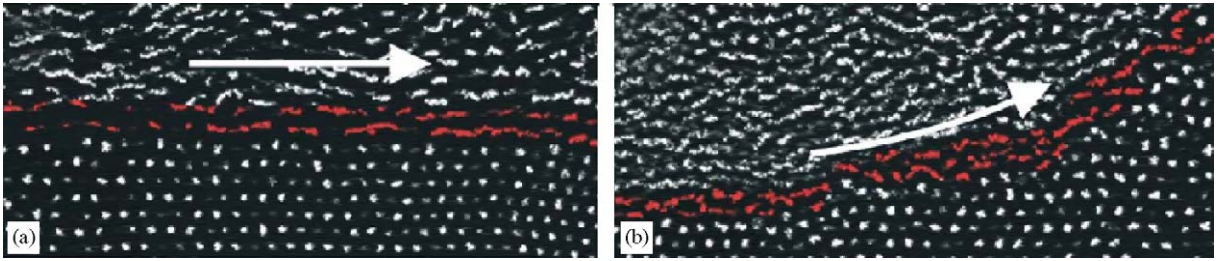


Fig. 38. Two examples of highly resolved complex plasma flows [191]. Experiments were performed in argon rf discharge with particles of diameter  $1.28\ \mu\text{m}$  at neutral gas pressure 22 Pa. The figures show (a) a shear flow over a flat surface plasma crystal and (b) a flow over a curved surface plasma crystal. Note the small angle perturbations in the particle trajectories in (a), and the considerably larger scattering in the curved flow in (b). The separation between the particles is of the order of  $100\ \mu\text{m}$ , the flow velocity is (a)  $\simeq 1\ \text{mm/s}$  and (b)  $\simeq 0.7\ \text{mm/s}$ .

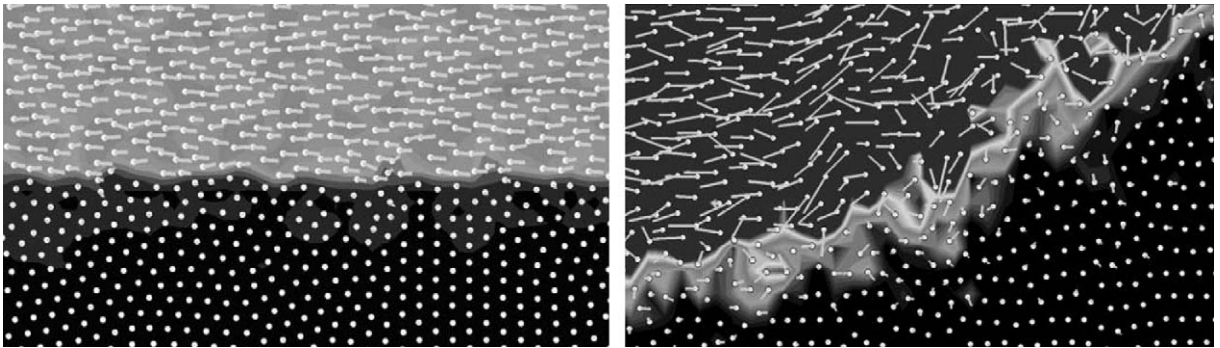


Fig. 39. Numerical simulations of the shear flows observed in experiments shown in Fig. 38. The simulations were performed for the plasma parameters relevant to the experiment.

images, one can quantify this perturbation in two ways—the fraction of interpenetrating particles, and the fraction of particles undergoing large angle collisions in the surface layer. For the straight flow, the quantities are (almost) 0%, and approximately 5%, for the curved flow approximately 5% and 30%. This can be understood kinetically in terms of the higher collision frequency with smaller impact parameter due to particle inertia at a curved surface. This has also been confirmed by numerical simulations as shown in Fig. 39 (particle velocities are grey-scaled, increasing from black to white). The simulations were conducted for similar geometry and flow conditions as in the experiments. The topology of the mixing layer found in the simulations corresponds closely to the measurements, which supports our kinetic interpretation.

Another example of the hydrodynamic behaviour of liquid complex plasmas [409] is shown in Fig. 40. Particles were flowing around an “obstacle”—the void of size  $\sim 100\ \Delta$  (equivalent to  $\sim 100$  “molecular” sizes). One can see stable laminar shear flow around the obstacle, the development of a “wake” exhibiting stable vortex flows, and a mixing layer between the flow and the wake. The mixing layer is observed to be quite unstable at the kinetic level, with instabilities becoming rapidly nonlinear. The width of the mixing layer grows monotonically with distance from the border where the laminar flow becomes detached from the obstacle. The growth length scale is of the order of a few  $\Delta$ , i.e., much smaller than the hydrodynamic scales  $n_d(dn_d/dx)^{-1}$  or  $u_d(du_d/dx)^{-1}$ , which would be expected macroscopically in fluids and refer to the Rayleigh–Taylor or Kelvin–Helmholtz instability, respectively. This rapid onset of surface instabilities followed by mixing and momentum exchange at scales  $\sim \Delta$ , i.e., the smallest interaction length scale (effective particle size) available, is not consistent, therefore, with conventional macroscopic fluid instability theories. While this could not rightfully be expected at the kinetic level, it clearly points to new physics and, possibly, a hierarchy of processes that is necessary to describe interacting fluid flows: first, binary collision processes provide particle and momentum exchange on kinetic scales (a few  $\Delta$ ), then collective effects (due to the correlations defining fluid flows) take over and “propel” this “seed” instability to macroscopic scales.

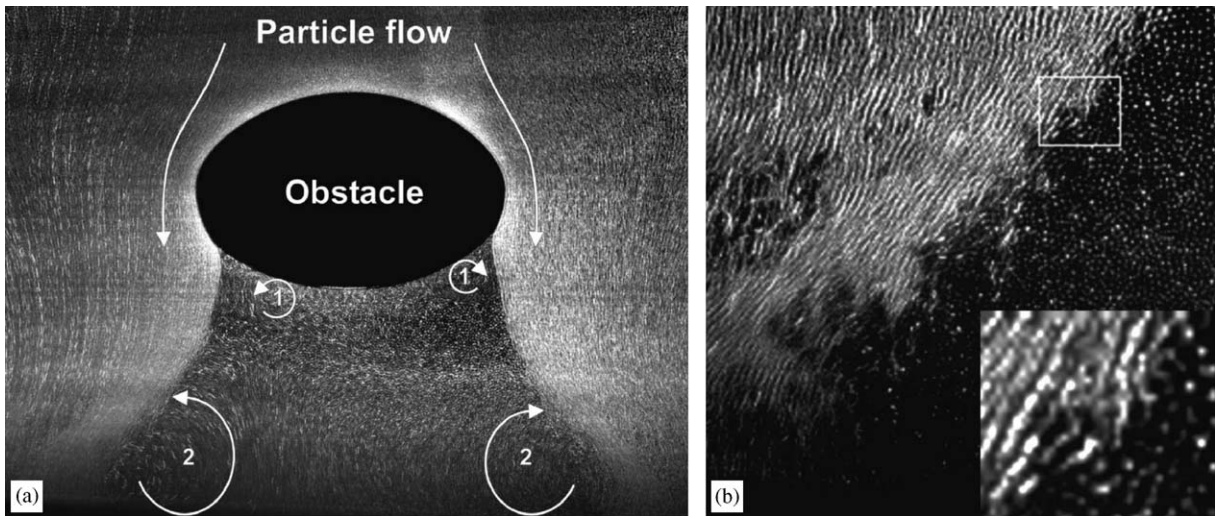


Fig. 40. (a) Topology of the particle flow around the void [409]. Experiments were performed in argon rf discharge with particles of diameter  $3.7\ \mu\text{m}$  at neutral gas pressure 64 Pa. The flow leads to a compressed laminar layer, which becomes detached at the outer perimeter of the wake. The steady vortex flow patterns in the wake are illustrated. The boundary between laminar flow and wake becomes unstable, a mixing layer is formed which grows in width with distance downstream. The system is approximately symmetric around the vertical axis, the vortices are tori and the wake has the shape of a flaring funnel (exposure time 1 s). (b) An example of the mixing layer—an enlargement of the left side of the flow regime shown in (a) (exposure time 0.05 s). The points (lines) represent traces of slow (fast) moving microparticles.

It is noteworthy that even for the planar flow the interface can be unstable, due to Kelvin–Helmholtz instability [191]. This has been observed in the simulations, but for a rather narrow shear velocity range. This can be understood as follows: first, the Reynolds number should exceed a certain threshold to trigger the instability (since the viscosity is finite) and hence there exists a lower velocity limit. Second, the collisional cross section of particles falls off rapidly with velocity ( $\propto u_d^{-4}$ ) which leads to a corresponding decrease in the momentum transfer efficiency. Hence a Kelvin–Helmholtz-type instability must be confined to a narrow flow velocity range. Whilst this principal argument appears to be well understood, there are some essential elements still unclear, viz. the kinetic trigger of the instability and the velocity range, quantitatively, where the flow energy can get converted to unstable particle motion.

## 12. Onset of cooperative phenomena in complex plasmas

Complex plasmas allow us to investigate mesoscopic systems at the “molecular level”, by observing the evolution of the dynamical and structural properties as the number of charged grains in the system gradually increases. A promising direction of study is the physics of crystalline and liquid systems in the limit where the correlation scales are comparable to or even larger than the system scales. Below we outline the progress achieved so far on these topics.

### 12.1. Coulomb clusters

Coulomb clusters are the ordered systems which consist of a finite number of microparticles interacting via a repulsive potential and confined by external forces (e.g., of electrostatic nature). In many cases, the interaction potential is believed to be of the Debye–Hückel (Yukawa) form, and therefore such systems are also called “Yukawa clusters”. The difference between the dust clusters and the dust crystals is rather conditional: both systems in fact consist of a finite number of particles. The term “clusters” is usually reserved for systems with the number of particles  $N \lesssim 10^2\text{--}10^3$ , while larger formations are referred to as “crystals”. A more precise definition of clusters would be the ratio of the number of particles in the outer shell to the total number of particles in the system. For crystals, this ratio should be small. Similar systems can be formed, for instance, in nonneutral plasmas in Penning or Paul traps [411,412], where the vacuum chamber is filled with the ions, as well as in colloidal solutions with macroscopic charged particles [413]. Examples



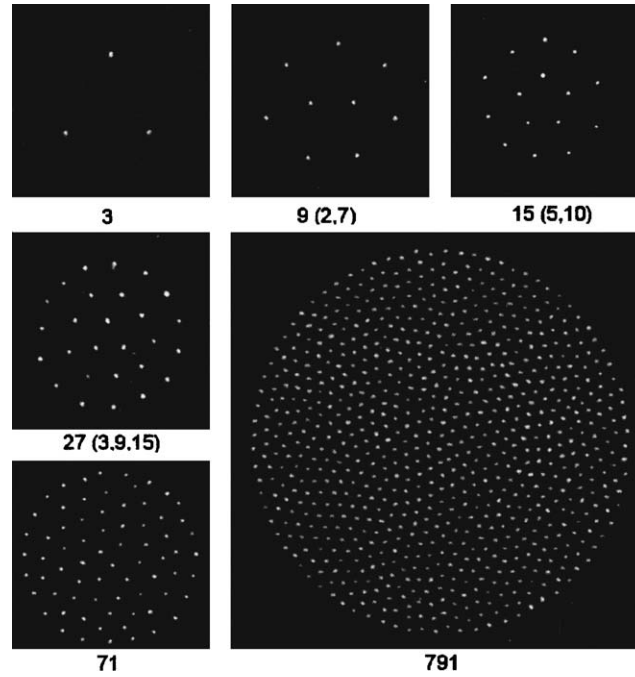


Fig. 41. Video images of typical Coulomb cluster structures consisting of different numbers of particles (the scales are not the same for the pictures, typical interparticle spacing is between 0.3 and 0.7 mm) [426].

of two-dimensional Coulomb clusters are electrons on the surface of liquid He [414] and electrons in quantum dots [415]. The distinctions between systems are mainly due to different types of interaction potential and different forms of confining potential.

Historically, clusters consisting of repulsive particles in an external confining potential were first investigated with the use of numerical modelling (mostly by MC and MD methods). Taking into account the possibility of applying the simulation results to dust clusters, we mention here Refs. [416–425]. Most simulations were performed for two-dimensional clusters in an external harmonic (parabolic) potential. Such a configuration is usually realized in ground-based experiments with dusty plasma in gas discharges. The simulations show that for a relatively small number of particles in the cluster the “shell structure” is formed with the number of particles  $N_j$  in the  $j$ th shell ( $\sum_j N_j = N$ ).

At zero temperature, the unique equilibrium configuration  $(N_1, N_2, N_3, \dots)$  exists for a given particle number  $N$ . Such configurations are analogous to the Mendeleev’s Periodic Table, the structure of which depends on the shape of the interaction potential, confining potential, and their relative strengths. At finite temperatures, metastable states with energies close to the ground state can also be realized.

The first experimental investigation of dust clusters was reported in Ref. [426]. The experiment was performed in the sheath of an rf discharge. A hollow coaxial cylinder of 3 cm in diameter and 1.5 cm in height was put on the bottom electrode to confine the dust particles. Clusters with a number of particles from a few up to 791 were investigated. Fig. 41 shows images of typical clusters with different numbers of particles, and Fig. 42 demonstrates a series of the observed configurations. For large  $N$ , the inner particles arrange themselves into a quasiuniform hexagonal structure, whereas near the outer boundary particles form several circular shells. The mean interparticle separation increases up to about 10% from the centre to boundary.

In Refs. [202,427,428], the rotation of dust clusters around the symmetry axis was studied. In the first work, the cluster rotation was caused by the laser pressure. Both the rigid body and the differential (intershell) rotation had been observed. In two other works, the cluster rotation was initiated by the presence of the magnetic field parallel to the cluster axis of symmetry (see Section 13). The rotational frequency was found to be linear with the weak magnetic field, although it saturates at moderate magnetic field strength [428], and it is inversely proportional to the field in the strong field limit [202].

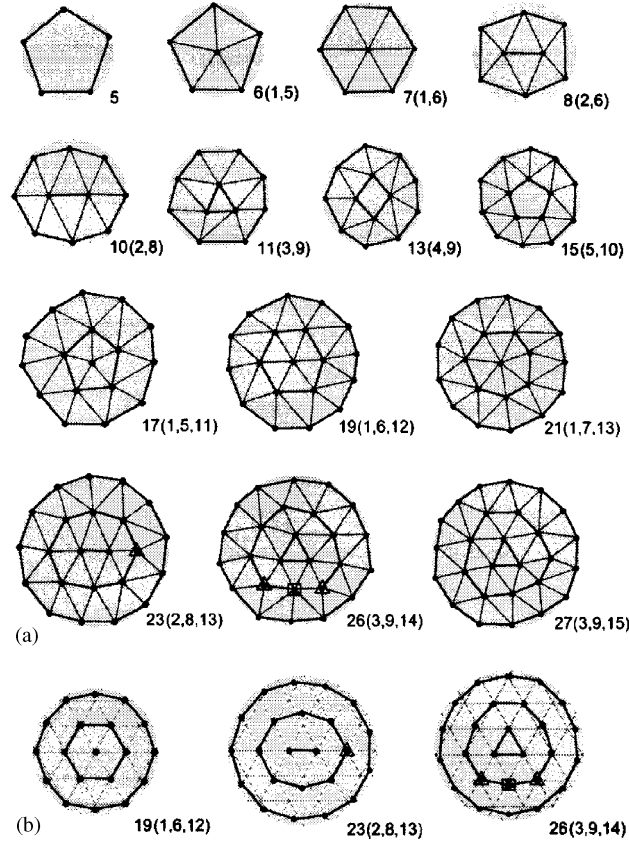


Fig. 42. Typical shell configurations of several dust clusters composed of different numbers of particles [426].

For two-dimensional clusters consisting of  $N$  particles and confined radially in a harmonic potential trap (characterized by the confinement frequency  $\omega_0$ ), there exist  $2N$  normal modes,  $\omega_\ell$  with  $1 < \ell < 2N$ . The normal modes are the eigenvalues of the cluster dynamical matrix, and the corresponding eigenvectors define the mode oscillation patterns [418]. For pure Coulomb interaction (lattice parameter  $\kappa$  is equal to zero) there are three normal modes that are independent of the particle number  $N$ : (i) the rotation of the entire cluster around the centre of the confinement at  $\omega = 0$ , (ii) the (twofold degenerate) sloshing oscillation of the centre of mass of the cluster in the horizontal potential well at  $\omega = \omega_0$ , and (iii) a coherent radial oscillation of all particles, the so called breathing mode, at  $\omega = \sqrt{3}\omega_0$ . For screened interaction ( $\kappa > 0$ ), the frequency of the first two modes is unaffected since they do not involve a relative particle motion. In contrast, the frequency of the breathing mode and all other modes becomes dependent on  $\kappa$  and on the particle number  $N$ .

The oscillations of particles in Coulomb clusters were investigated in [418,429–432]. To illustrate the experiments, we discuss the recent work of Melzer [431], where the normal modes of 2D Coulomb clusters of  $N = 1 - 145$  particles trapped in the sheath above the lower rf electrode were studied. The normal modes were obtained from the thermal Brownian motion of the particles around their equilibrium positions in the cluster. This method extends the thermal excitation technique by Nunomura et al. [256] (developed for extended 2D lattices) to the case of Coulomb clusters.

In Fig. 43a the particle trajectories in  $N = 3$  cluster are shown. One can see that the thermal fluctuations of the microspheres around their equilibrium positions are small, but they are nevertheless sufficient to determine the mode spectrum. The six eigenmodes of this cluster calculated for the Yukawa potential are depicted in Fig. 43b. There are the following modes: the breathing mode ( $\ell = 1$ ), rotation of the entire cluster ( $\ell = 2$ ), a twofold degenerate “kink” mode ( $\ell = 3, 4$ ), and the two sloshing modes ( $\ell = 5, 6$ ). The mode frequencies  $\omega_\ell^2$  (in units of  $\frac{1}{2}\omega_0^2$ ) are also indicated for  $\kappa = 0$ . For  $\kappa > 0$  the oscillation pattern of the eigenmodes is unchanged. Their frequencies, however, decisively depend

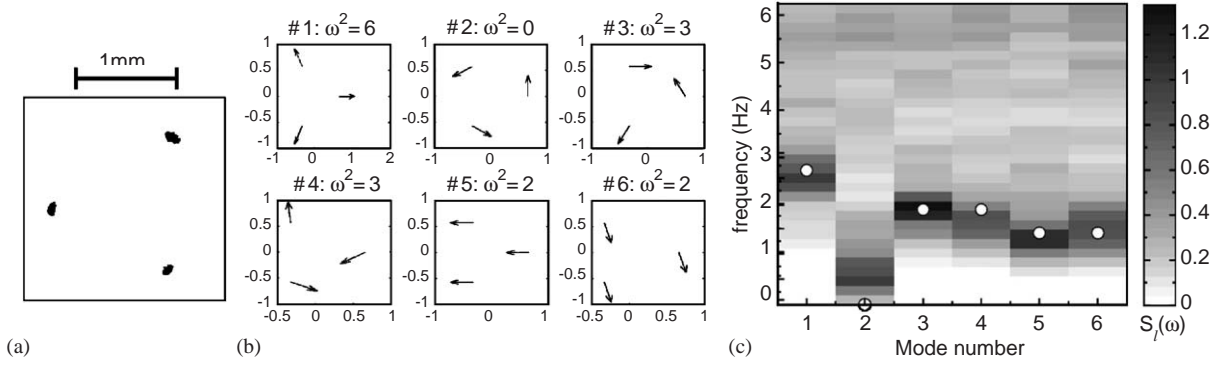


Fig. 43. Normal mode spectrum of a three-particle cluster [431]. (a) Particle trajectories over 1 min. (b) Six normal modes of the cluster, the mode frequencies  $\omega_\ell^2$  are normalized to  $\frac{1}{2}\omega_0^2$ . (c) Measured mode spectrum of the modes. The spectral power density is shown in grey scale, the circles correspond to the calculated mode frequencies.

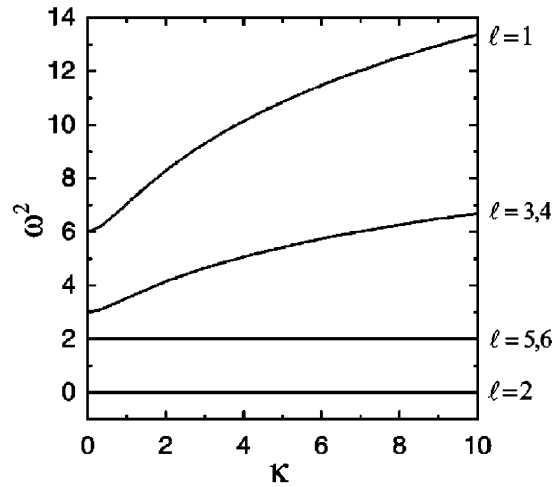


Fig. 44. Calculated mode frequencies of the three-particle cluster as a function of screening strength  $\kappa$  [431]. The modes are the breathing mode ( $\ell = 1$ ), the cluster rotation ( $\ell = 2$ ), the kink modes ( $\ell = 3, 4$ ), and the sloshing modes ( $\ell = 5, 6$ ).

on  $\kappa$  (see Fig. 44). Obviously, the cluster rotation and the sloshing mode are independent of  $\kappa$ . The frequencies of the kink mode and the breathing mode increase with  $\kappa$ .

The lowest-frequency mode (LFM) had been identified for different cluster sizes. For small particle numbers the intershell rotation was shown to be the LFM, whereas for larger clusters the formation of vortex–antivortex pairs were observed. This behaviour is generally within the theoretical expectations for pure Coulomb systems [418]. Analysis of the highest-frequency modes (HFM) had shown that for small clusters, the breathing mode with a coherent radial motion of all particles is the HFM. For larger clusters, modes with a relative three-particle oscillation localized in the centre of the cloud provide the highest frequencies. The mode-integrated spectrum shows two broad maxima which are explained from “shear-like” or “compression-like” modes. The transition from finite number to crystal-like properties was observed to occur around  $N = 12$  particles.

Also, we briefly mention results of recent experiments [335,386] where the three-dimensional clusters were observed. In Ref. [335], the experiments were performed in the adaptive rf electrode chamber (the rf electrode is an assembly of small pixels, each having an independent control of the rf voltage [433]) filled with argon at pressure 40–80 Pa, with plastic particles of 6.8  $\mu\text{m}$  diameter. By a fine adjustment of the rf applied to a dc-grounded pixel it was possible to control the number of particles in the cluster and also its shape. The number of particles varied from 4 up to about 200. In the equilibrium positions the vertical confinement is provided by the electric field of the double layers/striations



combined with suitable conditions for the charging. It is unclear if the horizontal confinement is due to plasma pressure or by internal forces among the cluster components, or by ion drag. More work is certainly needed in order to explain the formation of such structures. In another experiment [386], the so-called “Coulomb balls”—spherical particle clouds, in which hundreds or thousands of identical plastic spheres of 3.4  $\mu\text{m}$  diameter are arranged in clearly separated crystalline shells—were observed to form in a rf discharge at pressures 50–150 Pa. The particles were levitated by thermophoretic forces, which is accomplished by heating the lower plate, and the radial confinement was provided by a short upright glass tube. The highest order was observed at the outer shells, whereas in the centre the particles were in a liquid (amorphous) state with no significant orientational order.

## 12.2. Nanofluidics

The behaviour of ultrathin liquid confined in a mesoscopic gap is a fundamental problem in nanoscience and technology. As the gap width goes down to the molecular scale, structure and transport properties deviate from the bulk liquid, under the effects of discreteness, finite boundary, and thermal fluctuation. For instance, the formation of a layered structure next to the boundary and the sluggish flow with large fluctuation and nonlinear mean velocity response to the external stress have been observed [434–438].

In Ref. [439], the microscopic observation of the confinement-induced layering of quasi-2D complex plasma liquids is reported. The experiments were conducted in a rf discharge at  $\simeq 30$  Pa. Two parallel vertical plates were put on the centre region of the bottom electrode surface to laterally confine polystyrene particles of 7  $\mu\text{m}$  diameter and, hence, to form mesoscopic channels down to a few interparticle spacings in the width. Microscopically, the particle mutual interaction tends to generate ordered triangular lattice-type domains with small amplitude position oscillations, which can be reorganized through stick-slip string- or vortex-type hopping induced by stochastic thermal kicks [406]. However, the boundaries suppress the nearby transverse hopping. Fig. 45 shows the snapshots of particle configurations and the corresponding transverse density distribution for different “number of layers”,  $N$ . Basically, at larger  $N$ , the density profiles with decaying oscillation from both boundaries manifest the confinement-induced (two to three) outer layers near each boundary, which sandwich the more disordered isotropic liquid with a flat density profile in the centre region. The transition to the layered structure up to the centre at  $N < 7$  is evidenced by the appearance of sharp peaks of the density profile. Run G shows the ordered crystal-like structure with four layers.

It is known, that in contrast to the mean velocity profile with a uniform shear rate for a bulk Newtonian flow between two oppositely moving parallel plates, in sheared glassy materials such as foams, micelles, dense colloids, and dense granular systems shear banding is observed. The sheared flow tends to separate into bands with different shear rates through local stress relaxation [440–443]. It causes the formation of the outer shear bands in which the mean shear rate, the velocity fluctuations, and the structural rearrangement rate are all enhanced, and leaves a weakly perturbed centre band.

The microscopic dynamics of the shear flow in a 2D mesoscopic complex plasma liquids has been studied at the kinetic level [444] (with the experimental setup used for studying the confinement-induced layering in Ref. [439]). Due to the formation of the nearby layered structure shown in Fig. 45, the persistent and directional slow drive from the external stress along the boundary enhances stick-slip type structural rearrangements which cascade into the liquid through many-body interaction. It was found that the flow consists of two outer shear bands about three interparticle distance in width nearby boundaries and a centre low-rate zone. The former has higher levels of both longitudinal and transverse velocity fluctuations. The shear banding phenomenon originates from the local stress release through the local rearrangement events adjacent to the boundary.

## 13. Magnetized complex plasmas

In this section we discuss the influence of external magnetic fields on a complex plasma. In selecting the material, the priority has been given to the experimentally observed phenomena. For instance, we do not discuss here extensive literature existing on dust waves in the presence of magnetic fields (this topic has been well addressed in other reviews and monographs, see, e.g., [445]).

The influence of external magnetic fields on complex plasmas has been studied in different types of laboratory discharge plasmas. In the very first experiments by Sato et al. [446,447], where the vertical magnetic field of about

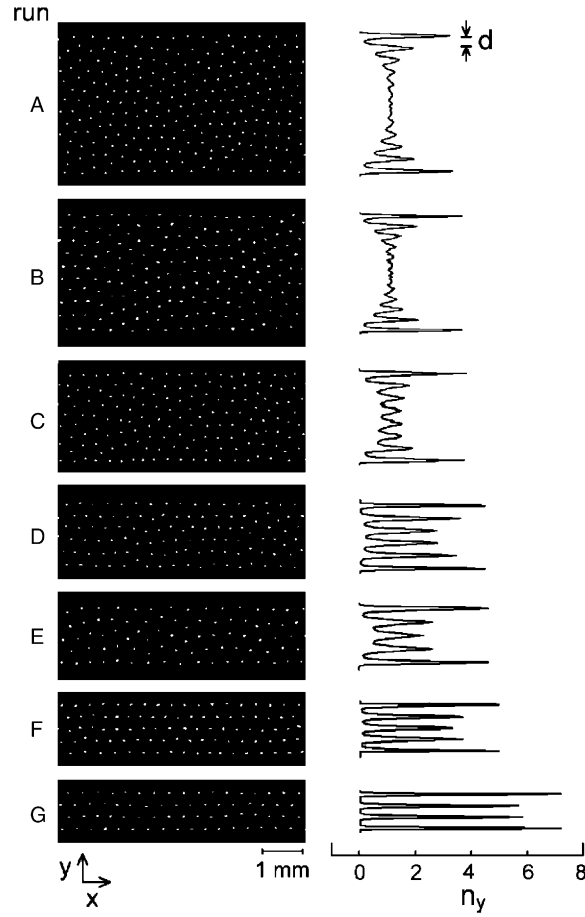


Fig. 45. The typical snapshots of the particle configurations and the transverse particle density distributions,  $n_y$ , for run A–G with decreasing “number of layers”  $N$  (width measured in units of the interparticle spacing), from 11 to 3 [439].

$4 \times 10^{-2}$  T was applied to an argon discharge at  $\simeq 10$  Pa, the cloud of electrostatically confined  $\simeq 10 \mu\text{m}$  grains rotated in the azimuthal direction (horizontally). It was clear immediately that this rotation has no relation to the magnetization of the particles themselves—neither the radius of rotation nor the frequency were comparable to the gyroradius and the cyclotron frequency of particles. Also, the neutral friction rate was much higher than the observed frequency of the rotation, so that the particle gyromotion was suppressed. Later on, similar experiments were performed by Konopka et al. [200] at  $\simeq 10^{-2}$  T in a rf discharge with a monolayer of  $8.9 \mu\text{m}$  particles, as shown in Fig. 46. The observed horizontal rotation of the particle cloud was attributed to the azimuthal component of the ion drag force. This component appears because of the azimuthal drift of the ions (flowing down to the rf electrode) in crossed vertical magnetic and radial electric fields (the latter arises because of weak radial confinement). The angular velocity of the cloud rotation is determined by the balance of the azimuthal ion drag and the neutral friction forces. Fig. 47 shows typical images of the rotating particle clouds observed in experiments [200].

In terms of magnetization of complex plasma species, one can naturally introduce three ranges for magnetic field  $B$ —“weak”, “medium”, and “strong” fields. For the weak fields the ions are not magnetized—the ion cyclotron frequency,  $\Omega_{ci} = eB/m_i$ , is smaller than the ion collision rate with neutrals,  $\nu_{in}$ . Ions become magnetized in the medium field range, and charged grains—in the strong field range (the latter means that the dust cyclotron frequency  $\Omega_{cd} = e|Z|B/m_d$  exceeds the neutral damping rate  $\nu_{dn}$ ). Obviously, the “transitional” magnitudes of  $B$  are proportional to the neutral gas pressure: for  $p \sim 10$  Pa, the ions typically become magnetized at  $B \sim 0.3$ –1 T, and the micronsize particles—at 10–30 T. While the meaning of the strong fields is clear—this is the range where the gyromotion of charged particles can be directly observed, the division into weak and medium fields is introduced because of the fact that the azimuthal

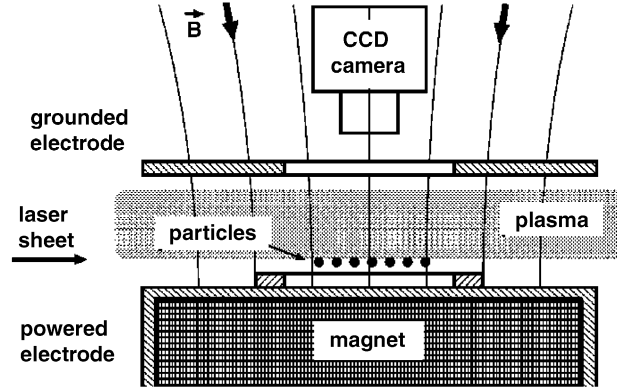


Fig. 46. Sketch of the experimental setup for the complex plasma experiments in a magnetic field [200].

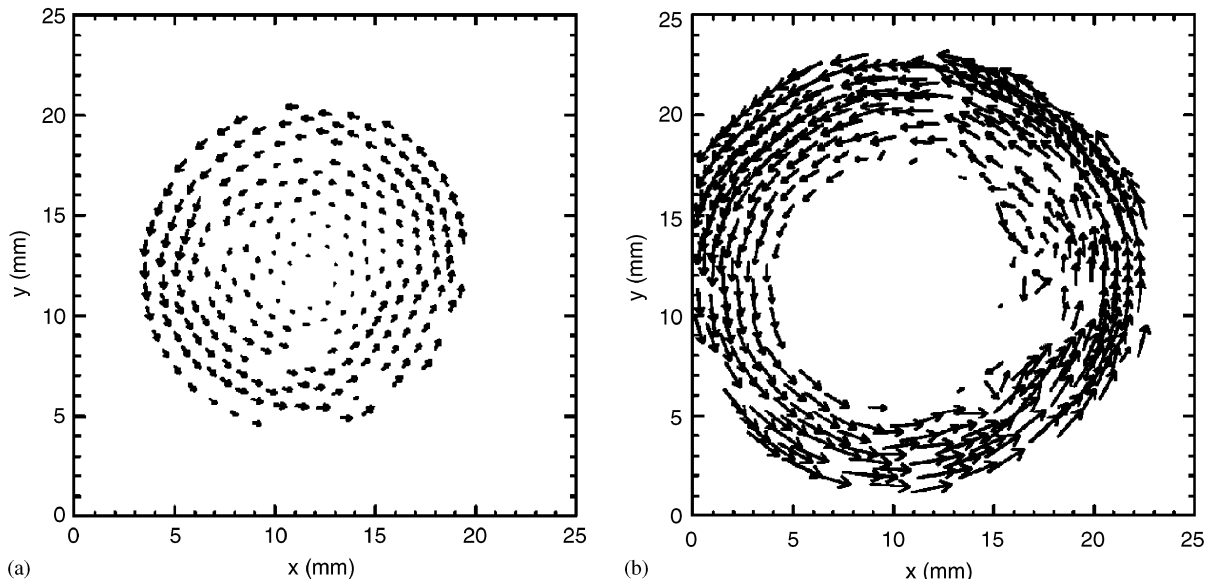


Fig. 47. Top view on typical configuration of the particle cloud rotating in the magnetic field [200]. The vectors indicate the particle displacement in 20 consecutive frames (frame rate 8 fps). The plots are made for different gas pressure  $p$  and the particle number in the cloud  $N$ : (a)  $p = 40$  Pa,  $N \simeq 250$  and (b)  $p = 30$  Pa,  $N \simeq 450$ .

ion velocity scales as  $\propto \Omega_{ci}/(\Omega_{ci}^2 + v_{in}^2)$  [201]. Since the motion of unmagnetized particles is mostly driven by the ion drag force, the rotation of the particle cloud should obey the same scaling. The angular velocity of the rotation should increase as  $\omega \propto B$  in the weak field range, attain a maximum at  $\Omega_{ci} \simeq v_{in}$ , and then decrease as  $\omega \propto B^{-1}$  in the medium field range. Such behaviour had been observed in experiments [448] and then was explained theoretically in Ref. [201].

The azimuthal ion drag,  $F_{id}^\phi$ , is proportional to the electric field of the radial confinement,  $E_r$ . Depending on the profile of  $E_r(r)$ , the particle cloud can rotate as a rigid body or exhibit a differential rotation, so that the angular velocity  $\omega$  varies with the distance to the rotation centre,  $r$ , and can even change the sign [200]. This gives us an opportunity to study shear flows in strongly coupled complex plasma and observe the shear-induced melting. Note that the friction force scales as  $F_{nd} \propto \omega r$  and, hence, the rigid body rotation will always be observed when  $E_r \propto r$ . However, the very fact of the rigid body rotation does not necessarily implies the linear increase of  $E_r$ , but can be just because the coupling

between particles in the cloud is strong enough [200,201]. In this case, the angular velocity of the cloud rotation is determined by the torque balance,  $[F_{\text{id}}^{\phi}(r) + F_{\text{nd}}(r)]r^2 dr = 0$ .

Recently, experiments with a new type of complex plasmas containing paramagnetic particles have been started [449,450]. Particles with diameter  $2a = 4.5 \mu\text{m}$  and the magnetic permittivity  $\mu \simeq 4$  were suspended in a argon rf discharge at pressure 46 Pa in inhomogeneous magnetic field. In the region where the particles levitated, the (tunable) magnetic field was up to  $B \sim 0.1 \text{ T}$  with the gradient  $|\nabla B| \simeq 5 \text{ T/m}$  pointed up. The magnetic field induced a magnetic moment at each particle,  $m_B \propto a^3 B$ , so that the particles were pulled upward in the direction of the magnetic field gradient. These experiments made possible to study interaction of magnetic particles with each other and with a magnetic field.

From the observed increase of the levitation height with the increase of the magnetic field, the particle charge and the thickness of the plasma sheath were estimated [449]. It was demonstrated that the force due to magnetic gradient,  $\propto m_B |\nabla B|$ , can compensate gravity. Therefore, the magnetic fields can serve as a diagnostic tool for the complex plasma parameters. Also, the possibility of magnetically induced formation of a plasma crystal was discussed. Various mutual dust–dust interactions, including the forces due to induced magnetic and electric moments of the grains were theoretically considered [450]. It turned out that the electromagnetic forces from particle magnetization and polarization may result in mutual repulsion as well as attraction. It was found that magnetized grains can coalesce, forming field-aligned chains. Analysis of the particle interaction forces showed that at intermediate magnetic fields (used in the experiment) the particles can agglomerate only if their kinetic energy is high enough to overcome the barrier in the electrostatic interaction potential.

The experimental results published so far on the magnetized complex plasmas clearly show that these investigations can lead to new effects in the study of dusty plasmas. The weak magnetic fields allow us to introduce a new degree of freedom into the system, which makes possible to control, e.g., the interparticle interaction, field of forces, etc. without considerable distortion of the discharge parameters. On the other hand, the properties of the discharge plasma itself are poorly known at the medium and, moreover, strong fields. Also, the grain charges may be significantly affected by the magnetic field. Therefore, comprehensive experimental investigations for such conditions should probably be one of the major directions for the future.

#### 14. Complex plasmas with nonspherical particles

Recently, the first investigations (both experimental and theoretical) of complex plasmas with asymmetric particles have been started [190,445,451–457]. In Ref. [451] the geometrical aspect ratio was  $\alpha \sim 3$ , and the first experiments with strongly asymmetric particles ( $\alpha = 40\text{--}80$ ) were carried out in Ref. [452]. It is well known that colloidal solutions, which have much in common with dusty plasmas, show a much broader spectrum of possible states in the case of strongly asymmetric cylindrical or disk particles. In such solutions, liquid phase and several liquid-crystal and crystal phases with different degrees of orientational and positional ordering can be observed. It is also well known that the use of cylindrical probes (in addition to spherical) considerably broadens the possibilities of low-temperature plasma diagnostics. In Ref. [452], where the experimental setup analogous to that shown in Fig. 4 was employed, nylon particles ( $\rho = 1.1 \text{ g cm}^{-3}$ ) of length  $300 \mu\text{m}$  and diameters  $7.5$  and  $15 \mu\text{m}$ , as well as particles of lengths  $300$  and  $600 \mu\text{m}$  and diameter  $10 \mu\text{m}$ , were introduced into the plasma of a dc discharge. The discharge was initiated in neon or a neon/hydrogen mixture at a pressure of  $10\text{--}250 \text{ Pa}$ . The discharge current was varied from  $0.1$  to  $10 \text{ mA}$ . In this parameter range, standing striations were formed in the discharge, which made possible particle levitation. A neon/hydrogen mixture was used to levitate heavier particles of larger diameter ( $15 \mu\text{m}$ ) or larger length ( $600 \mu\text{m}$ ). In this case, the particles formed structures consisting of  $3\text{--}4$  horizontal layers. Lighter particles levitated in pure neon and formed much more extended structures in the vertical direction.

The observed structures formed by microcylinders revealed clear ordering. All particles lay in the horizontal plane and were oriented in a certain direction. One could expect that the orientation should be determined by cylindrical symmetry of the discharge tube. However, no correlation between the particle orientation and the tube symmetry was found. Nor could the preferential orientation of the particles be explained by the interparticle interaction, because individual particles were oriented in the same direction. Presumably, the preferential orientation was related to a weak asymmetry in the discharge. This was confirmed by the fact that the orientation could be changed by introducing an artificial perturbation into the discharge. In later experiments [454], nylon particles of lengths  $300$  and  $600 \mu\text{m}$  and

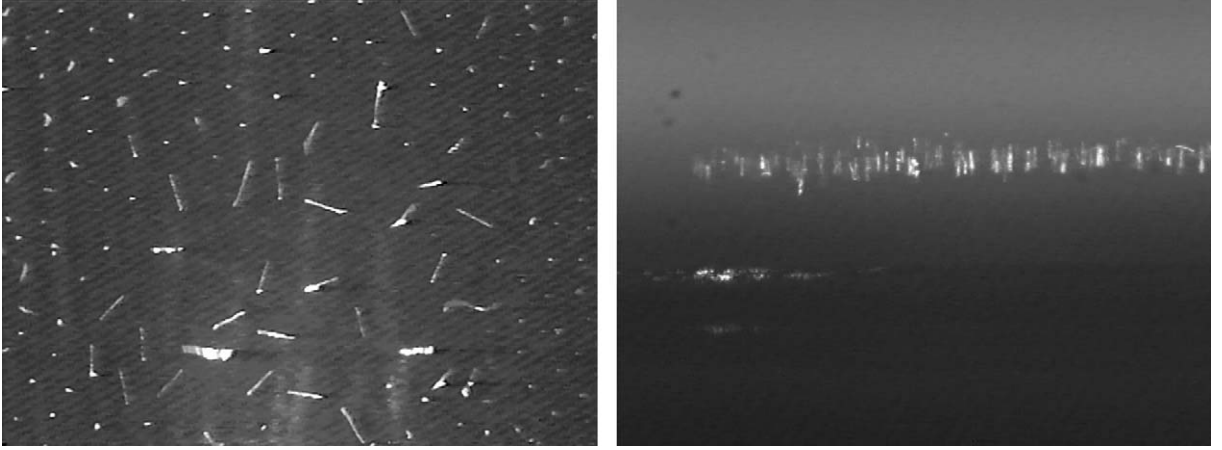


Fig. 48. Typical video images of structures formed by cylindrical particles levitating near the sheath edge of an rf discharge [453]. The discharge was initiated in krypton at a pressure of 52 Pa and discharge power of 80 W. The left figure shows a top view, dots correspond to vertically oriented particles, and the right figure gives a side view.

diameter 10  $\mu\text{m}$  coated by a thin layer of conducting polymer were utilized. In a dc discharge they formed structures identical to those formed by uncoated particles of the same size.

Levitation of cylindrical particles was also observed near the sheath edge of a capacitively coupled rf discharge [453]. In this experiment, the cylindrical particles of length 300  $\mu\text{m}$  and diameters 7.5 and 15  $\mu\text{m}$  were used, and a small fraction of very long particles (up to 800  $\mu\text{m}$ ) of 7.5  $\mu\text{m}$  in diameter was also present. A typical picture of a structure formed by these particles is shown in Fig. 48. Longer particles are oriented horizontally and mainly located in the central part limited by a ring placed on the electrode, while shorter particles are oriented vertically along the electric field. Levitation and ordering of the cylindrical particles occurred only for pressures higher than 5 Pa and a discharge power above 20 W. An increase in the discharge power did not significantly affect particle levitation. The average distance between vertically oriented particles varied from 1 to 0.3 mm. An increase in particle density leads to degradation of the quasicrystalline structure and increase of particle kinetic energies. The further increase in density is impossible because the particles start falling down from the structure. Levitation of particles coated by a conducting polymer was not observed in an rf discharge for the conditions at which the dielectric particles of the same size and mass could levitate. Instead, the conducting particles stuck to the electrode, preserving vertical orientation, and some stuck to each other forming multiparticle fractal clusters with up to 10 particles.

The preferential orientation of cylindrical particles is determined by an interplay between the interaction of nonuniform electric field  $\phi(h)$  in striations or sheaths with a particle charge  $eZ$  and induced dipole  $d$  and quadrupole  $D$  moments [456]. The equilibrium state of the rod—the levitation height  $h_0$  and the orientation angle  $\alpha_0$  with respect to the vertical axis, can be found considering the total potential energy of the particle, which includes the gravity contribution,  $mgh$ . For simplicity, we assume no dependence of the particle charge on  $h$  and  $\alpha$ . Then the energy is determined by expansion [456]

$$U(h, \alpha) \simeq mgh + eZ\phi - \frac{dE}{2}\cos^2\alpha - \frac{DE'}{12}(3\cos^2\alpha - 1) + \dots, \quad (94)$$

with  $E < 0$  and  $E' > 0$ . The magnitudes of the dipole and quadrupole moments are [458,459]  $d \simeq \frac{1}{24}EL^3/\Lambda < 0$  and  $D \simeq \frac{1}{6}eZL^2 < 0$ , where  $\Lambda = \ln(L/a)$  with  $L$  and  $a$  the rod length and radius, respectively. The equilibrium states are determined by extrema of Eq. (94). From  $\partial U/\partial h = 0$  (force balance) we get the levitation height  $h_0$ , which is implicitly determined by  $mg = eZE_0 + dE'_0\cos^2\alpha$  (subscript 0 denotes that the functions are taken at  $h = h_0$ ). This equation shows that in addition to the gravity and the monopole electric forces, the dipole force contributes to the balance in vertical direction. However, this force does not affect the balance noticeably and the levitation height is mostly determined by the balance of the gravity and the electric force on the total charge, like for a spherical particle.

The equilibrium orientation is given by the condition  $\partial U / \partial \alpha = 0$  (torque balance), which yields two angles,  $\alpha_0 = 0$  and  $\pi/2$ , i.e., the vertical or horizontal orientation of the rod is only possible. The condition for the stable angle we get from the second derivative:  $\partial^2 U / \partial \alpha^2 \propto (K - 1) \cos 2\alpha_0 > 0$ . Here we introduced the “orientation parameter”:

$$K = \frac{2d\ell_E}{D} \equiv \left( \frac{e|E_0|L}{\gamma_r T_e} \right) \frac{\ell_E}{L},$$

where  $\gamma_r = 2\Lambda e^2 |Z| / LT_e$  is the dimensionless particle potential and  $\ell_E = |E_0/E'_0|$  is the spatial scale of the field variation (in the approximation of a “weakly inhomogeneous field”  $\ell_E \gg L$ ). This shows that the quadrupole moment is important for the orientation—the equilibrium is determined by the competition between the dipole and quadrupole terms in Eq. (94). The dipole torque turns the rod along the electric field, whereas the quadrupole torque tends to make it horizontal. Hence, particles levitate horizontally,  $\alpha_0 = \pi/2$ , when  $K < 1$ , and vertically,  $\alpha_0 = 0$ , when  $K > 1$ . Using the equilibrium condition in the vertical direction,  $mg \simeq eZE_0$ , we eliminate the dependence on  $E_0$  in the expression for  $K$ , and applying the relation between  $\gamma_r$  and  $|Z|$  we derive the following scaling:  $K \propto \Lambda^2 a^4 E'_0{}^{-1} (\gamma_r T_e)^{-3}$ . If we assume that  $\gamma_r$  does not depend on  $L$  and  $E'_0 = \text{const}$  (the latter is usually true for rf sheaths), then  $K \propto \Lambda^2$ . Therefore, the relative contribution of the dipole term is stronger for a longer rod: if  $\Lambda$  is sufficiently large the rod can levitate vertically, but for smaller  $\Lambda$  the horizontal orientation is more preferable. Let us apply these results for the analysis of particle orientation observed in experiments. In a dc discharge, the particle charge is typically larger than in an rf discharge, allowing particle levitation in weaker electric fields. In this case, the dipole moment, which is proportional to the electric field strength squared, is much smaller than in an rf discharge. This can explain the different orientations of similar-sized particles: horizontal in a dc discharge, and vertical in an rf discharge. For long particles in rf sheaths, i.e., when the field is strongly inhomogeneous ( $\ell_E < L$ ), the balance of torques which determines the rod orientation is quite different. Let us consider the vertically oriented rod in the limit  $\ell_E \ll L$ . In this case, a significant electric field exists only in a vicinity of the lower tip of the rod. Therefore, the torque due to the dipole moment should be relatively small (compared to the weakly inhomogeneous case). In contrast, the quadrupole moment torque should be increased, since the centre of the electric force will be shifted from the centre downward to the lower tip. Thus, the vertical orientation is obviously unstable in the strongly inhomogeneous case, and the only possible orientation is the horizontal one.

Experimental observation of plasma crystals composed of elongated particles [451–453] and levitating in dc striations or in rf sheaths stimulated theoretical study of the wake potentials produced by rod-like charged particles [190,455]. In general, the appearance of a dipole moment affects the character of the wake—in particular, this provides the additional rotational degree of freedom related to the rotational inclination of the rod. This can lead to new effects. For instance, in addition to the longitudinal and transverse vibration modes, the lattices composed of rods can have new modes associated with their rotational motion, similar to those in liquid crystals [460,461]. Excitation and interactions of all these modes introduce new phase transitions and influence those existing in lattices composed of spherical grains. Also, since the wake can affect the interaction of the horizontal (longitudinal) and vertical (transverse) modes for spherical grains [341], the similar effects should exist for cylindrical particles as well.

## 15. Possible applications

Dusty plasmas have been present in various industrial applications for many decades. These are, e.g., precipitation of aerosol particles in combustion products of electric power stations, plasma spraying, and electrostatic painting. In the beginning of the 1990s it became clear that a large part of contamination found on the surface of silicon wafers after the manufacturing was not because of insufficient cleaning, but in fact was an inevitable consequence of plasma etching and deposition technologies. In most capacitively coupled rf discharge reactors, all particles are charged negatively and levitate close to one of the electrodes. After switching off the discharge they are deposited on the wafer surface. Submicron particles deposited on the wafer can reduce the working surface, cause dislocations and voids, and reduce adhesion of thin films. Enormous efforts put forth on reduction of the number of undesirable dust particles in industrial plasma reactors have recently brought positive results [6–8,462].

In recent years it has become obvious that the presence of dust in plasmas does not necessarily have undesirable consequences. Powders produced by employing plasma technologies can have interesting and useful properties: very small sizes (from a nanometer to micrometer range), monodispersity, and high chemical activity. The size, structure and



composition of the powder can be varied easily in compliance with the specific requirements of a certain technology. In this connection, two trends can be distinguished in applied dusty plasma research [8,462]. The first one represents a development of well-established technologies of surface modification, with the dust particles being now the subject of treatment. In order to create particles with specific properties, coating, surface activation, etching, modification, or separation of clustered grains in plasmas can be adapted. The second important trend is the creation of new nanostructure materials, like thin films with an inclusion of nanometer-size particles. The typical size of the elements of integrated circuits in microelectronics is reduced every year and in the nearest future it will likely reach 10 nm. Furthermore, there is a tendency to replace capacitively coupled rf discharges by inductively coupled ones: the particle trapping is more difficult in capacitive discharges, which leads to a significant amount of the particles dropping on the surface of the silicon wafer during plasma processing. Thus, the solution introduced in the 1990s, which was mostly based on dust particle confinement in special traps, does not work for these devices. This poses a serious problem for the production of integrated circuits of the next generation, which demands further applied research of the properties of dusty plasmas.

It is known that dust particles are present in the magnetic confinement fusion devices [190,463–469]. Their origin is mostly the plasma–surface interaction. In the framework of the development of the International Thermonuclear Experimental Reactor (ITER) project it became obvious that dust represents a serious safety hazard. ITER, as most of existing fusion devices, will have the wall parts made of graphite and carbon composites. The tritium implantation into the carbonaceous dust can result in appearance of dust particles where for one atom of carbon there are two atoms of tritium. The mass of tritium in large devices like ITER may be as high as dozens of kilograms. Such a high amount raises serious problems related to the safety of the operation—due to the high mobility and chemical reactivity, dust may operate as a potential carrier of tritium in the case of a severe reactor failure, contaminating substantial areas. Dust can also affect the plasma performance and stability, as well as the operation of fusion devices. Thus, the problem of dust removal from thermonuclear devices represents one of the most important scientific and technical problem. The main factor being used for its successful solution is presence of the electrical charge at the dust particles. In these conditions, the equilibrium particle charge is determined by competition of secondary electron emission and electron and ion absorption from the ambient plasma.

For the electric power supply of spacecrafts, automatic weather stations, antisubmarine buoys, etc., compact autonomous power-supply sources with a power about 1–10 kW and an operating lifetime of several years are necessary. At present, photoelectric converters of solar energy, thermoelectric sources with fuel elements made of  $^{90}\text{Sr}$ ,  $^{238}\text{Pu}$ , or  $^{210}\text{Po}$ , and thermoionic converters with  $^{235}\text{U}$  reactor used as the heat source, are provided. All these sources have disadvantages, in particular, very low efficiency. Moreover, a nuclear reactor is very complicated to produce. Recently, a new method of the nuclear-to-electric energy conversion was proposed [470,471]. The operating principle of the novel atomic battery is as follows: high-energy particles, which are formed during the decay of a radioactive material, ionize an inert gas such as xenon. The dissociative recombination of formed diatomic xenon ions results in the effective excitation of xenon excimers which emit vacuum ultraviolet photons with a wavelength of about 172 nm. These photons are absorbed on a wide band-gap diamond-based photoconverter and generate electron–hole pairs. Estimates indicate that the total efficiency of a battery utilizing this principle may be as high as 25–35%.

In order to use solid isotopes in the photovoltaic converters, it is necessary to have the isotope surface area as large as possible. This is because the mean free path of the ionizing particles in the isotope material is very short (e.g., the mean free path of  $\beta$ -radiation with the mean decay energy in  $^{90}\text{Sr}$  is about 180  $\mu\text{m}$ ). Therefore, a homogeneous mixture of gas and isotope dust is a very good option. Excitation of the gas mixture is performed by  $\alpha$ - or  $\beta$ -radiation from the radioactive dust. Estimates show that at a dust size of 1–20  $\mu\text{m}$  and dust number density of  $10^5$ – $10^9 \text{ cm}^{-3}$  it is possible to obtain the power density of  $\sim 1 \text{ W/m}^3$ . The gas pressure has to be on the order of 1–10 bar to ensure effective energy conversion of  $\beta$ - or  $\alpha$ -radiation into UV radiation. The main technical problem here is to have a homogeneous gas–dust mixture at high gas pressures. Recent experiments performed in such systems demonstrate that this is possible [85,86]. Processes of self-organization occurring in the nuclear-induced plasmas result in the formation of stationary structures and, hence, provide relatively homogeneous redistribution of particles over the plasma volume.

## 16. Interdisciplinarity and perspectives

In this review we have naturally concentrated on complex plasmas as a new physical, non-Hamiltonian state of matter that has already provided researchers over the last 10 years or so with many new challenges—both experimentally and

theoretically. We have discussed broad spectrum of numerous physical phenomena occurring in complex plasma, and have also pointed out some of the currently predictable developments expected on this new and exciting field in the next few years.

There is another issue, however, that promises to become as important—possibly even more so—than the investigation of complex plasmas per se. This we have termed “*interdisciplinarity*”, which means transferring some insights obtained from complex plasma research to other fields. This presupposes, of course, that we have “generic” processes or that understanding a particular process in one field will help with new and novel insights in another area.

The reasons why this “interdisciplinarity” could be of particular significance for complex plasmas are:

- Complex plasmas can be studied experimentally at the kinetic (individual particle) level—something that for most systems is only possible when they are static or, at best, exhibit secular variations.
- Complex plasmas are optically thin up to sizes of a few 10’s of cm—corresponding, e.g., to crystals with a few 1000 lattice planes. By selectively illuminating central or peripheral parts one can visualize particular regions of interest for detailed investigations.
- The characteristic time and length scales of complex plasmas are “stretched” with respect to e.g., atomic or molecular systems—by typically a factor of a million (atomic systems have scales  $\sim \text{\AA}$  and complex plasmas  $\sim 100 \mu\text{m}$ ; typical plasma frequencies at plasma densities of  $10^{12} \text{ cm}^{-3}$  are  $\sim 10^8 \text{ Hz}$  and complex plasma frequencies at similar charge densities are  $\sim 100 \text{ Hz}$ ). This allows studies at all the relevant physical parameters in “slow motion” and “high resolution”—and makes the transfer of insights gained from these otherwise inaccessible measurements (in particular for nonlinear processes) extremely valuable.
- Complex plasmas can be “engineered” in different ways, e.g., as predominantly one-component systems, as two-component systems, multi-component systems, anisotropic systems, stratified systems, etc. Hence, different dynamical properties can be studied under controlled conditions. This increases the scope for “interdisciplinarity” considerably.
- There is a class of problems (nano-dynamics) where progress requires studies at the kinetic level—and so far only complex plasmas offer the chance to do this directly, without using proxy data or accepting interference of the measurements on the process under study.
- Finally, there is a growing belief that self-organization, scale-free behaviour, universality and fractal structure growth are generic properties of matter that depend on the interaction forces and external (control) parameters only regarding their defined “modus operandi” and that the underlying principles are the same. Investigations at the most fundamental kinetic level can then be regarded as a “missing link” in our understanding of universality processes, one that complex plasmas may be able to provide.

Based on the known physical properties of complex plasmas discussed in the review, it is clear then that the “interdisciplinarity” may be categorized in at least seven areas:

*Crystals.* It has already been shown that many aspects of crystal physics (e.g., waves) are well reproduced at the kinetic level. The exciting tasks for the future lie in the areas of understanding the role of defects in the thermodynamics, investigate nonlinear wave interaction, magnetized and anisotropic crystals, etc. A number of these investigations will have an analogue in crystal physics and will lead to better understanding in time.

*Crystallization/melting.* So far, it was virtually impossible to investigate this at the kinetic level, although even without such research a great deal has been learned about different types of crystal growth (from epitaxial to dendritic), cluster formation, etc. Nevertheless, it is quite clear that detailed kinetic studies of phase transitions with complex plasmas will complement our understanding of the elementary processes considerably. This includes nucleation as well as the dynamics and structure of crystallization fronts.

*Fluids.* The onset of cooperative phenomena in fluid flows is one of the prime domains where complex plasmas can contribute substantial new physical insights. The same is true, however, for self-organization of fluid flows from laminar shears to turbulence, one of the outstanding problems of hydrodynamics. Investigations at the kinetic level promise a rich field of research in the years to come. The issues to investigate are, e.g., the onset of Kelvin–Helmholtz and Rayleigh–Taylor instabilities, interpenetrating flows, nonequilibrium phase transitions, etc., as well as the study of multi-fluid systems and their interfaces.

*Liquid/gas transitions.* Here the physical processes occurring at the “critical point” are of great fundamental interest. The main questions are: what is the universality class of complex plasmas? Is there a critical point in the system—and

if so, what are the bulk properties? What is the role of finite particle size? How does particle inertia affect the physics? and finally—What is the kinetic origin of the scale-free behaviour found at the critical point? There are other topics also, of course, such as condensation, wave propagation, etc.

*Surfaces.* One of the most exciting topics here is the study of the onset of “surface cooperative behaviour” when 3D clusters grow larger to become liquid or crystalline balls. This includes the development of surface global modes from a few discrete modes to finally a continuum treatment, issues that are equally interesting for physics as well as engineering.

*Magnetization.* The physics of cooperative phenomena and strong coupling under conditions when the gyroradius of thermal particles becomes smaller than their equilibrium separation is another “interdisciplinary” topic of interest in plasma physics, astrophysics, and solid states. Here, too, insights gained from kinetic measurements (ranging from mode coupling of different waves to flow properties) can be extremely valuable in understanding other natural systems.

*Exotic systems.* In future space experiments it may be possible to experiment with so-called “quantum gases” consisting of interacting Bose–Einstein condensates, each condensate consisting of many billions Rb atoms, for instance. Whilst this does not yet constitute a “quantum plasma”—the BECs are uncharged—it is nevertheless interesting to speculate on and to investigate what happens when, e.g., cold electrons are introduced into the system, or photoionization is attempted.

It must be recognized that efforts should be made in the near future for experts from various fields to discuss these “interdisciplinary” issues.

## 17. Conclusion

Despite an almost a century-long history—the first observations of dust in discharges were reported by Langmuir in 1924 [472], the investigation of dusty plasmas has acquired substantial attention only during the last decade, after the experimental discovery of the plasma crystals. The simplicity of visualization in complex plasmas provides us with unique opportunity to observe the ongoing processes at the individual particle level. This makes possible the detailed analysis of thermodynamics and kinetics in the crystalline and liquid phases, provides insights into the mesoscopic behaviour and onset of cooperative phenomena, yields crucial information about “microscopic” processes driving critical phenomena and self-organization, etc.

We should, however, also take the long view. Complex plasma research has already made remarkable progress in the investigations of some fundamental and generic processes—ranging from nanofluidics to crystallization at the kinetic level. This growth of knowledge, which has just begun, will ultimately help us to advance into other fields. This highlights the “interdisciplinarity” of the complex plasma research.

Advances in understanding the basic processes in complex plasmas can lead to a much broader application potential than dedicated technological development is often able to achieve. Complex plasma research—especially the fundamental insights gained through novel experiments in space, providing long observation times and conditions not available on Earth—has already shown that.

The authors tried not only to discuss the current status in the field, by highlighting the most significant experimental and theoretical results, but also pointed out some important issues to be solved. Now complex plasmas are one of the most rapidly growing fields in physics—on average, with more than one publication appearing every day. There is no doubt, therefore, that these studies will provide new insights into various fields of basic research in the future.

## Acknowledgements

The authors are deeply thankful to G. Joyce for valuable discussions and useful comments made when reading the manuscript. The work was partially supported by DLR under contracts No. 50 WP 0203 and 0204.

## References

- [1] C.K. Goertz, Dusty plasmas in the solar system, *Rev. Geophys.* 27 (1989) 271–292.
- [2] T.G. Northrop, Dusty plasmas, *Phys. Scripta* 45 (1992) 475–490.
- [3] V.N. Tsytovich, Dust plasma crystals, drops, and clouds, *Phys. Usp.* 40 (1997) 53–94.

- [4] E.C. Whipple, Potentials of surfaces in space, *Rep. Prog. Phys.* 44 (1981) 1197–1250.
- [5] P.A. Robinson, P. Coakley, Spacecraft charging-progress in the study of dielectrics and plasmas, *IEEE Trans. Electr. Insul.* 27 (1992) 944–960.
- [6] G.S. Selwyn, J. Singh, R.S. Bennett, In situ laser diagnostic studies of plasma-generated particulate contamination, *J. Vac. Sci. Technol. A* 7 (1989) 2758–2765.
- [7] A. Bouchoule, Technological impacts of dusty plasmas, in: A. Bouchoule (Ed.), *Dusty Plasmas: Physics, Chemistry and Technological Impacts in Plasma Processing*, Wiley, Chichester, 1999, pp. 305–396.
- [8] H. Kersten, H. Deutsch, E. Stoffels, W.W. Stoffels, G.M.W. Kroesen, R. Hippler, Micro-disperse particles in plasmas: from disturbing side effects to new applications, *Contrib. Plasma Phys.* 41 (2001) 598–609.
- [9] R.F. Wuerker, H. Shelton, R.V. Langmuir, Electrodynamic containment of charged particles, *J. Appl. Phys.* 30 (1959) 342–349.
- [10] H. Ikezi, Coulomb solid of small particles in plasmas, *Phys. Fluids* 29 (1986) 1764–1766.
- [11] J.H. Chu, L. I, Direct observation of Coulomb crystals and liquids in strongly coupled rf dusty plasmas, *Phys. Rev. Lett.* 72 (1994) 4009–4012.
- [12] H. Thomas, G.E. Morfill, V. Demmel, J. Goree, B. Feuerbacher, D. Möhlmann, Plasma crystal: Coulomb crystallization in a dusty plasma, *Phys. Rev. Lett.* 73 (1994) 652–655.
- [13] Y. Hayashi, S. Tachibana, Observation of Coulomb-crystal formation from carbon particles grown in a methane plasma, *Jpn. J. Appl. Phys.* 33 (1994) L804–L806.
- [14] A. Melzer, T. Trottenberg, A. Piel, Experimental determination of the charge on dust particles forming Coulomb lattices, *Phys. Lett. A* 191 (1994) 301–307.
- [15] V.E. Fortov, A.P. Nefedov, V.M. Torchinskii, V.I. Molotkov, A.G. Khrapak, O.F. Petrov, K.F. Volykhin, Crystallization of a dusty plasma in the positive column of a glow discharge, *JETP Lett.* 64 (1996) 92–98.
- [16] V.E. Fortov, A.P. Nefedov, O.F. Petrov, A.A. Samarian, A.V. Chernyshev, A.M. Lipaev, Experimental observation of Coulomb ordered structure in sprays of thermal dusty plasmas, *JETP Lett.* 63 (1996) 187–192.
- [17] V.E. Fortov, V.I. Vladimirov, L.V. Deputatova, V.I. Molotkov, A.P. Nefedov, V.A. Rykov, V.M. Torchinskii, A.V. Khudyakov, Ordered dusty structures in plasma produced by nuclear particles, *Dokl. Phys.* 44 (1999) 279–282.
- [18] U. Konopka, G.E. Morfill, L. Ratke, Measurement of the interaction potential of microspheres in the sheath of a rf discharge, *Phys. Rev. Lett.* 84 (2000) 891–894.
- [19] M. Zuzic, A.V. Ivlev, J. Goree, G.E. Morfill, H.M. Thomas, H. Rothermel, U. Konopka, R. Sütterlin, D.D. Goldbeck, Three-dimensional strongly coupled plasma crystal under gravity conditions, *Phys. Rev. Lett.* 85 (2000) 4064–4067.
- [20] G.E. Morfill, H.M. Thomas, U. Konopka, H. Rothermel, M. Zuzic, A. Ivlev, J. Goree, Condensed plasmas under microgravity, *Phys. Rev. Lett.* 83 (1999) 1598–1602.
- [21] A.P. Nefedov, G.E. Morfill, V.E. Fortov, H.M. Thomas, H. Rothermel, T. Hagl, A.V. Ivlev, M. Zuzic, B.A. Klumov, A.M. Lipaev, V.I. Molotkov, O.F. Petrov, Y.P. Gidzenko, S.K. Krikalev, W. Shepherd, A.I. Ivanov, M. Roth, H. Binnenbruck, J.A. Goree, Y.P. Semenov, PKE-Nefedov: plasma crystal experiments on the International Space Station, *New J. Phys.* 5 (2003) 33.1–33.10.
- [22] D. Samsonov, J. Goree, Instabilities in a dusty plasma with ion drag and ionization, *Phys. Rev. E* 59 (1999) 1047–1058.
- [23] J. Goree, G.E. Morfill, V.N. Tsytovich, S.V. Vladimirov, Theory of dust voids in plasmas, *Phys. Rev. E* 59 (1999) 7055–7067.
- [24] V.N. Tsytovich, S.V. Vladimirov, G.E. Morfill, J. Goree, Theory of collision-dominated dust voids in plasmas, *Phys. Rev. E* 63 (2001) 056609/1–11.
- [25] M. Kretschmer, S.A. Khrapak, S.K. Zhdanov, H.M. Thomas, G.E. Morfill, V.E. Fortov, A.M. Lipaev, V.I. Molotkov, A.I. Ivanov, M.V. Turin, Force field inside the void in complex plasmas under microgravity conditions, *Phys. Rev. E* 71 (2005) 056401/1–6.
- [26] A.M. Lipaev, V.I. Molotkov, A.P. Nefedov, O.F. Petrov, V.M. Torchinskii, V.E. Fortov, A.G. Khrapak, S.A. Khrapak, Ordered structures in a nonideal dusty glow-discharge plasma, *JETP* 85 (1997) 1110–1118.
- [27] V.E. Fortov, A.P. Nefedov, V.M. Torchinsky, V.I. Molotkov, O.F. Petrov, A.A. Samarian, A.M. Lipaev, A.G. Khrapak, Crystalline structures of strongly coupled dusty plasmas in DC glow discharge strata, *Phys. Lett. A* 229 (1997) 317–322.
- [28] A.P. Nefedov, O.F. Petrov, V.I. Molotkov, V.E. Fortov, Formation of liquidlike and crystalline structures in dusty plasmas, *JETP Lett.* 72 (2000) 218–226.
- [29] Y.B. Golubovskii, S.U. Nisimov, I.E. Suleimenov, 2-dimensional character of strata in low-pressure discharge in inert gases, *Tech. Phys.* 39 (1994) 1005–1008.
- [30] Y.B. Golubovskii, S.U. Nisimov, Two-dimensional character of striations in a low-pressure discharge in inert gases, II, *Tech. Phys.* 40 (1995) 24–28.
- [31] Y.B. Golubovskii, S.U. Nisimov, Ionization transport waves in a neon discharge, *Tech. Phys.* 41 (1996) 645–651.
- [32] Y. Nakamura, H. Bailung, A dusty double plasma device, *Rev. Sci. Instr.* 70 (1999) 2345–2348.
- [33] A.P. Nefedov, O.S. Vaulina, O.F. Petrov, V.I. Molotkov, V.M. Torchinskii, V.E. Fortov, A.V. Chernyshev, A.M. Lipaev, A.I. Ivanov, A.Y. Kaleri, Y.P. Semenov, S.V. Zaletin, The dynamics of macroparticles in a direct current glow discharge plasma under microgravitation conditions, *JETP* 95 (2002) 673–681.
- [34] V.E. Fortov, O.S. Vaulina, O.F. Petrov, V.I. Molotkov, A.V. Chernyshev, A.M. Lipaev, G. Morfill, H. Thomas, H. Rothermel, S.A. Khrapak, Y.P. Semenov, A.I. Ivanov, S.K. Krikalev, Y.P. Gidzenko, Dynamics of macroparticles in a dusty plasma under microgravity conditions (first experiments on board the ISS), *JETP* 96 (2003) 704–718.
- [35] V.E. Fortov, O.S. Vaulina, O.F. Petrov, V.I. Molotkov, A.M. Lipaev, V.M. Torchinsky, H.M. Thomas, G.E. Morfill, S.A. Khrapak, Y.P. Semenov, A.I. Ivanov, S.K. Krikalev, A.Y. Kalery, S.V. Zaletin, Y.P. Gidzenko, Transport of microparticles in weakly ionized gas-discharge plasmas under microgravity conditions, *Phys. Rev. Lett.* 90 (2003) 245005/1–4.
- [36] S. Ratynskaia, S. Khrapak, A. Zobnin, M.H. Thoma, M. Kretschmer, A. Usachev, V. Yaroshenko, R.A. Quinn, G.E. Morfill, O. Petrov, V. Fortov, Experimental determination of dust particle charge at elevated pressures, *Phys. Rev. Lett.* 93 (2004) 085001/1–4.

- [37] A. Usachev, A. Zobnin, O. Petrov, V. Fortov, M.H. Thoma, M. Kretschmer, S. Ratynskaia, R.A. Quinn, H. Höfner, G.E. Morfill, The project “Plasmakristall-4”—a dusty plasma experiment in a combined dc/rf(i) discharge plasma under microgravity conditions, *Czech. J. Phys.* 54 (2004) C639–C647.
- [38] V.E. Fortov, L.M. Vasilyak, S.P. Vetchinin, V.S. Zimmukhov, A.P. Nefedov, D.N. Polyakov, Plasma-dust structures at cryogenic temperatures, *Dokl. Phys.* 47 (2002) 21–24.
- [39] L.M. Vasilyak, S.P. Vetchinin, V.S. Zimmukhov, D.N. Polyakov, V.E. Fortov, Dust particles in a thermophoretic trap in a plasma, *JETP* 96 (2003) 436–439.
- [40] I.T. Yakubov, A.G. Khrapak, Thermophysical and electrophysical properties of low temperature plasma with condensed disperse phase, *Sov. Tech. Rev. B. Therm. Phys.* 2 (1989) 269–337.
- [41] V.E. Fortov, A.P. Nefedov, O.F. Petrov, A.A. Samarian, A.V. Chernyshev, Emission properties and structural ordering of strongly coupled dust particles in a thermal plasma, *Phys. Lett. A* 219 (1996) 89–94.
- [42] V.E. Fortov, A.P. Nefedov, O.F. Petrov, A.A. Samarian, A.V. Chernyshev, Particle ordered structures in a strongly coupled classical thermal plasma, *Phys. Rev. E* 54 (1996) R2236–R2239.
- [43] A.P. Nefedov, O.F. Petrov, V.E. Fortov, Quasicrystalline structures in strongly coupled dusty plasma, *Phys. Usp.* 40 (1997) 1163–1173.
- [44] V.E. Fortov, V.S. Filinov, A.P. Nefedov, O.F. Petrov, A.A. Samaryan, A.M. Lipaev, Creation of ordered structures in a classical thermal plasma containing macroparticles: experiment and computer simulation, *JETP* 84 (1997) 489–496.
- [45] V.E. Fortov, A.P. Nefedov, O.F. Petrov, A.A. Samaryan, A.V. Chernyshev, Highly nonideal classical thermal plasmas: experimental study of ordered macroparticle structures, *JETP* 84 (1997) 256–261.
- [46] A.P. Nefedov, O.F. Petrov, S.A. Khrapak, A.M. Lipaev, A.A. Samarian, Experimental determination of the diffusion coefficient for macroparticles in a thermal plasma by correlation spectroscopy, *High Temp.* 36 (1998) 137–142.
- [47] Y.K. Khodataev, S.A. Khrapak, A.P. Nefedov, O.F. Petrov, Dynamics of the ordered structure formation in a thermal dusty plasma, *Phys. Rev. E* 57 (1998) 7086–7092.
- [48] A.P. Nefedov, O.F. Petrov, Ya.K. Khodataev, S.A. Khrapak, Dynamics of formation of ordered structures in a thermal plasma with macroparticles, *JETP* 88 (1999) 460–464.
- [49] A.A. Samaryan, A.V. Chernyshev, A.P. Nefedov, O.F. Petrov, Y.M. Mikhailov, V.B. Mintsev, V.E. Fortov, Structures of the particles of the condensed dispersed phase in solid fuel combustion products plasma, *JETP* 90 (2000) 817–822.
- [50] V.I. Vladimirov, L.V. Deputatova, V.I. Molotkov, A.P. Nefedov, V.A. Rykov, V.S. Filinov, V.E. Fortov, A.V. Khudyakov, Ordered dusty structures in nuclear-track neon and argon plasmas, *Plasma Phys. Rep.* 27 (2001) 36–43.
- [51] V.E. Fortov, V.A. Rykov, V.I. Vladimirov, L.V. Deputatova, V.I. Molotkov, O.F. Petrov, V.S. Filinov, A.P. Budnik, P.P. D’yachenko, K.V. Rykov, A.V. Khudyakov, Dust particles in a track plasma produced by a proton beam, *Dokl. Phys.* 49 (2004) 497–500.
- [52] V.E. Fortov, V.A. Rykov, V.S. Filinov, V.I. Vladimirov, L.V. Deputatova, O.F. Petrov, V.I. Molotkov, A.P. Budnik, P.P. D’yachenko, K.V. Rykov, A.V. Khudyakov, Vortex dust structures in the track plasma of a proton beam, *Plasma Phys. Rep.* 31 (2005) 621–627.
- [53] P.M. Chung, L. Talbot, K.J. Touryan, *Electric Probes in Stationary and Flowing Plasmas: Theory and Application*, Springer, New York, 1975.
- [54] J.E. Allen, Probe theory: the orbital motion approach, *Phys. Scripta* 45 (1992) 497–503.
- [55] J. Goree, Charging of particles in a plasma, *Plasma Sources Sci. Technol.* 3 (1994) 400–406.
- [56] Y.L. Al’pert, A.V. Gurevich, L.P. Pitaevsky, *Space Physics with Artificial Satellites*, Consultants Bureau, New York, 1965.
- [57] S.A. Khrapak, A.V. Ivlev, G.E. Morfill, S.K. Zhdanov, Scattering in the attractive Yukawa potential in the limit of strong interaction, *Phys. Rev. Lett.* 90 (2003) 225002/1–4.
- [58] S.A. Khrapak, A.P. Nefedov, O.F. Petrov, O.S. Vaulina, Dynamical properties of random charge fluctuations in a dusty plasma with different charging mechanisms, *Phys. Rev. E* 59 (1999) 6017–6022 (Erratum in *Phys. Rev. E* 60 (1999) 3450).
- [59] S.A. Khrapak, G. Morfill, Waves in two component electron–dust plasma, *Phys. Plasmas* 8 (2001) 2629–2634.
- [60] O. Havnes, G.E. Morfill, C.K. Geortz, Plasma potential and grain charges in a dust cloud embedded in a plasma, *J. Geophys. Res.* 89 (1984) 999–1003.
- [61] A. Barkan, N. D’Angelo, R.L. Merlino, Charging of dust grains in a plasma, *Phys. Rev. Lett.* 73 (1994) 3093–3096.
- [62] J.E. Allen, B.M. Annaratone, U. de Angelis, On the orbital motion limited theory for a small body at floating potential in a Maxwellian plasma, *J. Plasma Phys.* 63 (2000) 299–309.
- [63] S.A. Khrapak, A.V. Ivlev, G.E. Morfill, Momentum transfer in complex plasmas, *Phys. Rev. E* 70 (2004) 056405/1–9.
- [64] R.V. Kennedy, J.E. Allen, The floating potential of spherical probes and dust grains. II: orbital motion theory, *J. Plasma Phys.* 69 (2003) 485–506.
- [65] A.V. Zobnin, A.P. Nefedov, V.A. Sinelshchikov, V.E. Fortov, On the charge of dust particles in a low-pressure gas discharge plasma, *JETP* 91 (2000) 483–487.
- [66] M. Lampe, V. Gavrishchaka, G. Ganguli, G. Joyce, Effect of trapped ions on shielding of a charged spherical object in a plasma, *Phys. Rev. Lett.* 86 (2001) 5278–5281.
- [67] M. Lampe, R. Goswami, Z. Sternovsky, S. Robertson, V. Gavrishchaka, G. Ganguli, G. Joyce, Trapped ion effect on shielding, current flow, and charging of a small object in a plasma, *Phys. Plasmas* 10 (2003) 1500–1513.
- [68] Z. Zakrzewski, T. Kopiczynski, Effect of collisions on positive ion collection by a cylindrical Langmuir probe, *Plasma Phys.* 16 (1974) 1195–1198.
- [69] Z. Sternovsky, S. Robertson, Effect of charge exchange ions upon Langmuir probe current, *Appl. Phys. Lett.* 81 (2002) 1961–1963.
- [70] Z. Sternovsky, S. Robertson, M. Lampe, Ion collection by cylindrical probes in weakly collisional plasmas: theory and experiment, *J. Appl. Phys.* 94 (2003) 1374–1381.
- [71] F. Taccogna, S. Longo, M. Capitelli, PIC model of the ion collection by a Langmuir probe, *Contrib. Plasma. Phys.* 44 (2004) 594–600.
- [72] G.J. Schulz, S.C. Brown, Microwave study of positive ion collection by probes, *Phys. Rev.* 98 (1955) 1642–1649.



- [73] S.A. Khrapak, S.V. Ratynskaia, A.V. Zobnin, A.D. Usachev, V.V. Yaroshenko, M.H. Thoma, M. Kretschmer, H. Höfner, G.E. Morfill, O.F. Petrov, V.E. Fortov, Particle charge in the bulk of gas discharges, *Phys. Rev. E* 72 (2005) 016406/1–10.
- [74] S.A. Khrapak, A.V. Ivlev, G.E. Morfill, H.M. Thomas, Ion drag force in complex plasmas, *Phys. Rev. E* 66 (2002) 046414/1–4.
- [75] S. Ratynskaia, M. Kretschmer, S. Khrapak, R.A. Quinn, M.H. Thoma, G.E. Morfill, A. Zobnin, A. Usachev, O. Petrov, V. Fortov, Dust mode in collisionally dominated complex plasmas with particle drift, *IEEE Trans. Plasma Sci.* 32 (2004) 613–616.
- [76] S. Khrapak, D. Samsonov, G. Morfill, H. Thomas, V. Yaroshenko, H. Rothermel, T. Hagl, V. Fortov, A. Nefedov, V. Molotkov, O. Petrov, A. Lipaev, A. Ivanov, Y. Baturin, Compressional waves in complex (dusty) plasmas under microgravity conditions, *Phys. Plasmas* 10 (2003) 1–4.
- [77] V.V. Yaroshenko, B.M. Annaratone, S.A. Khrapak, H.M. Thomas, G.E. Morfill, V.E. Fortov, A.M. Lipaev, V.I. Molotkov, O.F. Petrov, A.I. Ivanov, M.V. Turin, Electrostatic modes in collisional complex plasmas under microgravity conditions, *Phys. Rev. E* 69 (2004) 066401/1–7.
- [78] V.E. Fortov, O.F. Petrov, A.D. Usachev, A.V. Zobnin, Micron-sized particle-charge measurements in an inductive rf gas-discharge plasma using gravity-driven probe grains, *Phys. Rev. E* 70 (2004) 046415/1–6.
- [79] P. Bryant, Floating potential of spherical probes and dust grains in collisional plasmas, *J. Phys. D: Appl. Phys.* 36 (2003) 2859–2868.
- [80] J. Goree, Ion trapping by a charged dust grain in a plasma, *Phys. Rev. Lett.* 69 (1992) 277–280.
- [81] J.E. Daugherty, R.K. Porteous, M.D. Kilgore, D.B. Graves, Sheath structure around particles in low-pressure discharges, *J. Appl. Phys.* 72 (1992) 3934–3942.
- [82] H.S.W. Massey, E.H.S. Burhop, H.B. Gilbody, *Electronic and Ionic Impact Phenomena*, Oxford University Press, New York, 1969.
- [83] Yu.P. Raizer, *Gas Discharge Physics*, Springer, Berlin, 1991.
- [84] C.H. Su, S.H. Lam, Continuum theory of spherical electrostatic probes, *Phys. Fluids* 6 (1963) 1479–1491.
- [85] A.F. Pal', A.N. Starostin, A.V. Filippov, Charging of dust grains in a nuclear-induced plasma at high pressures, *Plasma Phys. Rep.* 27 (2001) 143–152.
- [86] A.F. Pal', A.O. Serov, A.N. Starostin, A.V. Filippov, V.E. Fortov, Non-self-sustained discharge in nitrogen with a condensed dispersed phase, *JETP* 92 (2001) 235–245.
- [87] A.F. Pal', D.V. Sivokhin, A.N. Starostin, A.V. Filippov, V.E. Fortov, Potential of a dust grain in a nitrogen plasma with a condensed disperse phase at room and cryogenic temperatures, *Plasma Phys. Rep.* 28 (2002) 28–39.
- [88] A.V. Filippov, N.A. Dyatko, A.F. Pal', A.N. Starostin, Development of a self-consistent model of dust grain charging at elevated pressures using the method of moments, *Plasma Phys. Rep.* 29 (2003) 190–202.
- [89] V.N. Babichev, A.F. Pal', A.N. Starostin, A.V. Filippov, V.E. Fortov, Stable dust structures in non-self-sustained gas discharge under atmospheric pressure, *JETP Lett.* 80 (2004) 241–245.
- [90] O. Bystrenko, A. Zagorodny, Screening of dust grains in a weakly ionized gas: effects of charging by plasma currents, *Phys. Rev. E* 67 (2003) 066403/1–5.
- [91] A.A. Uglov, A.G. Gnedovets, Effect of particle charging on momentum and heat-transfer from rarefied plasma-flow, *Plasma Chem. Plasma Proc.* 11 (1991) 251–267.
- [92] M.D. Kilgore, J.E. Daugherty, R.K. Porteous, D.B. Graves, Transport and heating of small particles in high density plasma sources, *J. Vac. Sci. Technol. B* 12 (1994) 486–493.
- [93] E.B. Tomme, D.A. Law, B.M. Annaratone, J.E. Allen, Parabolic plasma sheath potentials and their implications for the charge on levitated dust particles, *Phys. Rev. Lett.* 85 (2000) 2518–2521.
- [94] T. Nitter, Levitation of dust in RF and DC glow discharges, *Plasma Sources Sci. Technol.* 5 (1996) 93–99.
- [95] G. Lapenta, Simulation of charging and shielding of dust particles in drifting plasmas, *Phys. Plasmas* 6 (1999) 1442–1447.
- [96] I.H. Hutchinson, Ion collection by a sphere in a flowing plasma: 2. Non-zero Debye length, *Plasma Phys. Control. Fusion* 45 (2003) 1477–1500.
- [97] I.H. Hutchinson, Ion collection by a sphere in a flowing plasma: 3. Floating potential and drag force, *Plasma Phys. Control. Fusion* 47 (2005) 71–87.
- [98] A.V. Ivlev, G. Morfill, V.E. Fortov, Potential of a dielectric particle in a flow of a collisionless plasma, *Phys. Plasmas* 6 (1999) 1416–1420.
- [99] V.A. Schweigert, Dielectric permittivity of a plasma in an external electric field, *Plasma Phys. Rep.* 27 (2001) 997–999.
- [100] L.D. Landau, E.M. Lifshitz, *Mechanics*, Pergamon, Oxford, 1976.
- [101] T. Trottenberg, A. Melzer, A. Piel, Measurement of the electric charge on particulates forming Coulomb crystals in the sheath of a radiofrequency plasma, *Plasma Sources Sci. Technol.* 4 (1995) 450–458.
- [102] M. Zuzic, H.M. Thomas, G.E. Morfill, Wave propagation and damping in plasma crystals, *J. Vac. Sci. Technol. A* 14 (1996) 496–500.
- [103] A. Homann, A. Melzer, A. Piel, Measuring the charge on single particles by laser-excited resonances in plasma crystals, *Phys. Rev. E* 59 (1999) R3835–R3838.
- [104] A. Piel, A. Melzer, Dynamical processes in complex plasmas, *Plasma Phys. Control. Fusion* 44 (2002) R1–R26.
- [105] A. Piel, A. Homann, M. Klindworth, A. Melzer, C. Zafiu, V. Nosenko, J. Goree, Waves and oscillations in plasma crystals, *J. Phys. B: At. Mol. Opt. Phys.* 36 (2003) 533–543.
- [106] A.A. Samarian, S.V. Vladimirov, Charge of a macroscopic particle in a plasma sheath, *Phys. Rev. E* 67 (2003) 066404/1–5.
- [107] S. Peters, A. Homann, A. Melzer, A. Piel, Measurement of dust particle shielding in a plasma from oscillations of a linear chain, *Phys. Lett. A* 223 (1996) 389–393.
- [108] A. Homann, A. Melzer, S. Peters, A. Piel, Determination of the dust screening length by laser-excited lattice waves, *Phys. Rev. E* 56 (1997) 7138–7141.
- [109] A. Homann, A. Melzer, S. Peters, R. Madani, A. Piel, Laser-excited dust lattice waves in plasma crystals, *Phys. Lett. A* 242 (1998) 173–180.
- [110] S. Nunomura, D. Samsonov, J. Goree, Transverse waves in a two-dimensional screened-Coulomb crystal (dusty plasma), *Phys. Rev. Lett.* 84 (2000) 5141–5144.



- [111] S. Nunomura, J. Goree, S. Hu, X. Wang, A. Bhattacharjee, Dispersion relations of longitudinal and transverse waves in two-dimensional screened Coulomb crystals, *Phys. Rev. E* 65 (2002) 066402/1–11.
- [112] V.E. Fortov, A.P. Nefedov, V.I. Molotkov, M.Y. Poustynnik, V.M. Torchinsky, Dependence of the dust–particle charge on its size in a glow-discharge plasma, *Phys. Rev. Lett.* 87 (2001) 205002/1–4.
- [113] A.A. Samarian, S.V. Vladimirov, Comment on “Dependence of the dust–particle charge on its size in a glow-discharge plasma”, *Phys. Rev. Lett.* 89 (2002) 229501/1.
- [114] D.I. Zhukhovitskii, A.G. Khrapak, I.T. Yakubov, Ionization equilibrium in plasma with condensed disperse phase (in Russian), in: B.M. Smirnov (Ed.), *Khimiya Plazmy Plasma Chemistry*, vol. 11, Energo-atomizdat, Moscow, 1984, pp. 130–170.
- [115] M.S. Sodha, S. Guha, Physics of colloidal plasmas, *Adv. Plasma Phys.* 4 (1971) 219–309.
- [116] S.L. Soo, *Multiphase Fluid Dynamics*, Gower Technical, Brookfield, 1990.
- [117] P. Bliokh, V. Sinitsin, V. Yaroshenko, *Dusty and Self-Gravitational Plasmas in Space*, Kluwer, Dordrecht, 1995.
- [118] D.A. Mendis, Progress in the study of dusty plasmas, *Plasma Sources Sci. Technol.* 11 (2002) A219–A228.
- [119] V.E. Fortov, A.P. Nefedov, O.S. Vaulina, A.M. Lipaev, V.I. Molotkov, A.A. Samaryan, V.P. Nikitskii, A.I. Ivanov, S.F. Savin, A.V. Kalmykov, A.Ya. Soloviev, P.V. Vinogradov, Dusty plasma induced by solar radiation under microgravitational conditions: an experiment on board the Mir orbiting space station, *JETP* 87 (1998) 1087–1097.
- [120] A.A. Sickafoose, J.E. Colwell, M. Horanyi, S. Robertson, Photoelectric charging of dust particles in vacuum, *Phys. Rev. Lett.* 84 (2000) 6034–6037.
- [121] B. Walch, M. Horanyi, S. Robertson, Charging of dust grains in plasma with energetic electrons, *Phys. Rev. Lett.* 75 (1995) 838–840.
- [122] M. Rosenberg, D.A. Mendis, UV-induced Coulomb crystallization in a dusty gas, *IEEE Trans. Plasma Sci.* 23 (1995) 177–179.
- [123] M. Rosenberg, D.A. Mendis, D.P. Sheehan, UV-induced Coulomb crystallization of dust grains in high-pressure gas, *IEEE Trans. Plasma Sci.* 24 (1996) 1422–1430.
- [124] M. Rosenberg, D.A. Mendis, D.P. Sheehan, Positively charged dust crystals induced by radiative heating, *IEEE Trans. Plasma Sci.* 27 (1999) 239–242.
- [125] J.P. Boeuf, Characteristics of a dusty nonthermal plasma from a particle-in-cell Monte Carlo simulation, *Phys. Rev. A* 46 (1992) 7910–7922.
- [126] G.E. Morfill, E. Grün, T.V. Johnson, Dust in Jupiter’s magnetosphere—physical processes, *Planet. Space Sci.* 28 (1980) 1087–1100.
- [127] C. Cui, J. Goree, Fluctuations of the charge on a dust grain in a plasma, *IEEE Trans. Plasma Sci.* 22 (1994) 151–158.
- [128] T. Matsoukas, M. Russell, Particle charging in low-pressure plasmas, *J. Appl. Phys.* 77 (1995) 4285–4292.
- [129] T. Matsoukas, M. Russel, M. Smith, Stochastic charge fluctuations in dusty plasmas, *J. Vac. Sci. Technol.* 14 (1996) 624–630.
- [130] T. Matsoukas, M. Russell, Fokker-Planck description of particle charging in ionized gases, *Phys. Rev. E* 55 (1997) 991–994.
- [131] G.E. Uhlenbeck, L.S. Ornstein, On the theory of the Brownian motion, *Phys. Rev.* 36 (1930) 823–841.
- [132] O.S. Vaulina, S.A. Khrapak, A.P. Nefedov, O.F. Petrov, Charge fluctuations induced heating of dust particles in a plasma, *Phys. Rev. E* 60 (1999) 5959–5964.
- [133] O.S. Vaulina, A.P. Nefedov, O.F. Petrov, S.A. Khrapak, Role of stochastic fluctuations in the charge on macroscopic particles in dusty plasmas, *JETP* 88 (1999) 1130–1136.
- [134] O.S. Vaulina, S.A. Khrapak, A.A. Samarian, O.F. Petrov, Effect of stochastic grain charge fluctuations on the kinetic energy of the particles in dusty plasma, *Phys. Scripta T* 84 (2000) 229–231.
- [135] R.A. Quinn, J. Goree, Single-particle Langevin model of particle temperature in dusty plasmas, *Phys. Rev. E* 61 (2000) 3033–3041.
- [136] G. Morfill, A.V. Ivlev, J.R. Jokipii, Charge fluctuation instability of the dust lattice wave, *Phys. Rev. Lett.* 83 (1999) 971–974.
- [137] A.V. Ivlev, U. Konopka, G. Morfill, Influence of charge variations on particle oscillations in the plasma sheath, *Phys. Rev. E* 62 (2000) 2739–2744.
- [138] S.A. Khrapak, G.E. Morfill, Dust diffusion across a magnetic field due to random charge fluctuations, *Phys. Plasmas* 9 (2002) 619–623.
- [139] D.H.E. Dubin, Nonlinear Debye shielding in a dusty plasma, in: P.K. Shukla, D.A. Mendis, V.W. Chow (Eds.), *The Physics of Dusty Plasmas*, World Scientific, Singapore, 1996, pp. 15–21.
- [140] A.P. Nefedov, O.F. Petrov, S.A. Khrapak, Potential of electrostatic interaction in a thermal dusty plasma, *Plasma Phys. Rep.* 24 (1998) 1037–1040.
- [141] O. Bystrenko, A. Zagorodny, Critical effects in screening of high-Z impurities, *Phys. Lett. A* 255 (1999) 325–330.
- [142] J.G. Laframboise, L.W. Parker, Probe design for orbit-limited current collection, *Phys. Fluids* 16 (1973) 629–636.
- [143] V.N. Tsytovich, N. Gusein-Zade, G. Morfill, Dust–dust interactions and formation of helical dust structures, *IEEE Trans. Plasma Sci.* 32 (2004) 637–652.
- [144] I.B. Bernstein, I.N. Rabinowitz, Theory of electrostatic probes in a low-density plasma, *Phys. Fluids* 2 (1959) 112–121.
- [145] M. Lampe, G. Joyce, G. Ganguli, V. Gavrilshchaka, Interactions between dust grains in a dusty plasma, *Phys. Plasmas* 7 (2000) 3851–3861.
- [146] S.A. Khrapak, A.V. Ivlev, G. Morfill, Interaction potential of microparticles in a plasma: role of collisions with plasma particles, *Phys. Rev. E* 64 (2001) 046403/1–7.
- [147] A.F. Aleksandrov, L.S. Bogdankevich, A.A. Rukhadze, *Principles of Plasma Electrodynamics*, Springer, New York, 1984.
- [148] M. Nambu, S.V. Vladimirov, P.K. Shukla, Attractive forces between charged particulates in plasmas, *Phys. Lett. A* 203 (1995) 40–42.
- [149] S.V. Vladimirov, M. Nambu, Attraction of charged particulates in plasmas with finite flows, *Phys. Rev. E* 52 (1995) R2172–R2174.
- [150] S.V. Vladimirov, O. Ishihara, On plasma crystal formation, *Phys. Plasmas* 3 (1996) 444–446.
- [151] O. Ishihara, S.V. Vladimirov, Wake potential of a dust grain in a plasma with ion flow, *Phys. Plasmas* 4 (1997) 69–74.
- [152] B. Xie, K. He, Z. Huang, Attractive potential in weak ion flow coupling with dust–acoustic waves, *Phys. Lett. A* 253 (1999) 83–87.
- [153] D.S. Lemons, M.S. Murillo, W. Daughton, D. Winske, Two-dimensional wake potentials in sub- and supersonic dusty plasmas, *Phys. Plasmas* 7 (2000) 2306–2313.
- [154] G. Lapenta, Linear theory of plasma wakes, *Phys. Rev. E* 62 (2000) 1175–1181.

- [155] F. Melandsø, J. Goree, Polarized supersonic plasma flow simulation for charged bodies such as dust particles and spacecraft, *Phys. Rev. E* 52 (1995) 5312–5326.
- [156] S.A. Maiorov, S.V. Vladimirov, N.F. Cramer, Plasma kinetics around a dust grain in an ion flow, *Phys. Rev. E* 63 (2001) 017401/1–4.
- [157] D. Winske, Nonlinear wake potential in a dusty plasma, *IEEE Trans. Plasma Sci.* 29 (2001) 191–197.
- [158] G. Lapenta, Nature of the force field in plasma wakes, *Phys. Rev. E* 66 (2002) 026409/1–6.
- [159] S.V. Vladimirov, S.A. Maiorov, O. Ishihara, Molecular dynamics simulation of plasma flow around two stationary dust grains, *Phys. Plasmas* 10 (2003) 3867–3873.
- [160] B.M. Bolotovskii, S.N. Stolyarov, Radiation from and energy-loss by charged-particles in moving media, *Phys. Usp.* 35 (1992) 143–150.
- [161] V.L. Ginzburg, Radiation by uniformly moving sources (Vavilov–Cherenkov effect, transition radiation, and other phenomena), *Phys. Usp.* 39 (1996) 973–982.
- [162] L.-J. Hou, Y.-N. Wang, Z.L. Mišković, Induced potential of a dust particle in a collisional radio-frequency sheath, *Phys. Rev. E* 68 (2003) 016410/1–7.
- [163] M. Lampe, G. Joyce, G. Ganguli, Analytic and simulation studies of dust grain interaction and structuring, *Phys. Scripta T* 89 (2001) 106–111.
- [164] L.-J. Hou, Y.-N. Wang, Z.L. Miskovic, Interaction potential among dust grains in a plasma with ion flow, *Phys. Rev. E* 64 (2001) 046406/1–7.
- [165] O. Ishihara, S.V. Vladimirov, N.F. Cramer, Effect of dipole moment on the wake potential of a dust grain, *Phys. Rev. E* 61 (2000) 7246–7248.
- [166] G.E. Morfill, V.N. Tsytovich, H. Thomas, Complex plasmas: II. elementary processes in complex plasmas, *Plasma Phys. Rep.* 29 (2003) 1–30.
- [167] A.M. Ignatov, Lesage gravity in dusty plasmas, *Plasma Phys. Rep.* 22 (1996) 585–589.
- [168] V.N. Tsytovich, Ya.K. Khodataev, R. Bingham, Formation of a dust molecule in plasmas as a first step to super-chemistry, *Comments Plasma Phys. Control. Fusion* 17 (1996) 249–265.
- [169] A.M. Ignatov, Basics of dusty plasma, *Plasma Phys. Rep.* 31 (2005) 46–56.
- [170] J.E. Daugherty, D.B. Graves, Particulate temperature in radio frequency glow discharges, *J. Vac. Sci. Technol. A* 11 (1993) 1126–1134.
- [171] V.N. Tsytovich, Ya.K. Khodataev, G.E. Morfill, R. Bingham, D.J. Winter, Radiative dust cooling and dust agglomeration in plasmas, *Comments Plasma Phys. Control. Fusion* 18 (1998) 281–291.
- [172] U. Konopka, L. Ratke, H.M. Thomas, Central collisions of charged dust particles in a plasma, *Phys. Rev. Lett.* 79 (1997) 1269–1272.
- [173] K. Takahashi, T. Oishi, K.I. Shimonai, Y. Hayashi, S. Nishino, Analyses of attractive forces between particles in Coulomb crystal of dusty plasmas by optical manipulations, *Phys. Rev. E* 58 (1998) 7805–7811.
- [174] A. Melzer, V.A. Schweigert, A. Piel, Transition from attractive to repulsive forces between dust molecules in a plasma sheath, *Phys. Rev. Lett.* 83 (1999) 3194–3197.
- [175] G.A. Hebner, M.E. Riley, B.M. Marder, Dynamic probe of dust wakefield interactions using constrained collisions, *Phys. Rev. E* 68 (2003) 016403/1–5.
- [176] G.A. Hebner, M.E. Riley, Measurement of attractive interactions produced by the ion wakefield in dusty plasmas using a constrained collision geometry, *Phys. Rev. E* 68 (2003) 046401/1–11.
- [177] S.A. Khrapak, A.V. Ivlev, G.E. Morfill, S.K. Zhdanov, H.M. Thomas, Scattering in the attractive Yukawa potential: Application to the ion-drag force in complex plasmas, *IEEE Trans. Plasma Sci.* 32 (2004) 555–560.
- [178] G.H. Lane, E. Everhart, Calculations of total cross sections for scattering from Coulomb potentials with exponential screening, *Phys. Rev.* 117 (1960) 920–924.
- [179] S.A. Khrapak, A.V. Ivlev, G.E. Morfill, H.M. Thomas, Ion drag in complex plasmas, in: R. Bharuthram, M.A. Hellberg, P.K. Shukla, F. Verheest (Eds.), *Dusty Plasma in the New Millennium*, AIP Conference Proceedings, vol. 649, 2002, pp. 341–344.
- [180] V.E. Fortov, A.G. Khrapak, S.A. Khrapak, V.I. Molotkov, O.F. Petrov, Dusty plasmas, *Phys. Usp.* 47 (2004) 447–492.
- [181] H.-S. Hahn, E.A. Mason, F.J. Smith, Quantum transport cross sections for ionized gases, *Phys. Fluids* 14 (1971) 278–287.
- [182] E.M. Baroody, Classical scattering by some important repulsive potentials, *Phys. Fluids* 5 (1962) 925–932.
- [183] B.M. Smirnov, The hard-sphere model in plasma and gas physics, *Phys. Usp.* 25 (1982) 854–862.
- [184] M.D. Kilgore, J.E. Daugherty, R.K. Porteous, D.B. Graves, Ion drag on an isolated particulate in low-pressure discharge, *J. Appl. Phys.* 73 (1993) 7195–7202.
- [185] S.A. Khrapak, G.E. Morfill, Dusty plasmas in a constant electric field: Role of the electron drag force, *Phys. Rev. E* 69 (2004) 066411/1–5.
- [186] G.E. Morfill, B.M. Annaratone, P. Bryant, A.V. Ivlev, H.M. Thomas, M. Zuzic, V.E. Fortov, A review of liquid and crystalline plasmas—new physical states of matter?, *Plasma Phys. Control. Fusion* 44 (2002) B263–B277.
- [187] G.E. Morfill, H.M. Thomas, U. Konopka, M. Zuzic, The plasma condensation: Liquid and crystalline plasmas, *Phys. Plasmas* 6 (1999) 1769–1780.
- [188] Y. Hayashi, Structure of a three-dimensional Coulomb crystal in a fine-particle plasma, *Phys. Rev. Lett.* 83 (1999) 4764–4767.
- [189] H.M. Thomas, G.E. Morfill, Melting dynamics of a plasma crystal, *Nature (London)* 379 (1996) 806–809.
- [190] S.V. Vladimirov, K. Ostrikov, Dynamic self-organization phenomena in complex ionized gas systems: new paradigms and technological aspects, *Phys. Rep.* 393 (2004) 175–380.
- [191] G.E. Morfill, S.A. Khrapak, A.V. Ivlev, B.A. Klumov, M. Rubin-Zuzic, H.M. Thomas, From fluid flows to crystallization: new results from complex plasmas, *Phys. Scripta T* 107 (2004) 59–64.
- [192] G.E. Morfill, A.V. Ivlev, S.A. Khrapak, B.A. Klumov, M. Rubin-Zuzic, U. Konopka, H.M. Thomas, Ten years of plasma crystals—from ICPIG (Bochum) to ICPIG (Greifswald), *Contrib. Plasma Phys.* 44 (2004) 450–457.
- [193] P. Epstein, On the resistance experienced by spheres in their motion through gases, *Phys. Rev.* 23 (1924) 710–733.
- [194] B. Liu, J. Goree, V. Nosenko, L. Boufendi, Radiation pressure and gas drag forces on a melamine-formaldehyde microsphere in a dusty plasma, *Phys. Plasmas* 10 (2003) 9–20.

- [195] A.V. Ivlev, S.A. Khrapak, S.K. Zhdanov, G.E. Morfill, G. Joyce, Force on a charged test particle in a collisional flowing plasma, *Phys. Rev. Lett.* 92 (2004) 205007/1–4.
- [196] G.E. Morfill, E. Grün, The motion of charged dust particles in interplanetary space. I—The zodiacal dust cloud, II—Interstellar grains, *Planet. Space Sci.* 27 (1979) 1269–1292.
- [197] T.G. Northrop, T.J. Birmingham, Plasma drag on a dust grain due to Coulomb collisions, *Planet. Space Sci.* 38 (1990) 319–326.
- [198] M.S. Barnes, J.H. Keller, J.C. Forster, J.A. O'Neill, D.K. Coultas, Transport of dust particles in glow-discharge plasmas, *Phys. Rev. Lett.* 68 (1992) 313–316.
- [199] D. Samsonov, A.V. Ivlev, G.E. Morfill, J. Goree, Long-range attractive and repulsive forces in a two-dimensional complex (dusty) plasma, *Phys. Rev. E* 63 (2001) 025401(R)/1–4.
- [200] U. Konopka, D. Samsonov, A.V. Ivlev, J. Goree, V. Steinberg, G.E. Morfill, Rigid and differential plasma crystal rotation induced by magnetic fields, *Phys. Rev. E* 61 (2000) 1890–1898.
- [201] P.K. Kaw, K. Nishikawa, N. Sato, Rotation in collisional strongly coupled dusty plasmas in a magnetic field, *Phys. Plasmas* 9 (2002) 387–390.
- [202] O. Ishihara, T. Kamimura, K.I. Hirose, N. Sato, Rotation of a two-dimensional Coulomb cluster in a magnetic field, *Phys. Rev. E* 66 (2002) 046406/1–6.
- [203] N. D'Angelo, Dusty plasma ionization instability with ion drag, *Phys. Plasmas* 5 (1998) 3155–3160.
- [204] A.V. Ivlev, D. Samsonov, J. Goree, G. Morfill, V.E. Fortov, Acoustic modes in a collisional dusty plasma, *Phys. Plasmas* 6 (1999) 741–750.
- [205] S.A. Khrapak, V.V. Yaroshenko, Low-frequency waves in collisional complex plasmas with an ion drift, *Phys. Plasmas* 10 (2003) 4616–4621.
- [206] S.A. Trigger, Fokker-Planck equation for Boltzmann-type and active particles: transfer probability approach, *Phys. Rev. E* 67 (2003) 046403/1–10.
- [207] S.A. Trigger, W. Ebeling, A.M. Ignatov, I.M. Tkachenko, Fokker–Planck equation with velocity-dependent coefficients: application to dusty plasmas and active particles, *Contrib. Plasma Phys.* 43 (2003) 377–380.
- [208] W.B. Thompson, J. Hubbard, Long-range forces and the diffusion coefficients of a plasma, *Rev. Mod. Phys.* 32 (1960) 714–718.
- [209] D. Montgomery, G. Joyce, R. Sugihara, Inverse third power law for the shielding of test particles, *Plasma Phys.* 10 (1968) 681–685.
- [210] A.V. Ivlev, S.K. Zhdanov, S.A. Khrapak, G.E. Morfill, Ion drag force in dusty plasmas, *Plasma Phys. Control. Fusion* 46 (2004) B267–B279.
- [211] A.V. Ivlev, S.K. Zhdanov, S.A. Khrapak, G.E. Morfill, Kinetic approach for the ion drag force in a collisional plasma, *Phys. Rev. E* 71 (2005) 016405/1–7.
- [212] S.A. Khrapak, A.V. Ivlev, S.K. Zhdanov, G.E. Morfill, Hybrid approach to the ion drag force, *Phys. Plasmas* 12 (2005) 042308/1–8.
- [213] E.M. Lifshitz, L.P. Pitaevskii, *Physical Kinetics*, Pergamon, Oxford, 1981.
- [214] P.L. Bhatnagar, E.P. Gross, M. Krook, A model for collision processes in gases. I. Small amplitude processes in charged and neutral one-component systems, *Phys. Rev.* 94 (1954) 511–525.
- [215] M.A. Lieberman, A.J. Lichtenberg, *Principles of Plasma Discharges and Materials Processing*, Wiley, New York, 1994.
- [216] B.D. Fried, S.D. Conte, *The Plasma Dispersion Function*, Academic Press, New York, 1961.
- [217] S.A. Khrapak, A.V. Ivlev, G.E. Morfill, H.M. Thomas, S.K. Zhdanov, U. Konopka, M.H. Thoma, R.A. Quinn, Comment on “Measurement of the ion drag force on falling dust particles and its relation to the void formation in complex (dusty) plasmas” (*Phys. Plasmas* 10 (2003) 1278), *Phys. Plasmas* 10 (2003) 4579–4581.
- [218] C. Zafiu, A. Melzer, A. Piel, Response to “Comment on Measurement of the ion drag force on falling dust particles and its relation to the void formation in complex (dusty) plasmas””, *Phys. Plasmas* 10 (2003) 4582–4583 (*Phys. Plasmas* 10 (2003) 4579).
- [219] J.E. Daugherty, R.K. Porteus, D.B. Graves, Electrostatic forces on small particles in low-pressure discharges, *J. Appl. Phys.* 73 (1993) 1617–1620.
- [220] L. Talbot, R.K. Cheng, R.W. Schefer, D.R. Willis, Thermophoresis of particles in a heated boundary layer, *J. Fluid Mech.* 101 (1980) 737–758.
- [221] O. Havnes, T. Nitter, V. Tsytovich, G.E. Morfill, T. Hartquist, On the thermophoretic force close to walls in dusty plasma experiments, *Plasma Sources Sci. Technol.* 3 (1994) 448–457.
- [222] G.M. Jellum, J.E. Daugherty, D.B. Graves, Particle thermophoresis in low pressure glow discharges, *J. Appl. Phys.* 69 (1991) 6923–6934.
- [223] V.V. Balabanov, L.M. Vasilyak, S.P. Vetchinin, A.P. Nefedov, D.N. Polyakov, V.E. Fortov, The effect of the gas temperature gradient on dust structures in a glow-discharge plasma, *JETP* 92 (2001) 86–92.
- [224] H. Rothermel, T. Hagl, G.E. Morfill, M.H. Thoma, H.M. Thomas, Gravity compensation in complex plasmas by application of a temperature gradient, *Phys. Rev. Lett.* 89 (2002) 175001/1–4.
- [225] B.T. Draine, E.E. Salpeter, On the physics of dust grains in hot gas, *Astrophys. J.* 231 (1979) 77–94.
- [226] L.D. Landau, E.M. Lifshitz, *Fluid Mechanics*, Pergamon Press, Oxford, 1987.
- [227] A.V. Ivlev, R. Sütterlin, V. Steinberg, M. Zuzic, G. Morfill, Nonlinear vertical oscillations of a particle in a sheath of rf discharge, *Phys. Rev. Lett.* 85 (2000) 4060–4063.
- [228] C. Zafiu, A. Melzer, A. Piel, Nonlinear resonances of particles in a dusty plasma sheath, *Phys. Rev. E* 63 (2001) 066403/1–8.
- [229] Y.-N. Wang, L.-J. Hou, X. Wang, Self-consistent nonlinear resonance and hysteresis of a charged microparticle in a rf sheath, *Phys. Rev. Lett.* 89 (2002) 155001/1–4.
- [230] S. Nunomura, T. Misawa, N. Ohno, S. Takamura, Instability of dust particles in a Coulomb crystal due to delayed charging, *Phys. Rev. Lett.* 83 (1999) 1970–1973.
- [231] T. Misawa, N. Ohno, K. Asano, M. Sawai, S. Takamura, P.K. Kaw, Experimental observation of vertically polarized transverse dust–lattice wave propagating in a one-dimensional strongly coupled dust chain, *Phys. Rev. Lett.* 86 (2001) 1219–1222.
- [232] A.A. Samarian, B.W. James, S.V. Vladimirov, N.F. Cramer, Self-excited vertical oscillations in an rf-discharge dusty plasma, *Phys. Rev. E* 64 (2001) 025402(R)/1–4.

- [233] V.V. Zhakhovskii, V.I. Molotkov, A.P. Nefedov, V.M. Torchinskii, A.G. Khrapak, V.E. Fortov, Anomalous heating of a system of dust particles in a gas-discharge plasma, *JETP Lett.* 66 (1997) 419–425.
- [234] O.S. Vaulina, A.P. Nefedov, O.F. Petrov, V.E. Fortov, Instability of plasma-dust systems with a microparticle charge gradient, *JETP* 91 (2000) 1147–1162.
- [235] O.S. Vaulina, A.A. Samarian, O.F. Petrov, B. James, F. Melandsø, Formation of vortex structures in inhomogeneous gas-discharge plasmas, *Plasma Phys. Rep.* 30 (2004) 918–936.
- [236] A.V. Ivlev, S.K. Zhdanov, B.A. Klumov, V.N. Tsytovich, U. de Angelis, G.E. Morfill, Kinetics of ensembles with variable charges, *Phys. Rev E* 70 (2004) 066401/1–5.
- [237] U. de Angelis, A.V. Ivlev, G.E. Morfill, V.N. Tsytovich, Stochastic heating of dust particles with fluctuating charges, *Phys. Plasmas* 12 (2005) 052301/1–4.
- [238] A. Melzer, V.A. Schweigert, I.V. Schweigert, A. Homann, S. Peters, A. Piel, Structure and stability of the plasma crystal, *Phys. Rev. E* 54 (1996) R46–R49.
- [239] A.V. Ivlev, U. Konopka, G. Morfill, G. Joyce, Melting of monolayer plasma crystals, *Phys. Rev. E* 68 (2003) 026405/1–4.
- [240] V. Steinberg, R. Sütterlin, A.V. Ivlev, G. Morfill, Vertical pairing of identical particles suspended in the plasma sheath, *Phys. Rev. Lett.* 86 (2001) 4540–4543.
- [241] A.A. Samarian, S.V. Vladimirov, B.W. James, Dust particle alignments and confinement in a radio frequency sheath, *Phys. Plasmas* 12 (2005) 022103/1–6.
- [242] M. Lampe, G. Joyce, G. Ganguli, Structure and dynamics of dust in streaming plasma: dust molecules, strings and crystals, *IEEE Trans. Plasma Sci.* 33 (2005) 57–69.
- [243] V.N. Tsytovich, U. de Angelis, Kinetic theory of dusty plasmas I. General approach, *Phys. Plasmas* 6 (1999) 1093–1106.
- [244] V.N. Tsytovich, U. de Angelis, Kinetic theory of dusty plasmas II. Dust–plasma particle collision integrals, *Phys. Plasmas* 7 (2000) 554–563.
- [245] V.N. Tsytovich, U. de Angelis, Kinetic theory of dusty plasmas III. Dust–dust collision integrals, *Phys. Plasmas* 8 (2001) 1141–1153.
- [246] V.N. Tsytovich, U. de Angelis, Kinetic theory of dusty plasmas IV. Distribution and fluctuations of dust charges, *Phys. Plasmas* 9 (2002) 2497–2506.
- [247] V.N. Tsytovich, U. de Angelis, Kinetic theory of dusty plasmas V. The hydrodynamic equations, *Phys. Plasmas* 11 (2004) 496–506.
- [248] J.H. Chu, J.B. Du, L. I, Coulomb solids and low-frequency fluctuations in RF dusty plasmas, *J. Phys. D: Appl. Phys.* 27 (1994) 296–300.
- [249] A. Barkan, R.L. Merlino, N. D’Angelo, Laboratory observation of the dust–acoustic wave mode, *Phys. Plasmas* 2 (1995) 3563–3565.
- [250] V.I. Molotkov, A.P. Nefedov, V.M. Torchinskii, V.E. Fortov, A.G. Khrapak, Dust acoustic waves in a dc glow-discharge plasma, *JETP* 89 (1999) 477–480.
- [251] V.E. Fortov, A.G. Khrapak, S.A. Khrapak, V.I. Molotkov, A.P. Nefedov, O.F. Petrov, V.M. Torchinsky, Mechanism of dust–acoustic instability in a current glow discharge plasma, *Phys. Plasmas* 7 (2000) 1374–1380.
- [252] A.V. Zobnin, A.D. Usachev, O.F. Petrov, V.E. Fortov, Dust–acoustic instability in an inductive gas-discharge plasma, *JETP* 95 (2002) 429–439.
- [253] V.E. Fortov, A.D. Usachev, A.V. Zobnin, V.I. Molotkov, O.F. Petrov, Dust–acoustic wave instability at the diffuse edge of radio frequency inductive low-pressure gas discharge plasma, *Phys. Plasmas* 10 (2003) 1199–1207.
- [254] D. Samsonov, J. Goree, Z.W. Ma, A. Bhattacharjee, H.M. Thomas, G.E. Morfill, Mach cones in a Coulomb lattice and a dusty plasma, *Phys. Rev. Lett.* 83 (1999) 3649–3652.
- [255] D. Samsonov, J. Goree, H.M. Thomas, G.E. Morfill, Mach cone shocks in a two-dimensional Yukawa solid using a complex plasma, *Phys. Rev. E* 61 (2000) 5557–5572.
- [256] S. Nunomura, J. Goree, S. Hu, X. Wang, A. Bhattacharjee, K. Avinash, Phonon spectrum in a plasma crystal, *Phys. Rev. Lett.* 89 (2002) 035001/1–4.
- [257] S. Zhdanov, S. Nunomura, D. Samsonov, G. Morfill, Polarization of wave modes in a two-dimensional hexagonal lattice using a complex (dusty) plasma, *Phys. Rev. E* 68 (2003) 035401(R)/1–4.
- [258] S. Nunomura, S. Zhdanov, D. Samsonov, G. Morfill, Wave spectra in solid and liquid complex (dusty) plasmas, *Phys. Rev. Lett.* 94 (2005) 045001/1–4.
- [259] Y. Nakamura, H. Bailung, P.K. Shukla, Observation of ion-acoustic shocks in a dusty plasma, *Phys. Rev. Lett.* 83 (1999) 1602–1605.
- [260] Y. Nakamura, A. Sarma, Observation of ion-acoustic solitary waves in a dusty plasma, *Phys. Plasmas* 8 (2001) 3921–3926.
- [261] Y. Nakamura, Experiments on ion-acoustic shock waves in a dusty plasma, *Phys. Plasmas* 9 (2002) 440–445.
- [262] J.B. Pieper, J. Goree, Dispersion of plasma dust acoustic waves in the strong-coupling regime, *Phys. Rev. Lett.* 77 (1996) 3137–3140.
- [263] D. Samsonov, A.V. Ivlev, R.A. Quinn, G. Morfill, S. Zhdanov, Dissipative longitudinal solitons in a two-dimensional strongly coupled complex (dusty) plasma, *Phys. Rev. Lett.* 88 (2002) 095004/1–4.
- [264] D. Samsonov, S. Zhdanov, R.A. Quinn, S.I. Popel, G.E. Morfill, Shock melting of a two-dimensional complex (dusty) plasma, *Phys. Rev. Lett.* 92 (2004) 255004/1–4.
- [265] D. Samsonov, S. Zhdanov, G. Morfill, Shock waves and solitons in complex (dusty) plasmas, in: M.D. Furnish, Y.M. Gupta, J.W. Forbes (Eds.), *Shock compression of condensed matter-2003*, AIP, New York, 2004, pp. 111–114.
- [266] D. Samsonov, S. Zhdanov, G. Morfill, Vertical wave packets observed in a crystallized hexagonal monolayer complex plasmas, *Phys. Rev. E* 71 (2005) 026410/1–7.
- [267] C. Thompson, A. Barkan, N. D’Angelo, R.L. Merlino, Dust acoustic waves in a direct current glow discharge, *Phys. Plasmas* 4 (1997) 2331–2335.
- [268] R.L. Merlino, A. Barkan, C. Thompson, N. D’Angelo, Laboratory studies of waves and instabilities in dusty plasmas, *Phys. Plasmas* 5 (1998) 1607–1614.
- [269] Q.-Z. Luo, N. D’Angelo, R.L. Merlino, Experimental study of shock formation in a dusty plasma, *Phys. Plasmas* 6 (1999) 3455–3458.



- [270] Q.-Z. Luo, N. D'Angelo, R.L. Merlino, Ion acoustic shock formation in a converging magnetic field geometry, *Phys. Plasmas* 7 (2000) 2370–2373.
- [271] A. Melzer, S. Nunomura, D. Samsonov, Z.W. Ma, J. Goree, Laser-excited Mach cones in a dusty plasma crystal, *Phys. Rev. E* 62 (2000) 4162–4168.
- [272] A. Piel, V. Nosenko, J. Goree, Experiments and molecular-dynamics simulation of elastic waves in a plasma crystal radiated from a small dipole source, *Phys. Rev. Lett.* 89 (2002) 085004/1–4.
- [273] V. Nosenko, S. Nunomura, J. Goree, Nonlinear compression pulses in a 2D crystallized dusty plasma, *Phys. Rev. Lett.* 88 (2002) 215002/1–4.
- [274] S. Nunomura, S. Zhdanov, G.E. Morfill, J. Goree, Nonlinear longitudinal waves in a two-dimensional screened Coulomb crystal, *Phys. Rev. E* 68 (2003) 026407/1–7.
- [275] B. Liu, K. Avinash, J. Goree, Transverse optical mode in a one-dimensional Yukawa chain, *Phys. Rev. Lett.* 91 (2003) 255003/1–4.
- [276] V. Nosenko, K. Avinash, J. Goree, B. Liu, Nonlinear interaction of compressional waves in a 2D dusty plasma crystal, *Phys. Rev. Lett.* 92 (2004) 085001/1–4.
- [277] L.M. Vasilyak, S.P. Vetchinin, D.N. Polyakov, V.E. Fortov, Cooperative formation of dust structures in a plasma, *JETP* 94 (2002) 521–524.
- [278] L.M. Vasilyak, M.N. Vasil'ev, S.P. Vetchinin, D.N. Polyakov, V.E. Fortov, The action of an electron beam on dust structures in a plasma, *JETP* 96 (2003) 440–443.
- [279] D. Samsonov, G. Morfill, H. Thomas, T. Hagl, H. Rothermel, V. Fortov, A. Lipaev, V. Molotkov, A. Nefedov, O. Petrov, A. Ivanov, S. Krikalev, Kinetic measurements of shock wave propagation in a three-dimensional complex (dusty) plasma, *Phys. Rev. E* 67 (2003) 036404/1–5.
- [280] V.E. Fortov, O.F. Petrov, V.I. Molotkov, M.Y. Poustylnik, V.M. Torchinsky, A.G. Khrapak, A.V. Chernyshev, Large-amplitude dust waves excited by the gas-dynamic impact in a dc glow discharge plasma, *Phys. Rev. E* 69 (2004) 016402/1–5.
- [281] V.N. Tsytovich, U. de Angelis, R. Bingham, Low-frequency responses and wave dispersion in dusty plasmas, *Phys. Rev. Lett.* 87 (2001) 185003/1–4.
- [282] V.N. Tsytovich, U. de Angelis, R. Bingham, Low frequency responses, waves and instabilities in dusty plasmas, *Phys. Plasmas* 9 (2002) 1079–1090.
- [283] O. Havnes, C.K. Goertz, G.E. Morfill, E. Grün, W. Ip, Dust charges, cloud potential, and instabilities in a dust cloud embedded in a plasma, *J. Geophys. Res. A* 92 (1987) 2281–2293.
- [284] P.K. Shukla, V.P. Silin, Dust ion-acoustic wave, *Phys. Scripta* 45 (1992) 508.
- [285] A. Barkan, N. D'Angelo, R.L. Merlino, Experiments on ion-acoustic waves in dusty plasmas, *Planet. Space Sci.* 44 (1996) 239–242.
- [286] A. Barkan, N. D'Angelo, R.L. Merlino, Potential relaxation instability and ion acoustic waves in a single-ended Q-machine dusty plasma, *Phys. Lett. A* 222 (1996) 329–332.
- [287] N.N. Rao, P.K. Shukla, M.Y. Yu, Dust-acoustic waves in dusty plasmas, *Planet. Space Sci.* 38 (1990) 543–546.
- [288] F. Melandsø, T. Aslaksen, O. Havnes, A new damping effect for the dust-acoustic wave, *Planet. Space Sci.* 41 (1993) 321–325.
- [289] A.V. Ivlev, G. Morfill, Acoustic modes in a collisional dusty plasma: effect of the charge variation, *Phys. Plasmas* 7 (2000) 1094–1102.
- [290] M. Rosenberg, Ion- and dust-acoustic instabilities in dusty plasmas, *Planet. Space Sci.* 41 (1993) 229–233.
- [291] S.I. Popel, S.N. Andreev, A.A. Gisko, A.P. Golub', T.V. Losseva, Dissipative processes during the propagation of nonlinear dust ion-acoustic perturbations, *Plasma Phys. Rep.* 30 (2004) 314–329.
- [292] R.K. Varma, P.K. Shukla, V. Krishan, Electrostatic oscillations in the presence of grain-charge perturbations in dusty plasmas, *Phys. Rev. E* 47 (1993) 3612–3616.
- [293] M.R. Jana, A. Sen, P.K. Kaw, Collective effects due to charge-fluctuations dynamics in a dusty plasma, *Phys. Rev. E* 48 (1993) 3930–3933.
- [294] J.-X. Ma, M.Y. Yu, Self-consistent theory of ion acoustic waves in a dusty plasma, *Phys. Plasmas* 1 (1994) 3520–3522.
- [295] N. D'Angelo, Ion-acoustic waves in dusty plasmas, *Planet. Space Sci.* 42 (1994) 507–511.
- [296] N. D'Angelo, Ionization instability in dusty plasmas, *Phys. Plasmas* 4 (1997) 3422–3426.
- [297] X. Wang, A. Bhattacharjee, S.K. Gou, J. Goree, Ionization instabilities and resonant acoustic modes, *Phys. Plasmas* 8 (2001) 5018–5024.
- [298] R.L. Merlino, Current-driven dust ion-acoustic instability in a collisional dusty plasma, *IEEE Trans. Plasma Sci.* 25 (1997) 60–65.
- [299] B. Annou, Current-driven dust ion-acoustic instability in a collisional dusty plasma with a variable charge, *Phys. Plasmas* 5 (1998) 2813–2814.
- [300] M. Rosenberg, Ion-dust streaming instability in processing plasmas, *J. Vac. Sci. Technol. A* 14 (1996) 631–633.
- [301] N. D'Angelo, R.L. Merlino, Current-driven dust-acoustic instability in a collisional plasma, *Planet. Space Sci.* 44 (1996) 1593–1598.
- [302] P. Kaw, R. Singh, Collisional instabilities in a dusty plasma with recombination and ion-drift effects, *Phys. Rev. Lett.* 79 (1997) 423–426.
- [303] A.A. Mamun, P.K. Shukla, Streaming instabilities in a collisional dusty plasma, *Phys. Plasmas* 7 (2000) 4412–4417.
- [304] M. Rosenberg, A note on ion-dust streaming instability in a collisional dusty plasma, *J. Plasma Phys.* 67 (2002) 235–242.
- [305] G. Joyce, M. Lampe, G. Ganguli, Instability-triggered phase transition to a dusty-plasma condensate, *Phys. Rev. Lett.* 88 (2002) 095006/1–4.
- [306] K.N. Ostrikov, S.V. Vladimirov, M.Y. Yu, G.E. Morfill, Low-frequency dispersion properties of plasmas with variable-charge impurities, *Phys. Plasmas* 7 (2000) 461–465.
- [307] G. Kalman, K.I. Golden, Response function and plasmon dispersion for strongly coupled Coulomb liquids, *Phys. Rev. A* 41 (1990) 5516–5527.
- [308] M. Rosenberg, G. Kalman, Dust acoustic waves in strongly coupled dusty plasmas, *Phys. Rev. E* 56 (1997) 7166–7173.
- [309] G. Kalman, M. Rosenberg, H.E. DeWitt, Collective modes in strongly correlated Yukawa liquids: waves in dusty plasmas, *Phys. Rev. Lett.* 84 (2000) 6030–6033.
- [310] M.S. Murillo, Static local field correction description of acoustic waves in strongly coupling dusty plasmas, *Phys. Plasmas* 5 (1998) 3116–3121.
- [311] M.S. Murillo, Longitudinal collective modes of strongly coupled dusty plasmas at finite frequencies and wave vectors, *Phys. Plasmas* 7 (2000) 33–38.

- [312] P.K. Kaw, A. Sen, Low frequency modes in strongly coupled dusty plasmas, *Phys. Plasmas* 5 (1998) 3552–3559.
- [313] P.K. Kaw, Collective modes in a strongly coupled dusty plasma, *Phys. Plasmas* 8 (2001) 1870–1878.
- [314] B.S. Xie, M.Y. Yu, Dust acoustic waves in strongly coupled dissipative plasmas, *Phys. Rev. E* 62 (2000) 8501–8507.
- [315] D. Winske, M.S. Murillo, M. Rosenberg, Numerical simulation of dust–acoustic waves, *Phys. Rev. E* 59 (1999) 2263–2272.
- [316] H. Ohta, S. Hamaguchi, Wave dispersion relations in Yukawa fluids, *Phys. Rev. Lett.* 84 (2000) 6026–6029.
- [317] Ya.I. Frenkel, *Kinetic Theory of Liquids*, Clarendon, Oxford, 1946.
- [318] R.T. Farouki, S. Hamaguchi, Thermodynamics of strongly-coupled Yukawa systems near the one-component-plasma limit. II. Molecular dynamics simulations, *J. Chem. Phys.* 101 (1994) 9885–9893.
- [319] W.L. Slattery, G.D. Doolen, H.E. DeWitt, Improved equation of state for the classical one-component plasma, *Phys. Rev. A* 26 (1980) 2087–2095.
- [320] S. Ichimaru, H. Iyetomi, S. Tanaka, Statistical physics of dense plasmas: Thermodynamics, transport coefficients and dynamic correlations, *Phys. Rep.* 149 (1987) 91–205.
- [321] T. Saigo, S. Hamaguchi, Shear viscosity of strongly coupled Yukawa systems, *Phys. Plasmas* 9 (2002) 1210–1216.
- [322] G. Salin, J.-M. Caillol, Transport coefficients of the Yukawa one-component plasma, *Phys. Rev. Lett.* 88 (2002) 065002/1–4.
- [323] G. Salin, J.-M. Caillol, Equilibrium molecular dynamics simulations of the transport coefficients of the Yukawa one component plasma, *Phys. Plasmas* 10 (2003) 1220–1230.
- [324] V. Nosenko, J. Goree, Shear flows and shear viscosity in a two-dimensional Yukawa system (dusty) plasma, *Phys. Rev. Lett.* 93 (2004) 155004/1–4.
- [325] J. Pramanik, G. Prasad, A. Sen, P.K. Kaw, Experimental observations of transverse shear waves in strongly coupled dusty plasmas, *Phys. Rev. Lett.* 88 (2002) 175001/1–4.
- [326] A. Mishra, P.K. Kaw, A. Sen, Instability of shear waves in an inhomogeneous strongly coupled dusty plasma, *Phys. Plasmas* 8 (2000) 3188–3193.
- [327] C. Kittel, *Introduction to Solid State Physics*, Wiley, New York, 1976.
- [328] F. Melandsø, Lattice waves in dust plasma crystals, *Phys. Plasmas* 3 (1996) 3890–3901.
- [329] F.M. Peeters, X. Wu, Wigner crystal of a screened-Coulomb-interaction colloidal system in two dimensions, *Phys. Rev. A* 35 (1987) 3109–3114.
- [330] D.H.E. Dubin, The phonon wake behind a charge moving relative to a two-dimensional plasma crystal, *Phys. Plasmas* 7 (2000) 3895–3903.
- [331] X. Wang, A. Bhattacharjee, S. Hu, Longitudinal and transverse waves in Yukawa crystals, *Phys. Rev. Lett.* 86 (2001) 2569–2572.
- [332] S. Zhdanov, R.A. Quinn, D. Samsonov, G.E. Morfill, Large-scale steady-state structure of a 2D plasma crystal, *New J. Phys.* 5 (2003) 74.1–74.11.
- [333] S.V. Vladimirov, P.V. Shevchenko, N.F. Cramer, Vibrational modes in the dust–plasma crystal, *Phys. Rev. E* 56 (1997) R74–R76.
- [334] K. Qiao, T.W. Hyde, Dispersion properties of the out-of-plane transverse wave in a two-dimensional Coulomb crystal, *Phys. Rev. E* 68 (2003) 046403/1–5.
- [335] B.M. Annaratone, T. Antonova, D.D. Goldbeck, H.M. Thomas, G.E. Morfill, Complex-plasma manipulation by radiofrequency biasing, *Plasma Phys. Control. Fusion* 46 (2004) B495–B510.
- [337] M.O. Robbins, K. Kremer, G.S. Grest, Phase diagram and dynamics of Yukawa systems, *J. Chem. Phys.* 88 (1988) 3286–3312.
- [338] G.J. Kalman, M. Rosenberg, Instabilities in strongly coupled plasmas, *J. Phys. A: Math. Gen.* 36 (2003) 5963–5969.
- [339] F. Melandsø, Heating and phase transitions of dust–plasma crystals in a flowing plasma, *Phys. Rev. E* 55 (1997) 7495–7506.
- [340] V.A. Schweigert, I.V. Schweigert, A. Melzer, A. Homann, A. Piel, Plasma crystal melting: a nonequilibrium phase transition, *Phys. Rev. Lett.* 80 (1998) 5345–5348.
- [341] A.V. Ivlev, G. Morfill, Anisotropic dust lattice modes, *Phys. Rev. E* 63 (2000) 016409/1–3.
- [342] I.V. Schweigert, V.A. Schweigert, A. Melzer, A. Piel, Melting of dust plasma crystals with defects, *Phys. Rev. Lett.* 62 (2000) 1238–1244.
- [343] V.I. Karpman, *Nonlinear Waves in Dispersive Media*, Pergamon, Oxford, 1975.
- [344] R.Z. Sagdeev, Cooperative phenomena and shock waves in collisionless plasmas, in: M.A. Leontovich (Ed.), *Reviews of Plasma Physics*, vol. 4, Consultants Bureau, New York, 1966, pp. 23–93.
- [345] P.K. Shukla, Nonlinear waves and structures in dusty plasmas, *Phys. Plasmas* 10 (2003) 1619–1627.
- [346] R. Pillay, R. Bharuthram, Large amplitude solitons in a multi-species electron–positron plasma, *Astrophys. Space Sci.* 198 (1992) 85–93.
- [347] R. Bharuthram, P.K. Shukla, Large amplitude ion-acoustic solitons in a dusty plasma, *Planet Space Sci.* 40 (1992) 973–977.
- [348] G.O. Ludwig, J.L. Ferreira, Y. Nakamura, Observation of ion-acoustic rarefaction solitons in a multicomponent plasma with negative ions, *Phys. Rev. Lett.* 52 (1984) 275–278.
- [349] Y. Nakamura, Observation of large-amplitude ion acoustic solitary waves in a plasma, *J. Plasma Phys.* 38 (1987) 461–471.
- [350] S.I. Popel, A.P. Golub', T.V. Losseva, A.V. Ivlev, S.A. Khrapak, G. Morfill, Weakly dissipative dust ion–acoustic solitons, *Phys. Rev. E* 67 (2003) 056402/1–5.
- [351] S.I. Popel, A.P. Golub', T.V. Losseva, Dust ion-acoustic shock-wave structures: theory and laboratory experiments, *JETP Lett.* 74 (2001) 362–366.
- [352] R.J. Taylor, D.R. Baker, H. Ikezi, Observation of collisionless electrostatic shocks, *Phys. Rev. Lett.* 24 (1970) 206–209.
- [353] S.K. Zhdanov, D. Samsonov, G.E. Morfill, Anisotropic plasma crystal solitons, *Phys. Rev. E* 66 (2002) 026411/1–11.
- [354] A.V. Ivlev, S.K. Zhdanov, G.E. Morfill, Coupled dust–lattice solitons in monolayer plasma crystals, *Phys. Rev. E* 68 (2003) 066402/1–4.
- [355] F. Verheest, Nonlinear dust–acoustic waves in multispecies dusty plasmas, *Planet Space Sci.* 40 (1992) 1–6.
- [356] A.A. Mamun, R.A. Cairns, P.K. Shukla, Solitary potentials in dusty plasmas, *Phys. Plasmas* 3 (1996) 702–704.
- [357] J.X. Ma, J. Liu, Dust–acoustic soliton in a dusty plasma, *Phys. Plasmas* 4 (1997) 253–255.
- [358] B. Xie, K. He, Z. Huang, Dust–acoustic solitary waves and double layers in dusty plasma with variable dust charge and two-temperature ions, *Phys. Plasmas* 6 (1999) 3808–3816.



- [359] A.V. Ivlev, G. Morfill, Dust acoustic solitons with variable particle charge: role of ion distribution, *Phys. Rev. E* 63 (2001) 026412/1-5.
- [360] F. Melandsø, P.K. Shukla, Theory of dust–acoustic shocks, *Planet. Space Sci.* 43 (1995) 635–648.
- [361] S.I. Popel, M.Y. Yu, V.N. Tsytovich, Shock waves in plasmas containing variable-charge impurities, *Phys. Plasmas* 3 (1996) 4313–4315.
- [362] O. Havnes, T. Aslaksen, T.W. Hartquist, F. Li, F. Melandsø, G.E. Morfill, T. Nitter, Probing the properties of planetary ring dust by the observation of Mach cones, *J. Geophys. Res.* 100 (1995) 1731–1734.
- [363] O. Havnes, F. Li, F. Melandsø, T. Aslaksen, T.W. Hartquist, G.E. Morfill, T. Nitter, V. Tsytovich, Diagnostic of dusty plasma conditions by the observation of Mach cones caused by dust acoustic waves, *J. Vac. Sci. Technol. A* 14 (1996) 525–528.
- [364] V.A. Schweigert, I.V. Schweigert, V. Nosenko, J. Goree, Acceleration and orbits of charged particles beneath a monolayer plasma crystal, *Phys. Plasmas* 9 (2002) 4465–4472.
- [365] V. Nosenko, J. Goree, Z.W. Ma, D.H.E. Dubin, A. Piel, Compressional and shear wakes in a two-dimensional dusty plasma crystal, *Phys. Rev. E* 68 (2003) 056409/1-15.
- [366] V. Nosenko, J. Goree, Z.W. Ma, A. Piel, Observation of shear-wave Mach cones in a 2D dusty-plasma crystal, *Phys. Rev. Lett.* 88 (2002) 135001/1-4.
- [367] S.K. Zhdanov, G.E. Morfill, D. Samsonov, M. Zuzic, O. Havnes, Origin of the curved nature of Mach cone wings in complex plasmas, *Phys. Rev. E* 69 (2004) 026407/1-7.
- [368] K. Kremer, M.O. Robbins, G.S. Grest, Phase diagram of Yukawa systems: model for charge-stabilized colloids, *Phys. Rev. Lett.* 57 (1986) 2694–2697.
- [369] M.J. Stevens, M.O. Robbins, Melting of Yukawa systems: a test of phenomenological melting criteria, *J. Chem. Phys.* 98 (1993) 2319–2324.
- [370] S. Hamaguchi, R.T. Farouki, D.H.E. Dubin, Triple point of Yukawa systems, *Phys. Rev. E* 56 (1997) 4671–4682.
- [371] E.J. Meijer, D. Frenkel, Melting line of Yukawa system by computer simulation, *J. Chem. Phys.* 94 (1991) 2269–2271.
- [372] O.S. Vaulina, S.A. Khrapak, Simulation of the dynamics of strongly interacting macroparticles in a weakly ionized plasma, *JETP* 92 (2001) 228–234.
- [373] O. Vaulina, S. Khrapak, G. Morfill, Universal scaling in complex (dusty) plasmas, *Phys. Rev. E* 66 (2002) 016404/1-5.
- [374] H. Ohta, S. Hamaguchi, Molecular dynamics evaluation of self-diffusion in Yukawa systems, *Phys. Plasmas* 7 (2000) 4506–4514.
- [375] O.S. Vaulina, S.A. Khrapak, Scaling law for the fluid-solid phase transition in Yukawa systems (dusty plasmas), *JETP* 90 (2000) 287–289.
- [376] S. Ichimaru, Strongly coupled plasmas: high-density classical plasmas and degenerate electron fluids, *Rev. Mod. Phys.* 54 (1982) 1017–1059.
- [377] D.H.E. Dubin, First-order anharmonic correction to the free energy of Coulomb crystal in periodic boundary conditions, *Phys. Rev. A* 42 (1990) 4972–4982.
- [378] R.T. Farouki, S. Hamaguchi, Thermal energy of crystalline one-component plasma from dynamical simulation, *Phys. Rev. E* 47 (1993) 4330–4336.
- [379] F.A. Lindemann, The calculation of molecular vibration frequencies, *Z. Phys.* 11 (1910) 609–612.
- [380] J.P. Hansen, L. Verlet, Phase transitions of the Lennard–Jones system, *Phys. Rev.* 184 (1969) 151–161.
- [381] H. Löwen, T. Palberg, R. Simon, Dynamical criterion for freezing of colloidal liquids, *Phys. Rev. Lett.* 70 (1993) 1557–1560.
- [382] H. Löwen, Dynamical criterion for two-dimension freezing, *Phys. Rev. E* 53 (1996) R29–R32.
- [383] H.M. Thomas, G.E. Morfill, Solid/liquid/gaseous phase transitions in plasma crystals, *J. Vac. Sci. Technol. A* 14 (1996) 501–505.
- [384] A. Melzer, A. Homann, A. Piel, Experimental investigation of the melting transition of the plasma crystal, *Phys. Rev. E* 53 (1996) 2757–2766.
- [385] R.A. Quinn, C. Cui, J. Goree, J.B. Pieper, H. Thomas, G.E. Morfill, Structural analysis of a Coulomb lattice in a dusty plasma, *Phys. Rev. E* 53 (1996) 2049–2052.
- [386] O. Arp, D. Block, A. Piel, Dust Coulomb balls: three-dimensional plasma crystals, *Phys. Rev. Lett.* 93 (2004) 165004/1-4.
- [387] G.E. Morfill, H. Thomas, Plasma crystal, *J. Vac. Sci. Technol. A* 14 (1996) 490–495.
- [388] M. Rubin-Zuzic, G.E. Morfill, H.M. Thomas, A.V. Ivlev, B.A. Klumov, H. Rothermel, W. Bunk, R. Pompl, O. Havnes, A. Fouqué, Kinetic development of crystallisation fronts in complex plasmas, submitted to *Nature*.
- [389] B. Voigtländer, T. Weber, P. Smilauer, D.E. Wolf, Transition from island growth to step-flow growth for Si/Si(100) epitaxy, *Phys. Rev. Lett.* 78 (1997) 2164–2167.
- [390] M. Kästner, B. Voigtländer, Kinetically self-limiting growth of Ge islands on Si(001), *Phys. Rev. Lett.* 82 (1999) 2745–2748.
- [391] J.P. Hansen, I. McDonald, *Theory of Simple Liquids*, Academic, New York, 1986.
- [392] R.O. Rosenberg, D. Thirumalai, Structure and dynamics of screened-Coulomb colloidal liquids, *Phys. Rev. A* 33 (1986) 4473–4476.
- [393] K. Kremer, G.S. Grest, M.O. Robbins, Dynamics of supercooled liquids interacting with a repulsive Yukawa potential, *J. Phys. A: Math. Gen.* 20 (1987) L181–L187.
- [394] O.S. Vaulina, S.V. Vladimirov, Diffusion and dynamics of macro-particles in a complex plasma, *Phys. Plasmas* 9 (2002) 835–840.
- [395] J. Beran, *Statistics for Long-Memory Processes*, Chapman & Hall, New York, 1994.
- [396] S. Hergarten, *Self-Organized Criticality in Earth Systems*, Springer, Berlin, 2002.
- [397] W. Paul, J. Baschnagel, *Stochastic Processes, From Physics to Finance*, Springer, Berlin, 1999.
- [398] E. Lutz, Fractional Transport equations for Lévy stable processes, *Phys. Rev. Lett.* 86 (2001) 2208–2211.
- [399] E. Lutz, Fractional Langevin equation, *Phys. Rev. E* 64 (2001) 051106/1-4.
- [400] J.-P. Bouchaud, A. Georges, Anomalous diffusion in disordered media: statistical mechanisms, models and physical applications, *Phys. Rep.* 195 (1990) 127–293.
- [401] R. Metzler, J. Klafter, The random walk’s guide to anomalous diffusion: a fractal dynamics approach, *Phys. Rep.* 339 (2000) 1–77.
- [402] G.M. Zaslavsky, *Hamiltonian Chaos & Fractional Dynamics*, Oxford University Press, Oxford, 2005.
- [403] S. Ratynskaia, C. Knapek, K. Rypdal, S. Khrapak, G.E. Morfill, Statistics of particle transport in a two-dimensional dusty plasma cluster, *Phys. Plasmas* 12 (2005) 022302/1-11.
- [404] Wen-Tau Juan, L. I, Anomalous diffusion in strongly coupled quasi-2D dusty plasmas, *Phys. Rev. Lett.* 80 (1998) 3073–3076.

- [405] Wen-Tau Juan, Ming-Heng Chen, L. I, Nonlinear transports and microvortex excitations in sheared quasi-two-dimensional dust Coulomb liquids, *Phys. Rev. E* 64 (2001) 016402/1-5.
- [406] Y.-J. Lai, L. I, Avalanche excitations of fast particles in quasi-2D cold dusty-plasma liquids, *Phys. Rev. Lett.* 89 (2002) 155002/1-4.
- [407] W.-Y. Woon, L. I, Defect turbulence in quasi-2D creeping dusty-plasma liquids, *Phys. Rev. Lett.* 92 (2004) 065003/1-4.
- [408] A. Gavrikov, I. Shakhova, A. Ivanov, O. Petrov, N. Vorona, V. Fortov, Experimental study of laminar flow in dusty plasma liquid, *Phys. Lett. A* 336 (2005) 378–383.
- [409] G.E. Morfill, M. Rubin-Zuzic, H. Rothermel, A.V. Ivlev, B.A. Klumov, H.M. Thomas, U. Konopka, Highly resolved fluid flows: “liquid plasmas” at the kinetic level, *Phys. Rev. Lett.* 92 (2004) 175004/1-4.
- [410] M. Lesieur, *Turbulence in Fluids*, Kluwer, Dordrecht, 1991.
- [411] S.L. Gilbert, J.J. Bollinger, D.J. Wineland, Shell-structure phase of magnetically confined strongly coupled plasmas, *Phys. Rev. Lett.* 60 (1988) 2022–2025.
- [412] D.H.E. Dubin, T.M. O’Neil, Trapped nonneutral plasmas, liquids, and crystals (the thermal equilibrium states), *Rev. Mod. Phys.* 71 (1999) 87–172.
- [413] D.G. Grier, C.A. Murray, The microscopic dynamics of freezing in supercooled colloidal fluids, *J. Chem. Phys.* 100 (1994) 9088–9095.
- [414] P. Leiderer, W. Ebner, V.B. Shikin, Macroscopic electron dimples on the surface of liquid helium, *Surf. Sci.* 113 (1987) 405–411.
- [415] R.C. Ashoori, Electrons in artificial atoms, *Nature* 379 (1996) 413–419.
- [416] L. Candido, J.-P. Rino, N. Studart, F.M. Peeters, The structure and spectrum of the anisotropically confined two-dimensional Yukawa system, *J. Phys.: Condens. Matter* 10 (1998) 11627–11644.
- [417] V.M. Bedanov, F.M. Peeters, Ordering and phase transitions of charged particles in a classical finite two-dimensional system, *Phys. Rev. B* 49 (1994) 2667–2676.
- [418] V.A. Schweigert, F.M. Peeters, Spectral properties of classical two-dimensional clusters, *Phys. Rev. B* 51 (1995) 7700–7713.
- [419] Y.-J. Lai, L. I, Packings and defects of strongly coupled two-dimensional Coulomb clusters: numerical simulation, *Phys. Rev. E* 60 (1999) 4743–4753.
- [420] G.E. Astrakharchik, A.I. Belousov, Y.E. Lozovik, Properties of two-dimensional dusty plasma clusters, *Phys. Lett. A* 258 (1999) 123–130.
- [421] G.E. Astrakharchik, A.I. Belousov, Y.E. Lozovik, Two-dimensional mesoscopic dusty plasma clusters: structure and phase transitions, *JETP* 89 (1999) 696–703.
- [422] H. Totsuji, Structure and melting of two-dimensional dust crystals, *Phys. Plasmas* 8 (2001) 1856–1862.
- [423] H. Totsuji, C. Totsuji, K. Tsuruta, Structure of finite two-dimensional Yukawa lattices: dust crystals, *Phys. Rev. E* 64 (2001) 066402/1-7.
- [424] J.A. Drocco, C.J.O. Reichhardt, C. Reichhardt, B. Janko, Structure and melting of two-species clusters in a parabolic trap, *Phys. Rev. E* 68 (2003) 060401/1-4.
- [425] R. Ichiki, Y. Ivanov, M. Wolter, Y. Kawai, A. Melzer, Melting and heating of two-dimensional Coulomb clusters in dusty plasmas, *Phys. Rev. E* 70 (2004) 066404/1-4.
- [426] W.-T. Juan, Z.-H. Huang, J.-W. Hsu, Y.-J. Lai, L. I, Observation of dust Coulomb clusters in a plasma trap, *Phys. Rev. E* 58 (1998) R6947–R6950.
- [427] M. Klindworth, A. Melzer, A. Piel, Laser-excited intershell rotation of finite Coulomb clusters in a dusty plasma, *Phys. Rev. B* 61 (2000) 8404–8415.
- [428] F. Cheung, A. Samarian, B. James, Angular velocity saturation in planar dust cluster rotation, *Phys. Scripta* T107 (2004) 229–232.
- [429] A. Melzer, M. Klindworth, A. Piel, Normal modes of 2D finite clusters in complex plasmas, *Phys. Rev. Lett.* 87 (2001) 115002/1-4.
- [430] S.G. Amiranashvili, N.G. Gusein-Zade, V.N. Tsyrovich, Spectral properties of small dusty clusters, *Phys. Rev. E* 64 (2001) 016407/1-6.
- [431] A. Melzer, Mode spectra of thermally excited two-dimensional dust Coulomb clusters, *Phys. Rev. E* 67 (2003) 016411/1-10.
- [432] M. Kong, B. Partoens, A. Matulis, F.M. Peeters, Structure and spectrum of two-dimensional clusters confined in a hard wall potential, *Phys. Rev. E* 69 (2004) 036412/1-10.
- [433] B.M. Annaratone, M. Glier, T. Stuffer, M. Raif, H.M. Thomas, G.E. Morfill, The plasma-sheath boundary near the adaptive electrode as traced by particles, *New J. Phys.* 5 (2003) 92.1–92.12.
- [434] C.L. Rhykerd, M. Schoen, D.J. Diestler, J.H. Cushman, Epitaxy in simple classical fluids in micropores and near-solid surfaces, *Nature (London)* 330 (1987) 461–463.
- [435] P.A. Thompson, G.S. Grest, M.O. Robbins, Phase transitions and universal dynamics in confined films, *Phys. Rev. Lett.* 68 (1992) 3448–3451.
- [436] A.L. Demirel, S. Granick, Glasslike transition of a confined simple fluid, *Phys. Rev. Lett.* 77 (1996) 2261–2264.
- [437] J. Gao, W.D. Luedtke, U. Landman, Layering transitions and dynamics of confined liquid films, *Phys. Rev. Lett.* 79 (1997) 705–708.
- [438] M. Heuberger, M. Zöch, N.D. Spencer, Density fluctuations under confinement: when is a fluid not a fluid?, *Science* 292 (2001) 905–908.
- [439] L.W. Teng, P.S. Tu, L. I, Microscopic observation of confinement-induced layering and slow dynamics of dusty-plasma liquids in narrow channels, *Phys. Rev. Lett.* 90 (2003) 245004/1-4.
- [440] Y. Jiang, P.J. Swart, A. Saxena, M. Asipauskas, J.A. Glazier, Hysteresis and avalanches in two-dimensional foam rheology simulations, *Phys. Rev. E* 59 (1999) 5819–5832.
- [441] A. Kabla, G. Debrégeas, Local stress relaxation and shear banding in a dry foam under shear, *Phys. Rev. Lett.* 90 (2003) 258303/1-4.
- [442] J.B. Salmon, A. Colin, S. Manneville, F. Molino, Velocity profiles in shear-banding wormlike micelles, *Phys. Rev. Lett.* 90 (2003) 228303/1-4.
- [443] F. Varnik, L. Bocquet, J.-L. Barrat, L. Berthier, Shear localization in a model glass, *Phys. Rev. Lett.* 90 (2003) 095702/1-4.
- [444] C.-L. Chan, W.-Y. Woon, L. I, Shear banding in mesoscopic dusty plasma liquids, *Phys. Rev. Lett.* 93 (2004) 220602/1-4.
- [445] P.K. Shukla, A.A. Mamun, *Introduction to Dusty Plasma Physics*, IOP Publ., Bristol, 2001.
- [446] N. Sato, G. Uchida, R. Ozaki, S. Iizuka, Fine-particle Coulomb lattices formed and controlled in DC discharge plasmas, in: M. Horanyi, S. Robertson, B. Walch (Eds.), *Physics of Dusty Plasmas*, AIP, New York, 1998, pp. 239–246.
- [447] N. Sato, G. Uchida, R. Ozaki, S. Iizuka, T. Kamimura, in: Y. Nakamura, T. Yokota, P.K. Shukla (Eds.), *Frontiers in Dusty Plasmas*, Elsevier Science, Amsterdam, 2000, pp. 329–336.

- [448] N. Sato, G. Uchida, T. Kaneko, S. Shimizu, S. Iizuka, Dynamics of fine particles in magnetized plasmas, *Phys. Plasmas* 9 (2001) 387–390.
- [449] D. Samsonov, S. Zhdanov, G. Morfill, V. Steinberg, Levitation and agglomeration of magnetic grains in a complex (dusty) plasma with magnetic field, *New J. Phys.* 5 (2003) 24.1–24.10.
- [450] V.V. Yaroshenko, G.E. Morfill, D. Samsonov, S.V. Vladimirov, Mutual interactions of magnetized particles in complex plasmas, *New J. Phys.* 5 (2003) 18.1–18.8.
- [451] U. Mohideen, H.U. Rahman, M.A. Smith, M. Rosenberg, D.A. Mendis, Intergrain Coupling in dusty-plasma coulomb crystals, *Phys. Rev. Lett.* 81 (1998) 349–352.
- [452] V.I. Molotkov, A.P. Nefedov, M.Yu. Poustynnik, V.M. Torchinsky, V.E. Fortov, A.G. Khrapak, K. Yoshino, Liquid plasma crystal: Coulomb crystallization of cylindrical macroscopic grains in a gas-discharge plasma, *JETP Lett.* 71 (2000) 102–105.
- [453] B.M. Annaratone, A.G. Khrapak, A.V. Ivlev, G. Söllner, P. Bryant, R. Sütterlin, U. Konopka, K. Yoshino, M. Zuzic, H.M. Thomas, G.E. Morfill, Levitation of cylindrical particles in the sheath of rf plasma, *Phys. Rev. E* 63 (2001) 036406/1–6.
- [454] V.E. Fortov, A.G. Khrapak, V.I. Molotkov, A.P. Nefedov, M.Y. Poustynnik, V.M. Torchinsky, K. Yoshino, Behavior of rod-like dust particles in striations, *Proceedings of the XXV International Conference on Phenomena in Ionized Gases (ICPIG-2001)*, vol. 3, Nagoya, Japan, 17–22 July 2001, pp. 35–36.
- [455] S.V. Vladimirov, M. Nambu, Interaction of a rod-like charged macroparticle with a flowing plasma, *Phys. Rev. E* 64 (2001) 026403/1–7.
- [456] A.V. Ivlev, A.G. Khrapak, S.A. Khrapak, B.M. Annaratone, G. Morfill, K. Yoshino, Rod-like particles in gas discharge plasmas: theoretical model, *Phys. Rev. E* 68 (2003) 026403/1–10.
- [457] S.A. Maiorov, Charging of a rodlike grain in a plasma flow, *Plasma Phys. Rep.* 30 (2004) 766–771.
- [458] L.D. Landau, E.M. Lifshitz, *The Classical Theory of Fields*, Pergamon, Oxford, 1962.
- [459] L.D. Landau, E.M. Lifshitz, *Electrodynamics of Continuous Media*, Pergamon, Oxford, 1960.
- [460] S.V. Vladimirov, E.N. Tsoy, Oscillations in a chain of rod-shaped colloidal particles in a plasma, *Phys. Rev. E* 64 (2001) 035402(R)/1–4.
- [461] M.P. Hertzberg, S.V. Vladimirov, N.F. Cramer, Rotational modes of oscillation of rodlike dust grains in a plasma, *Phys. Rev. E* 68 (2003) 026402/1–8.
- [462] H. Kersten, H. Deutsch, E. Stoffels, W.W. Stoffels, G.M.W. Kroesen, Plasma-powder interaction: trends in application and diagnostics, *Int. J. Mass Spectrometry* 223–224 (2003) 313–325.
- [463] J. Winter, Dust in fusion devices—experimental evidence, possible sources and consequences, *Plasma Phys. Control. Fusion* 40 (1998) 1201–1210.
- [464] V.N. Tsytovich, J. Winter, On the role of dust in fusion devices, *Phys. Usp.* 41 (1998) 815–822.
- [465] J. Winter, G. Gebauer, Dust in magnetic confinement fusion devices and its impact on plasma operation, *J. Nucl. Mater.* 266 (1999) 228–233.
- [466] J. Winter, Dust: a new challenge in nuclear fusion research?, *Phys. Plasmas* 7 (2000) 3862–3866.
- [467] J. Winter, V.E. Fortov, A.P. Nefedov, Radioactive dust levitation and its consequences for fusion devices, *J. Nucl. Mater.* 290–293 (2001) 509–512.
- [468] S.I. Krashenninnikov, Y. Tomita, R.D. Smirnov, R.K. Janev, On dust dynamics in tokamak edge plasmas, *Phys. Plasmas* 11 (2004) 3141–3150.
- [469] J.D. Martin, M. Coppins, G.F. Counsell, Motion and lifetime of dust grains in a tokamak plasma, *J. Nuclear Mater.* 337–339 (2005) 114–118.
- [470] V.Y. Baranov, I.A. Belov, D.V. Dem'yanov, A.S. Ivanov, D.A. Mazalov, A.F. Pal', Y.V. Petrushevich, V.V. Pichugin, A.N. Starostin, A.V. Filippov, V.E. Fortov, Radioactive isotopes as source of energy in photovoltaic nuclear battery on basis of plasma-dust structures, in: V.Y. Baranov (Ed.), *Isotopes Properties: Production, and Applications* (in Russian), IzdAT, Moscow, 2000, pp. 626–641.
- [471] A.V. Filippov, A.F. Pal', A.N. Starostin, V.E. Fortov, O.F. Petrov, P.P. D'yachenko, V.A. Rykov, Atomic battery based on ordered dust-plasma structures, *Ukr. J. Phys.* 50 (2005) 137–143.
- [472] I. Langmuir, G. Found, A.F. Dittmer, A new type of electric discharge: the streamer discharge, *Science* 60 (1924) 392–394.
- [473] S.K. Zhdanov, A.V. Ivlev, G.E. Morfill, Non-Hamiltonian dynamics of grains with spatially varying charges, *Phys. Plasmas* 072312 (2005) 1–7.
- [474] A.V. Ivlev, S.K. Zhdanov, B.A. Klumov, G.E. Morfill, Generalized kinetic theory of ensembles with variable charges, *Phys. Plasmas* 092104 (2005) 1–8.